

IMPACT TRANSPORT ON THE MOON

A Dissertation

Submitted to the Faculty

of

Purdue University

by

Ya-Huei Huang

In Partial Fulfillment of the

Requirements for the Degree

of

Doctor of Philosophy

December 2018

Purdue University

West Lafayette, Indiana

THE PURDUE UNIVERSITY GRADUATE SCHOOL
STATEMENT OF DISSERTATION APPROVAL

Dr. Briony Horgan, Chair

Department of Earth, Atmospheric, and Planetary Sciences

Dr. Jay Melosh

Department of Earth, Atmospheric, and Planetary Sciences

Dr. James Richardson

Planetary Science Institute

Dr. Chris Andronicus

Department of Earth, Atmospheric, and Planetary Sciences

Dr. David Minton

Department of Earth, Atmospheric, and Planetary Sciences

Approved by:

Dr. Darryl Granger

Head of the School Graduate Program

To my beloved families and friends and life time here.

ACKNOWLEDGMENTS

Thanks to everyone that I met during the time I spent in Indiana, I would not have come this far without you all. I would like to express my enormous gratitude to all of people who helped and supported me during this period. I would like to especially thank my Ph.D. advisor, David Minton, for all of his support and advice. He has a strong work ethic and is one of the best mentors that I have ever worked with. His passion toward research and deep knowledge and perspective of the planetary science always inspire me to not give up. His brilliant ideas always motivate me to form new ideas on my own. I owe him a huge thank to his endless support and effort teaching me how to write better and also teaching me American idioms. He is also one of people that I know who loves learning and has a deep knowledge in a variety of topics. I would not have made it this far without his support and help. As well, I would like to thank Juliet Minton for her wonderful company during my research and advice on writing.

I thank Caleb Fassett for his great insight and bright ideas for how to interpret many of my simulation results. I thank Nicolle Zellner for her fascinating lunar impact glass spherule data, deep knowledge to $^{40}\text{Ar}/^{39}\text{Ar}$ dating method, as well as her prompt responses regarding my research questions. I thank Jay Melosh for his enthusiasm and brilliant thoughts to any question we come up with; he always sends out inspiring research papers. I also thank him for hosting Crater Café and bringing us Ellen's yummy cookies. I thank all the present and past members of Crater Café for exciting scientific discussions: Jenny Larson, Kelsey Warden, Alex Trowbridge, Brandon Johnson, Tim Bowling, Jordan Steckloff, Jordan Kendall, and Dave Blair. I thank Toshi Hirabayashi for his inspiring discussions and critical thinking during my research. I thank Briony Horgan for all her lovely and inspiring classes and her support of my research. I thank Chris Andronicus for his passion for petrology

regardless a planetary body and his help on my first postdoctoral job application. I thank Jim Richardson for allowing me to work on his code, CTEM, and his support of my research.

I am happy to thank my awesome Minton group colleagues, Andy Hesselbrock, Kevin Graves, Carlisle Wishard, and Jennifer Pouplin, the 2263 colleagues, Sheridan Ackiss, Jake Elliott, Marie McBride, Noel Scudder, Becky Smith, Laura Camila Chaves, and Prakhar Sinha. I would not have enjoyed much of my time in Indiana without you guys' laughs and conversations. I am happy to thank my friends, Mindy Lowery, Troy Lowery, Chin-Chai Huan (Hugo), Cathy Liu, Chuan-Hsun Li, Fangyu Hsu, Tuncer Asunakutlu, Chisa Fukusumi, Becky Bobick, Frank Fiarito, Collin Coffey, Sarah Wolf and my dear housemates, Kate Brubaker and Meaghan Murphy for their friendship and wonderful laughs and stories. Furthermore, I would like to thank all my friends, whose names are too many to list, for accompanying me during this journey.

Lastly, but most importantly, I would like to thank my mum, Huang Zhang Leng, sister, Ya-Ling Huang, my husband, Tsung-Han Lee, for always bearing with me. Also, I thank my parents-in-law, Bong-Che Lee and Sau-Chin Ting for always being there to support me pursuing my dreams. I have come a long way, and you guys are always there. Thank you all so much for the laughs and tears.

PREFACE

The texts of primary modeling results (chapters 3, 4 and 5) in this current thesis appear in the following previous publications from years of 2017 and 2018.

(Huang et al., 2017) Ya-Huei Huang, David A. Minton, Masatoshi Hirabayashi, Jacob R. Elliott, James R. Richardson, Caleb I. Fassett, Nicolle E. B. Zellner (2017), “Heterogeneous Impact Transport on the Moon.” *Journal of Geophysical Research: Planets*, 122, 1158-1180. (on Research Spotlight in *Eos*, June 7 2017)

(Huang et al., 2018) Ya-Huei Huang, David A. Minton, Nicolle E. B. Zellner, Masatoshi Hirabayashi, James R. Richardson, Caleb I. Fassett (2018), “No Change in the Recent Lunar Impact Flux Required Based on Modeling of Impact Glass Spherule Age Distributions.” *Geophysical Research Letters*, 45, 68056813. (On Daily News in *NewScientist*, “Why a rake on the moon messed up our theories of life on Earth”, September 14 2018 and News in *Phys.org*, “Age bias exists even in outer spacein samples collected by Apollo astronauts”, September 11 2018.)

The current thesis presents three primary modeling results based on four observed data sets from 1) Clementine Ultraviolet-visible (UV-VIS) light spectrometer multi-spectral data (Li and Mustard, 2000), 2) lunar in-situ samples and lunar meteorites (Rhodes, 1977; Marvin, 1978; Delano, 1986; Wentworth et al., 1979; Vaniman and Papike, 1977; Neal et al., 1994; Rhodes et al., 1977; Papike et al., 1976; Laul and Papike, 1980; Morris et al., 1983; Wentworth et al., 1994; Naney et al., 1976; Ridley et al., 1973; Kempa et al., 1980; Meyer et al., 1971; Norman et al., 2010; Korotev et al., 2003) (for lunar returned sample description refers to Lunar Sample Compendium website <https://curator.jsc.nasa.gov/lunar/samplecatalog/index.cfm>), 3) $^{40}\text{Ar}/^{39}\text{Ar}$

age measurements of Apollo impact glass spherules (Zellner et al., 2009; Zellner and Delano, 2015), and 4) assembled data sets of terrestrial impact melt products and microtektites (terrestrial analogue of lunar impact glass spherules) (Glass et al., 1997; Coney et al., 2010; Horton et al., 2007; Pope et al., 1999; Jéhanno et al., 1992; Schulte et al., 2003; Kyte et al., 1996; Fazio et al., 2014; Osae et al., 2005; Engelhardt et al., 1995).

Finally, Ya-Huei Huang was supported by Purdue Research Foundation Research Assistantship and NASA Earth and Space Science Fellowship between 2014 and 2018.

TABLE OF CONTENTS

	Page
LIST OF TABLES	xi
LIST OF FIGURES	xii
ABSTRACT	xx
1 INTRODUCTION	1
1.1 A brief history of lunar impact craters	2
1.2 Impact cratering mechanics	4
1.3 Morphology of impact craters	9
1.4 Lunar crater based chronology and the origin of a planetary cratered surface	12
1.5 Lunar origin and bombardment environment	16
1.6 The first billion lunar bombardment record and a relationship with returned samples	17
1.7 The last three billion years lunar bombardment record and a relation- ship with returned samples	22
2 METHODS	25
2.1 Introduction to CTEM	25
2.1.1 Background: A stochastic process of a cratered surface	27
2.1.2 Cratering and ejecta scaling model	30
2.2 Overview: A Three-Dimensional Regolith Transport Model	36
2.3 The Dynamic Stream Tube-Based Transport Model	37
2.4 Glass spherule production model	44
2.5 Impact shock pressure destruction	51
2.6 An Empirical Model for the Spatial Geometry of Crater Rays	53
2.7 A Vertical Mixing Model for Craters Under the Resolution Limit of CTEM	58
2.8 Modeling super-domain craters	61
3 HETEROGENEOUS IMPACT TRANSPORT ON THE MOON	65
3.1 Introduction	66
3.2 Two Sets of Contradictory Observational Constraints on Material Trans- port	71
3.3 Mare/Highland Boundary Diffusion Simulation	74
3.3.1 Mare/Highlands Contact Simulation Setup	75
3.3.2 Results of Our Mare/Highland Contact Simulations	80

	Page
3.4 Implications of Our Impact Transport Model for Evolution of Lunar Surface Materials	84
3.5 Conclusion	87
4 NO CHANGE IN THE RECENT LUNAR IMPACT FLUX REQUIRED BASED ON MODELING OF IMPACT GLASS SPHERULE AGE DIS- TRIBUTIONS	95
4.1 Introduction	95
4.2 Lunar impact glass spherule simulation modeling	98
4.2.1 Constraining lunar impact glass spherule production	99
4.2.2 Evaluating the importance of spherule breakage by high velocity landing	106
4.2.3 Modeling the distribution of spherule ages in lunar soil samples	109
4.3 Results	111
4.4 Discussion and Conclusion	113
5 WHAT HAPPENED ON THE MOON 800 MILLION YEARS AGO? . . .	129
5.1 Introduction	130
5.2 Provenance Analysis of Observed “Exotic” Impact Glass Spherules . .	137
5.3 Materials and Methods	148
5.3.1 A possible size frequency distribution of Copernicus Crater- forming sesquinary craters	149
5.3.2 A possible glass spherule production of Copernicus Crater’s sesquinary	152
5.4 Results and Discussion	156
5.5 Conclusion	160
6 SUMMARY	167
REFERENCES	174

LIST OF TABLES

Table	Page
4.1 Data re-compilation of $^{40}\text{Ar}/^{39}\text{Ar}$ -derived age measurements of lunar impact glass spherules and shards	117
4.2 The data of size and spatial distribution of terrestrial microtektites.	124
4.3 The impact conditions using for estimating transient crater sizes in this study.	125
4.4 The data of size and spatial distribution of impact melt products.	126
4.5 The five Apollo soil samples with corresponding collected depth	127
5.1 Summary of provenance analysis and $^{40}\text{Ar}/^{39}\text{Ar}$ ages of fifteen “exotic” lunar impact glass spherules.	141
5.2 Summary of REBOUND simulation result on the fraction of our 1000 test particles remaining in geocentric orbit system of Earth and Moon.	150

LIST OF FIGURES

Figure	Page	
1.1	Release adiabat curves after a high shock pressure. The Rayleigh line is a straight line connecting the initial pressure and volume to the final pressure and volume (final shock state). The Hugoniot curve depicts shocked (compressed) materials in the P–V diagram, in which shock compression is irreversible. Release from high shock pressure follows the adiabatic trend in the P–V diagram (reversible process). The final volume of release from high shock pressure is larger than the initial volume (V_0) because a fraction of materials is melted. The difference between triangle-shaped area bound by the Rayleigh line and vertical line at specific volume of V and horizontal line at zero pressure and an area bound by the Hugoniot curve is approximately heat waste by shock. The diagram to the right shows different release curves for different shock states (shock state 1, 2, 3, and 4), and the final state of those release curves depending on a phase diagram (S: solid; L: liquid; V: vapor) for a given geological material. Modified from Figure 3.10 in (Melosh, 1989).	6
2.1	The provenance of an ejecta parcel within a transient crater. Streamlines within a transient crater are highlighted in red and blue colors. The redder the color of a streamline, the faster the ejection speed of a streamline. The magnitude of ejection speed of a streamline is represented by the length of arrow in black color. The length of arrow is arbitrary, but it gives a sense of that the closer to the impact point, the faster a streamline. Slower streamlines deposit as closer to the crater (continuous ejecta), and faster streamlines land at large distances (distal ejecta). A single block of ejecta occupying a single grid cell (pixel) is highlighted in red or blue, depending on the speed of streamlines. The volume of the ejecta block is determined by the volume of material bounded by the streamlines that exit with velocities $v_{min} < v < v_{max}$, which define a stream tube. The horizontal dotted lines denote notional layers of compositionally distinct material. The final composition of the ejecta block is determined by the mixture of material contained within the stream tube.	39

Figure	Page
<p>2.2 A schematic of a three-dimensional circular stream tube. (a) Stream tube in side view as well as its corresponding ejecta deposit. A stream tube is characterized by a circular section of radius (δr) of a stream tube at the emerging location and radial distance from the impact site to the emerging location (r_o). The red dot in the center of the stream tube is the emerging location. The solid line outlined triangle filled with light orange color is the projection area of a stream tube on the surface. The centerline inside the triangle represents a projection of an axis of a stream tube (dashed line in orange color). (b) Stream tube within the grid space of CTEM. The intersection points between the centerline of a stream tube on the surface and the grid lines are labeled by r_1 and r_2, which characterize a segment of a stream tube within a pixel space. The dashed lines represent that a stream tube is under the surface. The vertical and dotted lines in gray color at the intersection points attempt to guide readers to the interface of a stream tube with the virtual grid underneath, which are circles outlined in dashed line and red color. The star filled in yellow color is the intersection point that a segment of a stream tube encounters a layer under surface.</p>	40
<p>2.3 The schematic of our model glass spherule zone. The melt zone consists of the melt body (red) and the destruction zone producing new spherules (yellow). The survival zone is where preexisting spherules can be preserved. No spherules are recorded in the shock fragmentation zone. Streamlines are used to describe the continuous ejecta in a proximal region of crater while the distal ejecta are deposited at large distances. Ejecta can become glass spherule-bearing (layers 1 – 3). The labels starting with R and r are for derivation purpose.</p>	46
<p>2.4 The fraction of total ejected melts over total melt volume as a function of transient crater size in diameter. The dotted dash line is directly taken from Fig. 16 of (Cintala and Grieve, 1998), in which the calculation is based on impact velocity of 15 km/s, anorthositic target, and chondritic impactor. The solid and dash lines are from our study.</p>	48

Figure	Page	
2.5	Normalized peak shock pressure within a transient crater from different hydrocode simulations. The points marked “P” are from CTH simulations (Pierazzo et al., 1997), and the points marked “M” are from iSALE simulations (Monteux and Arkani-Hamed, 2016). The numbers indicate the impact velocity in km/s. M10(A) is a simulation with acoustic fluidization. The x-axis is the distance normalized by the radius of impactor within a transient crater, and the y-axis is the relative peak shock pressure. The two straight lines are exponential fits for asymptotic behaviors of shock pressures beyond the isobaric pressure zone, and the numbers are the fitted exponents.	53
2.6	Comparison between an actual rayed crater and a model rayed crater. (a) Example of a fresh crater (LROC stamp: M1136364148RE) with a radius of ~ 6 m in radius. (b) Regolith map of a crater with our crater ray model. The crater is 0.146 km in diameter at 10 m/pixel resolution. The flowery rays surrounding the continuous ejecta extend to 7 radii from the craters center, and the spike rays extends outward until the regolith thickness reaches the cutoff value of 10^8 m (not shown here). The variation in color represents the thickness of regolith (ejecta), ranging from none (black) to maximum (red).	57
2.7	The fraction of surface that mixes to a given depth for a time interval from our vertical mixing model for subpixelsized craters. The x axis is the mixing depth, and the y axis is the fraction of area that is mixed to that depth. Each curve is labeled with its corresponding time, 1 Myr, 10 Myr, 100 Myr, 1 Gyr, and 10 Gyr. For 1 Myr time interval, the probability of a surface that mixes to 1 cm (0.01 m) is <0.2 , yet in that time, the whole surface has already mixed to 1 mm. Note that the 10 Gyr period at this constant impact flux rate is equivalent to a 3.65 Ga age accounting for the exponentially higher impact rate prior to 3 Ga (Neukum et al., 2001).	62
3.1	Abundance of nonmare material as a function of sampling distance from the highland and mare contact as measured by Clementine, Apollo, and Luna missions. This plot is modified from (Rhodes, 1977, Figure 1), with the addition of Clementine UV/VIS camera data for Grimaldi Crater (solid line) that is directly taken from (Li and Mustard, 2000, Figure 6). The vertical line at zero distance in the x axis is the geological contact between anorthositic highlands on the left-hand side (shadowed in gray color) and mare on the right-hand side. The Apollo 11, 12, 15, and 17 and Luna 16 data are hand samples assembled by (Rhodes, 1977). Apollo 15 and 16 samples are compared with Clementine data for all four contacts in greater detail in the inset.	69

Figure	Page
3.2 Crater size frequency distributions for the western Mare Grimaldi region. The solid black line shows the Neukum Production Function (NPF) age of 3.2 Gyr, and the red line shows the crater counts produced in our simulation with CTEM. The open square points with one sigma Poisson error bar (\sqrt{N}) are based on crater counts from Greeley1993.	76
3.3 A schematic of cross section of modeled mare and highland contact in CTEM. The mare side with a finite thickness is marked as dark gray color, and the highland side is light gray color. The left-hand side figure shows the beginning of an impact cratering process across the contact (t_1), and the middle represents a scenario of large crater showing up at $t_2 > t_1$. Note that a large crater on the highland side is able to deliver highland material to mare side (dashed circle in yellow color). The closeup of this region where highland material deposits on the top of the mare side is shown in the left-hand side figure.	78
3.4 A schematic of our model cases. Case A (top figure) includes only proximal ejecta. Case B (middle-top figure) includes proximal ejecta and sub-pixel mixing process. Case C (middle-bottom figure) and Case D (bottom figure) includes proximal ejecta and distal ejecta but difference between these two cases are sub-pixel mixing process turned on in Case D. Note that l is the ejecta extent, R is the crater radius, and d is the depth of sub-pixel mixing over a period of time.	79
3.5 The mare fraction for Cases A, C, and D result (Li and Mustard, 2000, similar to Figure 5). Each image is 200 by 1000 pixels. The lower part of the image represents the mare side, and the brighter part is the highland side. Each fraction image represents our simulation cases of (a) Case A (proximal eject with no subpixel crater mixing), (b) Case C (proximal and distal ejecta with no subpixel crater mixing), and (c) Case D (proximal and distal ejecta with subpixel crater mixing). Note that these mare fraction maps will not visually match the appearance of contacts on the lunar surface because it does not take into account optical maturation of rays with time.	90

Figure	Page	
3.6	The compositional gradient profile of the average mare abundance (AMA) within a distance of 26 km from mare (left-hand side) and highland (right-hand side) contact. The black line represents the Clementine data for Grimaldi Crater by Li and Mustard (Li and Mustard, 2000, Figure 6). The solid square point in gray color in each box represents the mean AMA of the total 1441 profiles from each case of (a) Case A, (b) Case C, and (c) Case D. One standard deviation across the contact is shown by a vertical line at every solid square point. The solid points in orange and blue color are Apollo 15 and 17 in situ mare soil samples (Rhodes, 1977, Figure 1), respectively.	91
3.7	Compositional map of our global mare/highland contact run with all model components turned on. The simulation size is 6000 km by 6000 km (2000 by 2000 pixels). The yellow arrow points to a ray patch at an equivalent distance of the Apollo 12 sites from our simulated mare/highland contact. The inset on the left-hand side is the close-up of the ray patch and nonray region on the right-hand side. Inside close-up, the square white box on the top is nonray region, and the square white box on the bottom is almost the center of ray patch.	92
3.8	The exotic component (highland) distribution with distance from mare and highland contact from our global run result. Composition distribution at a distance is plotted as a box and whisker plot. The line inside of the box is the median value of total composition distribution at a given distance. The upper and lower boundaries of the box represent the 25% of data above the median and the 25% of data below the median, respectively. The ends of the whiskers represent 99% of data. The solid circles in light gray color are outliers. The data points in black color with labels of “A-12”, “A-11” and “Luna-16” are from Apollo 12 and 11 and Luna 16 mare, respectively, soil samples. The black arrow denotes one example of a ray patch in our simulation domain (see close-up in Figure 3.7).	93
3.9	Histogram of highland abundance normalized by the total number of pixels inside a ray patch and nonray region shown in Figure 3.7. The bars in blue color are the nonray region population (36 pixels in total) in our global run, while the bars in gray color are the population sampled from a localized ray patch in our simulation result (36 pixels in total).	94

Figure	Page
4.1 The relative probability plot of five reported lunar regolith samples. The relative impact flux is calculated from the fraction of impact glass spherules and shards normalized by the overall number of impact glass spherules and shards from all five Apollo regolith samples. The data is directly taken from two studies, Zellner and Levine (Zellner and Delano, 2015; Levine et al., 2005). The spherule data of Culler and Hui (Culler et al., 2000; Hui et al., 2009) are not included.	97
4.2 An illustration of spherule production, transport, and destruction in CTEM. a) Spherules are produced within the melt zone for those streamlines that emerge inward of the onset distance for spherule production. b) Pre-existing spherules within regolith layers are destroyed in the melt and shock fragmentation zone. Old spherules entrained within streamlines that intersect the survival zone are mixed with fresh spherules produced as in a).	100
4.3 Our modeled impact glass spherule production model based on terrestrial impact crater glass/melt size data. The lower x axis represents the estimated launching position scaled by the calculated transient crater radius. The y axis is the reported maximum size of the impact melt product in millimeters (mm). The upper x axis is the equivalent landing distance under lunar gravity.	104
4.4 The relative probability plots calculated from all of our fifty simulated surfaces with our two free parameters varied: sampling depth (a and b) and glass distribution onset distance, where R is the crater radius (c-f). The x-axis is age (Ma), with the present day at the left. The relative probability of all model samples is calculated in a similar fashion as the observed data set given in Figure 4.1, but with the constant model resolution σ of 50 Ma. Panel f (highlighted in black, bold line) shows our result with a sampling/mixing depth most similar to the Apollo sampling depth, and with a glass onset distance closest to that from obtained from the terrestrial microtektite constraint. It shows a prominent bias in <500 Ma ages qualitatively similar to our observational data shown in Figure 4.1.	112
4.5 The relative probability plot calculated from all of our fifty simulated surfaces in the case of glass onset distance > 5 radii with three sampling depths: a) 3 m, b) 1 m, and c) 10 cm. The black curve represents the overall relative probability summed from all fifty simulated surfaces. The x-axis is age (Ma), with the present day at the left.	113
4.6 The half life of model glass spherules due to shielding as a function of sampling depth.	115

Figure	Page
4.7	116
<p>The fraction of super-domain spherule population as function of time with two sampling/mixing depths: a) 6 m, and b) 10 cm. The x-axis represents the time since the formation of each spherule population; the y-axis is the normalized distribution of spherules by the total amount of spherules generated. Points in colors depict different spherule populations that were produced in our fifty simulations. The arrow in a) shows excavation events occurring to this particular spherule population.</p>	
5.1	133
<p>The relative impact probability of exotic glass spherules and shards from Apollo 14259, 64501, 66041, 71501 from zellner201540, and one age (800 ± 15 Ma) from Apollo 12 ropy glasses from Bogard1994. The black curves are the total impact probability represented by the sum of Gaussian distributions for our compiled 37 $^{40}\text{Ar}/^{39}\text{Ar}$-derived ages of exotic glass spherules. The gray boxes are histogram of number of exotic glass spherules (number is shown on the right-hand side). The total number of $^{40}\text{Ar}/^{39}\text{Ar}$-derived age measurements is sixteen.</p>	
5.2	163
<p>Ternary diagram for our compiled exotic glass spherules and a diverse set of returned samples. The dashed line represents an approximate mixing boundary of lunar mare and highland (Delano et al., 2007). Black filled circles represent lunar volcanic glass spherules (Delano, 1986, Tables 3 and 5). Gray filled circles represent Apollo 17 high-Ti and very low-Ti mare basalts (Wentworth et al., 1979; Vaniman and Papike, 1977). Red filled circles represent Apollo 12 mare basalts (Neal et al., 1994; Rhodes et al., 1977; Papike et al., 1976). Orange filled circles represent Apollo 12 soils (Laul and Papike, 1980; Morris et al., 1983). Pink filled circles represent Apollo 12 ropy glasses (Wentworth et al., 1994). Magenta filled circles represent Apollo 16 HKFM glasses(Naney et al., 1976; Ridley et al., 1973; Kempa et al., 1980). Light and dark purple filled circles represent Apollo 12 gray-mottled KREEP breccias and KREEP glass fragments respectively (Meyer et al., 1971). Light and dark blue filled circles and yellow filled circles represents all glass spherules (Zellner and Delano, 2015, Appendix A). Green filled circles represent KREEP melt breccias (Sample No. 14063, 14078, 14276, 14310, 60315, 62235, 65015, and 63355) (Tera et al., 1974; Norman et al., 2010). Square symbols represent lunar Mg-suite (Sample No. 72415, 76535, 77075, and 78235). Cross symbols represent feldspathic lunar meteorites (Korotev et al., 2003). Plus symbols represent Ferroan anorthosites (Sample No. 60025 and 15415). The integers marked in dark blue color represent the $^{40}\text{Ar}/^{39}\text{Ar}$-derived ages of exotic spherules. Opaque colors are for overlapped circles.</p>	

Figure	Page
5.3 Cumulative number of fragments higher than ejection velocity from the SALES_2 simulation result for Copernicus Crater. The line points in black color represent the cumulative number of fragments that escaped the lunar gravity. The line points labeled by “All sesquinary impactors” depict the cumulative number of fragments that initially escaped the lunar gravity but later hit the Moon. The x-axis is the ejection velocity of escaped fragments, and the y-axis is the cumulative number of escaped fragments higher than ejection velocity. The number of total fragments and the precursor of sesquinary impactors are $\sim 10^{15}$ and $\sim 10^{13}$ respectively (>5 cm).	164
5.4 Cumulative size frequency distributions (CSFD) of all Copernicus Crater-forming sesquinary impactor fragments and sesquinary impactors launched at ~ 3 km/s.	165
5.5 Crater size frequency distributions (SFD) for Copernicus Crater-forming sesquinary craters. The solid black lines from the top to the bottom show total crater production of the lunar surface for 800 Ma, 10 Ma, 0.1 Ma, 50 years, and 1 year under the Neukum Production Function (NPF). The line marked in blue color represent the size frequency distribution of all sesquinary craters. The green line is sesquinary crater SFD for ejection velocity of ~ 3 km/s that we used the data of fragment sizes from SALES_2 code as impactor sizes and velocity distribution and converted them to crater sizes using π -group scaling laws. The red line is sesquinary crater population that may form melt.	166

ABSTRACT

Huang, Ya-Huei Ph.D., Purdue University, December 2018. Impact Transport on the Moon. Major Professor: David A. Minton.

The ultimate goal of this dissertation was to better understand what the Apollo sample collection tells us about the impact history of the Moon. My main research tool is a computer code called Cratered Terrain Evolution Model (CTEM). CTEM is a Monte Carlo landscape evolution code developed to model a planetary surface subjected to impacts. While the main effect of impact cratering that CTEM simulates is elevation changes of the landscape through the excavation process of craters and the deposition of ejecta, I worked to extend the capabilities of the code to study problems in material transport. As impact cratering is a dominant process on the surface of Moon, the stratigraphy of lunar geology is thought to be composed of stacks of impact-generated ejecta layers. Each individual impact generates ejecta that is sourced from varying depths of the subsurface. This ejecta contains a rich abundance of material containing information, including composition and datable impact products, such as impact glasses. The extensions to the CTEM code that I developed allows me to track all ejecta generated during a simulation and model the complex history of the lunar regolith.

The new impact-driven material transport component of the regolith transport code based on CTEM was calibrated with published remote sensing observations across mare and highland contacts on the Moon measured by Clementine UV/VIS camera. Material mixing process across mare and highland contacts is modeled by diffusion problem. With CTEM, I showed that spatial heterogeneity of crater rays (distal ejecta) is critical to model the impact-driven material transport process. Another new component that I have added to the CTEM code includes the production,

transport, and destruction of impact-generated melts on the Moon, in particular, lunar impact glass spherules. Impact glass spherules are submillimeter in size and produced by hypervelocity impacts. The size of a crater that is required to produce impact glass spherules is an ongoing work, but their ubiquity in the lunar soils suggests they are generated in a relative small impacts. Glass spherules are fascinating because their $^{40}\text{Ar}/^{39}\text{Ar}$ -derived ages potentially indicate an absolute time of an impact event in the past.

I have focused my work on modeling two observations that have been reported in the last two decades. One is that the distribution of $^{40}\text{Ar}/^{39}\text{Ar}$ -derived ages of impact glass spherules shows an excess over the last 500 Ma, and the other is that the ages of “exotic” glass spherules show an excess at $\sim 700\text{-}900$ Ma. I showed that a bias introduced by shallow sampling depth is potentially involved into the interpretation on the excess of young impact glass spherules with ages < 500 Ma. As the age distributions of glass spherules collected from a shallow depth may be dominated by young, large cratering events, the work on the age distribution of “exotic” glass spherules is attempted to not inflate an impact flux by double counting glass spherules that may have produced from the same impact. Because the age of the excess of “exotic” glass spherules coincides with a proposed formation age of Copernicus Crater, it has been suggested that a short-lived global impact spike on Moon occurred 800 Ma ago.

I investigated how likely Copernicus Crater-forming spherules contribute to the abundance of ~ 800 Ma-old, “exotic” glass spherules. I found that the origin location of observed “exotic” glass spherules are likely to be derived from hundred kilometers away from the site where they were collected from. Under an assumed stratigraphy for the region of Copernicus Crater, the ternary compositions of those “exotic” glass spherules cannot be explained by the mixing of those assumed substrate materials. This compositional heterogeneity suggests that either the melting as a result of the formation of glass spherules during crater excavation is different than it is thought or it indicates a diversity for origin locations for those 800 Ma-old exotic spherules. Alternatively, secondary and sesquinary craters produced by Copernicus

Crater-forming debris are too small and low in impact velocity for a sufficient amount of glass spherules. As a result, the Copernicus Crater alone cannot be responsible for the excess of “exotic” glass spherules. It further implies that either the global lunar impact flux increased ~ 800 Ma ago or a better understanding on “exotic” impact glass spherules is needed. In summary, we still have plenty of room for a better understanding of Earth’s Moon.

“All is Void and there is no Buddha.” Dajian Huineng

1 INTRODUCTION

“ ... I distinguish two parts of it, which I call respectively the brighter and the darker. The brighter seems to surround and pervade the whole hemisphere; but the darker part, like a sort of cloud, discolours the Moons surface and makes it appear covered with spots. Now these spots, as they are somewhat dark and of considerable size, are plain to everyone and every age has seen them, wherefore I will call them great or ancient spots, to distinguish them from other spots, smaller in size, but so thickly scattered that they sprinkle the whole surface of the Moon, but especially the brighter portion of it. These spots have never been observed by anyone before me; and from my observations of them, often repeated, I have been led to the opinion which I have expressed, namely, that I feel sure that the surface of the Moon is not perfectly smooth, free from inequalities and exactly spherical but that, on the contrary, it is full of inequalities, uneven, full of hollows and protuberances, just like the surface of the Earth itself, which is varied everywhere by lofty mountains and deep valleys. Some have learned the truth earlier and some have special talents.” *The Sidereal Messenger* (1610) by Galileo Galilei, translated by Edward Stafford Carlos (Galilei et al., 1880).

Impact cratering is not only a fascinating process to study but craters also provide us with a record of the bombardment history of our Solar System. Nearly every imaged planetary surface is visibly marked by one or more impact craters, and impact cratering is a dominant process among many planetary bodies. The study of impact craters itself has a long and rich history (Drake and Komar, 1984).

1.1 A brief history of lunar impact craters

With the invention of the telescope in the sixteenth century, in 1609 Galileo became the first to sketch the face of the Moon using a 5–6 inch long refraction telescope. In his notes, Galileo mentions “spots”, uneven or crude surface of the Moon that cast long shadows, for which he offered little explanation.

Lunar “spots”, circular depressions on the surface of Moon, were further studied by Hooke in 1665. Hooke believed these “spots” to be pits on the top of lunar hills, and that these pits were emptied of materials due to an eruptive force caused by Moon’s internal movement (quakes). However, it was later learned that the center depressions on the Moon are lower than their surrounding rims, leaving Hooke’s pits hypothesis unconvincing. Nevertheless, Hooke continued to study the formation of these depressions. He found that alabaster, after being removed from a boiling pot of water, had small pits all over the surface as a result of gas bubbles bursting after escaping the liquid. Unfortunately, there was no evidence supporting a liquid surface of the Moon, and again leaving Hooke’s pit hypothesis disfavored.

In 1790-1800, Johann Hieronymus Schröter and William Herschel and others started a systematic and comparative study of lunar craters, producing detailed lunar crater maps. The term “crater” was commonly used to describe circular depressions on the surface of the Moon visible through refraction telescopes from Earth (Sheehan and Baum, 1995). Because of their resemblance to volcanic craters, the features observed on the Moon were favorably accepted to be of the volcanic origin through nineteenth and early twentieth century.

In 1893, Grove Karl Gilbert presented a serious discussion of various hypotheses, including the impact theory or meteoritic origin of lunar craters (Gilbert, 1893). In his famous impact experiment, Gilbert dropped clay balls vertically onto clay surfaces and observed the outcome. Their resemblance to volcanic craters called into question the volcanic origin of lunar craters (Pyne, 1980; El-Baz, 1980). However, his experiment predicted an elliptical shape of a crater if the impactor was not dropped

exactly vertical to the surface. This seemed to suggest that the circularity of most lunar craters would require all impactors that struck the Moon to have dropped to the surface vertically, which is implausible.

The origin of lunar “craters” became clearer between 1910 and the mid-1950s. In 1916, Ernst Julius Öpik was the first to propose the idea that the lunar craters are associated with meteors and high-velocity collisions (Öpik, 1916; Racki et al., 2014). Öpik and Morozov used the physics of explosion to explain the fundamentals of impact cratering. This pioneering work was brilliant but not appreciated widely at that time. Despite opposition to Gilbert’s impact theory, in 1920-21, eight years after his hypothesis of continental drift, Alfred Lothar Wegener (Wegener, 1920a; Wegener, 1920b; Wegener, 1921) considered the impact origin of lunar craters. He realized that a lunar impact projectile must travel at a high velocity, greater than the lunar escape velocity of 2.38 km/s. Wegener experimented with cement powder for target and projectile (Wegener, 1921). During impact, the projectile disintegrated as it impacted into the target, and the target surface was hollowed because pre-existing materials were pushed outward. Furthermore, Wegener varied the color of the cement projectiles and observed ray patterns streaking across the gray colored target cement. These ray patterns are similar to the observed streaks surrounding some lunar craters.

As more and more explosion experiments were tested in World War I and World War II, the understanding of the impact cratering process improved. The progress is reflected in the literature terms used to describe lunar craters. For example, Ralph Belknap Baldwin in 1949 and Kathleen Mark in 1987 used the terms like “bomb craters” and “meteorite craters” to describe impact craters (Baldwin, 1949; Mark, 1987). Intriguingly, it is unknown who initially joined together “impact” and “craters” into the term that we used today (personal communication with Jay Melosh).

1.2 Impact cratering mechanics

Impact craters form when a projectile or impactor, moving at up to tens of kilometers per second, hits a planetary surface. The impact transfers a tremendous amount of energy to the target surface and immediately alters the geology of the region. When discussing the physics of impact cratering, it is common to divide the cratering process into three main stages (Melosh, 1989). The first stage, contact and compression, begins once a projectile touches down on a surface. This is a rapid process and creates a strong shock wave within the target surface and the projectile. Once the shock wave reaches the side of the projectile opposite the contact point, it reflects, and the rarefaction wave travels back toward the contact point. The target materials are compressed by the impactor until the shock rarefaction wave travels from the contact point to the end of the impactor. At this point the second stage, excavation, takes effect. The flow of excavating materials opens up a cavity, carrying with it fragmented, melted or vaporized target materials. The flow carries this mixture of materials and ejects it from the cavity, leaving behind a deep depression called transient crater. Meanwhile, materials left within the crater cavity begin to feel the force of gravity and undergo a collapse. This stage is called crater modification. Excluding post-cratering process in which high temperatures can linger for long after crater formation, the crater modification stage is the most protracted process. The modification stage has the most control over the final crater shape (simple crater, complex crater, peak-ring crater, or multi-ring basin) (Melosh, 1989).

The contact and compression stage lasts for as long as the projectile is penetrating the target (Shoemaker, 1959). Resistance upon penetration causes physical changes, including the distortion of an impactor and a high pressure phase of compressed materials. Materials within a region where the free surface of the target meets an edge of the impactor can be ejected the earliest (spallation)(Melosh, 1984). Once the propagating shock wave produced at the initial contact point reaches the rear side of the impactor, it reflects off as a rarefaction wave (tensional waves or expanding

waves). The complicated relationship between shock release and compressed materials, which are likely inhomogeneous geological materials, is commonly visualized by a P-V plot (pressure-volume diagram) and continuous thermodynamic paths (see Figure 1.1) (Melosh, 1989). The maximum shock pressure is achieved during the contact and compression stage. The average shock pressure, though lower than the maximum shock pressure that a material actually experiences, can be approximated by the planar impact approximation. In this approximation, a slab with a finite thickness moving at some velocity collides with an infinite half space (Melosh, 1989, Section 4.5). Since the contact and compression stage readily determines the distribution of shock pressure, a planar impact approximation provides the first order approximation of vapor and melt production for a given impact (Melosh, 1989). In the literature, researchers often combine the planar impact approximation (the estimates of maximum shock pressure) with a semi-analytical model, called the Gamma Model (Croft, 1982), to describe the distribution of shock pressure (see Section 2.5). Examples of the limitation on planar impact approximation include the inability to model either an oblique impact or effects of the shapes of the projectile. This approximation works the best along the normal direction of a moving projectile to the target surface (Melosh, 1989).

When rarefaction waves reflect off the rear side of an impactor, the tensile waves execute an upward motion through the compressed materials due to a reduction in pressure, unloading the compressed materials of the impactor (Bjork et al., 1967, Figure 2-1c). After unloading, the next phase, the excavation stage, roughly begins (Melosh, 1989). The excavation stage can be divided into two different physical processes: 1) shock detachment and 2) crater excavation flow (Bjork et al., 1967). Shock detachment occurs where shock fronts propagate away from the impact point (downward direction). Shock waves continue to accelerate more target materials as the wave propagates and weakens. The shock pressure falls off approximately as the inverse square of the distance from the impact point (Melosh, 1985). In a far-reaching

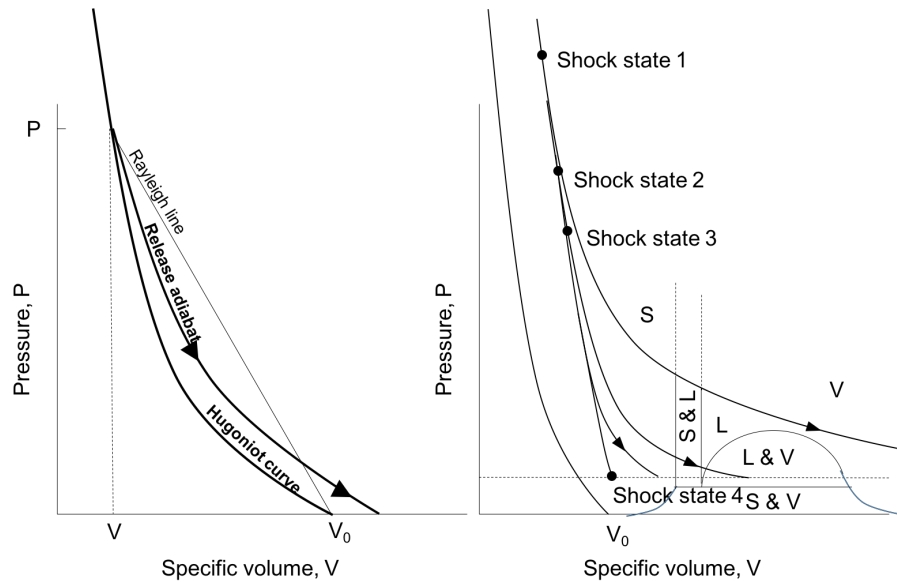


Figure 1.1.: Release adiabat curves after a high shock pressure. The Rayleigh line is a straight line connecting the initial pressure and volume to the final pressure and volume (final shock state). The Hugoniot curve depicts shocked (compressed) materials in the P - V diagram, in which shock compression is irreversible. Release from high shock pressure follows the adiabatic trend in the P - V diagram (reversible process). The final volume of release from high shock pressure is larger than the initial volume (V_0) because a fraction of materials is melted. The difference between triangle-shaped area bound by the Rayleigh line and vertical line at specific volume of V and horizontal line at zero pressure and an area bound by the Hugoniot curve is approximately heat waste by shock. The diagram to the right shows different release curves for different shock states (shock state 1, 2, 3, and 4), and the final state of those release curves depending on a phase diagram (S: solid; L: liquid; V: vapor) for a given geological material. Modified from Figure 3.10 in (Melosh, 1989).

field, the shock pressure essentially drops to zero. Once the shock waves are detached, it no longer interacts with the rest of the propagating shock waves (Bjork et al., 1967).

In nuclear explosion experiments, it was discovered that target materials far away from the center of an explosion still move at some residual velocity instead of zero velocity (Bjork et al., 1967). Although a shock pressure drops to almost zero in a large distance, the thermodynamic irreversible process of shock deformation during cratering causes a residual velocity field remaining in the target materials that begin to flow along with the opening of a crater cavity (Melosh, 1985). The residual velocity also relates to the movement of shock detachments and the growth of a transient crater (Bjork et al., 1967; O’Keefe and Ahrens, 1981). The opening and growth of a crater cavity stops as the strength of target surface and lithostatic pressure from surrounding rocks halts the motion. The growth of a crater cavity is approximately developed into vertical and lateral directions. The cessation of lateral direction of a crater cavity growth controls the crater diameter; it is relative easier to comprehend and may be analytically described using the concepts of Maxwell Z-model, the π -scaling laws, and residual velocity (Ivanov, 1983; Yamamoto et al., 2006; Richardson et al., 2007; Barnouin-Jha et al., 2007; Yamamoto et al., 2009; Yamamoto et al., 2017; Kurosawa and Takada, 2019). Excavation flow near the surface intersecting a growing hemisphere continues to move outward until reaching the maximum diameter. Right before a cavity undergoes gravitational collapse, the cavity is referred to as a transient crater (its diameter is measured from rim to rim). As for the vertical growth of a crater cavity (crater depth), it depends on the resistance raised from the target material strength and isostatic pressures of surrounding rocks during the downward displacement of an excavation flow (Croft, 1980; O’Keefe and Ahrens, 1981; Stewart and Valiant, 2006).

While the main shock wave sends materials downward, rarefaction waves moving downward reduce the pressure gradient and cause some shocked materials to move in an upward direction (Melosh, 1989). Assuming that the concept of residual velocity can characterize materials during excavation stage, the regions closer to the free surface attain more upward velocity from rarefaction waves than the regions in a lower part of the target surface (due to its weaker rarefaction). Overall, the inter-

action between the strong shock waves created by the plunging projectile inducing strong shock waves and rarefaction waves reflecting off from the free surface leads a unique geometry for the crater excavation flow (Melosh, 1989). Moreover, the maximum velocity of this excavation flow does not exceed the residual velocity, so the excavation flow can be considered as subsonic and treated as an incompressible flow or as streamlines. The sound speed of a geological material is on the order of few kilometers per second if the material is not porous.

A standard model that is used to describe a crater excavation flow is called the Maxwell Z-model (Maxwell and Seifert, 1974; Maxwell, 1977). This simplified analytical model provides an insight into the excavation velocity field before ejection from a transient crater and is widely used in impact cratering science (Austin et al., 1981; Croft, 1982; Richardson et al., 2007; Richardson, 2011; Kurosawa, 2015; Huang et al., 2017; Kurosawa and Takada, 2019). The streamlines in the Maxwell Z-model are used to connect materials within an excavation flow, in which each streamline describes the same magnitude of velocity. Those excavated materials, described by the same streamlines, emerge at the same position within a transient crater (Maxwell and Seifert, 1974; Maxwell, 1977). The streamlines emerging closer to a projectile are ejected at a higher velocity than the streamlines emerging farther away from a projectile. One can observe excavated materials forming an ejecta curtain that moves away from the rim of a crater (Oberbeck, 1975). For any given time, an ejecta curtain is made up of excavated materials emerging from the closest distance to an impact point (the fastest) to the distance closest to the rim (the slowest) (Maxwell and Seifert, 1974; Maxwell, 1977). Once separated from a transient crater, an ejecta curtain becomes independent of cratering motion and follows a ballistic trajectory for most of lunar craters (Oberbeck, 1975). As ejecta lands on the lunar surface, it forms ejecta deposits surrounding a crater. The appearance of ejecta deposits changes with distances from the center of a crater (Howard, 1974). For example, ejecta distributed within the distance of 1–3 crater radii from the center of a crater is called continuous ejecta, and beyond that, the ejected material breaks into streaks known as crater

rays (Howard, 1974). In addition, the landing process of ejecta deposits may cause ballistic sedimentation as energetic ejecta churns up the surface materials (Oberbeck, 1975).

The *modification stage* begins as soon as the transient crater forms (Melosh, 1989). Upward and outward motion of the transient crater cease, and subsequently the crater is subjected to the downward force of gravity, especially for materials at the rims of the transient crater (Melosh, 1989). Before the modification stage, the material in the rim were more or less fragmented and shocked in varying degrees. The downward pull of gravity turns those loose materials to flow easily. The outcome of this stage determines the final morphology of the impact crater. At this stage, the influence of gravity on the gravitational collapse is significant (see Section 1.3).

1.3 Morphology of impact craters

Just after formation, the morphology of most impact craters fits into one of four main types, which depends on most strongly on the size of the crater and the surface gravity of the target body: 1) simple craters, 2) complex craters, 3) peak-ring craters, and 4) multi-ring basins. Simple craters are pits with a bowl-shape and elevated rims. Most simple craters resemble the initial transient crater, but shallower. The bottom of a simple crater is usually filled with a mixture of fragmented, shocked, and melted rocks called breccia lens, which forms as a consequence of debris sliding back into the crater after the collapse of the transient crater (Shoemaker, 1959). The breccia lens is porous and if the crater formed in competent rock may be detected as a gravity anomaly (negative gravity anomaly or mass deficiency) (Pilkington and Grieve, 1992). The floor beneath the fragmented breccia lens is thought to be the bottom of a transient crater.

On the Moon, simple craters have a depth to diameter ratio of roughly 1:5 (Pike, 1977). This ratio changes when a final crater diameter reaches $\sim 15\text{--}20$ km (simple-to-complex crater transition) (Dence, 1965). This transition is abrupt; the morphology

of complex craters is distinct from the morphology of simple craters. The changes in the morphology from a simple crater to a complex crater include emergence of central peaks, flat floors, and terraced walls. The crater diameter for complex craters ranges from 20 to 100 km, yet the depth of complex craters is on the order of few kilometers (Pike, 1974). A well-known example of lunar complex craters is Copernicus Crater. In comparison with simple craters, the formation of complex craters suggests that the material strength of the surrounding rocks no longer supports the transient crater under the force of gravity. Examples of the influence of gravity on the stratigraphy of an impact structure include dense mantle materials found at the central peaks of lunar Copernicus Crater. An Earth-based telescopic observation of the central peaks of Copernicus Crater conducted by Pieters reveals spectral features of olivine that potentially originated in a deep part of the lunar surface (Pieters et al., 1985). In addition, the remnants of an olivine-rich materials at the central peak of Copernicus Crater may be due to the low impact velocity event (Yue et al., 2013). This finding suggests a central lifting mechanism occurring in the central peaks for complex craters (Melosh, 1982; Potter et al., 2013), which is consistent with observations of terrestrial complex craters. Terrestrial geologists found that the central peaks of complex craters on Earth are composed of highly fractured materials that originate stratigraphically from beneath the interpreted transient crater cavity.

As the size of a complex crater increases to >140 km in diameter, a transition occurs in which the central peak of a complex crater disappears (Wood and Head, 1976). Lunar complex craters larger than >140 km in diameter are known as peak-ring craters due to the absence of a central peak inside the crater (Wood and Head, 1976). Instead, ringed mountain ranges surround the center of a crater, and one of them is the crater rim locating at the outermost of ringed mountain ranges (Melosh, 1989, Chapter 8). The hypotheses that explains the formation of peak ring craters include the dynamic collapse of central peaks (Murray, 1980) and the strengthless melted materials upon forming central peaks (Cintala and Grieve, 1998). The dynamic collapse model suggests that a difference between complex craters and peak-ring craters

is the maximum height of central peaks reached during the formation. During the formation, it is theoretically possible that the maximum height of central peaks in peak ring craters tend to be higher than the ground surrounding the crater, leading to the collapse of the central peaks (not observed from the shape of the final crater) (see Figure 8.14 in the book by Melosh, 1989) (Murray, 1980). Alternatively, target rocks beneath the impact point would have been melted such that does not raise above the rim of a transient crater (Cintala and Grieve, 1998). The recent advances including numerical simulations, remote sensed data, and terrestrial drilling expedition appear to support the dynamic collapse model. For example, the drilling expedition to the peak ring of Chicxulub Crater by the International Ocean Discovery Program (IODP) and International Continental Scientific Drilling Program (ICDP) sampled a fractured and shocked materials sourced from the crystalline basement (Morgan et al., 2016), which is consistent with the prediction by the numerical simulation result for Chicxulub Crater (Collins et al., 2008).

With increasing the size of a crater, more than one ringed mountain range as seen in a peak-ring crater form surrounding the center of a crater. Multi-ring basins (Hartmann and Kuiper, 1962), such as Imbrium Basin and Orientale Basin, are among the largest impact features on the Moon. South Pole-Aitkin (SPA) Basin is the largest multi-ring impact basin on the Moon, but any of rims may have been gone. Orientale Basin is the youngest and best-preserved multi-ring basin on the Moon, consisting of at least four circular rings surrounding the center of the basin. The four rings of Orientale Basin form mountain ranges, with the outermost ring being the tallest. The highest peak formed by Orientale Basin is up to 6 km in elevation likely produced by Orientale Basin ejecta (Moore et al., 1974, Figure 13). In comparison, Mt. Everest, the highest continental mountain peak on Earth, is 8 km in elevation. Besides ring mountains, structures like escarpments, flat-lying plains and radial troughs scoured by energetic basin ejecta are also prominent geological features of multi-ring basins (Head, 1974; Moore et al., 1974). Large basins have a dominant positive gravity anomaly at the basin center due to a dense mantle plug formed during cratering

process (Melosh and McKinnon, 1978). These gravity anomalies, called mascons (Muller and Sjogren, 1968), can have a significant effect on the trajectory of a passing spacecraft. The origin of multi-ring basins is still debated, but the ring tectonic theory (Melosh and McKinnon, 1978) appears to achieve several predictions by numerical simulations and geophysical observation data for large lunar basins (Potter, 2015; Johnson et al., 2016). In particular, the observation data of GRAIL measurement and photometric examination of faults for Orientale Basin suggest that the ringed mountains are associated with the large-scale fault structures (Head, 1974; Nahm et al., 2013; Zuber et al., 2016). It is likely that due to the collapse of a transient crater of a multi-ring basin, the mantle materials that were initially uplifted slash inward and plunge into crust, creating an extensive fracture along the pull of cold crust materials with it (Potter, 2015; Johnson et al., 2016).

1.4 Lunar crater based chronology and the origin of a planetary cratered surface

Since the realization that lunar craters were formed by impact, speculation began as to the sources of the projectiles. In 1918, Hirayama proposed that some asteroids formed as a consequence of breakup of a larger body (Hirayama, 1918). Because those asteroids are fragments broken from their parent body, they share similar orbital elements. Asteroids with similar orbital elements are grouped as an asteroid family. As a small asteroid on a collision course with a massive body will accelerate to a velocity greater than the escape velocity, forming an impact crater on the surface of the massive body (Öpik, 1916; Gilbert, 1893). The distribution of impact craters on the surface is a potential record of the impactor population since the formation of the massive body. Knowing impactor populations in the past is important to us because those impactor populations may not exist today. Consequently, sampling impact records from different surfaces from either the same planetary body or different

planetary bodies can help us to understand how a primordial distribution of fragments leftover from the formation of the Sun may have evolved.

In 1960, Öpik was first to recognize the relationship between the dynamic origin of our Solar system and the evolution of a cratered surface (Öpik, 1960). Öpik in 1958 estimated the probability of small bodies (Apollo Near-Earth Objects and non-periodic comets) hitting the planets, such as Mars (Öpik, 1958). He used the 812 lunar craters on Western Mare Imbrium over $465,000 \text{ km}^{-2}$ counted by the author of a print from Mt. Wilson Observatory in 1919 (Fitzgerald, 1953). He assumed that those 812 lunar impact craters were formed over the 4.5 Gy of the Solar System history. The diameters of 812 counted craters, measured from rim to rim, range from 600 m to 73.2 km.

Öpik noticed that the formation of the maria must be more recent than the highlands (the continents in his original paper) due to the less-densely cratered surface of the maria (Öpik, 1960). Earlier, Baldwin had the statement on the observation of a younger maria than highlands in his book of *The Face of the Moon* in 1949. Öpik argued that small meteorites were prevented from forming craters by the dust cover of the maria that remnants of impact vapor and fragments had accumulated, so only large meteorites were responsible for craters forming on the top of the maria. As a result, the size frequency distribution of the crater population of the maria more closely related to the present-day size frequency distribution of asteroids than the size frequency distribution of the highlands. Once the scaling between impactor size and crater size is accounted for, Öpik used 20 for the size ratio of a crater to a projectile assuming impact velocity of 15 km/s (Öpik, 1958). The cumulative number of estimated projectiles in 4.5 Gy is consistent with his partly observed, partly extrapolated numbers of asteroids. In 1963, Baldwin in his book of *The Measure of the Moon* also recognized that the cratering rate in the past must have been higher than the present day.

Öpik concluded that the present frequency distribution of small bodies interpreted from the crater count of the maria might have remained constant since the formation

of the maria. The present-day size frequency distribution of small bodies might also be different from the primordial planetesimal distribution because the planetesimals were rapidly swept out in the early Moon. Öpik suggested that the surface of the maria serves as a “counter”, which records the impacts of present small bodies. In 1965, Hartmann used the known number of craters and average age of the Canadian Shield to estimate the terrestrial and lunar impact flux. He used an exposure age of <2 billion years for the Canadian Shield (Hartmann, 1965). Using his estimated impact flux, Hartmann obtained an age of 3 Gy for the average lunar mare, which is within the radiogenic ages of mare basalts returned from the later Apollo missions.

It is noteworthy that Öpik was perhaps the first to adopt the concept of the cumulative size-frequency distribution to characterize the distribution of impact craters on a planetary body (Öpik, 1960). In the same year, Kreiter converted the table data compiled by Öpik to a figure (Kreiter, 1960). Two years before 1960, Kuiper found that the mass distribution of asteroids in his systematic survey can be expressed as either a cumulative or incremental size-frequency distribution (Kuiper et al., 1958). The cumulative SFD is preferred over the incremental size-frequency distribution in which lists the number of craters within a range of sizes in diameter from D_i to D_{i+1} per unit area. The cumulative SFD calculates the number of craters greater than D per unit area, independent of bin size. More importantly, both size-frequency distributions are well-approximated using power-law functions of crater diameter, over some range,

$$N(> D) = CD^b \tag{1.1}$$

where $N(> D)$ represents the number of craters larger than the diameter of a crater (D) per unit area, C is a constant, equivalent to $N(> 1)$, which is the total number of counted craters per unit area for $D = 1$ in whichever the unit system is being used (typically km) D_s is the smallest crater in a counted area and b is an exponent or a population index in (Öpik, 1960). In modern crater counting, the cumulative crater

size-frequency distribution is widely used, and the selection of a crater count area is set to a homogeneous geological unit.

The production function for a given cratered surface represents a time-dependent size distribution of impactors (Neukum and Ivanov, 1994). To create a production function, a crater count study must be calibrated with radiogenic ages that are associated with surfaces of a single age and crater number density across a range of sizes. Because a production function serves as a chronology of a cratered surface, it can be used to assign a specific age to a crater counted unit (Neukum and Ivanov, 1994). Due to radiometrically-dated lunar samples from the U.S. Apollo and Soviet Luna programs and a rich bombardment record of the Moon, the lunar production function or lunar chronology is widely used and applied to planetary bodies other than the Moon using models to extrapolate the lunar cratering record to other bodies (Chapman and McKinnon, 1986).

One of the most commonly-used lunar chronology is the Neukum Production Function (NPF). The NPF is an 11th-degree polynomial function, which describes the cumulative size-frequency distributions of lunar craters larger than a specific size in diameter, and a mixed exponential decay and a linear function to describe the rate of crater accumulation over the age of the Solar System. The function was fit from crater counts obtained from different parts of the lunar surface for various ages (Neukum, 1983; Neukum et al., 2001; Neukum and Ivanov, 1994). The NPF is expressed as the cumulative number of craters with diameters larger than a given diameter of D normalized by the size of a crater counted area and an assigned surface age (impact flux, $\text{km}^{-2} \text{Gyr}^{-1}$). By normalizing area and time for a given counted surface, it is possible to account for all range of sizes of craters. For example, the small area of the Apollo 15 landing site does not contain larger craters (e.g., 20 km in diameter) because large craters are only statistically expected over a long-term period and a large area. On the other hand, small craters on a large area are subject to degradation and obliteration processes that make them uncountable. Normalized SFDs obtained from different areas of a lunar surface can be used to construct a full

range of a production function. However, the NPF assumes that the size-frequency distribution of an impactor population was remained the same over time (<4 Ga).

1.5 Lunar origin and bombardment environment

Not only has the Moon been a constant companion to us and our ancestors, the Moon is also the site of the first extraterrestrial human exploration. The Apollo missions have inspired many generations of scientists. The valuable samples returned by the Apollo missions contain physical evidence of geological processes that have occurred on the Moon over time (Wood, 1970; Wood et al., 1970c; Wood et al., 1970a). For example, dark basaltic fragments found in returned lunar soils originate in the extensive volcanic mare plains. These basalt plains are visible to the naked eye as dark patches on the lunar surface. Light-toned anorthosites found in lunar mare soils originate in the relative brighter highland plains. The anorthositic highlands dominate the lunar surface, occupying 83% of the surface (Head and Wilson, 1992). This observation supports the hypothesis that the primary compositional highlands units formed as a floating layer on an early magma ocean (Wood et al., 1970b). The oldest anorthosites returned from the Apollo missions range from 4.56 Gyr to 4.29 Gyr in age and may represent the most ancient lunar crust (Alibert et al., 1994; Borg et al., 1999).

As soon as the first crust formed on the Moon, it was subjected to intense impact cratering, which formed the fractured and porous surface layer called “regolith” and “megaregolith” (Hartmann, 1975; McKay et al., 1991). This continuous cratering process operated when lunar volcanism may have been active, and the impact rate was much higher than it is today. Just a few grams of lunar soils contain a variety of materials, including from mare basalt fragments, impact breccias, agglutinates, impact glass spherules, and lunar highland crustal materials. In particular, impact breccias and impact glass spherules are of great interest to the lunar bombardment community because these can be used to derive a radiogenic age for the sample. In

many case, the radiogenic age of these melts is that of the cratering event that formed it. A compiled radiogenic age distribution of impact-related fragments from a landing site may be correlated to an impact rate experienced by the landing site over its history. By linking samples collected from various lunar landing sites, it is possible to derive a global lunar impact rate or a lunar bombardment history, potentially dating back to the very beginning of our Solar System.

Radiometrically-dated age distributions of impact generated melt or glass samples have created at least two long-standing open questions concerning the lunar impact flux, 1) the duration and magnitude of Late Heavy Bombardment (LHB) 3.9 Ga ago, and 2) whether or not the impact rate has been constant over the last three billion years. This dissertation will focus on the second of these two questions, however, for completeness, the rest of the introduction here will be devoted to a brief description to the first of these two controversies.

1.6 The first billion lunar bombardment record and a relationship with returned samples

The most well-known controversy in the field of a lunar bombardment is the hypothesis of Late Heavy Bombardment ending at ~ 3.9 Ga (Tera et al., 1974; Turner and Cadogan, 1975). Most recently, the Late Heavy Bombardment has been linked to a dynamical scenario called the Nice Model, which suggests that a giant planet orbital instability-driven impactor population bombarded the inner Solar System 500-600 million years after the early phase of planetesimal accretion (Gomes et al., 2005). This model was initially created to explain an excess of the radiometrically-dated age distributions of returned lunar impact melt rocks and breccias (Bottke and Norman, 2017). Impact melt rocks (whole rocks broken from a massive impact-generated melt body) and impact melt breccias (assemblage of broken rocks with different types that may be glued together by fine-grained matrix such as silicate melts for the Moon) are considered melt products of basin scale cratering events. The U–Pb, Rb–Sr, and

Ar–Ar-derived ages of impact melt rocks and breccias in Apollo 12, 14, 15, and 16 samples show that a cluster of impact events occurred at ~ 3.9 Ga, and very few ages are older than 4.1 Ga (Tera et al., 1973; Tera et al., 1974). The initial finding by Tera et al. shows that in the Apollo 14 impact melt breccias, several U–Pb radiometric ages with a wide range of composition were clustered in less than two hundred million years (Tera et al., 1974). Because the wide range of composition among their analyzed samples indicates different provenances of the lunar surface, they suggested that one or more impacts must have occurred at ~ 3.9 Ga.

In order to explain an excess of radiogenic ages at ~ 3.9 Ga derived from impact melt rocks and breccias, Tera et al. proposed the terminal lunar cataclysm hypothesis (Tera et al., 1973; Tera et al., 1974). The terminal lunar cataclysm hypothesis states that our Moon experienced several possible episodes of intense bombardment in a short period of time. The most recent bombardment all ended at ~ 3.9 Ga, and that they all formed Imbrium, Crisium, Orientale Basin and also possibly others formed within a period of ~ 30 Ma. Ryder proposed a scenario of the terminal lunar cataclysm in which essentially very few impacts occurred before ~ 3.9 Ga, and then all large basins on the lunar nearside formed in a very short period of time around 3.85 Ga (Ryder, 1990; Dalrymple and Ryder, 1993; Dalrymple and Ryder, 1996).

Besides a similarity in ages, many of the lunar impact samples carry an enhanced concentration of incompatible elements and heat-producing elements, such as Potassium (K), Rare Earth Elements (REE), and Phosphor (P), also known as KREEP. KREEP was first discovered as a mysterious component in Apollo 12 mare soil samples but the link between KREEP and Imbrium Basin was not recognized until the Apollo 14 mission, and the geological provenance now known as KREEP terrain where Imbrium Basin formed was not mapped until Apollo 15 and 16 (Metzger et al., 1973; Metzger et al., 1977).

Planners for the Apollo 14 mission hoped to sample impact ejecta from Imbrium Basin, the second largest impact basin on the Moon (LSPET, 1971). The purpose of obtaining Imbrium basin ejecta samples was to determine the absolute age of Imbrium

Basin, and in doing so to determine the ages of the other large basins that appear to have formed in the same period of time (LSPET, 1971). The Apollo 14 crew and spacecraft landed in the Fra Mauro Formation, thought to have been formed from Imbrium Basin ejecta. A local young crater, Cone Crater, ~ 340 meters in diameter, would have excavated the Imbrium Basin ejecta, bringing it to the surface and allowing it to be sampled by the Apollo 14 crew (Swann et al., 1977). Interestingly, many Apollo 14 rocks and mare soil samples are enriched in KREEP material (LSPET, 1971). It was not until the Apollo 15 and 16 missions, with their orbital X-Ray and Gamma-Ray spectrometer experiments that it was understood that Imbrium Basin lies entirely in a region with a high concentration of Thorium (Metzger et al., 1973; Metzger et al., 1977). Thorium behaves chemically similar to rare earth elements, so it is used to map the boundary of the Procellarum KREEP Terrane (Jolliff et al., 2000). It is highly likely, therefore, that KREEP materials sampled by the Apollo 14 crew and the Procellarum KREEP Terrane mapped by Apollo 15 and 16 orbital spectrometers have a similar origin. The relative chronological order of the Imbrium Basin forming event and the formation of the enhanced Thorium region are still debated, but it is likely that Imbrium Basin has poked through the underlying enhanced Thorium region and excavated them to the surface (Wilhelms, 1987).

The age of Imbrium Basin is estimated from 3770 Ma to 3938 Ma based on Apollo 15 KREEP basalt rock (Appennine Bench Formation), Apollo 16 melt rocks, and Apollo 14 impact melt breccias (BVSP, 1981; Deutsch and Stöffler, 1987; Stadermann et al., 1991; Merle et al., 2014). An exact age of Imbrium Basin is still controversial because some suggest the high concentration of KREEP material in impact breccias does not necessarily prove the Imbrium Basin's ejecta (Merle et al., 2014). Despite this, those radiometric ages can be linked to the crater density that has been counted on Imbrium Basin's ejecta. Other crater densities counted from geological units can be compared to the crater density of Imbrium Basin ejecta, thus their approximate ages can be inferred. The inferred ages based on Imbrium Basin ejecta's radiometric age are one of the calibration points used to establish the lunar chronology (Neukum,

1983; Neukum et al., 2001), and other radiometric ages obtained for the purpose of calibration include mare basalt rocks and ejecta or rimmed material of local young craters such as North Ray Crater from Apollo 16 landing site and Cone Crater from Apollo 14 landing site.

Using the age of impact basins to calibrate the lunar chronology is problematic for two main reasons. First, a correlation between an impact melt and an individual basin is unclear. Even today, there are major uncertainties regarding the relationship between the formation of Imbrium Basin and KREEPy materials that the Apollo astronauts sampled. Second, almost all the samples returned from the lunar manned missions are sourced from the region around Imbrium Basin. It is likely that Imbrium Basin ejecta could be a main contributor to the radiometrically-derived ages of KREEPy materials. Regardless, attempts have been made to distinguish those radiogenic ages of ~ 3.9 Ga and associate it to specific basins (Stöffler et al., 1985). As a consequence of basing the lunar chronology on those radiogenic ages derived from samples highly contaminated by KREEPy materials, the chronology prior to the oldest dated mare basalts (James and Wright, 1972, e.g., 3.8 Ga-old sample 10062) could be biased.

The origin of ~ 3.9 Ga-old impact melt samples still remains debated. One of the uncertainties regarding their origin is related to compositional variation. Researchers are not in agreement about the interpretation of compositional variation in the 3.9 Ga-old melt samples collected from different landing site (e.g., Apollo 16) (Ryder, 1990; Haskin et al., 1998). We noted that the abundance of KREEP concentration or Uranium measured from returned lunar samples appears to correlate with radiogenic ages (Maurer et al., 1978; Norman and Nemchin, 2014). For example, Maurer show that potassium contents in Apollo 17 sample 73215 and several grouped Apollo 16 samples (63503,17, 67603,1 and 67703,1) tend to be higher in younger fragments (< 4 Ga) (Maurer et al., 1978).

Other hypotheses disputing the LHB are concerned with the preservation of ancient impact records, as well as reliability of radiometric techniques. The stonewall

hypothesis proposed in Hartmann describes an impact rate prior to 4 Ga as being so high that all older datable impact melt products were destroyed due to the pulverization of grains (Hartmann, 1975). Although modeling of the pulverization of melt-bearing lunar grains is needed for a further examination of the stonewall hypothesis, evidence for preservation of older impact records is not uncommon. Volcanic basalts older than 4 Ga have not been dispersed or buried, suggesting destruction from previous impacts >4 Ga is not the primary cause for a perceived spike around 3.9 Ga (Ryder, 1990). Moreover, impact melt ages of L and H chondrites (though no LL) as old as 4.4 Ga can survive (Swindle and Kring, 2008). This opposes the destruction sampling bias described by the stonewall hypothesis. Besides destruction sampling bias as proposed by the stonewall hypothesis, other types of sampling bias, such as partial argon resetting and impact gardening, call the interpretation of bombardment history into question (Boehnke and Harrison, 2016; Michael et al., 2018).

Alternatively, impact glass spherules and zircons, as opposed to impact melt rocks and breccias, may provide some insights to the occurrence of Late Heavy Bombardment. Zellner reported that lunar impact glass spherules older than 3.8 Ga are uncommon in regolith samples (Zellner, 2018). They proposed that, over time, impacts might destroy older glass spherules (Zellner and Delano, 2015; Zellner, 2017). Moreover, thermal destruction of a glass spherule, especially argon diffusion, has a selection preference on composition of glass spherules (basaltic versus anorthositic) (Zellner and Delano, 2015). Zircons also appear to tell a different story about the early bombardment history of the Moon. Instead of a spike at 3.9 Ga, the U–Pb zircon geochronology from Apollo 16 melt breccia and 14 and 17 melt breccias show a wide range of age distribution prior to 4 Ga (Hopkins and Mojzsis, 2015; Nemchin et al., 2008; Nemchin et al., 2009; Grange et al., 2009; Norman and Nemchin, 2014). In these studies, the relative probability for an age of 4.35 Ga is actually more prominent than a LHB-like spike at \sim 3.9 Ga (Hopkins and Mojzsis, 2015). As a result, some researcher proposed multiple cataclysms occurring prior to 4 Ga (Hopkins and Mojzsis, 2015).

1.7 The last three billion years lunar bombardment record and a relationship with returned samples

The second long-standing open question in the field of lunar bombardment regards the more recent lunar impact flux and is the primary focus of this dissertation. According to the standard crater based lunar chronology by Neukum, the Moon experienced little change in the impact rate over the last three billion years. However, two independent sets of lunar impact glass spherules from different regolith samples collected from different landing sites suggest that their $^{40}\text{Ar}/^{39}\text{Ar}$ -derived age distributions may be contradictory to a constant impact flux model. The first data set shows an apparent excess of impact glass spherules and shards (spherule fragments) with ages of ~ 500 Ma (Culler et al., 2000; Levine et al., 2005; Hui et al., 2009). The second data set was obtained by selecting only “exotic” glass spherules, which are geochemically-distinct to local regolith. The exotic spherules show a higher number of ages between 700 and 900 Ma; that range of ages overlaps with the formation age of Copernicus Crater at ~ 800 Ma (Zellner et al., 2009; Zellner et al., 2003).

Our aim goal was to examine whether or not the lunar impact flux has remained constant over the last three billion years. It appears that both long-standing open questions in lunar cratering history (the LHB and the impact flux < 3 Ga) might involve with some degree of sampling bias. The LHB is interpreted from returned lunar impact melt rocks and breccias, and the recent impact flux is challenged by at least two independent data sets of lunar impact glass spherules. As an interpretation of these samples has not always been straightforward, this dissertation is devoted to resolving observational inconsistencies and to explaining a phenomenon that is coupled with lunar sampling bias. Much research has been devoted to studying the formation of single craters in isolation. However, the lunar surface has been bombarded by countless craters, not a single crater in isolation. Therefore, a sample picked up from the lunar surface has experienced the collective effects of numerous cratering events.

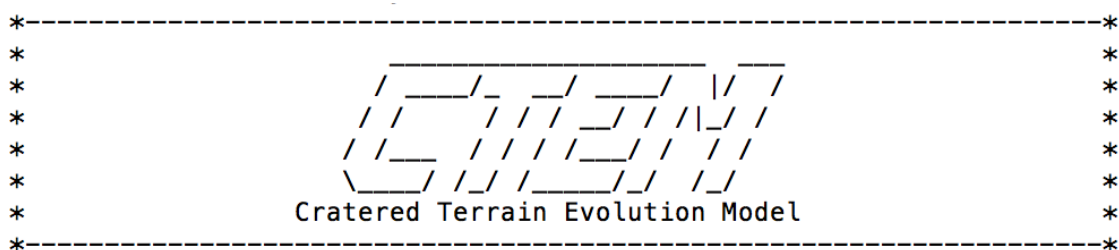
The sheer number of impact craters on the lunar surface makes the impact history of a single sample challenging to model.

Fortunately, computer technology has advanced rapidly in recent years and tools are available to deal with large amounts of data. We developed a three-dimensional regolith tracking model based on Cratered Terrain Evolution Model (CTEM) (Richardson, 2009; Minton et al., 2015; Huang et al., 2017), a Monte-Carlo code that models a heavily cratered surface, to track a variety of information (e.g., composition, glass spherules, and ages) during a bombardment simulation (Huang et al., 2017; Huang et al., 2018). I present the model in Section 2 in which I describe the concept of crater excavation flow model (Maxwell Z-model), its implementation in CTEM, and other critical model components such as impact gardening by craters smaller than a pixel resolution of CTEM and ejecta deposition in the form of crater rays. The streamline based model, the crater scaling laws used in CTEM, and the regolith tracking component in CTEM make the code more or less a study of the redistribution and mixing of materials driven by impacts. To validate the code, I used two independent data sets: Clementine UV/VIS reflectance measurements taken across mare and highland contacts at Grimaldi Crater, and non-mare abundance of lunar mare soils (see results in Chapter 3). In Chapters 4 and 5, we extended the code and work to investigate the possibility of sampling bias on $^{40}\text{Ar}/^{39}\text{Ar}$ -derived age distributions of lunar impact glass spherules, assuming a constant impact flux model. Although the code appears to work successfully explaining observation data sets that this dissertation presented here, a summary is discussed in Chapter 6.

2 METHODS

”FORTRAN is not a flower but a weed – it is hardy, occasionally blooms, and grows in every computer.” Alan J. Perlis. Computer scientist and professor (Yale).

2.1 Introduction to CTEM



The Cratered Terrain Evolution Model (CTEM) was initially proposed and developed by James E. Richardson for his dissertation work on crater-induced seismic shaking process for small bodies back in 2005. The code uses the Monte-Carlo technique (Press et al., 1992) to populate a discretized surface with model impact craters over time. Similar computer models also worked to study the evolution of a cratered surface (Cross and Fisher, 1968; Woronow, 1978; Chapman and McKinnon, 1986). CTEM takes advantage of modern computation technology (high performing memory), crater counting calibration, and crater and ejecta scaling laws to understand the erasing mechanisms of impact craters on a given target surface. For the erasing mechanisms, it includes cookie cutting of old craters by new craters, sandblasting that erodes craters by smaller craters, ejecta burial, and crater degradation induced by distal ejecta. CTEM was written in Fortran 77 by James E. Richardson but transitioned to Fortran 2003 for more extensibility and modularity at ease of code development.

The current version of CTEM is suitable for problems such as crater saturation and equilibrium, surface porosity evolution, material transport and numerical sampling process (Richardson, 2009; Minton et al., 2015; Minton et al., 2018; Huang et al., 2017; Huang et al., 2018; Hirabayashi et al., 2018).

A bombardment simulation setup in CTEM initially discretizes a user-defined planetary surface grid into square pixels that each represents a portion of the modeled planetary surface. Each pixel is available to store a variety of data in order to perform further analysis. For example, the elevation data for an entire grid constructs a Digital Elevation Model (DEM) of a surface. An elevation that a specific pixel stores can be altered in response to the topographic changes due to the formation and degradation of craters. The elevation information stored in a pixel serves as a three dimensional parameter in our grid space; an advantage of it allows us to simulate subsequent physical processes such as crater collapse or other types of degradation. Also, the square grid of pixels possesses periodic boundary conditions so that the grid represents a single contiguous surface.

The current CTEM can only readily produce a crater size-frequency distribution that mimics observed lunar impact craters, and for other celestial objects it requires further investigation for generating a production function for calibration purpose. Based on determinations of the size of a grid space that a user sets up in CTEM, CTEM chooses the impactor's size and velocity distribution and multiple sets of scaling law parameters from appropriate probability distributions such that the numerically-obtained crater size-frequency distribution matches a standard crater-based lunar chronology, such as Neukum Production Function (NPF) (Neukum, 1983; Neukum et al., 2001). Once the impactor size, the impact velocity and the impact angle are determined, CTEM creates the crater based on π -group scaling laws. Subsequently, CTEM is programmed to perform the following steps in order: 1) crater formation, 2) ejecta deposition, and 3) crater collapse or subsequent degradation processes. The location of a crater in CTEM is randomly chosen, but the form of a final crater comfortably aligns to the direction of a local slope that is averaged out by

all pixels where this crater occupies. Using the chosen impactor parameters, CTEM creates a crater whose morphology is determined using appropriate crater scaling relationships. The size of each crater is determined based on the π -group scaling laws (see Section 2.1.2, in which we combined the work from Melosh, Holsapple, and Richardson to have a coherent derivation (Holsapple, 1993; Melosh, 1989; Richardson, 2009). CTEM modifies the surface elevation to reflect the effect of a local slope on a final crater shape.

Regarding the formation of ejecta of a given size of a crater in CTEM, the code emplaces it to corresponding pixels by adding the numerical value of ejecta thickness to an elevation that is stored at a pixel. The emplacement of ejecta concerning with ejecta thickness and spatial distribution is adopted from observational constraints. Lastly, CTEM models slope collapses when the calculated topographic slopes exceed the angle of repose. We noted that CTEM does not require information of time step in the sense of a finite difference algorithm. Instead, a time step in CTEM uses the time elapsed during the generation of every single crater, which corresponds to a variable time in Poisson statistics. The overview of CTEM as described here is given for an interested reader to find more details in the following sub-sections that include derivation of crater scaling laws, as well as technical details on crater degradation mechanisms and crater counting calibration in the work of Minton (Minton et al., 2015).

2.1.1 Background: A stochastic process of a cratered surface

A fascinating, long-standing problem regarding the evolution of a planetary cratered surface is saturation state, and CTEM, of course, is one of many numerical codes to address this issue. The evolution of a cratered surface itself is exciting because it is hoped to restore an impactor population from a planetary cratered surface (e.g., the Moon). However, our ability to do so has also been controversial, especially for a heavily cratered surface (e.g., the ancient highlands) (Cross and Fisher, 1968; Marcus,

1970; Woronow, 1978; Chapman and McKinnon, 1986; Strom et al., 2005; Hartmann, 1984; Hartmann, 1988; Hartmann, 1995; Hartmann and Gaskell, 1997).

An inference of an impactor distribution can be made if a surface is young or overlapping craters on the top of a surface can be distinguished. For an interpretation of a heavily-cratered surface, it becomes tricky because craters start to obliterate other craters generated from previous impact processes. The obliteration process of older craters is initiated when subsequent craters overlap with one or more craters. An overlapped crater loses parts of a rim and may be buried by a thick ejecta blanket until it cannot be recognized. The obliteration process is important because it continuously erases any old craters that are superposed by new craters.

The definition of crater saturation is somewhat ambiguous because the process that populates craters on a surface depends on the size of a crater and the spatial distribution of craters. For the spatial distribution parameter, geometric saturation and randomly-distributed saturation yield a different efficiency of packing craters into a surface. The simplest saturation problem is when we pack craters with the same diameter of a size (D) into an area. For geometric saturation, it packs craters with the same diameter into a surface in a hexagonal configuration. This is considered as the maximum number of craters without overlaps (N_s) or equivalent to the maximum size of an occupied area using the same number of craters. The fraction of cratered area over the reference area (cratered area and non-cratered area) is about 0.905, equivalent to $\sim 10\%$ of an entire area that is not occupied by craters (Gault, 1970). Randomly-distributed saturation is to randomly populate a surface with the same sized craters; overlapping of craters decreases the size of an occupied area. For the same distribution of craters, the size of an occupied area for randomly-distributed saturation is smaller than the size of an occupied area for geometric saturation so a random distribution requires more number of craters to reach saturation. In crater counting community it uses the maximum number of craters that reaches geometric saturation as a reference to describe the degree of saturation of a cratered area that they perform a crater counting (Gault, 1970).

In a realistic planetary cratered surface, we deal with a randomly distributed impactor population that is often characterized by a power-law function of sizes and is converted to crater sizes ($N \propto D^b$) (see Section 1.5). Without testing the evolution of craters with each class of sizes on a surface, Gault generated craters with size ratios of 1:5, 1:10, and 1:16 in a 2.5 cm-square and 30 cm-deep sandbox filled with quartz sand that correspond to the various exponents of b from -2.5 to -4.0 (Gault, 1970). The laboratory experiment conducted by Gault shows that for all ratios the area of a cratered surface increases with the number of impacts until reaching $\sim 1-10\%$ of N_s (Gault, 1970). Beyond 10% of N_s , the number of countable craters remaining on the surface of a sandbox changes a little. Gault suggested that once reaching this state, the appearance of a surface looks similar, but just the locations of craters are different (Gault, 1970). So-called crater equilibrium expresses an idea that the formation of a new crater simultaneously destroys an old crater. They also found that crater equilibrium is a size-dependent process; a cratered surface can be saturated with a larger crater for a sufficient amount of time. For example, in the most densely cratered parts of ancient lunar farside highlands as an example, the crater densities for craters larger than 20 km in diameter ($N(20)$) are in the range between 100 and 280 are equivalent to 3% to 10% geometric saturation (Head et al., 2010).

As observed by Gault in his laboratory work and the others, it is intriguing that after the surface reaches a crater equilibrium, the distribution of observable craters remained on the surface (the number of craters) is in a power-law function of diameter with the exponent of b from -1.8 and -2 regardless of the original exponent of an impactor distribution (< -2) (Gault, 1970; Hartmann, 1984; Chapman and McKinnon, 1986; Xiao and Werner, 2015; Hirabayashi et al., 2017). The “magic number” of -2 in crater size-frequency distribution yields a dimensionless crater density, suggesting a scale-free crater density for all sizes of craters (Melosh, 2011). We noted that the exponent of b in a power-law function of crater diameter is conventionally called a slope. This phenomenon has been reported by not only the laboratory experiment of Gault but also several crater count studies, as well as the theoretical and numerical

framework (Cross and Fisher, 1968; Woronow, 1978; Chapman and McKinnon, 1986; Marcus, 1970; Richardson, 2009; Hirabayashi et al., 2017; Hirabayashi et al., 2018; Minton et al., 2018). The underlying causes of a change in the crater size-frequency distribution are mainly driven by erasure of craters. Erasure mechanism of craters includes cookie cutting (a new crater cuts an old crater), sandblasting (erosion of a crater by small craters), ejecta blanket burial (infilling of an old crater), and erosion by distal ejecta. Contributions of each erasure mechanism to characterize a crater equilibrium have also been analytically examined (Hirabayashi et al., 2017; Minton et al., 2018; Ross, 1968; Soderblom, 1970). In summary, the previous analytical work on the contribution of sandblasting to the distribution of craters that reach equilibrium by Ross and Soderblom found the slope of a crater size-frequency distribution to be -2 (Ross, 1968; Soderblom, 1970). Recent Monte-Carlo computation work from CTEM and their theoretical analyses successfully characterized each contribution of erasure mechanism to equilibriums and explained an observational deviation seen in the slope (Hirabayashi et al., 2017; Minton et al., 2018).

2.1.2 Cratering and ejecta scaling model

CTEM is primarily constructed of cratering and ejecta scaling-laws. Scaling-laws are established by a series of experiments, utilizing the same outcome under different experimental conditions, in which variables can be scaled. Once scaled constants of variables are derived, one uses the set of scaling laws to predict the outcome from the other condition. In the field of impact cratering, the first use of scaling-laws was in TNT explosions studied by Lampson in 1950. Lampson found that the either crater size or depth excavated by an explosion is proportional to the cubic root of the explosive energy (Lampson, 1950). Later it was found that the depth of a burial of an explosive influences the estimate of the excavated size. Still, the explosion scaling laws provide an insight to the understanding of cratering scaling-laws.

CTEM uses impact crater size scaling laws to model a crater with calculated size under a given impact conditions. In the example of deriving impact crater size scaling-laws, a series of impact experiments is designed to produce impact craters with the same size while varying an impact velocity or impactor size. Because an impact velocity and impactor size, possibly other parameters that can be factored in, relate the size of a final impact crater, those impact experiment outcome are used to determine the dependence of impact crater size on those parameters. The purpose of impact crater size scaling-laws is to estimate a entire range of sizes of impact craters. This is considered significant because we have not witnessed or been able to produce an impact crater larger than tens of meters. As a planetary impact crater easily exceeds the size of tens of meters, impact crater size scaling-laws allow us to extrapolate it to a larger crater.

The consequence of using cratering scaling-laws neglects the complex process of impact cratering (early stage of shock wave development) and physical parameters of impactor (shape, size and composition). The neglect of complex process and projectile-related parameters in deriving cratering scaling-laws is reasonable after considering the concept of “late-stage equivalence” (Dienes and Walsh, 1970) or a mathematical assumption of point source (impact energy in an infinitesimal area). “Late-stage equivalence” was discovered by Dienes and Walsh in their numerical impact flow calculations in 1960s. In their hypervelocity impact calculations, the results with a specific combination of diameter and velocity of an impactor can be grouped together. Each group of numerical calculations yields the same value of scaling laws (Lv_i^n where n is derived from numerical calculations). Despite of the complex process of cratering in a hypervelocity impact, “Late-stage equivalence” states that the complex process of cratering would not influence the outcome that appears in later stages.

In 1980s, Holsapple proposed a similar concept to late-stage equivalence, “coupling parameter”, that uses point source solutions to approximate the energy and momentum of an impactor into target (Holsapple and Schmidt, 1987). A point source

solution is a single source identified, in which the extent of the source is negligible relative to the scale of a modeling. A point source approximation mathematically simplifies an analysis. In particular, when using a point source approximation to obtain cratering scaling-laws, it is useful to study the asymptotic behavior of cratering scaling-law functions. For example, the limit of a point source solution for a cratering scaling-law should reach a finite number as the size of an impactor approaches zero and an impact velocity is exceedingly large or fixed. The point source approximation approach also yields a single coupling parameter. In other words, one single valued function controls the outcome of a cratering. Whether or not more than one coupling parameter involve with an interpretation of cratering outcome, a further investigation is needed (Melosh, 1989).

In “coupling parameter” approach, it provides a systematic way to factor in variables that are involved during different stages of a cratering process (Holsapple and Schmidt, 1987; hol,). Regarding the impact crater size scaling laws, Hoalsapple expressed the volume of a transient crater as a functional with functions of coordinates, time, gravity, size and impact velocity of a projectile, and material properties in response to a wide range of pressures and temperatures. For a given time frame of a transient crater, the coordinates and time in the functional of a transient crater volume can be eliminated. If experimenting the same set of impactor and projectile, this functional can be further reduced to depend on gravity, size and impact velocity of a projectile, material densities, and target strength:

$$V = F(v_i, \rho_i, \rho_t, Y, g, m) \quad (2.1)$$

where V is the transient crater volume, F is the functional of V , v_i is the impact velocity, ρ_i is the impactor density, ρ_t is target density, Y is target strength, g is the gravitational acceleration, and m is the impactor mass ($\rho_i \times \frac{4\pi}{3} a_i^3$, where a_i is the radius of an impactor). The functional as well as its functions are dimensionless, such that the importance of different physical processes is evaluated. Among dimensionless

analyses, researchers commonly use the π -theorem, originally proposed by Buckingham in 1914, to group all relevant physical variables to a number of dimensionless parameters. In equation 2.1, the dimensions on both sides of the equation must be the same. Since there are six unknown variables in the equation 2.1, the number of unknown dimensionless parameters is three after subtracting three dimensions involved (mass, length, and time). These three required dimensionless parameters are conventionally chosen in the following:

$$\pi_2 = \frac{g}{v_i^2} \left(\frac{m_i}{\rho_i} \right)^{1/3} = 3.22 \frac{ga_i}{v_i^2} \quad (2.2)$$

$$\pi_3 = \frac{Y}{\rho_t v_i^2} \quad (2.3)$$

$$\pi_4 = \frac{\rho_t}{\rho_i} \quad (2.4)$$

where π_2 is “gravity-scale size” (Melosh, 1989, page 177), which is related to the importance of a gravity in a cratering event, and the factor of 3.22 given by $(4\pi/3)^{1/3}$ is neglected, π_3 is “non-dimensional strength” (Richardson, 2009, Equation 3), which is the measure of importance of target strength, π_4 is the ratio of target and impactor densities. Lastly, the crater volume term on the left-hand side of the equation 2.1 must be expressed in the dimensionless form, π_V :

$$\pi_V = v \left(\frac{\rho_t}{m_i} \right) \quad (2.5)$$

This dimensionless measure of a transient crater volume is well-known as “crater efficiency”, π_V (simply defined as the volume ratio of crater cavity and impactor).

The dimensionless form of the equation 2.1 can be rewritten, F' :

$$\pi_V = F'(\pi_2, \pi_3, \pi_4) \quad (2.6)$$

As described by π -theorem, the crater efficiency for a given crater is controlled by gravity-scale size, non-dimensional strength, and material densities. The equation 2.6 can be simpler if only one dimensionless parameter is considered. Researchers recognized two different regimes, gravity-dominated and strength-dominated, regarding the scale of a cratering event. If target strength is negligible during cratering process, cratering scaling-laws are within gravity-dominated regime. For a given ratio of target density and impactor density, it is simply the relationship between the crater efficiency and the gravity-scale size:

$$\pi_V = F''(\pi_2) \quad (2.7)$$

where F'' is the functional of a crater transient volume under a gravity-dominated regime. For a laboratory cratering experiment, the displacement volume of a crater cavity is measured under a set of combination of impactor size and impact velocity (determining a gravity-scale size). Interestingly, the relationship between a crater efficiency and a gravity-scale size is found in a power-law function,

$$\pi_V = C_V \pi_2^{-\alpha} = C_V \left(\frac{ga_i}{v_i^2} \right)^{-\frac{3\mu}{2+\mu}} \quad (2.8)$$

where C_V and α are experimentally-derived constants, and α was found equivalent to $-\frac{3\mu}{2+\mu}$ in Holsapple (1993) where μ is a experimentally-determined constant related to the dependence of impact velocity on the coupling parameter defined as $C = a_i v_i^\mu \delta^\nu$ (Holsapple and Schmidt, 1987; hol,). In laboratory experiments, under a gravity-dominated regime, crater efficiency decreases as the size of an impactor increases. On the other hand, the crater efficiency under a strength dominated regime depicts a similar power-law function of nondimensional strength parameter with the exponent of $-\frac{3\mu}{2}$. If taking into account the ratio of target density and impactor density, it affects crater efficiency for gravity-dominated and strength-dominated regimes by some factors (π_V^G and π_V^S):

$$\pi_V^G \propto \pi_2^{-3\mu/(2+\mu)} \pi_4^{(2+\mu-6\nu)/(2+\mu)} \quad (2.9)$$

$$\pi_V^S \propto \pi_3^{-3\mu/2} \pi_4^{1-3\nu} \quad (2.10)$$

where ν is a constant related to the dependence of impactor density on the coupling parameter. Conveniently, the scaling-laws for a crater efficiency are often expressed in four π -theorem-based dimensionless parameters:

$$\pi_V = K_1 \left[\pi_2 \pi_4^{-\frac{6\nu-2-\mu}{3\mu}} + \left[K_2 \pi_3 \pi_4^{\frac{6\nu-2}{3\mu}} \right]^{\frac{2+\mu}{2}} \right]^{-\frac{3\mu}{2+\mu}} \quad (2.11)$$

where ν is onventionally taken as $\frac{1}{3}$, and K_2 can be treated as unity, in which $K_2 Y$ in $K_2 \pi_3$ term becomes the effective target strength of \bar{Y} , which is determined from strength-dominated crater results. Finally, we substitute $\pi_{i=1,4}$ into the equation 2.11, and it becomes:

$$V = K_1 \left(\frac{m_i}{\rho_t} \right) \left[\left(\frac{ga_i}{v_i^2} \right) \left(\frac{\rho_t}{\rho_i} \right)^{-\frac{1}{3}} + \left(\frac{\bar{Y}}{\rho_t v_i^2} \right)^{\frac{2+\mu}{2}} \right]^{-\frac{3\mu}{2+\mu}} \quad (2.12)$$

CTEM uses the prescribed shape of a parabola as a transient crater. The volume of a parabolic shaped crater is $1/24\pi D^3$ where D is the diameter of a transient crater. In particular, we noted that it still needs work to understand what sets the value of μ defined in the single coupling parameter. In general, the parameter of μ determines what coupling scheme governs a cratering process. If a cratering process is primarily governed by impactor's kinetic energy, the parameter of μ is set as $2/3$ ($C \propto a_i v_i^{2/3}$). On the other hand, the parameter of μ is $1/3$ if impactor's momentum controls a cratering process. More importantly, it was discovered that material properties set a specific value of μ regarding the energy and momentum coupling during a cratering

process. Other material-related factors such as porosity are critical to understand the cratering scaling laws (Melosh, 1989).

2.2 Overview: A Three-Dimensional Regolith Transport Model

Our three-dimensional regolith transport model is based on the CTEM Monte Carlo cratering code (Richardson, 2009; Minton et al., 2015). CTEM was originally designed to study how impact cratering shapes the topography planetary surface and tracks the number of countable craters over time. We modified the code so that ejecta accumulation includes not only the thickness but also the composition and other types of information of a parcel of ejecta. For the ease of a derivation, up to Section 2.3, we derived an implementation of Maxwell Z-model streamlines in CTEM by using a two component material model that represents the relative abundance in each ejecta parcel of either mare basalt or highland anorthosite.

We introduce the discussions in the following sections. The volume of material that is transported across contacts is critical, and in Section 2.3, we describe how CTEM calculates each craters ejecta volume and how we can use the concept of streamlines (Maxwell Z model) to estimate the mixture of our two material components found in each craters ejecta parcels. In the Sections 2.4, we extended CTEM from a binary component of regolith transport model to multiple components that record ages and number of glass spherules. In these two sections, it contains a technical methodology that you may wish to skip. In the Section 2.5, we presented a shock pressure gradient model using the Gamma model for the destruction of glass spherules within a transient crater. Following the sections 2.5, we were inspired by lunar impact crater rays, e.g. Tycho Crater's long rays across the Moon. CTEM mimicked the shape of crater ejecta distribution by using a generic mathematic formula, which is known as Superformula, that can produce various shapes of natural objects, such as starfish, flowers, or bacteria by different parameter values (Gielis, 2003). In the last two sections 2.7 and 2.8, we focused on two processes: 1) material mixing by craters that

are smaller than the grid cell resolution that produces both primary craters and their distal ejecta, and 2) material deposition by craters that are larger than the total grid space where we simulate all primary craters (we called ‘super-domain’ craters).

2.3 The Dynamic Stream Tube-Based Transport Model

Our task is somewhat more complex. We must be able to quickly determine the fraction of mare and highland material that is entrained in the excavation flow that makes up each parcel of ejecta. A parcel of ejecta in CTEM is a cuboid of material that occupies a single grid cell with a height determined by the paraboloid shell-based ejecta thickness calculation (Richardson, 2009, Equation 22). To determine the amount of mare and highland material of a parcel of ejecta during excavation, we need to know the makeup of material that was intersected by the streamlines that made up the excavation flow of each ejecta parcel. As regolith is reworked, the composition of any given grid cell will take on a very complex layered structure. By overlying each ejecta parcels streamlines onto the preexisting compositional layers at the site of the excavation, we can estimate the new composition of each ejecta parcel.

The relationship between radial distance of an ejecta and its ejection velocity or launching velocity is key to ejecta emplacement in CTEM. CTEM uses crater ejecta scaling laws derived from the work of (Housen et al., 1983). CTEM traces the ejecta to the transient crater and uses the paraboloid shell to approximate the total volume of ejecta in any direction at the distance. The thickness of ejecta at this distance is averaged over the landed area (Richardson, 2009, Equations 25-27). Because the geometry of the true excavation flow is different than a paraboloid shell, this technique is inaccurate when attempting to map the provenance of ejecta back to the excavation flow volume. We therefore will use a hybrid approach, where the ejecta thickness is obtained by a simple empirically derived power law function, but the compositional ratio of ejecta is determined using the Maxwell Z model. We must note that the implementation of Maxwell Z-model in CTEM is only for the first-order

approximation and works the best for a point-source approximation (Austin et al., 1981, see a detailed description on the limitation of Maxwell Z-model for crater ejecta excavation process). We must keep in mind a better treatment to crater ejecta plume dynamics (Richardson et al., 2007; Richardson, 2011, see the detailed analysis of the Deep Impact ejecta plume).

To model the bulk composition of the material within each parcel of ejecta, we make use of the Maxwell Z model. In the Maxwell Z model, excavated materials from a transient cavity are treated as an incompressible fluid (Maxwell, 1977; Maxwell and Seifert, 1974). The flow of excavated material within a transient crater is often formulated as streamlines in polar coordinates,

$$r(\theta) = r_o(1 - \cos \theta)^{\frac{1}{Z-2}} \quad (2.13)$$

where Z determines the shape of a streamline ($Z = 3$ in our model), r_o is the radial distance from the center of the impact site to location at which the streamline emerged from the free surface, $r(\theta)$ is the radial distance from the center of the impact site to the current location of a streamline within a transient crater, and θ is the polar angle measured from the local vertical. At the emerging location, $\theta = 90^\circ$. Note that the choice of $Z = 3$ in this study is the simplest (and analytically solved) for implementation. A lower value of Z (e.g., 2.7) would be a better choice, yet $Z = 3$ is overall reasonable for approximating the crater excavation stage (Melosh, 1989).

Figure 2.1 shows that streamlines closer to the impact point are faster resulting in distal ejecta, while continuous ejecta blanket mostly comes from streamlines closer to the edge of a transient cavity. Each ejecta parcel is bounded by four corners of a square grid cell. As a result, the ejecta is created by a stream tube with a highly distorted quadrilateral cross section. The distortion of the quadrilateral cross section is due to a difference in the ejection velocities for each corner of the square grid cell corresponding to each ejecta parcel. Calculating the exact shape of this highly distorted stream tube is computationally expensive and impractical to do in CTEM.

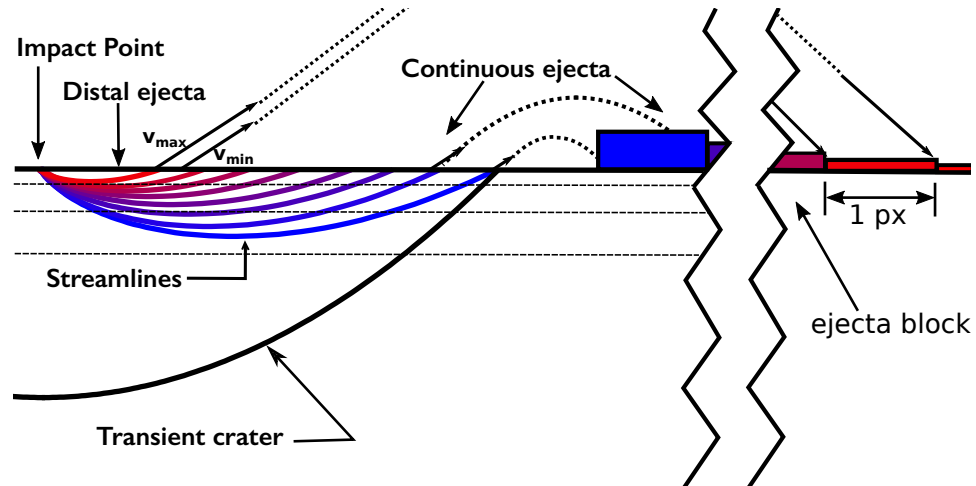


Figure 2.1.: The provenance of an ejecta parcel within a transient crater. Streamlines within a transient crater are highlighted in red and blue colors. The redder the color of a streamline, the faster the ejection speed of a streamline. The magnitude of ejection speed of a streamline is represented by the length of arrow in black color. The length of arrow is arbitrary, but it gives a sense of that the closer to the impact point, the faster a streamline. Slower streamlines deposit as closer to the crater (continuous ejecta), and faster streamlines land at large distances (distal ejecta). A single block of ejecta occupying a single grid cell (pixel) is highlighted in red or blue, depending on the speed of streamlines. The volume of the ejecta block is determined by the volume of material bounded by the streamlines that exit with velocities $v_{min} < v < v_{max}$, which define a stream tube. The horizontal dotted lines denote notional layers of compositionally distinct material. The final composition of the ejecta block is determined by the mixture of material contained within the stream tube.

However, our goal is not to accurately model each stream tube, but to quickly estimate the mixing ratio of material along the stream tubes path. We therefore approximate each stream tube as having a circular cross section, with the total volume determined using the paraboloid shell approximation. Figure 2.2 shows a schematic of our three-dimensional circular stream tube with its corresponding landing distance.

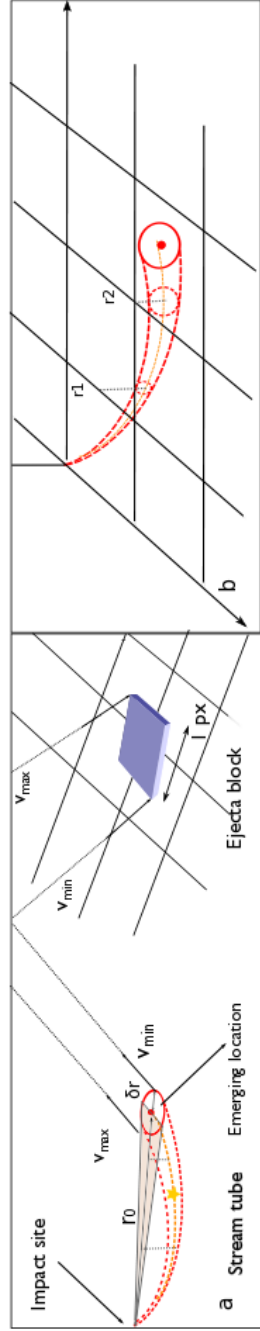


Figure 2.2.: A schematic of a three-dimensional circular stream tube. (a) Stream tube in side view as well as its corresponding ejecta deposit. A stream tube is characterized by a circular section of radius (δr) of a stream tube at the emerging location and radial distance from the impact site to the emerging location (r_o). The red dot in the center of the stream tube is the emerging location. The solid line outlined triangle filled with light orange color is the projection area of a stream tube on the surface. The centerline inside the triangle represents a projection of an axis of a stream tube (dashed line in orange color). (b) Stream tube within the grid space of CTEM. The intersection points between the centerline of a stream tube on the surface and the grid lines are labeled by r_1 and r_2 , which characterize a segment of a stream tube within a pixel space. The dashed lines represent that a stream tube is under the surface. The vertical and dotted lines in gray color at the intersection points attempt to guide readers to the interface of a stream tube with the virtual grid underneath, which are circles outlined in dashed line and red color. The star filled in yellow color is the intersection point that a segment of a stream tube encounters a layer under surface.

We characterize our three-dimensional stream tube with two parameters: the radius of a circle at the emerging location (δr) and the radial distance from the emerging location to the impact site (r_o) as shown in Figure 2.2b. In the following paragraphs we first introduced an analytical equation of a stream tubes volume then described a stream tube residing in a layer system based on linked list structure, which allows us to gain the information of depth for a given pixel.

First of all, given the circular cross section of a stream tube, one can integrate the volume along the direction of radial distance even though the radius of a circular cross section varies along the stream tube. The total volume of our circular stream tube, V_{st} , is given as,

$$V_{st} = \int_0^{r_o} \pi [\delta r(r(\theta))]^2 dr \quad (2.14)$$

where $r(\theta)$ is the radial distance at a given polar angle measured from local vertical and $\delta r(r(\theta))$ is the radius of a cross section at a given radial distance from the impact site. Here the volume of a stream tube and the integration range (radial distance) can be obtained from CTEM. The relationship between the radius of a cross section and its radial position along the stream tube is the only unknown. This relationship is independent of crater size and can be described by a tangential function,

$$\delta r(r(\theta)) \propto \frac{a}{r_o} \tan \left[\frac{b}{r_o} r(\theta) \right] \quad (2.15)$$

where a and b are fitting parameters for all stream tubes within a transient crater for a given size. We find these to be $a \approx 0.936457$ and $b \approx 1.12368$, respectively. Then, by integrating this scaling relationship along the stream tube, an analytical function for the volume as a function of radius, δr , and radial position, r , is given as,

$$V_{st}(\delta r, r_o) = \frac{1}{4} \pi (\delta r)^2 a^2 \frac{r_o}{b} (\tan b - b) + \frac{\pi}{\sqrt{2}} (\delta r)^3 \quad (2.16)$$

Equation 2.16 only leaves δr unknown. For a given volume of a stream tube, the variable of δr in equation 2.16 can be solved. The total volume of an ejecta ($V_{st}(\delta r, r_o)$) for a given pixel is expressed by $A_{pixel} \times t_e$, where A_{pixel} is the area of a pixel and t_e is the thickness of the ejecta parcel as determined using the paraboloid shell model used in CTEM (Richardson, 2009).

We next need to know the makeup of preexisting material of the stream tube. We first identify all pixels that overlap with a stream tube by projecting the axis of a stream tube onto the surface (see Figure 4a). Each of these pixels will have one or more layers that intersect a stream tube at some depth, and we need to calculate the volume of intersection between the stream tube and these layers. Before we consider each layer, we first calculate the volume of intersection between the stream tube and the total column of material beneath each pixel it intersects. The segment of a stream tube starts from the radial distance of r_1 to the radial distance of r_2 relative to the center of a crater (see Figure 2.2a). By using equation 2.16, the volume of intersection between the stream tube segment and the pixel is the subtraction between $V_{st}(\delta r, r_1)$ and $V_{st}(\delta r, r_2)$. It can be analytically expressed in equation 2.16,

$$V_{seg} = \frac{1}{4}\pi(\delta r)^2 a^2 \frac{r_o}{b} \left\{ \left[\tan\left(\frac{b}{r_o}r_2\right) - \frac{b}{r_o}r_2 \right] - \left[\tan\left(\frac{b}{r_o}r_1\right) - \frac{b}{r_o}r_1 \right] \right\}; r_2 > r_1 \quad (2.17)$$

where V_{seg} is the volume of a segment with the length of $r_2 - r_1$ within a pixel. As a result, a stream tube can be dissected into one or more than one segments depending on the location of a stream tube within a transient crater and the size of a pixel in CTEM. We expect some minor error in the estimate of a segments volume because for expediency, we only locate pixels that overlap along the center line of a stream tube. From a practical standpoint, we find that most stream tubes are narrow and confined within a pixel along the path.

Using equation 2.17, we can quickly estimate the volume fraction of material entrained along the excavation flow of each parcel of ejecta. Each parcel of ejecta

is tracked as a compositionally distinct layer and is emplaced on the top of any preexisting layers. As subsequent craters may excavate one or more than one of those compositionally distinct pixels, recording all deposits from each cratering event is mandatory for this study. For our current problem, each ejecta block is tracked with a single number that stores the mare fraction: 0 equals pure highlands and 1 equals pure mare.

To keep track of each distinct ejecta layer from a cratering event over time, we use a dynamic data structure called a linked list to record every ejecta block as a distinct layer at each grid cell. This dynamic data structure has more flexibility than a fixed array, as the number of layers can be redefined on the fly using two main operations (executed in a first in/last out manner). When an ejecta block is deposited in a given grid cell, a “push” operation is executed, basically adding a new layer of specified thickness and mixing ratio on the top of the surface at that location. If a grid cell experiences an excavating event, such as within a transient crater, for example, a “pop” operation is executed, and a layer, or several layers depending on the excavation depth, will be removed from that location. Each grid cell location records a compositionally unique layered structure as a result of impact excavation and deposition.

To obtain the amount of mare and highland material of each ejecta parcel, we need to estimate the intersected volume between a segment of a stream tube and a layer. Figure 2.2b shows how a segment of a stream tube looks like under a surface. We traced the centerline of a stream tube in a layer structure and projected the intersection point to the surface for obtaining the radial distance so that the volume between neighboring intersection points can be calculated by equation (5). Continue to the example of Figure 2.2a, if this segment with the length of $r_2 - r_1$ is sitting between two layers, we can obtain the location of an intersection point between the depth of the first layer and the centerline of a segment (see yellow star in Figure 2.2a). Assuming that each of these two layer contains a mare fraction, f_1 and f_2 , the final

mare fraction of a segment is the total mare volume normalized by the total volume of the segment,

$$f_{seg} = \frac{f_1 \times V_{seg}^1 + f_2 \times V_{seg}^2}{V_{seg}} \quad (2.18)$$

where V_{seg}^1 and V_{seg}^2 are the volume of a segment intersected with the first and second layers, respectively. Here we illustrate a calculation of mare fraction for a segment of a stream tube for an example of a two-layer structure. As more ejecta layers build up over time, a segment of a stream tube may overlap with several layers. Note that the approximated volume of a segment with a layer is not aligned up with horizontal layer but perpendicular to the layer. However, we confirm that our estimates are efficient and only have some small difference from exact volume. The total volume of both materials is conserved over the course of a single full simulation. Finally, CTEM loops over all pixels that a stream tube superposes, and the calculation of a mare fraction for a whole stream tube follows the same manner.

2.4 Glass spherule production model

Previously, we obtained an analytical expression of crater excavation flow by using the concept of Maxwell Z-model (see the section 2.3). This analytical expression allows us to approximate the volume and provenance of an excavation flow emerging from a crater transient crater that depends on different impact conditions. This expression can be worked with the geometry of a subsurface structure. We have demonstrated that our streamtube calculation can be adjusted to a dynamic subsurface structure in which consists of stack of cratered materials from the formation of each crater over time. All pixels where stores this rich information such as the amounts of basaltic and anorthostic materials are accessed and approximated before a next crater forms in CTEM. By doing so, we can fast approximate the composi-

tion of a subsurface structure where a crater forms in CTEM and extract all possible information before forming subsequent craters.

Our streamtube based transport code is capable of estimating bulk volumes of binary materials in a target surface where a crater forms and placing those compositionally-distinct materials to varying distances in a ballistic manner. We made use of remote sensing reflectance measurements taken on lunar mare and highland contacts for the calibration purpose of our transport code (see Chapter 3). As the use of Maxwell Z-model to approximate the crater excavation flow appears successful (see Figure 3.6), this implies that the information other than binary composition during a crater excavation flow can be approximated. For example, the intense shock heating during contact stage melts target materials, and sooner after crater excavation begins a portion of this impact-generated melt was ejected.

In particular, lunar impact glass spherules, a kind of Impact melt products, are thought to have originated in an impact-generated melt. Radiometric age measurements of those glass spherules, such as $^{40}\text{Ar}/^{39}\text{Ar}$ ages, provide some insight to lunar impact flux. Because of their formation upon high temperatures induced by impact argon within a spherule that had retained before the impact occurred were degassed. As a result, initial zero argon upon the formation of a spherule is interpreted as the time when the impact that formed it occurred. By the time we sampled, a spherule (potassium-bearing material) would have retained argon since the last heating event, which could be the impact event that formed it.

Fortunately, scaling laws for impact melts are relatively well-established; estimates of impact melts' volume and distribution in terms of impact conditions can be obtained. This set of scaling laws for impact-generated melts is valuable to a code like CTEM that takes an analytical approach, because the CTEM code must be able to simulate glass spherules produced by large numbers of craters in a single simulation. Using the concept of streamlines, as well as the scaling laws for the volume of impact melts, it allows us to estimate the provenance of glass spherules in a very simple way.

Glass spherules as well as crater ejecta originate in the excavation zone of an impact transient crater, where streamlines emerge from, as shown in an enclosed area between the impact plane and streamlines in Figure 2.3. In general, the temperature is highest as a streamline is close to the impact point. Near the impact point materials experience extreme shock heating and can reach melting temperature regardless of target strength, forming an impact generated melt zone (O’Keefe and Ahrens, 1977). Most of the impact melted materials remain inside a crater (impact melt body) while the rest of the melted materials are ejected. Some fraction of the ejected melt becomes glass spherules. Although the origin of impact glass spherule within an impact melt zone is loosely constrained, the parameter of cutoff deposition distance in our simple spherule production model can be linked to the launching position within a crater cavity (see Eqs. 4.1 and 4.2).

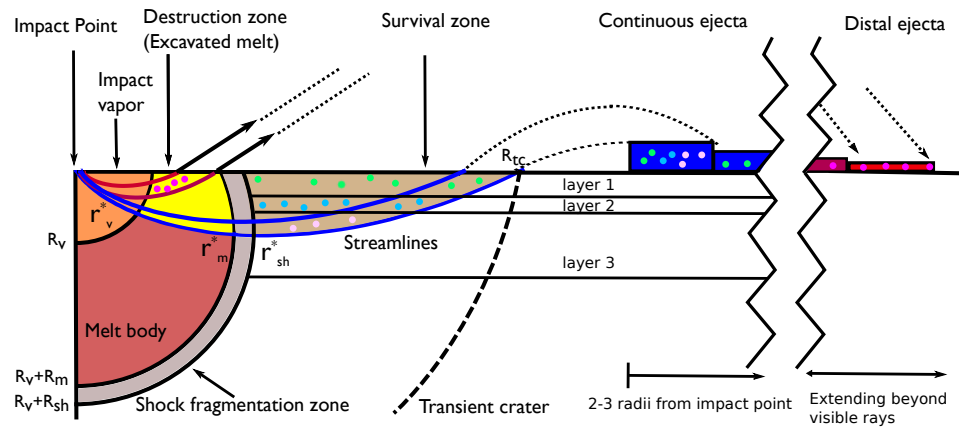


Figure 2.3.: The schematic of our model glass spherule zone. The melt zone consists of the melt body (red) and the destruction zone producing new spherules (yellow). The survival zone is where preexisting spherules can be preserved. No spherules are recorded in the shock fragmentation zone. Streamlines are used to describe the continuous ejecta in a proximal region of crater while the distal ejecta are deposited at large distances. Ejecta can become glass spherule-bearing (layers 1 – 3). The labels starting with R and r are for derivation purpose.

An excavation flow within a crater cavity may carry not only newly-forming spherules that originate in a melt zone but also any preexisting spherules outside a melt zone. The volume of an excavation flow, including a volume that is intersected with a melt zone, and any glass spherule bearing layers must be estimated. Based on the Maxwell-Z model of excavation dynamics developed in Section 2.3, we can use its analytical approach to obtain this excavation flow volume and provenance information. Starting with the volume that an melt zone intersects with an excavation zone, we defined our impact-generated melt zone by using an analytical expression describing the size of an impact melt zone based on varying impact conditions (Abramov et al., 2012),

$$\frac{V_{melt}}{V_{tc}} = 2.9E_m^{-0.85}D_i^{0.66}g^{0.66}v_i^{0.37} \quad (2.19)$$

where V_{melt} is the total impact melt volume, V_{tc} is the impact transient crater volume, E_m is the specific internal of melting the target material, D_i is the impactor diameter, g is the lunar gravitational acceleration, and v_i is the impact velocity. Here we used 3.42×10^6 J/Kg of specific internal energy for highland anorthostic material, as the lunar surface is composed of 83% of highland (Head and Wilson, 1992). The center of an impact melt zone is placed at the depth of one radius of impactor (Pierazzo et al., 1997). Figure 2.4 shows that our ejected melt calculation for a given size of a crater is consistent with the previous theoretical study, in which the trend of fraction of total ejected melts over the total impact-generated melts decreases with increasing size of a crater (Cintala and Grieve, 1998; Dence, 1971). The calculated melt zone is where CTEM models impact melt products; otherwise no melt outside the melt zone is produced. As a result, we assumed a sharp boundary of temperatures between an impact melt zone and the rest of an excavation zone. To be cautious our modeled impact melt zone only provides an approximate location of melted materials, due to a limitation of that CTEM is not a hydrodynamic based code.

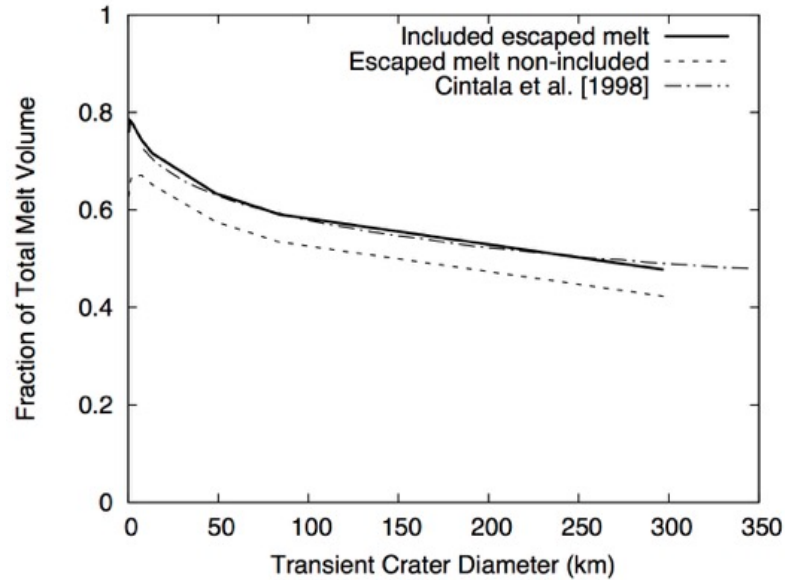


Figure 2.4.: The fraction of total ejected melts over total melt volume as a function of transient crater size in diameter. The dotted dash line is directly taken from Fig. 16 of (Cintala and Grieve, 1998), in which the calculation is based on impact velocity of 15 km/s, anorthositic target, and chondritic impactor. The solid and dash lines are from our study.

To model the evolution of glass spherules, we needed to track how many of them survived or were destroyed, by either re-melting or mechanical shattering by the passage of a strong shock wave. As shown in Figure 2.3, the excavated melt zone consists of a destruction zone (Zone I), survival zone (Zone II), and a shock fragmentation zone (Zone III). Zone I is where the newly-formed excavated melt is generated, which overlaps our calculated melt zone (Eq. 2.19) and the excavation zone described by streamlines. Any age information from modeled glass spherules in Zone I is destroyed and CTEM may instead generate new model glass spherules tagged with the time of the new crater's formation. Zone II is called the impact glass spherule survival zone, which is outside the melt zone, and any original age information and abundance of preexisting glass spherules are kept and recorded in new ejecta layers. However, a

small fraction of the survival zone that the overlaps with shock fragmentation zone contains no surviving spherules, because its impact shock is expected to exceed the yield strength of spherules. For each ejecta voxel, we calculate the total volume of material within the streamtubes that originate from these three zones, and deposit a new layer downrange with a mix of old and new spherules.

The volume of materials in Zone I, which are newly-forming excavated melts, can be obtained by the same method we employed in Section 2.3:

$$V_{st}^m = \frac{1}{4}\pi(\delta r)^2 a^2 \frac{r_0}{b} \left\{ \left[\tan\left(\frac{b}{r_0} r_m^*\right) - \frac{b}{r_0} r_m^* \right] - \left[\tan\left(\frac{b}{r_0} r_v^*\right) - \frac{b}{r_0} r_v^* \right] \right\} \quad (2.20)$$

where V_{st}^m is the melted-only part of a streamtube (excavated melt), δr is the cross section of radius of a circular streamtube, r_0 is the radial distance of emerging point of a streamtube, a and b are derived constants, r_m^* is the distances from the impact point to the intersection point between a melt zone and a streamtube, and r_v^* is the distance from the impact point to the intersection point between a vapor zone, which is the size of an impactor, and a streamtube. For Zone III, the volume of shock damaged material within a streamtube is V_{st}^{sh} ,

$$V_{st}^{sh} = \frac{1}{4}\pi(\delta r)^2 a^2 \frac{r_0}{b} \left\{ \left[\tan\left(\frac{b}{r_0} r_{sh}^*\right) - \frac{b}{r_0} r_{sh}^* \right] - \left[\tan\left(\frac{b}{r_0} r_m^*\right) - \frac{b}{r_0} r_m^* \right] \right\} \quad (2.21)$$

where r_{sh}^* is the distance from the impact point to the intersection point between a shock zone (>5 GPa) and a streamtube (see Figure 2.5). For a shock zone, we used a semi-analytical model, the Gamma Model, to describe the maximum shock distribution within a transient crater (see details in Section 2.5). As a result, the volume of materials in the survival zone is $V_{st} - V_{st}^m - V_{st}^{sh}$. A stream tube within an impact glass survival zone must contain information for a preexisting surface layer structure. Our regolith transport model applied a dynamic layer structure (linked-list data structure) to allow each pixel to stack a collection of ejecta layers over time.

Each ejecta layer is unique and contains information about thickness, composition, and the amount of glass spherules. As craters populate our simulated surface, layers are stacked up or excavated from the top of the grid space forming a subsurface structure. As the excavation flow from each new crater traverses the source region, the streamtubes that supply each ejecta voxel may contain multiple layers of pre-existing deposited ejecta. By obtaining intersection points between a streamtube and layers, a streamtube is dissected. Each dissected tube contains a portion of information of a layer that is assumed to be uniformly distributed. The portion of information of a layer retained by a dissected tube is based on the ratio of the volume of the dissected tube to the volume of a layer,

$$V_i^{surv} = \frac{V_i}{V_{layer}} \times (V_{layer}^m - V_{layer}^{sh}) \quad (2.22)$$

where V_i^{surv} is the volume of the i -th dissected tube, which is located in Zone II, that retains melted-only materials from a layer that this i -th dissected tube resides in, V_i is the total volume of the i -th dissected tube, which can be computed using Eq. 2.20, V_{layer} is the total volume of a layer that the dissected tube resides in, V_{layer}^m is the volume of melted-only material stored in the layer, and V_{layer}^{sh} is the volume of material in the layer inside the shock fragmentation zone.

To record the formation age and the amount of model spherules through a simulation, each newly-generated layer in CTEM is binned into 50 Ma age bins, yielding 60 bins stored in each layer. Through the 3 Ga-long bombardment, the volume of melted material is either added into or subtracted from one of 60 bins that is based on its modeled age, regardless of newly-formed spherules and previous spherule populations. By doing so, each layer carries a unique age distribution, which experiences a varying degree of deposition and excavation, such as an addition of newly-formed spherules, retention of previous spherule populations, or a loss of spherule populations due to destruction in Zone I or III. Our dynamic streamtube approach takes into account the subsurface structure dynamically as the simulation evolves. The glass onset distance

model for the production of glass spherules simplifies how we interpret the amount of model glass spherules (Zone 1) within a crater cavity. While CTEM estimates the relative abundance of materials from three zones for any deposition distance up to ~ 200 crater radii for a given crater, we only treat newly-forming excavated melts as model glass spherules when their deposition distance exceeds a onset distance that depends on which of four onset distances is used.

2.5 Impact shock pressure destruction

Beyond the destruction zone where newly-forming glass spherules are produced, impact shock waves may not have enough energy to melt target materials, yet the magnitude of few GPa of shock exceeds the yield strength of impact glass spherules. We adopted the value of 5 GPa as the yield strength of lunar impact glass spherules (Rasorenov et al., 1991). We characterized the region where materials are shocked up to 5 GPa as an impact-generated shock fragmentation zone.

While impact shock waves propagate fast, they decay rapidly due to energy dissipation by material frictional heating and acoustic fluidization (Melosh, 1979). In impact cratering literature, a semi-analytical approach, the Gamma model, is used to describe the maximum impact shock distribution within a transient crater, also called peak shock pressure (Croft, 1982). The peak pressure is the maximum shock pressure experienced by a parcel of material for a given distance from an impact center. The Gamma model describes two distinct regimes where peak shock pressure remains constantly high in an isobaric core, and decays in a power law relationship as a function of distance,

$$P_{sh}(r) = P_0 r^n \quad (2.23)$$

where $P_{sh}(r)$ is the peak shock pressure as a function of distance from impact center (r), P_0 is the constant peak shock pressure within an isobaric core, and n is the index

of power law (< 0). In one study, the size of an isobaric core is assumed to be the size of an impactor (Pierazzo et al., 1997). And the magnitude of P_0 can be estimated by the planar impact approximation (Melosh, 1989). We used the simplest solution, in which impactor and target are the same materials,

$$P_0 = \rho u_{sh} u_p \quad (2.24)$$

where the particle velocity, $u_p = \frac{1}{2}v_{imp}$, is the half of impact velocity, the shock velocity, u_{sh} , is approximated by a linear relationship with the particle velocity, $u_{sh} = c + s u_p$, in which the parameters of c and s are empirically derived (Melosh, 1989, Table AII.2).

The size of our shock fragmentation zone is mainly controlled by the isobaric shock pressure as well as the index of power law, n . The index of the power law in describing shock decay regime is dependent on the impact velocity. From our two collected data sets, in which one (“P”) used impact velocities ≥ 10 km/s (Pierazzo et al., 1997) and the other (“M”) used impact velocities of ≤ 10 km/s (Monteux and Arkani-Hamed, 2016), we normalized the measured peak shock pressures by our estimated isobaric pressure from Eq. (2.24). In particular, as shown in Figure A1 the asymptotic behavior of peak shock pressures at the distance of $> 2-3$ impactor radii shows that the fitted power law index becomes more negative with increasing impact velocity changing from -1.4 to -2.85 .

A discrepancy between these two asymptotic behaviors may be caused by a transition between different impact velocity regimes. Figure 2.5 also shows the “M” data set for 10 km/s with acoustic fluidization turned on in their iSALE simulation runs. It appears that acoustic fluidization significantly decreases the shock pressure in the far field, aligning with the “P” data points for 60 km/s. As acoustic fluidization may decrease shock pressure, thus increasing the survival of glass spherules, we chose a faster decay rate of -2.85 in this study. A further investigation on a relationship between acoustic fluidization and shock pressure is needed but beyond our scope.

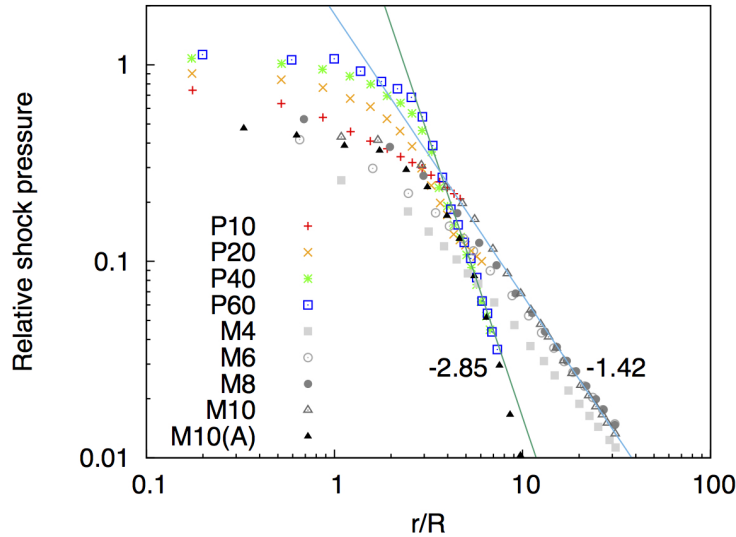


Figure 2.5.: Normalized peak shock pressure within a transient crater from different hydrocode simulations. The points marked “P” are from CTH simulations (Pierazzo et al., 1997), and the points marked “M” are from iSALE simulations (Monteux and Arkani-Hamed, 2016). The numbers indicate the impact velocity in km/s. M10(A) is a simulation with acoustic fluidization. The x-axis is the distance normalized by the radius of impactor within a transient crater, and the y-axis is the relative peak shock pressure. The two straight lines are exponential fits for asymptotic behaviors of shock pressures beyond the isobaric pressure zone, and the numbers are the fitted exponents.

2.6 An Empirical Model for the Spatial Geometry of Crater Rays

In observed lunar craters, the continuous ejecta blanket usually extends to 2-3 radii from the center of the crater. Beyond this range, the ejecta breaks up into discontinuous structures in the form of crater rays and secondary craters. The anomalous diffusion model by Li and Mustard did not take into account the discontinuous nature of distal ejecta but instead modeled each crater as having an infinite continuous ejecta blanket (Li and Mustard, 2000). The Lunar Reconnaissance Orbiter Camera (LROC) instrument (50 cm/pixel) has imaged fresh crater rays (Robinson et al., 2010), which

display the nearly pristine original ejecta pattern of a fresh crater. Initial crater ray material may be brighter than surrounding background material, but cosmic rays, solar wind, or micrometeoroids weather that bright material, resulting in a decrease in their albedo over time until they are no longer distinguishable from the surrounding lunar background. Most craters have no visible rays, which is accounted for by their long exposure time on the lunar surface.

Elliott mapped lunar rayed craters and performed a systematic study of the distribution of their morphology, length, number, and width (Elliott et al., 2018). In general, ray morphology is divided into two types: flowery rays and spike-like rays. Flowery rays exhibit feathered boundaries that often overlap with neighboring flowery rays. Spike-like rays show a sharp boundary between rays and surroundings and are commonly observed in large or fresh craters. These two types of crater rays are usually found together in a single crater. For some craters those flowery rays are shorter than spike-like rays. Some craters may be dominated by one of these two patterns. For example, the ray system of Copernicus Crater is dominated by flowery rays. The ray morphology data of Elliott suggests that the number of spike-like rays ranges from 6 to 14 per crater (Elliott et al., 2018). The average length of flowery rays is about 5 to 7.5 crater radii, and the average length of the observable spike-like rays ranges from 5 to 55 crater radii.

Ray length highly depends on the efficiency of transport of distal ejecta. Baldwin studied crater ray length distribution of 50 lunar craters (Baldwin, 1963) using photometric images of lunar crater taken by Kuiper (Kuiper, 1960). Baldwin summarized the measurements of 50 lunar crater ray lengths in “diameter” in Table 32 of his book (Baldwin, 1963). It is unclear about what he meant by crater ray diameter; yet, suggestions to the measurement method were offered (Baldwin, 1963; Moore et al., 1974; Elliott et al., 2018, Figure 14). Likely, the “diameter” of a crater ray length is determined from drawing a circle that goes from the end of a longest ray to the end(s) of ray(s) along the direction (Elliott et al., 2018). Moore used least square method to fit the data directly from Table 32 of Baldwin and obtained a power law function of a

crater’s radius for observed craters’ length (Moore et al., 1974). Elliott suggests that their least square analysis mistook the value of Ray Diameter as a single ray length, leading to a ray length as twice as the measured ray length in Baldwin (Elliott et al., 2018). This empirical power law function that is corrected:

$$R_{ray} = 5.25R_{crat}^{1.25}, \quad (2.25)$$

where R_{ray} is the median length of a crater’s observable rays, and R_{crat} is crater radius. The original power law function is simply multiply 2 to 5.25 in front of R_{crat} to compensate for a realistic crater’s ray length. In addition, Elliott found that the end of rays may be determined by the point where the primary crater ejecta have become too small to overturn space-weathered “skin” that exists on the lunar surface (Borg et al., 1976).

This hypothesis suggests that the measured length of crater rays is likely shorter than the true length because the ejecta material becomes too small to affect the surface enough to be seen. Li and Mustard reproduced the width of the mare/highland mixing zone from Clementine UV/VIS data, assuming an infinite extent of distal ejecta in their mathematical model (Li and Mustard, 2000). Therefore, we assume that a crater ray could potentially reach farther than we observe them, but for numerical expediency, our crater ray extends until its vertical thickness reaches 10^{-8} m, which is an order of magnitude smaller than the penetration depth of the UV/VIS wavelength region measured by Clementine.

We currently model ejecta blankets and rays as symmetrical, although we know that oblique impacts have an asymmetric ejecta distribution (Moore and Baldwin, 1968; Howard and Wilshire, 1973; Gault and Wedekind, 1978). We assume that the effects of oblique impact angles are averaged out over a large number of cratering events. Using an empirically derived number and length of rays based on the mapping data of Elliott, we use a function called the Superformula to approximate the spatial geometry of rays on the lunar surface (Gielis, 2003) . This formula can reproduce

a wide variety of morphologies found in nature, ranging from basic shapes (circle, square, ellipse, and rose curve) to biological shapes (starfish, marine diatom, and flowers). It is not meant to model any kind of physical process that gives rise to crater rays, but rather to approximately mimic ray morphology and allow us to model the spatial heterogeneity of distal ejecta in a way constrained from observations of ray morphology.

The Superformula in polar coordinates is defined as,

$$r(\phi) = \left\{ \left[\left| \frac{1}{a} \cos\left(\frac{m}{4}\phi\right) \right|^{n_2} + \left| \frac{1}{b} \sin\left(\frac{m}{4}\phi\right) \right|^{n_3} \right]^{\frac{1}{n_1}} \right\}^{-1} \quad (2.26)$$

in which the six parameters: a , b , m , n_1 , n_2 , and n_3 , control shape (see detail below); ϕ is polar angle ranging from 0 to 2π ; and $r(\phi)$ is the radius or distance from a point in polar coordinates to the origin of coordinates and can be expressed as $\sqrt{x^2 + y^2}$ in Cartesian coordinates. In general, a is always equal to b for symmetric shapes. We used a specific parameter set for both spike-like and flowery rays in CTEM and superpose them to generate the complete ray geometry. The superposition of the Superformula equations that we developed for both ray patterns outlines the contour of rays (Figure 2.6).

The parameter of m determines the number of rays. For spike-like rays, it ranges from 6 to 14 per crater, and as a result, the values of m within the range of 6 and 14 with the exact number of any particular crater are determined using a random number generator. For flowery rays, we use 20 for the values of m parameter. The parameter of n_1 controls the shape. We use 4.0 for spike-like rays and 1.0 for flowery rays. The parameters of n_2 and n_3 have an equal value, but their values depend on the length of the ray. By equaling the $r(\phi)$ of the Superformula in equation 2.27 to a desired ray length, we are able to derive a relationship between the value of n_2 (n_3) and a desired ray length,

$$n_2 = n_3 = 8 \times \left[\log_{10} \left(0.5 \times \frac{r_{ray}}{r_{CE}} \right) \right] + 2 \quad (2.27)$$

where r_{ray} can be the length of either spike-like rays or flowery rays, in which default length of spike-like ray is set 100 times longer than the extent of continuous ejecta blanket, r_{CE} . The output of shape of our crater rays is shown in Figure 2.6b.

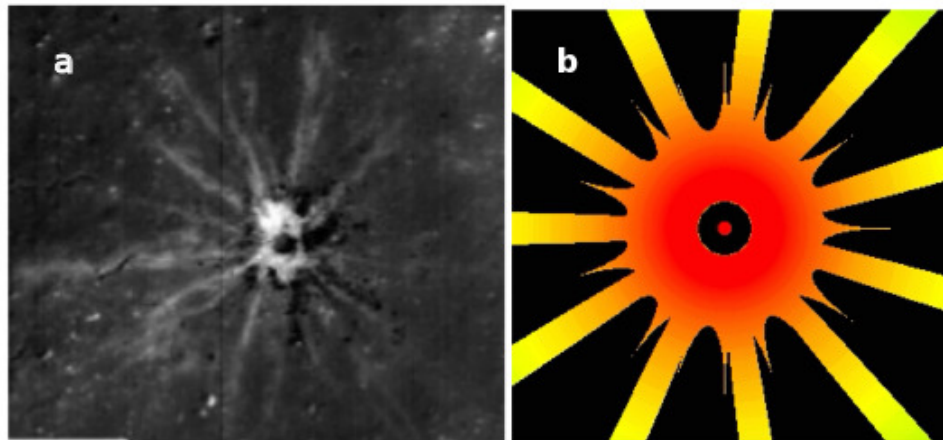


Figure 2.6.: Comparison between an actual rayed crater and a model rayed crater. (a) Example of a fresh crater (LROC stamp: M1136364148RE) with a radius of ~ 6 m in radius. (b) Regolith map of a crater with our crater ray model. The crater is 0.146 km in diameter at 10 m/pixel resolution. The flowery rays surrounding the continuous ejecta extend to 7 radii from the craters center, and the spike rays extends outward until the regolith thickness reaches the cutoff value of 10^8 m (not shown here). The variation in color represents the thickness of regolith (ejecta), ranging from none (black) to maximum (red).

The Superformula gives the spatial geometry of the ray, but we must also adjust the ejecta thickness within the ray to account for the inhomogeneity of the distal ejecta. In the distal ejecta regime in our model, only the rays contain ejecta mass. To conserve the total mass of ejecta in the distal rays, we calculate the areal fraction that

is covered by ray material at any given landing distance, $f(r)$. The ejecta thickness inside a ray at a given landing distance (t'_e) is then modified from an equivalent thickness (t_e) if the ejecta were continuous by $t'_e = t_e/f(r)$. The ejecta thickness outside a ray is zero. In other words, at any given radial distance in the distal ejecta region, the amount of ejecta volume contained in rays is equal to the total volume of the excavation flow at the launching point corresponding to that distance, just as it is in the continuous ejecta blanket. This makes the ejecta thickness versus radial distance slightly less steep along the centerpoint of a ray compared to what it is in the continuous ejecta blanket.

2.7 A Vertical Mixing Model for Craters Under the Resolution Limit of CTEM

The excavation flow model developed in section 2.3 accounts for the mixing and transport of material from craters that CTEM can resolve. Craters smaller than the size of a grid cell cannot be generated, and as a result, we lose information about how small craters affect material mixing. The mixing of material by small craters was investigated by Gault, who developed a framework for understanding the reworking zone based on Poisson statistics (Gault et al., 1974). They parameterized the time scale for the overturn of material by impacts as the time needed to cover a surface completely by craters of a given size. After a surface is completely covered by craters of size D_{crat} , the whole area of the surface will have been mixed to a depth at which the deepest streamline in the excavation flow can reach, which Gault took as $D_{crat}/8$. Because each cratering event occurs independently, regardless of crater size, the total overturning time scale is simply a superposition of overturning time scales of all craters in the crater production population.

To derive the probability that a surface has been excavated to some depth h , we developed a model similar to that of Gault and also Hirabayashi and Costello (Hirabayashi et al., 2017; Costello et al., 2018). From Poisson statistics, Gault found

that for a model of a production population with a single crater size, the probability that any point on a cratered surface has been filled by craters that occupy an area of $A = \pi r^2$ is,

$$P(r, t) = 1 - \exp \left[-\frac{dN(r)}{dr} At \right] \quad (2.28)$$

where $P(r, t)$ is the fraction of a surface occupied by craters with a radius r as a function of time t and $\frac{dN(r)}{dr}$ is the number of craters that fall within the range of r and $r + dr$ that form per unit area per unit time (the differential form of impact flux size-frequency distribution). Because each crater size has its own independent probability given by equation 2.28, the probability that the surface is covered by craters over the size range ($r_{min} < r < r_{max}$):

$$P(r, t) = 1 - \exp \left[-t \int_{r_{min}}^{r_{max}} \frac{dN(r)}{dr} A dr \right] \quad (2.29)$$

For equation 2.29 we seek a fraction of a surface that is excavated to a depth. We assume that the shape of the excavation zone is approximately parabolic (Melosh, 1989). Therefore, the excavation depth for each crater is given by a function, $h(x, r)$, which,

$$h(x, r) = h_{excav} \left(1 - \frac{x^2}{r^2} \right) \quad (2.30)$$

where x is radial distance from the center of each crater of radius r and h_{excav} is the excavation depth at the crater center, which is where the excavation depth is a maximum. In this model, the area of the mixing zone in equation 2.29 is $A = \pi x^2$. Equation 2.29 becomes,

$$P(r, t) = 1 - \exp \left[-t \int_{r_{min}}^{r_{max}} \frac{dN(r)}{dr} \pi x^2 dr \right] \quad (2.31)$$

We can link the relationship between a mixing zone and the size of a crater from equation 2.30,

$$\frac{x^2}{r^2} = \begin{cases} 1 - h/h_{excav} & \text{if } x < r \\ 0 & \text{if } x \geq r \end{cases} \quad (2.32)$$

The maximum excavation depth, h_{excav} , is given by $h_{excav} = \alpha D = 2\alpha r$, where α is a parameter that sets the maximum excavation of a crater relative to its diameter. The value of α can range from $\alpha = 1/8$, assuming that mixing is due to the excavation and deposition of the proximal ejecta blanket (Gault et al., 1974), to $\alpha = 1/3$, assuming that the area between the floor of the final crater and the floor of the transient crater is fully mixed (Collins, 2014). In this study, we only consider the value of maximum excavation depth as $h_{excav} = D_{crat}/8$ because our preliminary investigation for excavation depth as great as $D_{crat}/3$ yields significant inconsistencies with the Clementine observational data. This may be because the region between the floor of the final crater and the floor of the transient crater is only partially mixed.

Equation 2.32 defines the mixing zone for a given crater size r , in which the mixing zone is limited to the radius of a crater. We then substituted equation 2.32 to A into equation 2.31, and we now have for our mixing probability equation:

$$P(h, t) = 1 - \exp \left[-t \int_{\max(r_{min}, \frac{h}{2\alpha})}^{r_{max}} \frac{dN(r)}{dr} \pi r^2 \left(1 - \frac{h}{2\alpha r}\right) dr \right] \quad (2.33)$$

The reason the lower limit on the integral in equation 2.33 can take two possible values is because at any given depth h , only craters with $h_{excav} > h$ can contribute to mixing.

Using an input of time and a crater size frequency distribution, equation 2.33 allows us to calculate the probability that the regolith at depth h has been mixed at time t . Because equation 2.33 considers a constant impact flux, we can convert the

time scale into actual time scale by using the Neukum chronology function (Neukum et al., 2001). Figure 2.7 shows the mixing depth probability at different time intervals (1 Myr-10 Gyr) under a constant impact flux rate. The 10 Gyr constant impact flux rate is equivalent to a 3.65 Ga age in the Neukum chronology. Our median mixing depth in 3.65 Ga is ~ 4 m, which falls into the range of 210 m for typical regolith depth in mare regions (Oberbeck and Quaide, 1967; Oberbeck and Quaide, 1968; Quaide and Oberbeck, 1968; Quaide and Oberbeck, 1975; Oberbeck et al., 1973; Bart et al., 2011).

We use equation 2.33 to implement a subpixel vertical mixing model into CTEM. Our subpixel crater mixing model runs between each creation of a resolvable crater. For the time interval between a resolvable craters production, one can draw a probability function as shown in Figure 2.7. The short time interval gives a greater probability of a shallow mixing depth; however, there is a chance that a deeper mixing depth could occur. A random depth is drawn from the probability function given by equation 2.33 and then we create a mixed layer of material at each grid cell with this random depth.

2.8 Modeling super-domain craters

We included a model for what we call “super-domain” craters. These are large craters that form outside our simulation domain, but whose ejecta cross the domain. We do not model the formation of the crater cavity of super-domain craters inside our simulated domain. To obtain the numbers and sizes for super-domain craters occurring in our simulated domain, we first applied the same crater production function that is used in our simulated domain. Even though many more craters with all sizes are expected in our super domain due to its larger area, the actual ejecta deposition of a crater depends on the distance between the super-domain crater and our simulated domain. This affected area is defined as the circle area with a radius of length of its ejecta extent, which is ~ 200 radii, subtracted by the total simulated domain area. A

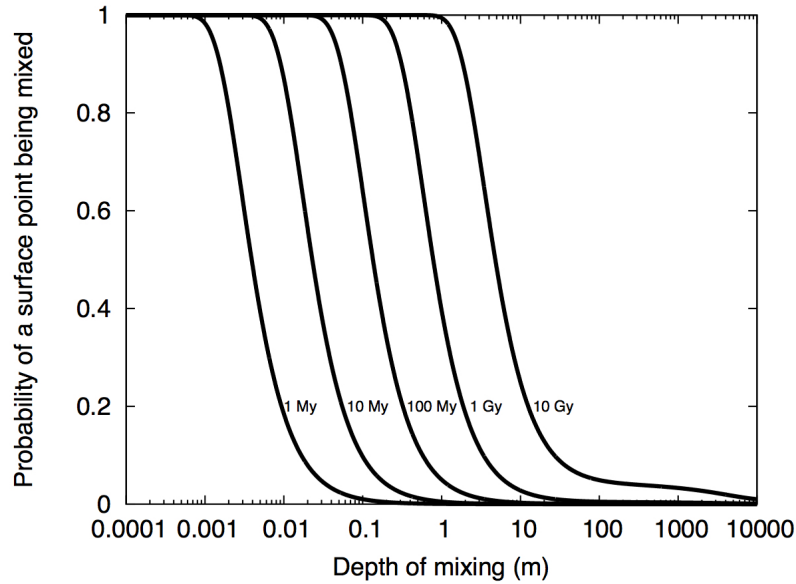


Figure 2.7.: The fraction of surface that mixes to a given depth for a time interval from our vertical mixing model for subpixelsized craters. The x axis is the mixing depth, and the y axis is the fraction of area that is mixed to that depth. Each curve is labeled with its corresponding time, 1 Myr, 10 Myr, 100 Myr, 1 Gyr, and 10 Gyr. For 1 Myr time interval, the probability of a surface that mixes to 1 cm (0.01 m) is <0.2 , yet in that time, the whole surface has already mixed to 1 mm. Note that the 10 Gyr period at this constant impact flux rate is equivalent to a 3.65 Ga age accounting for the exponentially higher impact rate prior to 3 Ga (Neukum et al., 2001).

larger crater has a bigger affected area than smaller craters. When we calculated the numbers of craters from crater production distribution, we kept a crater as long as its affected area is larger than the total area of a simulated domain, but otherwise it is discarded. Then the number of super-domain craters given by the elapsed time between the formations of two resolvable craters and its affected area was obtained.

To estimate ejecta deposition from super-domain craters as well as modeled glass spherules, we must calculate the size of the transient crater of each super-domain

crater. To do so, some assumptions such as impact velocity and impact angle are useful to obtain the amount of modeled glass spherules inside the ejecta. We assume for these craters that they have an impact velocity of ~ 18.3 km/s, which is similar to the root mean square of the velocity distribution of asteroidal impactors on the Moon (Yue et al., 2013). The impact angle is assumed to be 45 degrees. We applied the same impact conditions to each generated super-domain crater. With these prescribed values, we can estimate the location of ejecta inside a melt zone and obtain melt fraction within its stream tube. The fraction of modeled glass spherules inside the ejecta depends on whether its deposition distance reaches the glass onset distance for the production of impact glass spherules. Because we do not model the detailed formation of super-domain craters outside our simulated domain and cannot obtain information of the subsurface, each super-domain crater ejecta only deposits newly-formed glass spherules, and only does so within the segment of the crater ray that crosses the simulated domain.

HERE MEN FROM THE PLANET EARTH
FIRST SET FOOT UPON THE MOON
JULY 1969, A.D.
WE CAME IN PEACE FOR ALL MANKIND
Neil Armstrong

3 HETEROGENEOUS IMPACT TRANSPORT ON THE MOON

Acknowledgement: A version of this chapter has been published in *Journal of Geophysical Research: Planets*. Reference: Huang, Y. H., Minton, D. A., Hirabayashi, M., Elliott, J. R., Richardson, J. E., Fassett, C. I., and Zellner, N. E. (2017). Heterogeneous impact transport on the Moon. *Journal of Geophysical Research: Planets*, 122(6), 1158-1180, DOI:10.1002/2016JE005160

Abstract: Impact cratering is the dominant process for transporting material on the Moon's surface. An impact transports both proximal material (continuous ejecta) locally and distal ejecta (crater rays) to much larger distances. Quantifying the relative importance of locally derived material versus distal material requires understandings of lunar regolith evolution and the mixing of materials across the lunar surface. The Moon has distinctive albedo units of darker mare basalt and brighter highland materials, and the contacts between these units are ideal settings to examine this question. Information on the amount of material transported across these contacts comes from both the sample collection and remote sensing data, though earlier interpretations of these observations are contradictory. The relatively narrow ($\sim 4\text{-}5$ km wide) mixing zone at mare/highland contacts had been interpreted as consistent with most material having been locally derived from underneath mare plains. However, even far from these contacts where the mare is thick, highland material is abundant in some soil samples ($>20\%$), requiring transport of highland material over great distances. Any model of impact transport on the Moon needs to be consistent with both the observed width of mare/highland contacts and the commonality of nonmare material in mare soil samples far from any contact. In this study, using a three-dimensional regolith transport model, we match these constraints and demonstrate that both local and distal material transports are important at the

lunar surface. Furthermore, the nature of the distal material transport mechanism in discrete crater rays can result in substantial heterogeneity of surface materials.

3.1 Introduction

Impactors not only bombard the Moon but also initiate the transport of material across the Moons surface. An impact excavates material from below the surface and emplaces it as a continuous ejecta blanket surrounding the crater and distal ejecta in rays at large distances. The proximal material in the continuous ejecta deposit is transported at low velocities and thus deposited locally. Most of the excavated mass is deposited locally. On the other hand, material originating in a region closer to the impact point can be thrown to much larger distances, forming secondary crater fields and crater rays (Shoemaker, 1965). This distal ejecta is widely dispersed, relatively low in mass, and mixes more with preexisting material upon deposition (Oberbeck, 1975). The first Apollo mare soil samples returned to Earth consisted of material of a variety of compositions, including both local mare basalts and more distantly sourced highland anorthosites (Wood, 1970; Wood et al., 1970c; Wood et al., 1970a). The anorthositic material in mare soil samples could either been derived from the underlying highland layer beneath mare surface or may have originated far from the sampling site (Arvidson et al., 1975; Rhodes, 1977; Hörz, 1978; McKay et al., 1978; Labotka et al., 1980; Laul and Papike, 1980; Simon et al., 1981; Simon et al., 1990; Farrand, 1988; Fischer and Pieters, 1995). The hypothesis that the source of anorthositic material in a mare soil came from beneath the mare deposit was favored until it came to be understood that the majority of mare plains are thick: up to kilometers at their center, decreasing to approximately hundred meters at the edges of the plains (De Hon, 1974; Hörz, 1978; Head, 1982; Budney and Lucey, 1998; Evans et al., 2016). Only the largest postmare craters can excavate underlying highland materials, and the presence of a substantial anorthositic component in a mare soil samples must therefore originate from far away. Material transport by impacts is an

important process across all size scales. Small impacts constantly mix the uppermost layers of the lunar soil. Mixing of local materials leads to a well-mixed layer called the reworking zone (Gault et al., 1974; Morris, 1978; McKay et al., 1991). For example, the Apollo 15 deep drilling core has been interpreted as having ~ 242 well-mixed layers with thicknesses between a few millimeters and ~ 13 cm (Taylor, 1982). Additionally, the transport of material by impacts is apparent in the Apollo 14 impact glasses (Zellner et al., 2002). For example, impact glasses with feldspathic compositions are abundant even though the typical Apollo 14 regolith is mostly potassium, rare earth element, and phosphorus (KREEPy). It remains unclear, however, how much proximal ejecta versus distal ejecta contributes to the makeup of lunar regolith.

One way to evaluate the relative importance of proximal ejecta and distal ejecta is to examine how the basalt/anorthosite material mixing ratio changes as a function of distance from a mare/highland boundary (Schonfeld and Meyer, 1972; Rhodes et al., 1974; Rhodes, 1977; Li et al., 1997; Li and Mustard, 2000). The material mixing process across mare/highland contacts is driven by impacts, and the area where this mixing occurs is called the mixing zone. Immediately following the eruption and emplacement of the mare basalts, this mixing zone was a very narrow and sharp contact existed between the mare and highland plains. If local material transport dominates, then an insignificant amount of material would be transported across the contact, so the expectation is that boundaries would remain relatively sharp. On the other hand, if distal ejecta dominates, one would expect a wider mixing zone. The Apollo and Luna sample sites were located at a wide range of distances from mare/highlands boundaries, allowing us to see how the basalt/anorthosite mixing ratio varies with distance.

The mare soil samples of Apollo 15/17, Apollo 12, Apollo 11, and Luna 16 were taken at less than 0-4 km, ~ 20 km, ~ 50 km, and ~ 110 km from their nearest mare/highland boundary, respectively. When we examine the basaltic/anorthositic mixing ratio with each sampling distance, it appears that the samples collected further away from the nearest contacts are not as strongly correlated to sampling distance

as the samples collected at a much closer distance. The amount of nonmare material in Apollo 11, Apollo 12, and Luna 16 mare soil samples, which extend up to 100 km from the nearest highland contact, is about 20% on average, with the exception of a few Apollo 12 samples, which are ~ 20 km from the highlands and reach nonmare fractions of up to 70% (Figure 3.1) (Wood, 1970; Goles et al., 1971; Hubbard et al., 1971; Schnetzler and Philpotts, 1971; Schonfeld and Meyer, 1972; Wanke et al., 1972). The elevated abundance of nonmare material found in most mare soil samples at these large distances would suggest their origin as distal ejecta.

In contrast, the Apollo 15 and 17 missions were near the edge of the maria and close to the contact with highlands. The astronauts collected samples at varying distances but all within 4 km of the contact (NASA Technical Report Server, 1972; NASA Technical Report Server, 1973). The amount of highland material in mare soils sampled by both missions decreased rapidly with distance from the contact (Figure 1). The narrow mixing zones observed in these near-contact sampling sites are suggestive of a different trend in exotic material abundance as a function of distance compared to the more distant Apollo 11 and 12 and Luna 16 samples. The observations of an active reworking zone and narrow mixing zones seen at the Apollo 15 and 17 sites imply that a proximal ejecta-dominated local mixing process is most important, while the amount of nonmare material in the more distant mare soils implies distal ejecta-dominated mixing (Shoemaker, 1970; Wasson and Baedeker, 1972; Oberbeck et al., 1973; Gault et al., 1974; Rhodes, 1977; Hörz, 1978). This discrepancy has remained unresolved.

The impact transport process can be further constrained using remote sensing observations. The Clementine UV/VIS (ultraviolet/visible) camera obtained 120-170 m/pixel resolution multispectral reflectance data for the Moon (Nozette et al., 1994). Because of the albedo contrast between darker basaltic mare and brighter anorthositic highlands, Li and Mustard used this Clementine reflectance data to quantitatively estimate how much material has been transported across mare/highland contacts for four basins (Li and Mustard, 2000). The UV/VIS imaging data revealed a sharp

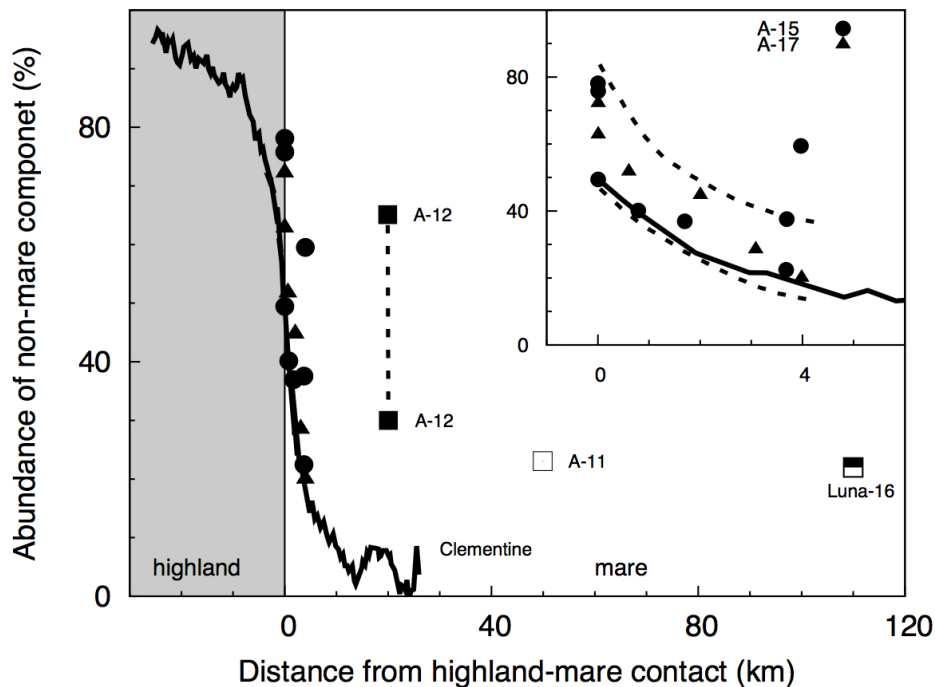


Figure 3.1.: Abundance of nonmare material as a function of sampling distance from the highland and mare contact as measured by Clementine, Apollo, and Luna missions. This plot is modified from (Rhodes, 1977, Figure 1), with the addition of Clementine UV/VIS camera data for Grimaldi Crater (solid line) that is directly taken from (Li and Mustard, 2000, Figure 6). The vertical line at zero distance in the x axis is the geological contact between anorthositic highlands on the left-hand side (shadowed in gray color) and mare on the right-hand side. The Apollo 11, 12, 15, and 17 and Luna 16 data are hand samples assembled by (Rhodes, 1977). Apollo 15 and 16 samples are compared with Clementine data for all four contacts in greater detail in the inset.

decrease in the abundance of foreign material, dropping from $\sim 50\%$ at the contact to 10-30% at 4-5 km from the contact (see inset of Figure 1). This analysis is consistent with the in situ sampling results of the Apollo 15 and 17 missions, both of which are highly correlated with sampling distance from the contact. Thus, the narrow

mixing zones seen in both the Apollo 15 and 17 sampling and Clementine data seem to support the hypothesis that local material dominates at the lunar surface.

If locally derived materials dominate on the lunar surface, and distal ejecta is insignificant, then the mixing process across mare/highland contacts can be modeled by only considering deposition of the proximal continuous ejecta. Li modeled the material exchange between mare and highland plains as a classical diffusion process (Li et al., 1997), which describes the movement of a particle as random walk, with each step of motion spanning a finite distance. The finite step that a crater generates is limited to the extent of the continuous ejecta blanket. However, the classical diffusion model results in an even narrower mixing zone (<1 km) than is observed, which conflicts with both the Clementine and Apollo 15 and 17 results. Thus, Li concluded that local material transport could not be the dominant mixing process at mare/highland contacts (Li et al., 1997). Therefore, some amount of distal ejecta must play an important role in transporting material across mare/highland contacts.

Instead of the classical diffusion model, Li and Mustard used an anomalous diffusion model in which the movement step is not limited to the extent of the continuous ejecta blanket but can be larger or even infinite (Li and Mustard, 2000). The anomalous model is more realistic because large craters deposit material far from their source region. Their anomalous diffusion model successfully reproduced the 45 km wide mixing zone seen in the Clementine data. They suggested that distal ejecta is what determines the width of this narrow mixing zone. With some simplifying assumptions, such as that the ejecta was radially homogeneous and followed a simple power law thickness profile that extended to infinite distance, Li and Mustard were able to reveal the relative importance of proximal (local) ejecta and distal ejecta on the Moon. Yet this result is still at odds with the observed elevated abundances of exotic material seen in the Apollo 11 and 12 and Luna 16 samples that are much farther away from the source of highland material.

Here we propose a new model that accounts for the spatially heterogeneous nature of distal ejecta. The ejecta are only continuous to ~ 2 -3 radii distance, and beyond

that, they break into discontinuous rays (Howard, 1974). By accounting for this nature of the ejecta, we investigate both the 45 km wide mixing zone across contacts and the elevated nonmare abundances at further distances. We model the impact-driven material transport and mixing processes across mare/highland contacts with a fully three-dimensional regolith tracking code. Our code includes treatments of the reworking zone of locally derived material, as well as both continuous proximal and discontinuous distal ejecta (crater rays, see Chapter 2). In section 3.2 we discuss the observational constraints on transport of material by impacts in detail.

In section 3.3 we apply our new code to the problem of material transport across the mare and highland boundary of Grimaldi Crater. In section 3.4 we discuss how discontinuous distal ejecta may explain the discrepancy between the wide mixing zone implied by the Apollo 11 and 12 and Luna 16 samples and the narrower mixing zone implied by the Apollo 15 and 17 samples and Clementine remote sensing observations. Finally, in section 3.5 we use our simulation results to discuss the implications of the heterogeneous nature of distal ejecta.

3.2 Two Sets of Contradictory Observational Constraints on Material Transport

In our study, we wish to understand what processes are responsible for transporting and mixing material at the lunar surface. We will use two data sets that will constrain the material fraction as a function of distance from a highland/mare contact. These data sets are distinguished by their sampling distance from the nearest mare/highland contact. The first data set includes Apollo 12 and 11 and Luna 16 soil samples, which are sampled at large distances from the contact: 20, 50, 110 km, respectively. Wood (1970) classified 1676 lithic fragments in the 1-5 mm size range from 11.1 g of the Apollo 11 coarse fines (sample (10085,24) with sizes >1 mm) (Wood, 1970). The visible anorthositic fragment (5%) and some anorthositic component embedded in basalt breccia amount to 20% in their Apollo 11 soil sample.

The chemical mixing model of Schonfeld and Meyer also showed the Luna 16 soil has 20% anorthositic gabbro and 2% KREEP as representative of nonmare components (Schonfeld and Meyer, 1972). Intensive compositional analysis on Apollo 12 soil samples presents a mixture of up to 30-70% KREEP material and basalt (Goles et al., 1971; Hubbard et al., 1971; Schnetzler and Philpotts, 1971; Wanke et al., 1972). These mare soil samples show >20% anorthositic material, with some Apollo 12 samples reaching up to 70% (Figure 3.1). Later, the Apollo 15 and 16 orbital X-ray experiments created compositional maps of several mare surfaces (e.g., Mare Imbrium and Mare Serenitatis). The compositional maps closely match the soil samples, with elevated levels of aluminous or anorthositic material (Trombka et al., 1974). The more anorthositic mare surfaces indicate that distal materials from the highlands contaminate the mare surfaces.

The second data set consists of Apollo 15 and 17 mare soil samples and Clementine remote sensing data sets that sampled the spectral reflectances of Mares Grimaldi, Tsiolkovsky, Orientale, and Fecunditatis from mare/highland contacts at a short distance (4-5 km). Rhodes assembled component estimates of those in situ Apollo 15 and 17 mare soil sample collected from mare plains (Rhodes, 1977; Rhodes et al., 1974; Schonfeld and Meyer, 1972; Duncan et al., 1975). The inset of Figure 1 shows the strong correlation between nonmare abundance and distance. Although the abundances of the anorthositic component in the Apollo 15 and 17 mare soil samples appear to vary by location, they still show a decrease from 50-80% at the mare/highland contact to 20-40% at the edge of the mixing zone. Despite the compositional variability seen in the Apollo 15 and 17 samples, Clementine UV/VIS data sets for all four basins fall within the range of the samples, except for Mare Tsiolkovsky, whose mixing zone is narrower than that of each of the other three basins. Both Clementine UV/VIS data sets and Apollo 15/17 mare soil samples are consistent with each other, although the Apollo 15 and 17 mare soil samples were taken only on the mare side and only within 4 km of the mare/highland contact. The Clementine data sets cover a much larger distance and contain observations from both the mare and highland side of the

boundaries. The Clementine data suggest $<10\%$ exotic material at a distance of 20 km from the boundary, while the Apollo 11 and 12 and Luna 16 mare soil samples are composed of $>20\%$ nonmare component at further distances.

As crater rays commonly cross mare surfaces, they may deliver anorthositic material from highland regions. For example, the ray material from Theophilus Crater (100 km in diameter), which is ~ 8 crater radii away from the Apollo 11 landing site, may be a significant contributor to the highland component of the Apollo 11 samples (Pieters et al., 1985; Hawke et al., 1999). Similarly, the ejecta from Copernicus Crater (96 km in diameter), which is $\sim 8-9$ radii from the Apollo 12 and 14 landing sites, could contribute a large portion of the material in the samples collected at those sites (Pieters et al., 1985). The Copernicus ejecta are potentially sourced from the highland-like layers beneath the mare plain. As a result, the Apollo 12 landing site, which is crossed by a ray of Copernicus Crater, could have higher abundances of anorthositic materials than other nearby mare plains. In addition, rays from either Autolycus or Aristarchus Crater are seen crossing the Apollo 15 landing site area (Carr et al., 1971).

We propose a hypothesis that could account for the discrepancy between the inferred widths of the mixing zones seen in the different data sets. We suggest that because distal impact ejecta are concentrated into thin rays, there is large spatial variability, on small spatial scales, in the abundance of nonlocal material. Therefore, samples from the surface should show greater variability in nonlocal abundance compared to remote sensing observations, which average out the spatial heterogeneities. For example, the Apollo 15 lunar module site was in the secondary field (South Cluster) of rays of either Autolycus or Aristarchus Crater (Swann et al., 1972). Li suggest that distal ejecta from distances of >100 km away could explain an elevated amount of nonlocal material in a sampling location (Li and Mustard, 2005), though, again, they did not consider the heterogeneous nature of this distal ejecta.

The above demonstrates a need for a material-transport model that takes into account the spatial heterogeneity due to crater ray emplacement. In Chapter 2,

we have presented our three-dimensional regolith transport model including the main three components. The first component is an efficient approximation to the excavation flow within a transient crater that is based on the Maxwell Z model (Maxwell and Seifert, 1974; Maxwell, 1977). This component of our model allows us to model the mixture of material that is incorporated into ejecta during the excavation process. The second component is an empirically derived geometric model for crater rays. This component allows us to model the spatial heterogeneity of distal ejecta deposits. The last component is a mixing component that allows us to model the local zone reworked by those craters that are smaller than our code can directly resolve.

3.3 Mare/Highland Boundary Diffusion Simulation

For our simulations of the mare and highland contact, the CTEM grid space is split in half, where one half contains a layer of mare basalt 4 km thick on top of a highland anorthosite layer and another half is purely highlands anorthosite (Figure 3.3). Figure 3.3 illustrates a schematic of the cross section of our modeled mare and highland contact both near the beginning of the simulation and later as the simulation has progressed and impacts have redistributed material around the domain. To model the transportation process, the ejecta from each impact must be traced back to its source location within the transient crater in order to calculate its unique compositional mixture (see full description of methodology in the section 2.1).

Our goal is to model material transport by impacts at a mare/highland contact. We use the Clementine UV/VIS reflectance data set compiled by Li and Mustard for Grimaldi Crater as a constraint on our model, which shows a symmetric material fraction distribution on either side of the contact (Li and Mustard, 2000). We will also use the measured abundances of nonmare material within Apollo mare soil samples as additional constraints. These data are plotted in Figure 3.1. Then we will test the hypothesis of Li and Mustard that the 4-5 km width of the mixing zone across this contact is determined primarily by the transport of distal ejecta.

Grimaldi Crater is a 173 km diameter mare-filled crater and one of the four basins studied by Li and Mustard. Grimaldi Crater is located on the western shore of Oceanus Procellarum; thus, the lava that filled it is thought to have the same source as Oceanus Procellarum, which is the largest mare area on the Moon. The crater itself is a double-ring impact structure that is pre-Nectarian in age (Wilhelms, 1987). Later Orientale basin-forming material, the Hevelius Formation, may have covered much of the Grimaldi region (Hawke et al., 1995). When the mare basaltic lava was initially emplaced, it formed a sharp boundary with the older anorthositic highland bedrock. The mare abundance at the center of the geological contact between Grimaldi’s mare and the surrounding highlands is about 50% (Li and Mustard, 2000), which suggests that the influence of large craters outside Grimaldi is not significant to the makeup of the regolith near the mare/highland contact.

Inside Grimaldi Crater, there is an up to 3.6 km thick mare basalt layer at the center of the crater, sitting atop of possible Orientale basin-forming ejecta and pre-Nectarian highland crustal material (Solomon and Head, 1980). The largest crater found in the Mare Grimaldi is about 4 km in diameter (Figure 3.2), suggesting that locations where the mare basalt thickness is thinner than ~ 400 m could have exposed the underlying highland material. However, we neglect this contamination of highland material because there are few large craters, and the contamination of highland material from the mare side to the highland side by these large craters would be insignificant. In addition, because the observed material fraction distribution is symmetrical across the contact, this local mixing of highlands from beneath the mare must be negligible; otherwise, the highland material fraction would be skewed toward the mare side.

3.3.1 Mare/Highlands Contact Simulation Setup

For our simulation domain, we took the area of Grimaldi Crater ($D = 175$ km) as the total area of our simulated mare. We also assume that the size of our simu-

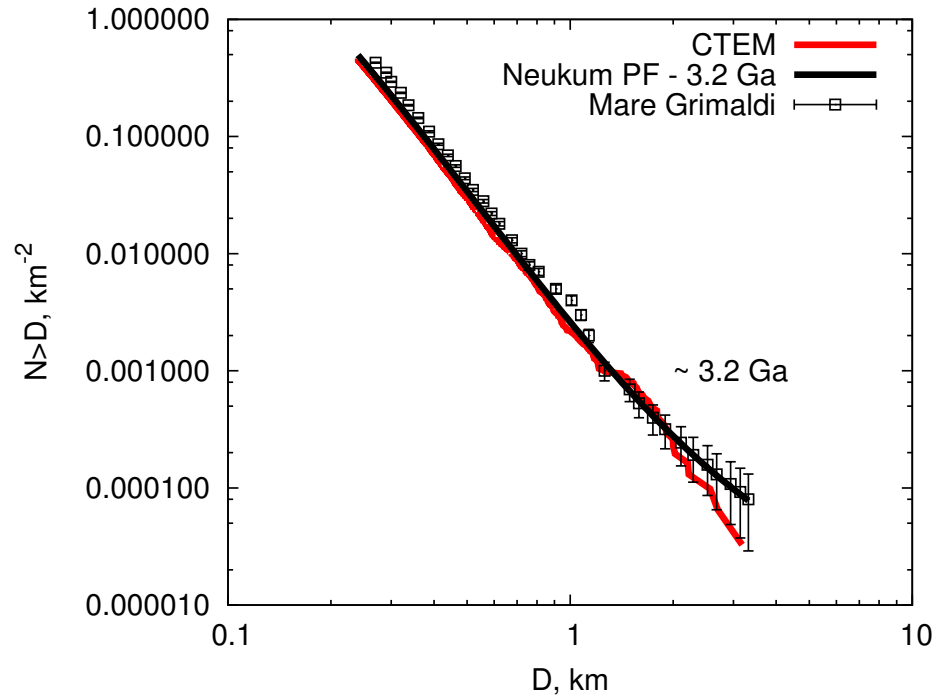


Figure 3.2.: Crater size frequency distributions for the western Mare Grimaldi region. The solid black line shows the Neukum Production Function (NPF) age of 3.2 Gyr, and the red line shows the crater counts produced in our simulation with CTEM. The open square points with one sigma Poisson error bar (\sqrt{N}) are based on crater counts from Greeley1993.

lated highland is equal to the size of our simulated mare. Therefore, there are equal opportunities for cratering on both sides of the contact. Our simulated square grid dimensions are thus 175 km by 175 km, and our pixel resolution is equal to that of Clementine data at 120 m/pixel (Li and Mustard, 2000, Table 2). This gives us a 1460 pixel by 1460 pixel simulation domain, with a repeating boundary condition. The smallest crater we directly model is 1 pixel in diameter. For craters smaller than 120 m, we must use our subpixel crater mixing model, as described in section 2.5.

Our initially defined surface has a mare side on the left and a highland side on the right (see Figure 3.3). The mare side has one mare basalt layer that is 4 km thick, to

match the observed thickness of the Grimaldi Crater mare (Solomon and Head, 1980), sitting on the top of the highland layer that has effectively infinite thickness. The highland side is one single layer that has infinite thickness of only highland material. We model the thickness of the mare layer as uniform and neglect the underlying shape of Grimaldi basin near the rim (gradual decrease of mare thickness toward the contact). If this thinning out of the mare near the boundary were important, we might expect an asymmetric material fraction distribution, with proportionally more highland material on the mare side. However, this is not observed in the data, and therefore, we assume that this component is future lunar missions. We also ignore topography differences between the mare and highland. Although the steeper slopes of the highlands along the contact would tend to transport material downward to the mare side, the material was only found to extend to several hundred meters for high slopes (Young, 1976), and again, one would expect the material distribution to be asymmetric at the boundary if this effect were important. This suggests that the slope effect of the highlands plays a less important role in transporting to the mare side, as the observed mixing zone has a scale of a few kilometers.

Our simulation time is set by the crater-derived age of the southwestern part of the mare deposit examined by Li and Mustard, which is 3.2 Gyr old based on crater counts (Greeley et al., 1993). This region has no evidence for discrete resurfacing events occurring after the mare basalt emplacement. We use an impactor population and velocity distribution that result in a crater production function that is identical to the Neukum Production Function (Neukum et al., 2001). Figure 3.2 shows the crater size frequency distribution from CTEM compared with both the crater counting study of Greeley and the Neukum production function for a 3.2 Gyr old lunar surface. Note that the largest crater that we allow in a simulation is constrained by the Grimaldi Crater count so as to attempt to mimic Grimaldi Crater's western mare/highland contact. Because the compositional profile that Li and Mustard obtained from the western mare/highland contact of Grimaldi Crater does not include a crater larger than 4 km near the contact, we restricted our simulation to craters between 120 m

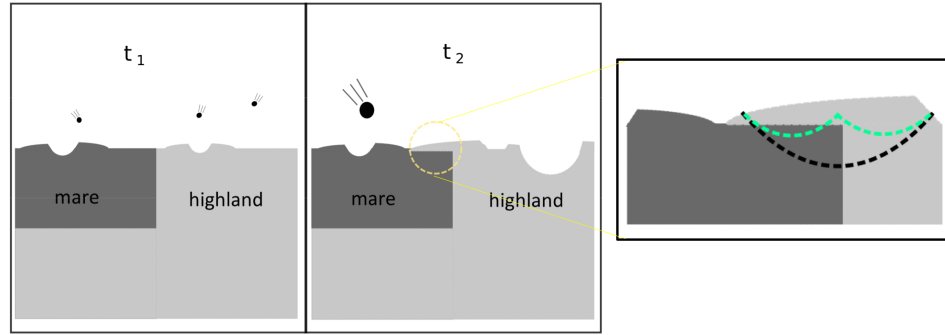


Figure 3.3.: A schematic of cross section of modeled mare and highland contact in CTEM. The mare side with a finite thickness is marked as dark gray color, and the highland side is light gray color. The left-hand side figure shows the beginning of an impact cratering process across the contact (t_1), and the middle represents a scenario of large crater showing up at $t_2 > t_1$. Note that a large crater on the highland side is able to deliver highland material to mare side (dashed circle in yellow color). The closeup of this region where highland material deposits on the top of the mare side is shown in the left-hand side figure.

(the grid cell resolution) and 4 km in diameter. Our subpixel mixing model considers the contribution from craters as small as 1 mm in diameter.

Our model includes multiple material transport mechanisms, as described in detail in Method chapter (Chapter 2). These mechanisms include transport by distal ejecta (crater rays), transport by proximal ejecta of resolvable craters (continuous ejecta blankets), and mixing by subpixel craters (craters smaller than a grid cell). We performed four sets of simulations to test the hypothesis of Li and Mustard that distal ejecta control the width of the mixing zone across contacts like Grimaldi basin. These simulations are distinguished from each other by which components of our transport model are active (see Figure 3.4). These simulations are proximal ejecta only with no subpixel crater mixing (Case A), proximal ejecta only with subpixel crater mixing (Case B), proximal and distal ejecta with no subpixel crater mixing (Case C), and

proximal and distal ejecta with subpixel crater mixing (Case D). These different cases allow us to see the relative importance of each component of our model.

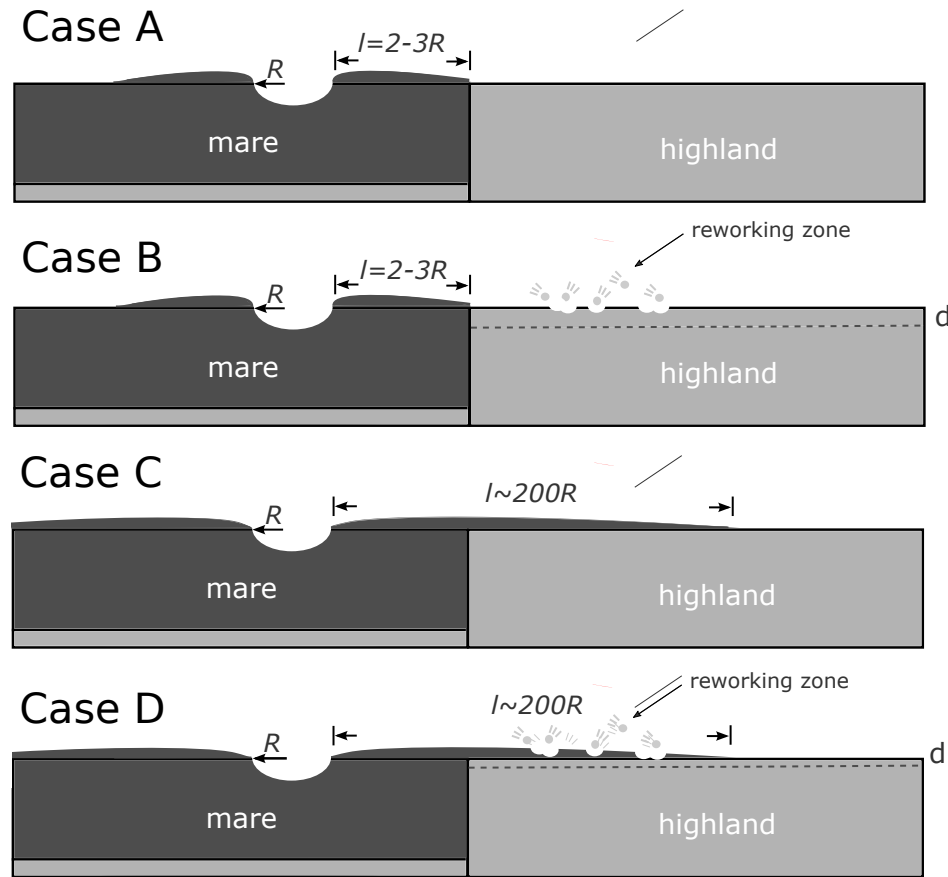


Figure 3.4.: A schematic of our model cases. Case A (top figure) includes only proximal ejecta. Case B (middle-top figure) includes proximal ejecta and sub-pixel mixing process. Case C (middle-bottom figure) and Case D (bottom figure) includes proximal ejecta and distal ejecta but difference between these two cases are sub-pixel mixing process turned on in Case D. Note that l is the ejecta extent, R is the crater radius, and d is the depth of sub-pixel mixing over a period of time.

The simulation set, Case D, combines all components of our transport model and is closest to what the lunar surface experiences, while Case A is the most restricted and simulates only regolith transport due to resolvable craters. The Case D simulation is

also closest to what Li and Mustard assumed for their anomalous diffusion model and includes all components. Their distal ejecta dominated anomalous diffusion model allows them to consider craters down to microns in size, which is the scale of our subpixel crater mixing model. More importantly, with a better treatment of the spatial distribution of distal ejecta, our results enable us to investigate discrepancy between the two different observations: the narrow (4-5 km) and wide (>20 km) mixing zones seen in the data (Figure 3.1). All simulation results will be compared with Clementine UV/VIS camera reflectance data and Apollo mare soil samples.

3.3.2 Results of Our Mare/Highland Contact Simulations

The initial mare and highland contact is sharp, with the pure mare on the left-hand side and the pure highland on the right-hand side. For each case described in Figure 3.4, we performed one run with the same random seed in CTEM. In all of our simulation cases the mare/highland boundary becomes more diffuse with time, but the amount of transported material across the contact depends on which components of our transport model are active.

In Figure 3.5, fraction images from each case show how the contact is changed by adding a component in the model. For example, the mixing zone in the proximal ejecta-only models (Cases A and B) is always limited to <1 km wide. Figure 3.5a shows that the mare/highland contact remains sharp, and exotic material is barely transported across the boundary (Case A). Only a crater that is close to the edge of the mare/highland contact would deposit its continuous ejecta across the contact. Assuming that a 1 km diameter crater occurs at the contact, it would create ~ 2 km of continuous ejecta across the contact. The probability of a few km diameter crater occurring at the contact is relatively small, and it appears that such a crater has not occurred to our study area (mare/highland contact of southwestern Grimaldi Crater) at least from the observation of Clementine data. In fact, the contribution of a few km diameter crater at the contact to the exotic component would be smoothed out by

averaging methods that are used in processing Clementine data and our simulation results. As a result, the material transport of proximal ejecta in Cases A and B appears limited.

Figure 3.5b shows a mixing zone that is ~ 10 km wide for Case C. The sharp boundary seen in Cases A and B is now crossed by rays. The contrast is high between rays and background surface material (mare or highland side). The fresh appearance of rays at the contact would be similar to how a ray may appear as soon as it forms and before small crater gardening mixes and dilutes the exotic material. Because small crater gardening is not modeled in Case C, any exotic material in a ray stays at the surface until a subsequent excavation or deposition occurs. Figure 3.5c shows the fuzzy appearance of the boundary in our Case D simulation, in which subpixel mixing is turned on. When we turn on subpixel mixing in Case D, the transported exotic material gets reworked into the local regolith and the surface albedo looks much closer to the natural surface at the Grimaldi crater contact.

To quantitatively compare our simulation results with Clementine data, we obtained a compositional gradient profile similar to that which Li and Mustard used to analyze all four basin measurements taken by the Clementine UV/VIS camera. The compositional gradient profile describes the mare abundance at a specific distance from the mare/highland contacts, and one can plot how the mare abundance changes with distance from the contacts. For each compositional gradient profile, Li and Mustard extracted reflectance values averaged over 20 pixels, each at a specific distance from a mare/highland contact, to mitigate the effects of noise of Clementine UV/VIS reflectance measurements, variability in apparent reflectance due to surface roughness, and other pixel-scale sources of stochastic variability. They created only two compositional gradient profiles for each of the four basins. In each of our simulations, we ran through all pixels parallel to the contact and collected 1441 profiles in which each profile is averaged over 20 pixels to enable direct comparison with the measurements of Li and Mustard. We can calculate the mean mare abundance at a specific distance from those 1441 profiles as well as the standard deviation of mare

abundance. Figure 3.6 shows the average mare abundance and one standard deviation among all 1441 profiles for each case.

The results of the Cases A and B simulations, which include only continuous ejecta, lead to a mixing zone less than 1 km in width, closely consistent with the classical diffusion model result of Li (Figure 3.6a) (Li et al., 1997). In Figures 3.6b and 3.6c, the Cases C and D simulations, which include both continuous and distal ejecta, have mixing zones wider than 1 km. The Case C result (Figure 3.6b) contains the largest width of mixing zone, up to 10 km on a side. This is much wider than the Clementine UV/VIS measurement for Grimaldi Crater's contact. Case C also has the largest variation of mare abundance across the contact, indicating that the compositional gradient profile is highly affected by distal ejecta in rays. As a result, the dependence of mare abundance on the sampling distance is the smallest. As we added the subpixel crater mixing component and, eventually, the ray mixing component into Case C, the result of Case C shows a larger variability of composition across the contact than in Case D. With consideration of subpixel craters mixing, the mean mare abundances across the contact show a match with Clementine data. The addition of subpixel crater mixing component in Case D is important because both rework the resolvable crater ejecta deposits that are only generated in Case C. Among resolvable crater ejecta deposits, their crater rays often transport exotic material across mare/highland contacts; thus, their deposits are relatively less mixed.

Because the scale of excavation depth for a resolvable crater that generates crater rays is usually larger than the thickness of preexisting ejecta layers created by previous impacts, it deposits mostly pure exotic material to the other side. When subpixel crater mixing and ballistic sedimentation are neglected (Case C), both proximal and distal ejecta stay on the surface. For the same deposit, but with the subpixel craters mixing model enabled (Cases D), the subsequent small impacts or energetic ejecta penetrate through this ejecta deposit layer and mix it with the underlying local (nonexotic) material. In this case, the exotic component becomes mixed with local material, leading to a lower exotic abundance compared to the exotic abundance in

Case C. Thus, as expected, Case C results in a higher exotic component at the surface on either side of the contact (Figure 3.6b). The role of both the subpixel crater mixing model is to process (and dilute) distal material. A significant reduction of the exotic component on both sides of the contact in Case D result can be explained by this diluting process. Both results suggest that all scales of craters are important to determine what material is at the surface across the Moon, as well as the ultimate fate of material transported across contacts.

The variability of mare abundance in results from Case D is smaller than in Case C because subpixel crater mixing may bury fresh distal material. For example, the range of one standard deviation in the Case C simulation result completely encompasses the variability of mare abundance revealed in both Apollo 15 and 17 mare soil samples (see Figure 3.6b). Yet the average mare abundance from Case C is highly inconsistent with the observed compositional profile of Clementine data. On the other hand, the Apollo 15/17 sample data are within the error bars of the Case D results, except for one data point at the distance of 4 km, only 40%, compared to the average mare abundance of 60-80% of the other soil samples. The Case D simulation results show a slightly higher exotic abundance on both sides than the Clementine data.

In general, the majority of spatial variation of composition within this 4-5 km wide mixing zone can be accounted for by local craters near the mare and highland contact. Beyond the local scale, the stochastic nature of cratering process sometimes means that large specific craters act as a source for exogenic material that is transported more broadly and may be present in many mare soil samples. For example, there are two Apollo 15 mare soil samples (15101 and 15923) collected at stations 2 and 6 closer to the contact (Apennine Front) with low mare abundances (<30%). Their relatively high nonmare abundances could be associated with a ray from nearby craters Aristillus or Autolycus, which were large enough to excavate below the mare (Carr et al., 1971; LSPET, 1972; Spudis and Ryder, 1985). Russ used low-energy fluence data from the Apollo 15 drill core (the lunar module site) to show that there was no indication of the ray deposition, which contradicts the explanation of ray

material in a sample (Russ et al., 1972). The distances from Autolycus or Aristillus Crater to the Apollo 15 landing site are 150 km and 250 km respectively, which are greater than the length of our simulation domain. Craters of similar diameter, ~ 39 km for Autolycus Crater and ~ 55 km for Aristarchus Crater, were not generated in our simulation. Large craters may have randomly thrown a broad ray patch containing considerable amounts of nonmare material or KREEP material to the landing site (see section 3.4). As a result, the higher nonmare abundance observed in the mare soil sample collected at the Apollo 15 lunar module site might have been affected by a ray from a large crater beyond the local scale of the mare and highland contact.

3.4 Implications of Our Impact Transport Model for Evolution of Lunar Surface Materials

Based on comparisons of our Case C and Case D results, we suggest that larger craters are capable of delivering exotic material to a distal location, while small and local craters serve to bury those exotic and distal ejecta materials (due to reworking and mixing). Without large craters, exotic material from one side of the mare/highland contact cannot reach the other side. Once those distal ejecta materials arrive at the other side, they are buried or comminuted or recycled by local small craters. The combination of these two transport processes leads to this 4-5 km wide mixing zone. Our new three-dimensional regolith transport model provides more detail about how impacts transport material over the lunar surface.

For all of our simulation results, mean mare abundance profiles at an equivalent distance of the Apollo 11 and 12 landing sites (Luna 16 is beyond our simulated mare domain) remain $>90\%$; therefore, the nonmare abundance is less than 10%. All our final results (Figure 3.6) appear to fail to explain the elevated nonmare abundances present in Apollo 11 and 12 and Luna 16 mare soil samples. The $<10\%$ of nonmare abundance in our simulation is about half that of Apollo 11 and 12 and Luna 16

mare soils (>20-70%), even though we take into account the variation of nonmare abundance in Case C (the largest variation of all cases).

Our results suggest that the primary difference between the Clementine data for the contact of Grimaldi Crater and Apollo 11 and 12 and Luna 16 mare soil samples is sampling scale. The remote sensing data, and our simulation results, are averaged over a spatially extended region of ~ 120 m, while the scale of Apollo 11 and 12 and Luna 16 mare soil samples is limited to a handful amount of soils (centimeter, finer scale compared to the order of 100 m) at “astronaut” scales (\sim m). This scale discrepancy between data sets at these different spatial scales may be a direct result of the high spatial heterogeneity inherent in distal transport of ejecta because it is concentrated into rays. The averaging methods that were used in our simulations and the processed Clementine data might have smoothed out spatially dependent anomalies of nonmare abundance that result from crater rays caused by the random nature of the cratering process.

Li suggested that large craters >100 km away from contacts may explain the elevated nonmare abundance of >20% in most mare soil samples (Li and Mustard, 2005). To test this large crater hypothesis, we performed a global run to account for the effect of larger craters at large distances from the mare/highland contact. Ideally, it would be best to test how large craters distribute their distal ejecta on a spherical globe, yet at present, CTEM cannot account for lunar curvature. In this study, we simulated the global lunar surface as 6000 km by 6000 km square, which is 2000 pixels by 2000 pixels at a resolution of 3 km/pixel. Our global square is 17% mare plains and 83% highlands (Head and Wilson, 1992). We assume that the contamination of the underlying highland material beneath our global mare layer to a mare soil sample can be neglected. This assumption allows us to see the contribution of distal ejecta from larger craters to mare soil samples without worrying about locally excavated contamination.

We set the thickness of mare in our global domain as 4 km and the underlying highland material that is effectively infinitely deep. On the highland side, there is

a single layer of highland material. In our global run, we produced about eight large craters (100-200 km) in total, and the larger craters (>160 km) occur at our global highland side. Figure 3.7 shows broad and long rays from $D > 160$ km craters crossing the global mare/highland contact. On the other hand, there were a few craters on the order of ~ 100 km that formed on the mare side of our global run (close to mare/highland contact at the bottom). For example, a crater from the mare side that is close to the mare/highland contact at the bottom in Figure 3.7 excavates to the underlying highland material, leaving a bright crater floor on the mare side.

Figure 3.8 shows the highland component transported to the mare in our global run. We use the box and whisker plot to present the distribution of highland component at a given distance. With a resolution of 3 km in our global domain, each box represents the total distribution of 2000 pixels at a given distance from the contact. The upper and lower boundaries of the box represent the 25% of total pixels above the median and the 25% of total pixels below the median, respectively. The error bars bound 99% of total pixels. Outliers are shown outside the error bars. As shown in Figure 10, the typical highland abundances from the Apollo 11 and 12 and Luna 16 mare soil samples fall within the majority of the population at a given sampling distance. In detail, the median nonmare abundances from our simulation result are slightly higher than the nonmare abundance of the Apollo 11 and 12 and Luna 16 mare soil samples. For example, Figure 3.8 shows $\sim 30\%$ of median nonmare abundance at our simulated Apollo 12 landing site and $\sim 26\%$ for our simulated Luna 16 landing site.

Figure 3.9 shows the relative frequency of nonmare abundance for both the nonray region and the extremely localized ray in proximity to the Apollo 12 landing site. We show an example of 8 pixel wide ray at this distance (see the yellow rectangular on the left-hand side of Figure 3.7). We highlighted ray and nonray regions to see both distributions of highland material abundance (see the white square boxes on the right-hand side of Figure 3.7). The highland abundances in ray and nonray regions exhibit a bimodal distribution (Figure 3.9). In nonray region (top white box in the inset of

Figure 3.7), about 70% of all pixels (36 pixels) span 20-40% highland abundance and 14% of pixels have 10-20% highland abundance. In contrast, the ray region (bottom white box in the inset of Figure 3.7), consisting of 36 pixels, has >80% of pixels with the range of 50 and 70% of highland abundance. This simulated Apollo 12 landing site is similar to the Apollo 12 landing site because the Apollo 12 landing site is seen superposed by a Copernicus ray (LSPET, 1970).

Thus, the easiest explanation is that the exceptionally high nonmare abundance at Apollo 12 is a result of spatial heterogeneity caused by a ray from Copernicus Crater. Hubbard and Meyer also proposed that the KREEP material seen in these samples arrived by means of distal ejecta/rays from Copernicus Crater and the Fra Mauro region (Hubbard et al., 1971; Meyer and Hubbard, 1970; Meyer et al., 1971). For example, the Apollo 12 12033 soil sample was sampled from the bottom of a 15.24 cm deep trench near the north rim of Head Crater, and 66% of the glass fragment from the 12033 sample is KREEP material. The Apollo 12 12070 soil taken from the north side of Surveyor Crater is 25% KREEP (Hubbard et al., 1971). It is clear that the nonmare component within a ray patch contains a portion of pure highland material mixed with local mare basalt. More importantly, our modeling demonstrates that the abundance of exotic material at specific locations is highly variable spatially.

These arguments strengthen the case that the highly elevated abundances in nonmare material in certain Apollo 12 samples are attributable to Copernicus Crater and that the attribution of the ~ 800 Ma age of Apollo 12 KREEPy samples to Copernicus is correct (Bogard et al., 1994; Barra et al., 2006). This is significant because of Copernicuss role as a potential anchor point for lunar chronology (Stöffler et al., 2006; Hiesinger et al., 2012).

3.5 Conclusion

Both proximal and distal ejecta transported by impacts are important to the distribution of material across the lunar surface. To separate the effect of local and distal

ejecta on the material exchanged across contacts, we modeled three main components: proximal/distal ejecta, subpixel crater mixing, and ray/ejecta mixing. By adding each component one-by-one to our model, we investigated how craters formed in proximity to the mare/highland contact influence the compositional variation within the 4-5 kmwide mixing zone. Our regional run results (Case D) can explain observed changes in composition across mare and highland contacts that are seen in Clementine data. As the average mare abundances of the Case D results are consistent with the Clementine data, the varying mare abundances seen in the Case D simulation can also explain the majority of mare abundances of Apollo 15/17 soil samples. Low nonmare abundances are present in our simulated Apollo 11 and 12 landing sites unless we take into account the contribution of specific large craters (e.g., Copernicus Crater) that appear to contribute to the global elevated nonmare abundance.

As seen in the patchy rays in our global model result (Figure 3.7), the superposition of large crater rays may result in the elevated nonmare abundance in mare soil samples. Crater ray deposits, particularly from large craters, are a source of exotic material, and this exotic material is then either distributed or diluted by smaller craters as time passes. As these processes proceed, mare soils become more contaminated by anorthositic material, and a sample scooped from a mare plain is likely to include this reworked material. However, when the Apollo missions landed at places superposed by rays and close to specific large young craters, the chance of acquiring samples of this ray material was greatly enhanced (much more so than the chance of collecting “average” mare). The fact that this material was patchy and localized and only a few Apollo 12 soil samples had much higher concentration of nonmare materials is consistent with our understanding of the transport and mixing process. Thus, our results support the earlier interpretation that Copernicus Crater ray was the source of highland material at the Apollo 12 landing site area, contaminating and skewing the mare soil and regolith record. The Copernicus Crater ray material in Apollo 12 mare soil samples is an example of the stochastic nature of the cratering process and demonstrates how a large crater can affect even distant landing sites sam-

ples. It would be useful for future lunar missions to test whether or not the elevated nonmare abundance seen in Apollo 11 and 12 and Luna 16 samples and orbital data is biased by rays by sampling at regions with less contamination by rays.

An example of a region with less complicated geology is the contact between mare and highlands in the western part of Grimaldi Crater. Our model is able to reproduce the 4-5 km width of the mixing zone in this region and demonstrates that both distal and proximal ejecta materials are important for regolith evolution.



Figure 3.5.: The mare fraction for Cases A, C, and D result (Li and Mustard, 2000, similar to Figure 5). Each image is 200 by 1000 pixels. The lower part of the image represents the mare side, and the brighter part is the highland side. Each fraction image represents our simulation cases of (a) Case A (proximal ejecta with no subpixel crater mixing), (b) Case C (proximal and distal ejecta with no subpixel crater mixing), and (c) Case D (proximal and distal ejecta with subpixel crater mixing). Note that these mare fraction maps will not visually match the appearance of contacts on the lunar surface because it does not take into account optical maturation of rays with time.

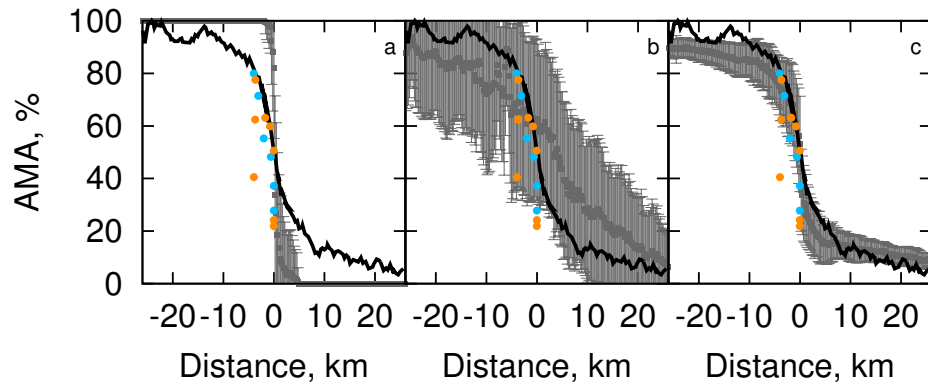


Figure 3.6.: The compositional gradient profile of the average mare abundance (AMA) within a distance of 26 km from mare (left-hand side) and highland (right-hand side) contact. The black line represents the Clementine data for Grimaldi Crater by Li and Mustard (Li and Mustard, 2000, Figure 6). The solid square point in gray color in each box represents the mean AMA of the total 1441 profiles from each case of (a) Case A, (b) Case C, and (c) Case D. One standard deviation across the contact is shown by a vertical line at every solid square point. The solid points in orange and blue color are Apollo 15 and 17 in situ mare soil samples (Rhodes, 1977, Figure 1), respectively.

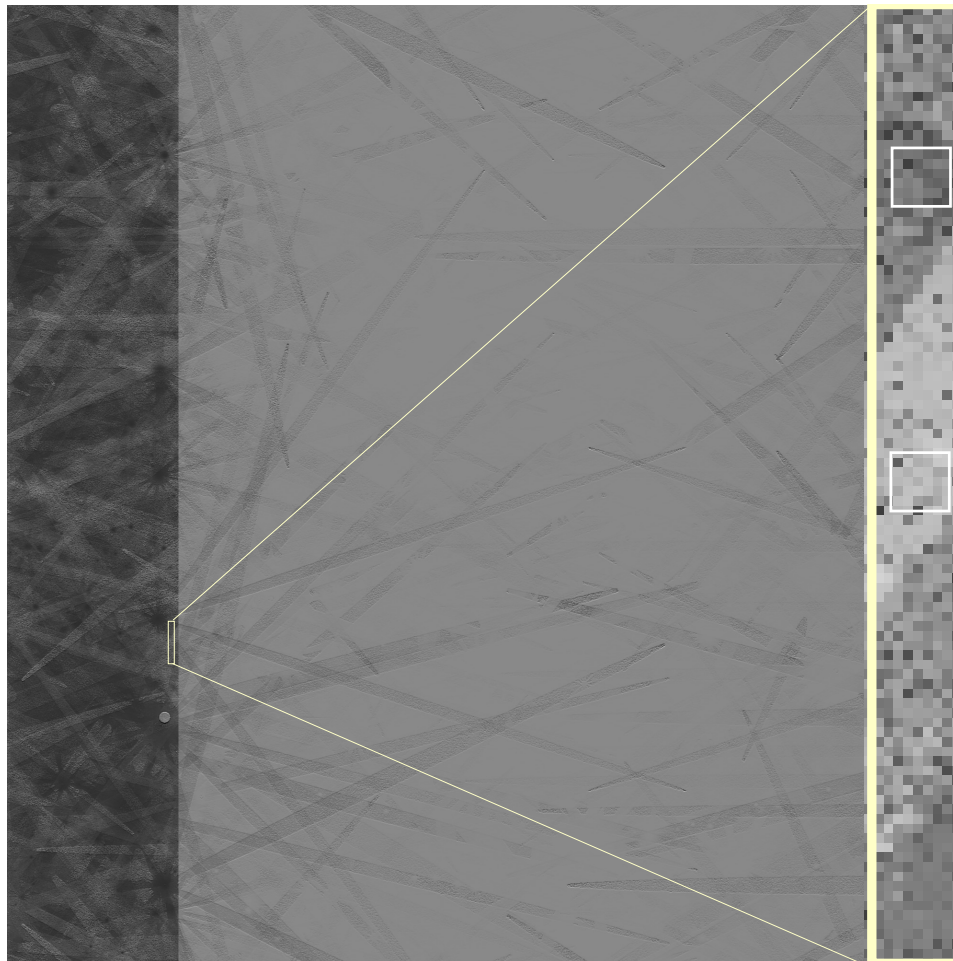


Figure 3.7.: Compositional map of our global mare/highland contact run with all model components turned on. The simulation size is 6000 km by 6000 km (2000 by 2000 pixels). The yellow arrow points to a ray patch at an equivalent distance of the Apollo 12 sites from our simulated mare/highland contact. The inset on the left-hand side is the close-up of the ray patch and nonray region on the right-hand side. Inside close-up, the square white box on the top is nonray region, and the square white box on the bottom is almost the center of ray patch.

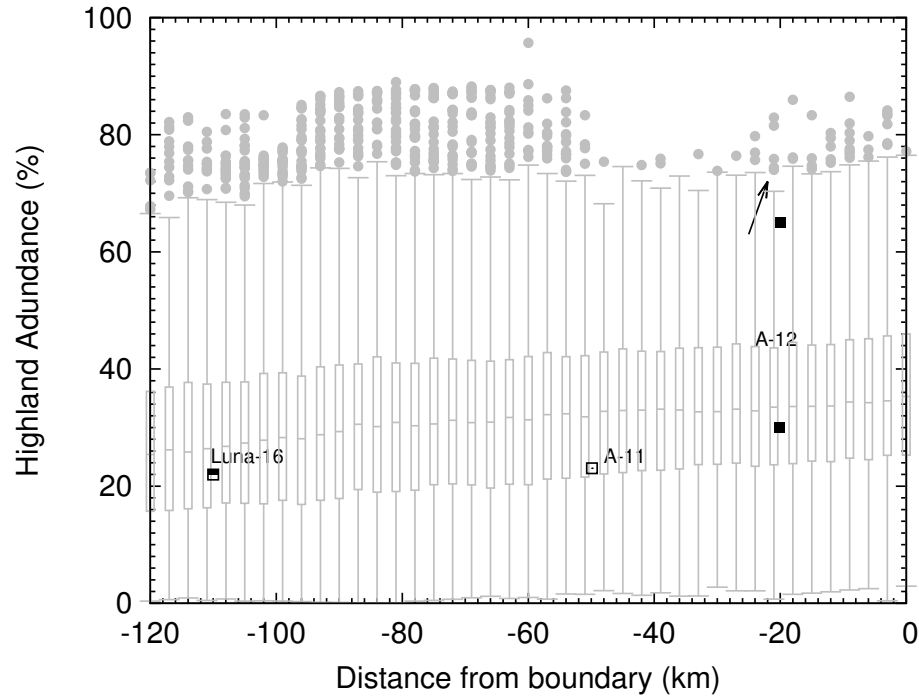


Figure 3.8.: The exotic component (highland) distribution with distance from mare and highland contact from our global run result. Composition distribution at a distance is plotted as a box and whisker plot. The line inside of the box is the median value of total composition distribution at a given distance. The upper and lower boundaries of the box represent the 25% of data above the median and the 25% of data below the median, respectively. The ends of the whiskers represent 99% of data. The solid circles in light gray color are outliers. The data points in black color with labels of “A-12”, “A-11” and “Luna-16” are from Apollo 12 and 11 and Luna 16 mare, respectively, soil samples. The black arrow denotes one example of a ray patch in our simulation domain (see close-up in Figure 3.7).

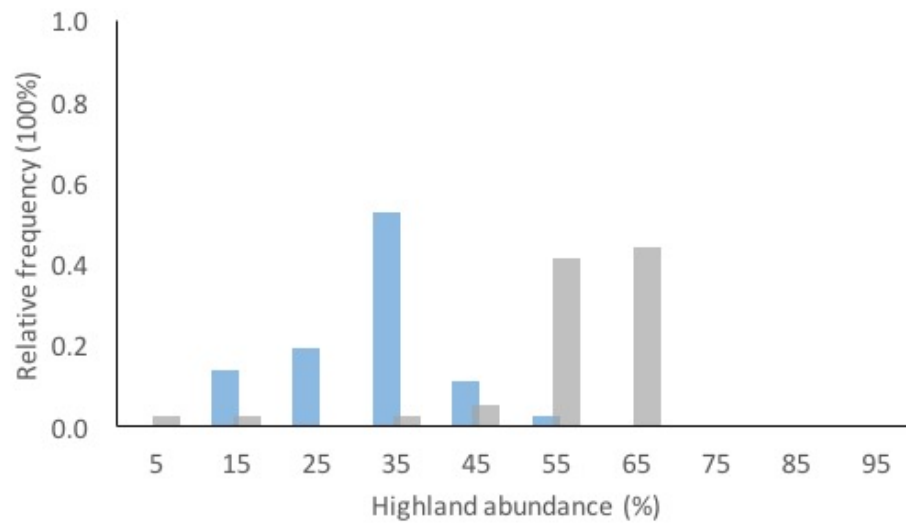


Figure 3.9.: Histogram of highland abundance normalized by the total number of pixels inside a ray patch and nonray region shown in Figure 3.7. The bars in blue color are the nonray region population (36 pixels in total) in our global run, while the bars in gray color are the population sampled from a localized ray patch in our simulation result (36 pixels in total).

4 NO CHANGE IN THE RECENT LUNAR IMPACT FLUX REQUIRED BASED ON MODELING OF IMPACT GLASS SPHERULE AGE DISTRIBUTIONS

Acknowledgement: A version of this chapter has been published in *Geophysical Research Letters*. Reference: Huang, Y. H., Minton, D. A., Zellner, N. E., Hirabayashi, M., Richardson, J. E., and Fassett, C. I. No Change in the Recent Lunar Impact Flux Required Based on Modeling of Impact Glass Spherule Age Distributions. *Geophysical Research Letters*, DOI:10.1029/2018GL077254

Abstract: The distributions of $^{40}\text{Ar}/^{39}\text{Ar}$ -derived ages of impact glass spherules in lunar regolith samples show an excess at <500 Ma relative to older ages. It has not been well understood whether this excess of young ages reflects an increase in the recent lunar impact flux or is due to a bias in the samples. We developed a model to simulate the production, transport, destruction, and sampling of lunar glass spherules. A modeled bias is seen when either (1) the simulated sampling depth is 10 cm, consistent with the typical depth from which Apollo soil samples were taken, or (2) when glass occurrence in the ejecta is limited to >10 crater radii from the crater, consistent with terrestrial microtektite observations. We suggest that the observed excess of young ages for lunar impact glasses is likely due to limitations of the regolith sampling strategy of the Apollo program, rather than reflecting a change in the lunar impact rate.

4.1 Introduction

Most lunar crater chronologies assume that the impact flux in the inner Solar System has been constant for the last ~ 3 Ga (Neukum, 1983; Neukum et al., 2001;

Robbins, 2014). Some researchers have suggested that the impact rate over this time period instead increased sometime in the last ~ 1 Ga (McEwen et al., 1997; Grieve, 1984; Shoemaker et al., 1990; Culler et al., 2000; Fassett and Thomson, 2014; Mazrouei et al., 2015; Vokrouhlický et al., 2017) or possibly declined (Hartmann et al., 2007; Quantin et al., 2007). Impact melts provide one of the most important records for constraining the lunar impact flux. Impact glass spherules, a kind of impact melt product, are up to 1 mm diameter in size and produced by hypervelocity impacts (Reid et al., 1977; Delano et al., 1982; Melosh and Vickery, 1991). The ubiquity of spherules and their age distribution suggests that they are produced in relatively small impacts (Hörz and Cintala, 1997; Norman et al., 2012; Zeigler et al., 2006; Delano, 1991; Symes et al., 1998; Korotev et al., 2010), and therefore are potentially a powerful record of the impact history since the end of the basin-forming epoch at 3.9 Ga (Tera et al., 1974; Tera et al., 1973; Turner and Cadogan, 1975).

The analysis of lunar regolith soil samples collected from the Apollo 12, 14, 16, and 17 landing sites shows an excess of impact glass spherules with derived $^{40}\text{Ar}/^{39}\text{Ar}$ ages of $<400\text{-}500$ Ma (Culler et al., 2000; Levine et al., 2005; Hui et al., 2009; Zellner and Delano, 2015) (see Figure 4.1). A straightforward explanation for the excess of impact glass spherules in this period is an increase in the impact flux by a factor of 2–3 during the late Copernican. Because the impact flux is a potentially important factor for biotic evolution on Earth (Alvarez et al., 1980), understanding its history is an important issue. However, it is not known how much the observed age distribution of lunar glass spherules is affected by biases (Hörz, 2000; Hartmann et al., 2007).

A young age bias in the $^{40}\text{Ar}/^{39}\text{Ar}$ age distribution of impact glass spherules could arise as a result of several processes. Once formed, spherules in the lunar regolith can be destroyed by subsequent impacts over time, resulting in a preservation bias (Zellner and Delano, 2015). In addition, lunar diurnal temperature cycling may cause argon diffusion of glass spherules exposed on the surface, leading to a lower abundance of argon that is measured as a younger age in a sample (Zellner and Delano, 2015). After accounting for an argon diffusion bias for spherules from several Apollo 14, 16,

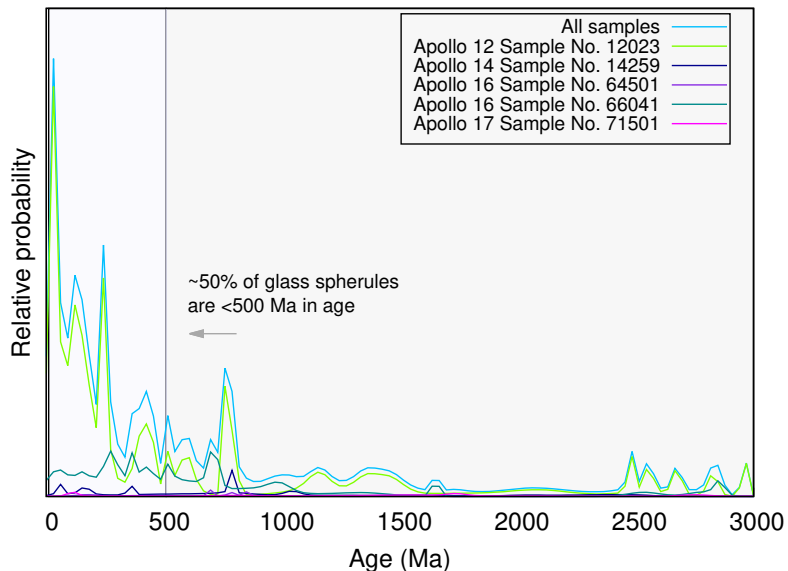


Figure 4.1.: The relative probability plot of five reported lunar regolith samples. The relative impact flux is calculated from the fraction of impact glass spherules and shards normalized by the overall number of impact glass spherules and shards from all five Apollo regolith samples. The data is directly taken from two studies, Zellner and Levine (Zellner and Delano, 2015; Levine et al., 2005). The spherule data of Culler and Hui (Culler et al., 2000; Hui et al., 2009) are not included.

and 17 regolith samples, Zellner and Delano show a uniform age distribution over the last one billion years (Zellner and Delano, 2015). Even after correcting for a bias arising from diffusive loss of argon, the glass spherules from Apollo 12 12023 regolith still show a prominent spike in the late Copernican (see Figure 4.1). The geochemical composition data of the Apollo 12 12023 regolith were not available for argon diffusion bias correction, and therefore further analysis is needed to understand the source of this late Copernican excess of glass ages. This motivates us to seek other possible sources of young age bias that are inherently present in lunar regolith samples.

To date there is no comprehensive, three-dimensional model that tracks the fate of spherules from the time of their production on the lunar surface through their

sampling by the Apollo astronauts. Here, we used the model that is introduced in Section 2.4 to understand the expected age distribution of impact glass spherules in the lunar regolith. Using the new capabilities of the code, we generate the expected age distribution of glass spherules for a model impact flux. We then compare our calculated age distributions of glass spherules with the observed age distribution collected from lunar regolith samples. In our model, we set the impact rate to be constant over the last 3 Ga to show that the excess of spherules with ages of <500 Ma can be due to a sampling bias (see Figure 4.1). We cannot rule out a possibility of that the lunar impact flux increased, however we will show the spherule age distribution does not require any temporal change.

4.2 Lunar impact glass spherule simulation modeling

We divide our problem into four model components, which simulate the processes involved in spherule production, transport, destruction, and sampling. In this work “production” refers to the component of the code that models both the total abundance of spherules that are generated in any given impact, and how those spherules are distributed in the ejecta of their source crater. We derived a model constrained by terrestrial microtektite data for the production and distribution of lunar impact glass spherules in Section 4.2.1. “Transport” refers to the component of the code that models how subsequent impacts re-distribute spherules, which makes use of methods developed Section 2.4 (Huang et al., 2017). “Destruction” refers to the component of the code that models how impacts destroy old spherules (see Section 2.5). In Section 4.2.2, we evaluated the destruction of a glass spherule caused by physical breakage upon high-speed landing. Finally, in Section 4.2.3, “sampling” refers to the way we process the output of our simulations to obtain a representative age distribution of spherules such that we mimic the sampling of lunar regolith by the Apollo astronauts. In this section we give an overview of how each of these model components was implemented and constrained by observations.

4.2.1 Constraining lunar impact glass spherule production

Lunar impact glass spherules form as molten droplets entrained within impact-excavated ejecta during hypervelocity impact cratering events (Delano, 1991; Melosh and Vickery, 1991). In order to model the production of impact glasses within individual lunar impact events in CTEM, we require constraints on both the abundance of mm-sized spherules produced by an impact of a given size, as well as how those spherules are distributed within the ejecta of their source crater.

Despite efforts to detect impact glasses remotely, their abundance and distribution within the ejecta and abundance relative to the crater’s size remain unknown for the Moon (Tompkins and Pieters, 2010; Schultz and Mustard, 2004; Cannon and Mustard, 2015). This motivates us to look to the terrestrial impact record for possible constraints on the abundance and distribution of impact glasses in ejecta. The closest terrestrial analogue to the lunar impact spherules used in our observational data shown in Figure 4.1 are the terrestrial microtektites (Donnelly and Chao, 1973). Microtektites are glassy mm-sized or smaller impactites that are morphologically similar to lunar impact glass spherules (Glass and Simonson, 2012).

We use observational constraints on the abundance and distribution of terrestrial microtektites relative to their source craters to provide constraints on our glass spherule production model. To do so, we need to understand the relationship between the spatial distribution of spherules relative to their source crater. Because CTEM generates large numbers of craters in a single simulation, it uses a very simplified impact excavation scheme based on the Maxwell Z-model, which connects parcels of ejecta back to the excavation flow within the transient crater (Maxwell and Seifert, 1974; Maxwell, 1977). A 2D schematic of the simplified model is shown in Figure 4.2, though in CTEM the calculations are done in 3D (see Figure 2.1 in section 2.1).

For this work we conceptualize spherules (or microtektites) as originating in the melt zone of the transient crater. We only produce spherules in our model arising from resolved primary craters, not secondary craters or subpixel craters. Secondary craters

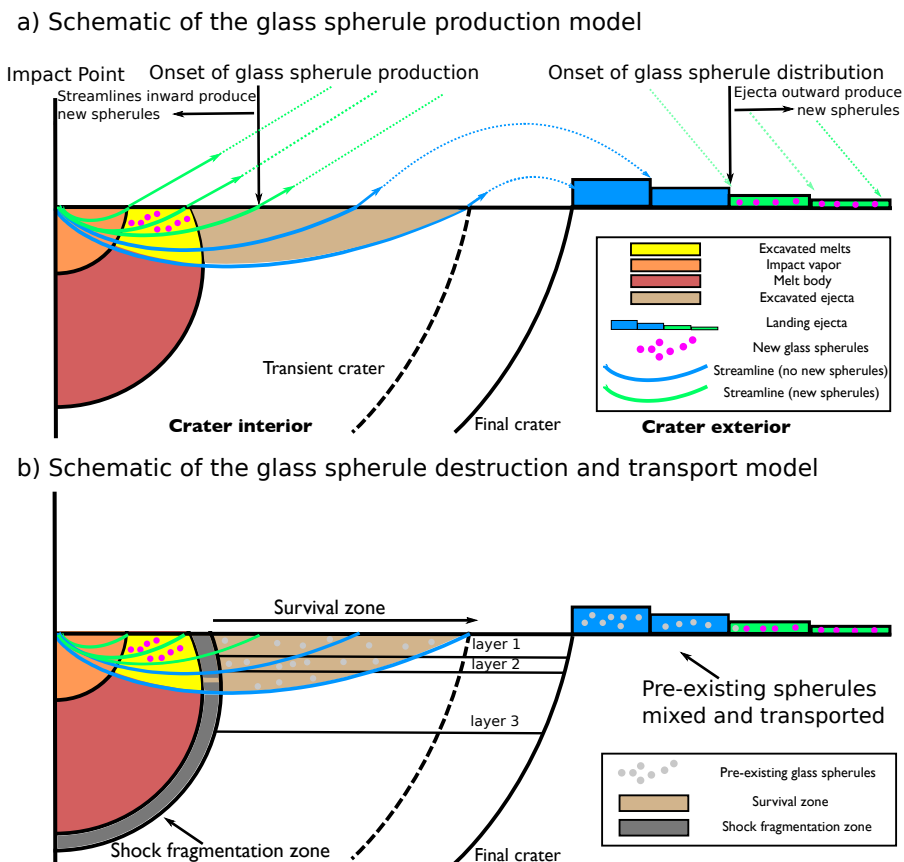


Figure 4.2.: An illustration of spherule production, transport, and destruction in CTEM. a) Spherules are produced within the melt zone for those streamlines that emerge inward of the onset distance for spherule production. b) Pre-existing spherules within regolith layers are destroyed in the melt and shock fragmentation zone. Old spherules entrained within streamlines that intersect the survival zone are mixed with fresh spherules produced as in a).

are less energetic and produce little melt (Bjorkman and Holsapple, 1987). While Hörz proposed micrometeorites as a source of spherules (Hörz and Cintala, 1997), we consider this unlikely based on the fact that micrometeorites form agglutinates, which are a distinct kind of melt product from the spherules modeled in our study.

Figure 4.2a shows the relevant processes in our spherule production model. Inside the transient crater we have included a vapor zone and a melt zone, whose volumes

are constrained by π -scaling laws in the literature study (Cintala and Grieve, 1998; Abramov et al., 2012). The pixels that make up an ejecta block can be traced back to volumes that are bounded by the streamlines within the transient crater. We further restrict spherule production to occur only in the melt zone for those streamtubes that emerge inward what we call the spherule production onset distance. Because the streamtubes that emerge closest to the impact point have the highest ejection velocity, fresh glass spherules are only distributed in the ejecta outward of a specific range. The onset distance for glass spherule distribution in the ejecta for lunar craters is calculated assuming ballistic flight in lunar gravity from the ejecta launch position given by:

$$l(r, R_{tc}) = r + \frac{2v_e^2(r, R_{tc}) \sin \theta_e \cos \theta_e}{g} \quad (4.1)$$

where $l(r, R_{tc})$ is the ballistic range from impact center as function of launching position (r) and transient crater radius (R_{tc}), $v_e(r, R_{tc})$ is the launching velocity as function of launching position and transient crater size, and θ_e is launching angle, in which 45 degree is assumed. Using the Pi theorem of dimensional analysis, the launching velocity of an ejecta can be associated with its source transient crater size (Housen et al., 1983).

The spherule production onset distance that we used also implies that not all excavated melt will form spherules. While the provenance of impact glass spherules within the melt zone is poorly constrained, we assume that lunar impact glass spherules are a terrestrial analogue of lunar impact glass spherules. From the three well-recognized microtektite strewn fields (Lake Bosumtwi, Chesapeake Bay, and Chicxulub Crater), microtektites are found ~ 100 – 1000 km away from their source crater center with diameters of 10.8, 85, and 180 km respectively (Glass, 1968; Donnelly and Chao, 1973; Glass et al., 1973; Alvarez et al., 1980; Smit and Hertogen, 1980; Bohor et al., 1984). Assuming that microtektites follow a ballistic trajectory, we can infer their launching position (provenance) within a transient crater from a given ballistic range (Eq. 4.1).

Using the π -group theorem of dimensional analysis, the launching velocity of an ejecta can be associated with its source transient crater size (Housen et al., 1983),

$$v_e(r, R_{tc}) = \left[C_{vpg}^2 g_E R_{tc} \left(\frac{r}{R_{tc}} \right)^{-2/\mu} - C_{vpg}^2 g r - C_{vps}^2 \frac{\bar{Y}}{\rho_t} \right]^{\frac{1}{2}} \quad (4.2)$$

where μ , $C_{vpg} = \frac{\sqrt{2}}{0.85} \frac{\mu}{\mu+1}$, and C_{vps} are constants, which depend on target materials, \bar{Y} is the effective target strength, ρ_t is the target density, and g_E is terrestrial gravitational acceleration. We collected the size versus spatial distribution of microtektites from the three terrestrial craters as shown in Table 4.2. For such large craters, the term of C_{vps} can be neglected. Equation 4.1 and 4.2 can be solved together for the launching position of r if one estimates the size of a transient crater.

To properly estimate the size of a transient crater, we referred to each individual impact simulation study from the literature for their impact conditions where possible. The types of target materials chosen for these three terrestrial craters in previous impact simulations are competent rock or sedimentary rocks, except for a lower density wet tuff used in simulating Chesapeake Bay Crater (Artemieva et al., 2004; Collins and Wünnemann, 2005; Collins et al., 2008). As a result, we chose hard rock scaling laws for our estimated transient crater size, in which $\mu = 0.55$, the strength of target material is 18 MPa, and the density of target is 2500 kg/m³ (Holsapple, 1993). Assuming that the same density of projectiles as target material, impact conditions for these three impact craters as well as our calculated transient crater sizes are summarized in Table 4.3. Given that we estimated transient crater sizes for these three craters, we can infer launching positions of microtektites.

In addition, we also estimated the provenance of other forms of impact melt products collected from terrestrial craters (Lake Lonar, Kamil, Ries) and lunar ropy glasses that are thought to have come from Copernicus Crater (Wentworth et al., 1994). Table 4.4 lists the size data from various studies, impact conditions for the crater sizes of Kamil, Lake Lonar, Apollo 12 ropy glasses. For Ries Crater we used a numerical simulation result in the literature (Artemieva et al., 2013). All estimations of craters'

transient craters also refer to the hard rock scaling law. Consequently, we suggest that an integrated approach regarding melt fragmentation, e.g. glass spherules and melt breccia, during cratering is beyond the scope of this study. Here we provided the first-order approximation of types of melt products with varying deposition distances from the center of a crater. Often mixed types of melt products are found along deposition distances, because an interaction between the impact vapor plume and ejecta curtain is dynamic and requires a physical modeling to constrain the relative abundance of different melt products within ejecta curtain.

Figure 4.3 shows our estimated launching position with the maximum sizes of melt products that have been linked to terrestrial craters and found at a specific site. The reason we only use the maximum size data of microtektites is to reduce the effect of atmosphere and terrestrial impact vapor plume on the further breakup process of melt particles. Because the lunar impact environment experiences little atmosphere and impact vapor plume, using the data of maximum sizes of terrestrial microtektite is more likely to reflect the actual distribution of impact glass spherules. The results of this calculation for all of the impact-generated melt products with associated craters is plotted as the lower x-axis of Figure 4.3. We can then estimate the equivalent deposition distance of products for the Moon, which shown as the upper x-axis of Figure 4.3.

The sizes of Chicxulub microtektite-like spherules that were found in Beloc and La Sierrita site are ~ 10 mm, which is larger than the typical size range of terrestrial microtektites (Thein, 1987) and the sizes of lunar impact glass spherules. These two data points depict corresponding lunar landing distances of 14 and 23 radii. For the rest of Chicxulub microtektites, the data point at Shell Creek (~ 3 mm) reaches the shortest distance of 26 radii under lunar gravity. We used 20 radii for our modeled impact glass spherules by averaging 14 and 26 radii.

We caution that glass spherules can be deposited at proximal distances, smaller than 20 radii, yet the types of more proximal melt particles appear to be larger and mixed with solid fragments (as seen from terrestrial impact records), as shown in the

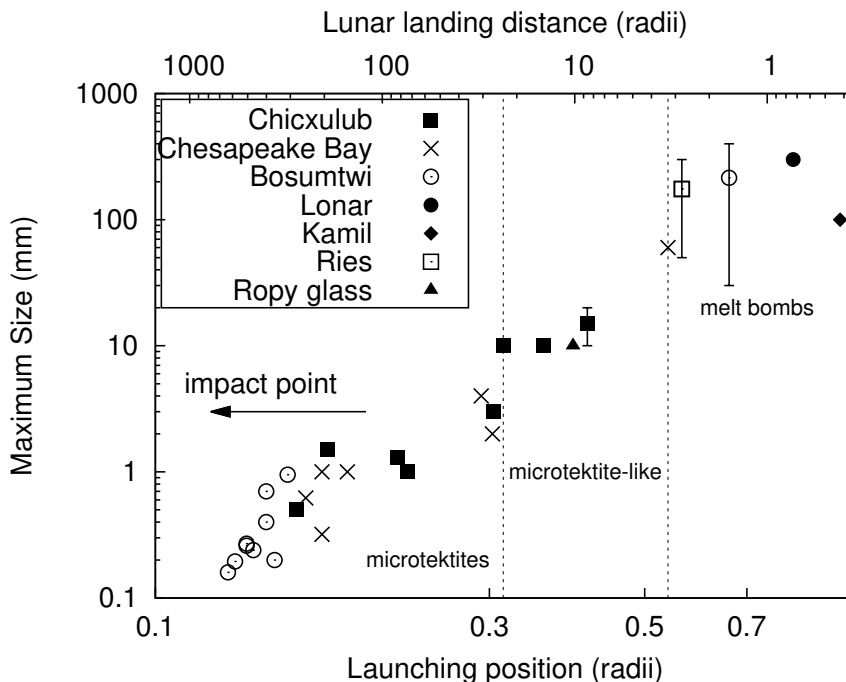


Figure 4.3.: Our modeled impact glass spherule production model based on terrestrial impact crater glass/melt size data. The lower x axis represents the estimated launching position scaled by the calculated transient crater radius. The y axis is the reported maximum size of the impact melt product in millimeters (mm). The upper x axis is the equivalent landing distance under lunar gravity.

right panel of Figure 4.3. This result suggests that lunar spherules are likely to be produced in ejecta found at >20 crater radii away from the source crater. These sub-mm sized lunar impact glass spherules are expected to be found in ejecta that is beyond the visible crater rays, because the visible rays of craters are typically <10 radii in length (Baldwin, 1963).

From Figure 4.3, there is a relationship between the deposition distance (or equivalently, the launching position) and the size of the melt product. This suggests that terrestrial microtektites appear to be more efficiently produced in ejecta deposited farther away from crater centers than nearby crater deposits. For example, several terrestrial microtektite strewn fields are known from deposits obtained from deep

drilling in the Pacific Ocean (Glass and Simonson, 2012). From this, we can estimate the onset distance for production of microtektites as 0.3 radii, which becomes an onset distance for spherule deposition of >20 crater radii distance for the Moon (see Figure 4.2a).

Those modeled glass spherules, due to higher kinetic energy, are subsequently dispersed in the form of crater rays in CTEM. The spatial distribution of glass spherules with their source crater's ejecta deposit is also uncertain. Yet, the spatial distribution of glass spherules is likely correlated with the ray pattern that forms the distal ejecta of fresh craters (Bohor and Glass, 1995). Although impact glass spherules have not been reported to occur in association with crater rays, other impact-generated melt products, e.g. Apollo 16 impact glass bombs and Apollo 12 roapy glasses, were found to be associated with rays of craters (Meyer et al., 1971; Morris et al., 1986). In addition, the locations of microtektite layers associated with the Chicxulub and Chesapeake crater on Earth have been suggested to appear ray-like (Pollastro, 1993; Bohor and Glass, 1995; McHugh et al., 1998).

To obtain our onset distances for glass spherule production and distribution, we made many simplifying assumptions. To account for uncertainties we consider in our modeling four different values for our glass distribution onset distances of 0, 5, 10, and 20 crater radii from the rim of the crater. The onset distance of 0 is equivalent to assuming that all ejected melts that were produced during cratering are in the form of mm diameter glass spherules, which is highly unlikely, but we included it to test the limits of our model. Although further investigation is needed to understand the origin of lunar impact glass spherules, our analysis suggests that they are deposited in distal ejecta, and their abundance and scales linearly with crater size. Thus, we applied this simple spherule production model to all sizes of craters in CTEM.

4.2.2 Evaluating the importance of spherule breakage by high velocity landing

We estimate here whether we need to consider breakage of spherules that arrive from distant impact craters. Contact mechanics has been used to study the deformation of two approaching objects (Hertz, 1896, Chapter 5). The contact behavior between two elastic bodies is demonstrated by Hertz, who considered the pressure on a curved surface. For brittle materials such as glass spherules, we can use an elastic loading estimation for a lower bound of destruction conditions in which a glass spherule is not broken (before reaching plastic deformation).

The approach to estimate the critical landing speed for glass spherule breakage on the lunar surface is to calculate the average pressure at the contact area between a finite size glass sphere and an infinite flat surface. The applied force on the sphere can be obtained from the impulse over the contact time, in which the impulse is the change of an object's momentum assuming the mass of an object is unchanged before breakage. It is written in a simple form,

$$\Delta p = mv_f - mv_i \quad (4.3)$$

where Δp is impulse, m is the mass of a glass sphere, v_i and v_f are initial landing velocity and rebound velocity respectively. As a result, the pressure at the contact of a glass sphere is the impulse over both contact time ($t_{contact}$) and contact area ($A_{contact}$). Our master equation is,

$$P = \frac{\Delta p/t_{contact}}{A_{contact}} \quad (4.4)$$

Assuming the circular shape for a contact area, the radius of the contact area can be estimated based on the elasticities of the target surface and glass sphere, and normal loading (Timoshenko and Goodier, 1982, Chapter 13),

$$a = \left(\frac{3}{4} N k R \right)^{\frac{1}{3}} \quad (4.5)$$

where a is the radius of the contact circle, N is the normal loading force, k is $\left(\frac{1-\mu_1^2}{E_1} + \frac{1-\mu_2^2}{E_2} \right)$, in which E_1 , μ_1 , and E_2 , μ_2 are Young's moduli and Poisson's ratio for the surface and glass sphere respectively, R is the radius of a glass sphere. Given that the impact velocity is less than the elastic wave velocity in the glass sphere. We can relate the normal loading of the contact process to the impact velocity by assuming that the kinetic energy of a glass sphere is equivalent to the work of reaching the compression (Knight et al., 1977),

$$\frac{1}{2} \left(\rho \frac{4\pi}{3} R^3 \right) v_i^2 = \int_0^{z_{max}} N(z) dz \quad (4.6)$$

where z is the mutual distance between a point at the glass sphere and the contact point, which is parallel to the direction of impact velocity of a glass sphere. The relation between the radius of a contact circle and the mutual distance is $a = \sqrt{Rz}$. As a result, the normal loading can be expressed as a function of the mutual distance from Eq. 4.5,

$$N(z) = \frac{4}{3k} R^{\frac{1}{2}} z^{\frac{3}{2}} \quad (4.7)$$

Replacing N in Eq. 4.6 with Eq. 4.7, we can obtain the integral on the right hand-side of Eq. 4.6, it becomes,

$$\frac{1}{2} \left(\rho \frac{4\pi}{3} R^3 \right) v_i^2 = \frac{2}{5} \frac{4}{3k} R^{\frac{1}{2}} z_{max}^{\frac{5}{2}} \quad (4.8)$$

The glass sphere reaches the maximum normal loading as the mutual distance becomes zero (z_{max} at initial). Finally, Eq. 4.8 shows a maximum loading distance as a function

of impact velocity. We can replace the parameter of z in Eq. 4.7 with the maximum loading distance obtained from Eq. 4.8. As shown in Eq. 4.9, the maximum normal loading is the power of $\frac{6}{5}$ of impact velocity,

$$N = \left[\frac{5\pi}{3} \rho \right]^{\frac{3}{5}} \left[\frac{3k}{4} \right]^{\frac{-2}{5}} R^2 v_i^{\frac{6}{5}} \quad (4.9)$$

We then substitute N in Eq. 4.5 with Eq. 4.9, and the contact area, a , in Eq. 4.5 can be fully expressed in terms of known parameters. For our elastic bodies, the contact time for a sphere striking a flat surface with impact velocity can be analytically solved (Timoshenko and Goodier, 1982, Chapter 13),

$$t_{contact} = 2.94 v_i^{\frac{-1}{5}} \left(\frac{5\pi \rho k}{4} \right)^{\frac{2}{5}} R \quad (4.10)$$

Next we substituted the contact area and contact time into our master equation from Eq. 4.4 and obtained the pressure. When assuming the coefficient of restitution as 1 (elastic collision), it provides a upper bound of pressure at the contact of a sphere,

$$P = 0.3 \rho^{\frac{1}{5}} k^{-\frac{4}{5}} v_{imp}^{\frac{2}{5}} \quad (4.11)$$

Equation 4.11 shows that the stress at the contact of a sphere has a stronger dependence on elastic properties than the impact velocity. In other words, this equation describes that for a given elasticity the greater the impact velocity the stronger the stress at the contact.

Considering a landing lunar glass spherule at the lunar surface, Young's modulus of glass spherule is large while soft, porous lunar surface materials have a smaller Young's modulus. Intuitively, glass spherules landing in lunar surfaces would not break. From the active seismic experiment at the Apollo 14 landing site, the P-wave velocity at the upper 8.5 meter thick regolith of Fra Mauro site is 104 m/s (Kovach

et al., 1971). The Young’s modulus estimates range from 1 MPa to 20 MPa (Mitchell et al., 1972). On the other hand, the Young’s modulus of a glass sphere on the order of 10 GPa is 3–4 order of magnitudes of Young’s modulus of lunar soil (Swain and Hagan, 1976). This gives us an estimation of elastic constant (k). Given that the highest impact velocity of 2.38 km/s as lunar escape velocity, our estimated stress from Eq. 4.11 is much lower than the yield strength of a glass sphere.

We conclude that glass spherules impacting the Moon at high velocity as distal ejecta should be able to maintain their intact shape from our sphere stress estimation. Therefore in our model we assumed no destruction of modeled glass spherules occurs upon landing.

4.2.3 Modeling the distribution of spherule ages in lunar soil samples

We next simulated a 1 km by 1 km lunar surface with 10 m by 10 m pixels that is subject to 3 Ga of impact bombardment. The area of 1 km by 1 km for our initial simulated surface is roughly on the order of Apollo mission traverse scale; the astronaut traverse scales range from 100 meter for Apollo 11 mission to tens of km for Apollo 17 mission. We used a constant bombardment rate with a crater size-frequency distribution as defined by the Neukum Production Function (NPF) (Neukum et al., 2001).

CTEM generated a few tens of thousands of primary craters in total for each run, ranging from 10–500 m in diameter. To track all ejecta that is produced by each crater, CTEM creates a distinct layer for each ejecta blanket at a corresponding deposition distance. This ejecta layer originates in a crater cavity and contains a mixture of transported old spherules as well as fresh spherules (see Figure 4.2b).

Craters smaller than the 10 m were modeled using subcrater mixing of our layer system. We also model spherules produced by large craters that form outside of the simulated domain, which we call “super-domain” craters, which can be as large as 100 km diameter (see Section 2.8). During the excavation of each crater on the simu-

lation domain, pre-existing spherules in layers at the impact site may be destroyed by melting or shock destruction. Shock destruction of pre-existing glass spherules occurs as impact shock pressure exceeds the elastic limit for a glass sphere.

To account for the natural variation from multiple sampling sites from which our observed data set was derived (Figure 4.1), we performed 50 independent lunar surface simulations. In each individual simulation, we treat each 10 m by 10 m pixel as a model landing site. This yields 500,000 model landing sites from which we derive our model age distribution statistics. Over the course of 3 Ga-long impact bombardment, each model landing site will contain hundreds of ejecta layers in a stack, with each layer containing a unique population of simulated spherules. We mimicked how lunar astronauts scooped up soils by mixing simulated layers at a given pixel down to a specified depth.

We considered this numerical sampling/mixing depth as an additional model parameter, though sampling depths from each of five glass spherule collection in our observed data set were typically <10 cm depth of lunar surface, with the exception of the sample 12023 which was collected from 20 - 23 cm (see Table 4.5). We tested 10 cm, 1 m and 3 m for model sampling/mixing depths. The total abundance of glass spherules of a particular age is the weighted average of spherule abundance from all mixed regolith layers down to the sampling/mixing depth.

Our observed data set uses a Gaussian distribution to characterize the relative probability of each individual glass spherule having a particular age, t ,

$$t = \frac{A}{\sqrt{2\pi}\sigma} \exp \left[-(x - t)^2 / 2\sigma^2 \right],$$

where A is the amplitude of relative probability of a glass spherule, which is the likelihood of impact events that formed it around the time t , σ is the analytical error of measured ages of observed impact spherules (<1 Ma - 2 Ga). The median value of age analytical errors from our observed data set is 46 Ma (see the last row in Table 4.1). The amplitude of each glass spherule sample is scaled by the total number of

glass spherules. To obtain a relative probability from our model samples, all modeled spherules produced within a 50 Ma interval of time are tagged with the same age.

4.3 Results

We varied two parameters in our model: the glass onset distance, and the sampling/mixing depth. First, we sampled our model spherules to a depth of 10 cm to test how changing the glass onset distance affects the modeled spherule age distribution (see Figure 4.4c - f). Next, we fixed the onset distribution distance to 20 radii to test how different model sampling depths affects the modeled spherule age distribution. (see Figures 4.4a and b).

The glass onset distance parameter affects our model spherule age distribution in our model samples for our simulated sampling/mixing depth of 10 cm. If we parameterize the model to distribute glass spherules either at all distances where the ejecta is deposited or beyond the continuous ejecta blanket (2 - 3 radii), the relative probability of older and younger model spherules are similar (see Figures 4.4c and d).

However, when glass spherules are only generated at >10 radii, the relative probabilities of cratering events as old as 2 - 3 Ga are reduced (see Figures 4.4e and f). This contrast of relative probabilities between the last 500 Ma and older ages becomes more defined as the onset distance of spherule distribution is increased to 20 radii, leading to a much stronger young age bias. Nevertheless, for the onset distance of >10 radii, and assuming a 10 cm sampling/mixing depth, we reproduce the observed excess in impact glasses with ages <500 Ma.

In addition to the shallow sampling depth of 10 cm, we also modeled sampling/mixing depths up to 3 m, which represents the deepest lunar drilling core sample. For our 3 m sampling/mixing depth case, we found little evidence for a young age bias in the relative probability of the spherule ages. Figure 4.4a illustrates another age distribution of model samples collected from the depth of 1 m. The relative probability appears to have a young age bias, though not as strong as the 10 cm sampling/mixing

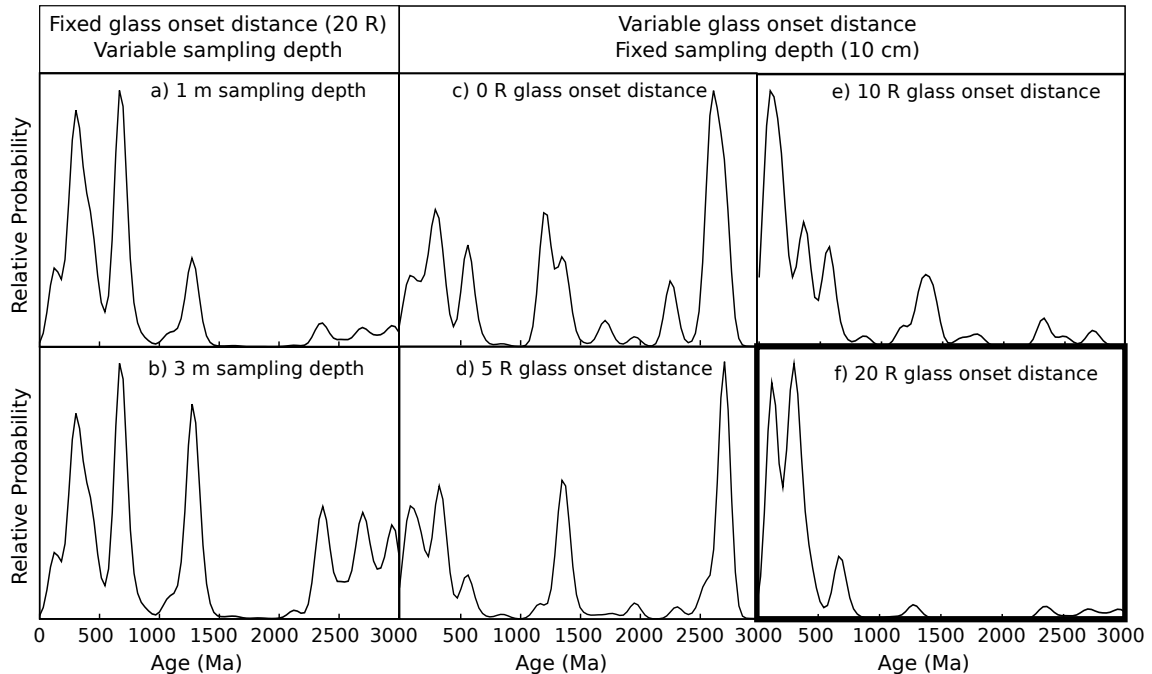


Figure 4.4.: The relative probability plots calculated from all of our fifty simulated surfaces with our two free parameters varied: sampling depth (a and b) and glass distribution onset distance, where R is the crater radius (c-f). The x-axis is age (Ma), with the present day at the left. The relative probability of all model samples is calculated in a similar fashion as the observed data set given in Figure 4.1, but with the constant model resolution σ of 50 Ma. Panel f (highlighted in black, bold line) shows our result with a sampling/mixing depth most similar to the Apollo sampling depth, and with a glass onset distance closest to that from obtained from the terrestrial microtektite constraint. It shows a prominent bias in <500 Ma ages qualitatively similar to our observational data shown in Figure 4.1.

depth case. We found that a young age bias in the case of other glass onset distance (e. g. >5 radii) does not correlate well with sampling/mixing depths (see Figure 4.5).

Several older cratering events can still be seen from our shallowly-collected samples, yet the fraction of their population within the depth of 10 cm is much smaller than for the younger cratering events. We found that those spherules typically come

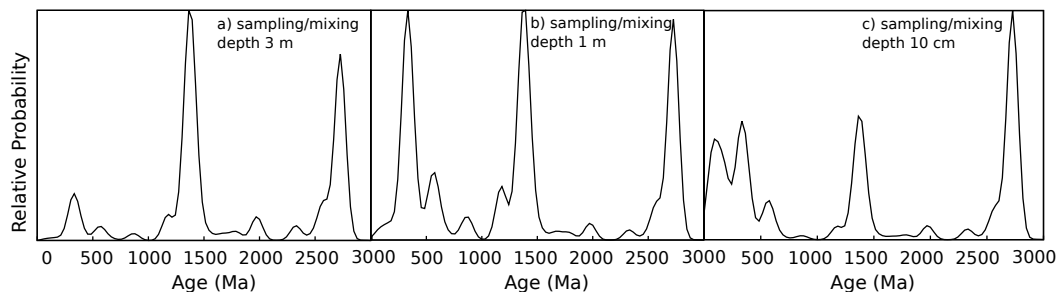


Figure 4.5.: The relative probability plot calculated from all of our fifty simulated surfaces in the case of glass onset distance > 5 radii with three sampling depths: a) 3 m, b) 1 m, and c) 10 cm. The black curve represents the overall relative probability summed from all fifty simulated surfaces. The x-axis is age (Ma), with the present day at the left.

from tens of kilometer sized craters that formed very far from the simulated domain. With increasing sampling depth, the magnitudes of relative probabilities for cratering events older >1 Ga become more visible. The age distribution derived from our simulation of deeper sampling (Figure 4.4b) shows a more uniform distribution of ages, reflecting a less biased record. We also note that the young age bias becomes more severe when the assumed shock damage zone in the model is extended, though sampling depth appears to be the main driver controlling the magnitude of the young age bias.

4.4 Discussion and Conclusion

Despite uncertainties of our spherule onset distance model, we can quantitatively reproduce the <500 Ma excess in the age distribution of impact glasses seen in Figure 4.1 under the assumption of a constant impact flux and a shallow sampling depth of 10 cm (Figure 4.4f). Our results suggest that a young age bias in lunar glass spherule populations strongly correlates with the sampling depth. If the use of terrestrial microtektite data to infer the lunar impact glass spherule distribution onset distance

of 20 crater radii is reasonable, then there is a very strong depth-dependent young age bias in the age distribution of spherules, as seen in Figure 4.4a, b and f.

The source of the depth-dependent young age bias is likely related to the process of impact gardening. Ejecta that includes glass spherules deposits on top of older terrain, and subsequent impact events alter the topmost layer of the local surface. This topmost mm and cm-thick layer is characterized as being well-mixed (Gault et al., 1974; Oberbeck, 1975; Hörz and Cintala, 1997; Speyerer et al., 2016; Costello et al., 2018). This reworking process incorporates a fraction of old deposits into younger deposits.

As older impact events can be readily seen in our model samples from deeper sampling depths, we suggest a shielding effect for older distal ejecta products (>500 Ma) that preserves them against reworking. If the fraction of older glass spherules is minor, it is likely to be diluted by younger ejecta deposits. Over time the tendency of impacts to preferentially rework the topmost layer leads to a concentration of younger ejecta and spherules deposited at the uppermost surface. Using impact glass spherule ages within this reworked zone as a window to the lunar impact flux is prone to this natural bias in the sampling process. The competition between near surface destruction and burial naturally gives rise to a depth-dependent destruction rate for spherules. As a result, the pre-existing glass spherules in a deeper part of surface are shielded. Impact glass spherules at ≥ 1 m depth can become shielded from destruction by impact gardening over the last ~ 3 Ga. The weaker shielding further implies that the residence time of a glass spherule population in shallower depths is shorter than for deeper depths.

We observed that the residence time of model glass spherule populations within the range of sampling depths between 1 cm and 6 m approximately follow a single half-life exponential function (Figure 4.6). For each of fifty simulations, we identified a spherule population that is generated by our super-domain, and then monitored their concentration within a desired depth once they were deposited on the local simulated domain. The half-life of a specific spherule population is determined by

both destruction by subsequent cratering events and shielding from sampling by the burial of subsequent ejecta. For this specific spherule population, we selected the most significant contribution of spherules to the local simulated domain. At the end of a simulation, each pixel of our model stratigraphy can contain hundreds of unique ejecta layers with different depths and spherule populations. We can extract the information from these layers and perform a weighted mixing of the different populations down to any arbitrary depth at any given model site (consisting of 1 pixel area). Once a candidate spherule population is identified, we record their concentration within a desired depth over time.

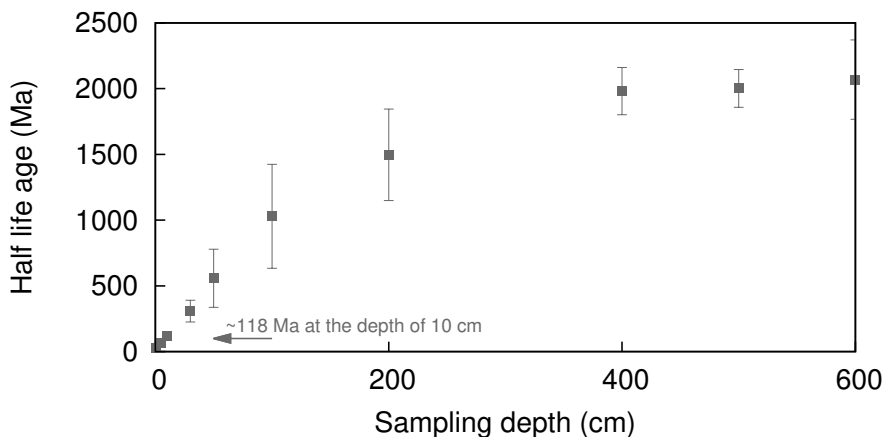


Figure 4.6.: The half life of model glass spherules due to shielding as a function of sampling depth.

Figure 4.7 shows that how the fraction of a spherule population from one of our fifty identified super domain craters changes over time within two resident depth, 10 cm and 6 m. The fraction of a spherule population is scaled by its total amount of model spherules; over time this fraction decreases. We determined that the error of fitting a single exponential function to the half-life of residence of a spherule population becomes larger in model samples that are collected from a shallower depth. This is because some of them experience near-surface excavation from large local craters, and so their lifetimes cannot strictly be fit with one single exponential function. Nev-

ertheless, using a simple exponential function, we were able to obtain 37 out of 50 spherule populations for resident depth of 10 cm, and 42 for resident depth of 6 m.

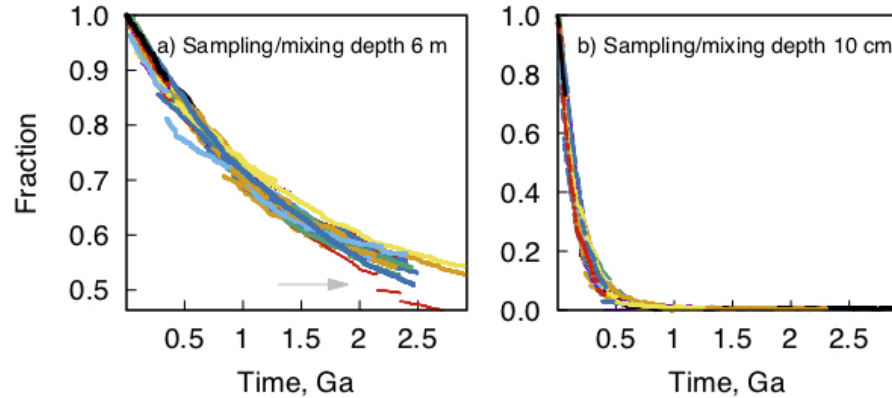


Figure 4.7.: The fraction of super-domain spherule population as function of time with two sampling/mixing depths: a) 6 m, and b) 10 cm. The x-axis represents the time since the formation of each spherule population; the y-axis is the normalized distribution of spherules by the total amount of spherules generated. Points in colors depict different spherule populations that were produced in our fifty simulations. The arrow in a) shows excavation events occurring to this particular spherule population.

We computed the half-life for glass spherule preservation for the 10 cm sampling depth to be 118^{+8}_{-12} Ma, while the half-lives of spherule populations at deeper sampling depths can increase to ~ 2 Ga. It should be noted that an individual spherule population may experience anomalous episodes of excavation or ejecta shielding such that a single half-life exponential function will not necessarily fit at any specific location.

To conclude, our modeling results are consistent with the excesses of young impact glass spherule ages in the last 500 Ma being a result of a depth-dependent age bias and the shallow sampling depth of the Apollo regolith samples, and that the spherule age distributions are consistent with a constant impact flux over the last 3 Ga.

Table 4.1.: Data re-compilation of $^{40}\text{Ar}/^{39}\text{Ar}$ -derived age measurements of lunar impact glass spherules and shards

Apollo 14, 14259,624		
Spherule number	Age (Ma)	Age error ($\pm\sigma$, Ma)
7	45	12
10	1624	140
31	1300	200
66	1037	32
88	116	66
100	783	76
168	451	228
14	983	216
30	681	200
44	250	250
54	2040	100
74	500	500
90	783	8
124	603	160
130	155	20
135	769	8
143	2292	100
154	2476	92
165	345	10
Apollo 16, 64501,225		
195	686	10
202	1530	70
239	778	18

continued on next page

Table 4.1.: *continued*

Spherule number	Age (Ma)	Age error ($\pm\sigma$, Ma)
209	1860	1883
211	165	40
247	250	250
250	432	100
251	805	218
254	847	14
Apollo 17, 71501,262		
292	2500	1500
301	102	20
304	1540	140
311	774	114
322	1289	415
349	1650	400
352	1400	300
360	250	250
291	2750	60
361	1733	40
382	2960	1600
383	2533	632
Apollo 16, 66041,127		
427	361	10
437	2786	64
438	257	22
443	510	16
455	988	44

continued on next page

Table 4.1.: *continued*

Spherule number	Age (Ma)	Age error ($\pm\sigma$, Ma)
469	559	55
471	250	250
478	699	16
491	1100	200
493	404	100
526	914	188
530	948	54
531	685	40
533	304	140
540	2533	68
542	273	22
404	550	550
413	422	24
417	250	250
421	583	52
423	1348	100
424	244	54
440	23	36
441	696	38
448	50	50
462	2855	21
466	255	92
468	302	300
484	707	16
495	394	58

continued on next page

Table 4.1.: *continued*

Spherule number	Age (Ma)	Age error ($\pm\sigma$, Ma)
502	250	250
505	820	64
506	250	250
511	250	250
513	250	250
532	250	250
538	51	40
15343,28	1647	11
LS1-21	142	26
Apollo 12, 12023		
C03	2674	20
C09	590	24
C16	-6	14
C21	375	17
C25	234	2.7
C29	18.8	3.9
C33	252.2	7.8
C37	12.7	8
C38	2476	12
C46	16.42	0.46
C48	374.7	6.7
D01	127	22
D08	4.1	8.2
D21	48	10
D34	2380	930

continued on next page

Table 4.1.: *continued*

Spherule number	Age (Ma)	Age error ($\pm\sigma$, Ma)
H02	133	39
H06	1351	42
H08	421	14
H10	2090	120
H14	36	35
H15	18	44
H17	94	25
H26	747.9	8.3
H28	267	75
H31	4	17
H36	24.75	0.95
H39	38	53
H40	137	48
H42	1438	53
H43	109	38
H45	9.4	9.5
H46	115	21
H48	29.7	9.1
H49	100.5	8
H50	61	71
I05	1291	75
I14	186	18
I20	426.2	6.3
I21	773.1	8.7
I24	1650	210

continued on next page

Table 4.1.: *continued*

Spherule number	Age (Ma)	Age error ($\pm\sigma$, Ma)
I27	562	42
I29	791	17
I30	23	45
I31	587	53
I36	443	14
I40	3250	210
J03	163	98
J05	745.4	9.6
J26	2050	230
J27	62	22
J28	165	32
J44	100	40
K08	135	32
K10	498.5	6
K32	2962	13
L01	229	47
L39	1132	61
L40	1040	130
L51	244	22
M13	20.6	6
M15	146	88
M18	2827	23
M23	2540	120
M31	2552	21
M43	225	85

continued on next page

Table 4.1.: *continued*

Spherule number	Age (Ma)	Age error ($\pm\sigma$, Ma)
N01	141	20
N02	1460	62
N03	320	180
N08	1154	41
N14	15	75
N17	421	63
N29	149	46
Median age error		46

Table 4.2.: The data of size and spatial distribution of terrestrial microtektites.

Core/site	Distance from crater (km)	Maximum size (mm)
Ivory Coast strewnfield (Glass et al., 1997)		
Outcrop 4 (Coney et al., 2010)	7.8	400.0
Outcrop 3 (Coney et al., 2010)	7.8	30.0
V19-297	1250	0.95
ODP 663	1441	0.2
V27-239	1585	0.4
K9-56	1613	0.7
RC13-213	1881	0.24
V19-300	1996	0.26
RC13-210	2009	0.27
K9-57	2287	0.195
ODP 664	2529	0.16
North American strewnfield (Glass et al., 1997)		
USGS North core (Horton et al., 2007)	39.0	60
ODP 904	332	4
DSDP 612	339	2
DSDP 94	1888	1
DSDP 149	2545	1
RC9-58	2569	0.32
Barbados	3145	0.62
K/T boundary strewnfield		
Albion Island (Pope et al., 1999)	300	10-20
Beloc (Jéhanno et al., 1992)	500	10
La Sierrita (Schulte et al., 2003)	800	10
Shell Creek (Schulte et al., 2003)	900	3
Dogie Creek (Schulte et al., 2003)	2500	1
DSDP 396 (Schulte et al., 2003)	2800	1.3
ODP 886 (Kyte et al., 1996)	6450	1.5
DSDP 577 (Kyte et al., 1996)	9300	0.5

Table 4.3.: The impact conditions using for estimating transient crater sizes in this study.

	Estimated	Simulated	Impactor size	Impact velocity	Impact angle
	R_{tc} (km)	R_{tc} (km)	R_p (km)	v_i (km/s)	θ_i ($^\circ$)
Lake Bosumtwi	4.03	4.5 (Artemieva et al., 2004)	0.425	20	45
Chesapeake Bay	12.6	14.0 (Collins and Wünnemann, 2005)	1.6	17.8	45
Chicxulub	33.83	35.0 (Collins et al., 2008)	7	12	90

Table 4.4.: The data of size and spatial distribution of impact melt products.

Crater	Crater diameter (km)	Distance (km)	Max. size (mm)	R_p (m)	v_i (km/s)	θ_i ($^\circ$)
Kamil (Fazio et al., 2014)	0.045	0.0745	100	1.25	20.0	45
Lake Lonar (Osae et al., 2005)	1.8	1.05	300	50.0	20.0	45
Ries (Engelhardt et al., 1995)	24.0	17.0	200-300	550.0 (Artemieva et al., 2013)	18.0	90
Apollo 12 ropy glass (Marvin, 1978)	93.0	400	>100.0	4000.0	18.3	90

Table 4.5.: The five Apollo soil samples with corresponding collected depth

Soil sample no.	Apollo mission	Depth
12023 (Shoemaker et al., 1970)	12	>20 cm and <23 cm
14259 (Swann et al., 1977)	14	<1 cm
64501	16	<10 cm
66041	16	<10 cm
71501 (Berg et al., 1973)	17	<4 cm

5 WHAT HAPPENED ON THE MOON 800 MILLION YEARS AGO?

Acknowledgement: A version of this chapter is being prepared for submission. Reference: Huang, Y. H., Minton, D. A., Elliott, J. R., Nguyen, P. Q., and Zellner, N. E. (2018). A short-lived lunar impact spike induced by Copernicus Crater-forming sesquinarities against a possibly long-duration global impact resurfacing 800 Ma ago from modeling perspective.

Abstract: Lunar “exotic” impact glass spherules most likely originated in geochemically distinct regions that are few hundred kilometers away from the sites where they were collected. There have been reported that “exotic” glass spherules clustered at $\sim 700\text{-}900$ Ma. Coincidentally, a well-known cratering event of Copernicus Crater possibly formed 800 Ma ago on the Moon. As a consequence of this concurrence, the excess of $\sim 700\text{-}900$ Ma ages of “exotic” glass spherules may suggest either that a global lunar impact spike that also formed Copernicus Crater occurred at the same time or that exotic glass spherules were a direct product of the formation of Copernicus Crater. In this study, we attempted to clarify the relation between the formation of Copernicus Crater and the excess of $\sim 700\text{-}900$ Ma ages of “exotic” glass spherules. We examined the contribution of glass spherules directly produced by Copernicus Crater, as well as through the re-impact of ejecta that initially escaped lunar gravity, but not Earth’s, which formed “sesquinary craters”. We found that Copernicus Crater-forming glass spherules cannot be a primary contributor to the excess of $\sim 700\text{-}900$ Ma old “exotic” glass spherules. A compositional diversity in the provenances of our compiled $\sim 700\text{-}900$ Ma-old exotic spherules is challenging to reconcile with mixing substrate materials potentially sourced from beneath Copernicus Crater. On the other hand, Copernicus Crater sesquinary-forming glasses, if exist, are too low in comparison with the amount of glasses produced by primary bombardment. Our

result suggests that the formation of Copernicus Crater is independent of the concurrence of the excess of ~ 700 - 900 Ma ages of “exotic” glass spherules. This further implies that either a short-lived lunar impact spike occurred 800 Ma ago or a better understanding of how “exotic” glass spherules form is needed.

5.1 Introduction

The heavily cratered surface of the Moon contains a unique bombardment record in the Solar System. As far as biotic evolution is concerned, interpreting a recent impact rate from the current lunar surface is challenging. The state of the current lunar surface may have reached crater saturation for small craters. Nevertheless, a few lunar crater count studies reported a possible change in a lunar impact flux in the last 3 billion years. The first example comes from the crater count study for young rayed craters on the farside of the Moon, suggesting an increase in a global lunar impact flux by a factor of 2-3 (McEwen et al., 1997). Another example is a crater count study concerning the formation age of Copernicus Crater (Neu,). Using the age of 800 Ma from the derived ages of the Apollo 12 ropy glasses that are thought to be Copernicus Crater’s ejecta, the number of craters on the top of Copernicus Crater’s ejecta blanket larger than 1 km in diameter is considered too high (treated as an outlier in the standard lunar chronology). Interestingly, a careful crater count study for Copernicus Crater that avoided some areas for visible secondary craters suggests that the scenario of a constant lunar impact rate may still hold (Hiesinger et al., 2012).

Terrestrial impact record is often compared with lunar bombardment record. On Earth, instead of crater counting as for Moon, fireballs or meteorite falls are used to establish a recent terrestrial impact record (Shoemaker et al., 1990). Terrestrial meteorites are unusual samples because they could be collisional remnants directly from asteroid breakup events (primary sources of impacts). A well-known collisional breakup event of a large asteroid dated back to ~ 400 – 500 Ma ago, which is thought

to be the parent body of L chondrite (Schmitz et al., 2003). From hydrodynamic modeling results for Earth's meteorite re-entry simulation (taking into account deceleration, ablation, and fragmentation) such an event can lead to an increase in the Earth's impact flux by a factor of 2 within <1 Ma. A detailed examination on the orbit dynamics of Flora Family breakup event, a potential candidate of L-chondrite parent body (Nesvorný et al., 2002), suggests that a few tens of kilometer sized asteroids struck the Moon between 900 Ma and 1.2 Ga (Bottke et al., 2018). As a breakup event can reset the radiometric isotope systems of fragments or parent body, multiple, old heating events are well-documented in some of the meteorites. For example, Cat Mountain and Northwest Africa 091 meteorite samples are shown experiencing old heating events at ~ 800 -900 Ma (Kring et al., 1996). While the source of which asteroid family accounts for those heating, breakup events that bombarded Earth remain debated, it makes sense to assume that lunar surface, in proximity to Earth, could have also been bombarded by a similar breakup event. The returned lunar samples are a treasure for this kind of a recent record because the ages of <1 Ga is relatively young that this kind of a recent record may still be present at the lunar surface (Kring et al., 1996; Swindle et al., 2009; Weirich et al., 2012; Righter et al., 2015; Park et al., 2015; Lindsay et al., 2015).

One of the clues of a possible change in an impact rate on Moon is lunar impact glass spherules (Culler et al., 2000; Levine et al., 2005; Hui et al., 2009; Zellner et al., 2009; Zellner and Delano, 2015). Lunar impact glass spherules, up to 1-mm diameter in size, are melt products formed in a hypervelocity impact (Reid et al., 1977; Delano et al., 1982; Melosh and Vickery, 1991; Johnson and Melosh, 2014). A particular kind of impact glass spherules, referred to as "exotic", can be geochemically separated from the local regolith where the "exotic" spherule was collected (Zellner et al., 2003; Zellner et al., 2005). An "exotic glass spherule carries a unique provenance, revealing the location of the source crater that formed it. Where an impact probability is concerned, the purpose of using only "exotic"-origin glasses is not to inflate the impact flux by double-counting a glass spherule population produced from the same

impact event (Zellner et al., 2009). The impact probability interpreted from the age distributions of “exotic” glass spherules may reflect distant, large cratering events.

A successful application of geochemical provenance analysis onto “exotic” Apollo 16 impact glass spherules reveals an individual cratering event occurring at ~ 800 Ma while several other “exotic” glass spherules spikes in the Late Heavy Bombardment era (3.8 Ga) (Zellner et al., 2003). This particular age, 800 Ma, is similar to the estimated formation age for Copernicus Crater; the age determination for the formation of Copernicus Crater was interpreted from returned Apollo 12 samples including ropy glasses (Delano et al., 2007) and coarse, non-mare fines (Wentworth et al., 1994; Barra et al., 2006; Bogard et al., 1994). An impact glass bomb, other type of melt products, collected from Apollo 16 landing site (sample No. 67567,4) also shows an age of ~ 800 Ma. The origin of the sample 67567,4 glass bomb is considered exotic because its composition cannot be achieved by mixing local regolith (Borchardt et al., 1986).

Followed by the analyses of 800 Ma-old glassy and exotic materials, Zellner reported more exotic lunar impact glass spherules and shards (spherule fragments) from Apollo 14, 16, and 17 landing sites (Zellner et al., 2009). The $^{40}\text{Ar}/^{39}\text{Ar}$ -derived age distributions of “exotic” lunar impact glass spherules and shards from Apollo 14, 16, and 17 regolith samples show an excess of glasses with ages of ~ 700 -900 Ma than glasses at other ages (see Figure 5.1 and Table 5.1). As an “exotic” glass spherule is associated with a specific impact crater on Moon, multiple “exotic” glass spherules, in which their provenance are not overlapped, represent multiple impacts. Reasonably, it seems straightforward to interpret that several other large cratering events, including Copernicus Crater, occurred 800 Ma ago on Moon. As a result, Zellner et al., 2009 have suggested that the excess of “exotic” impact glasses with measured ages of ~ 700 -900 Ma implies an increase in the lunar impact flux 800 Ma ago (Zellner et al., 2006; Zellner et al., 2009).

A relation between the ages of ~ 700 -900 Ma of “exotic” impact glasses from Apollo 14, 16, and 17 regolith samples and the formation age of Copernicus Crater is uncertain. As the most of those ~ 700 -900 Ma-old “exotic” glasses from the Apollo

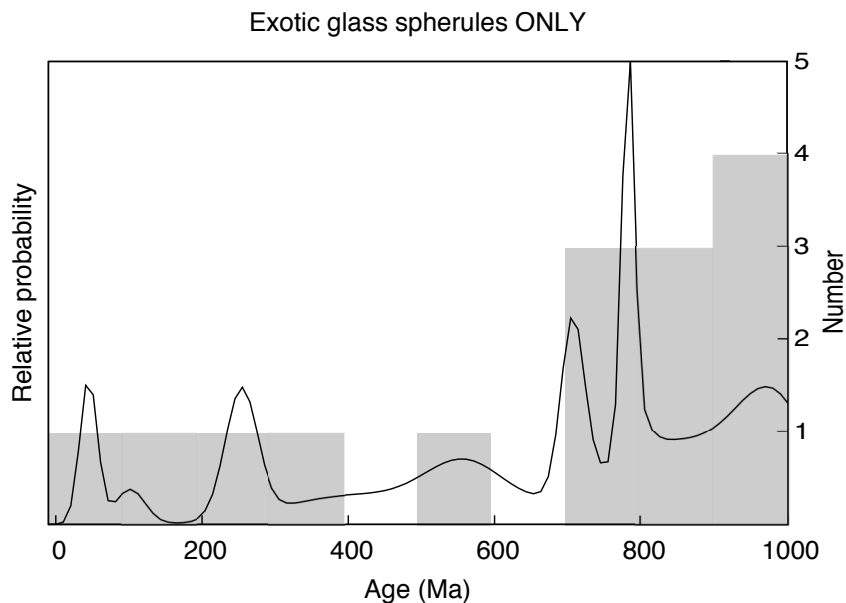


Figure 5.1.: The relative impact probability of exotic glass spherules and shards from Apollo 14259, 64501, 66041, 71501 from Zellner201540, and one age (800 ± 15 Ma) from Apollo 12 ropy glasses from Bogard1994. The black curves are the total impact probability represented by the sum of Gaussian distributions for our compiled 37 $^{40}\text{Ar}/^{39}\text{Ar}$ -derived ages of exotic glass spherules. The gray boxes are histogram of number of exotic glass spherules (number is shown on the right-hand side). The total number of $^{40}\text{Ar}/^{39}\text{Ar}$ -derived age measurements is sixteen.

14, 16, and 17 landing sites is geochemically different from the composition of Apollo 12 ropy glasses (representative of Copernicus Crater), Copernicus Crater alone is unlikely to generate glasses that derive from multiple source locations (Zellner et al., 2009). Consequently, this concurrence is mainly attributed to an increased impact flux that the formation of Copernicus Crater was one of them. However, considering that this 800 Ma-old coincidence is less investigated, we cannot easily rule out the possibility that an impact record may be affected as a consequence of the formation of Copernicus Crater. For example, Barra found that the most of their examined twenty-one coarse, non-mare fines from Apollo 12 landing site (only one mare basaltic fine is

included) experienced some degree of degassing events at 700-800 Ma (Barra et al., 2006). Barra suggested that Copernicus Crater may have directly added degassed material to a local site or its warm ejecta deposit degassed localities, yet being as part of global cratering events cannot be excluded (Barra et al., 2006).

Given the concurrence of the formation age of Copernicus Crater and the glass spherules, we feel this confusion can be better clarified by ruling out the most-likely cases that the excess of glasses with ages of $\sim 700-900$ Ma can be accounted for by the formation of Copernicus Crater. Copernicus Crater-forming event owns two possible sources of glass spherules to alter the abundance of “exotic” glass spherules occurring at 800 Ma. For such a large crater, it is expected to generate an extensive amount of melts that some of them also forms glass spherules. Melts and glass spherules are re-melting of materials that underlie the target surface of Copernicus Crater. Heterogeneity of composition of 800 Ma-old exotic glass spherules may be consistent with the fact that Copernicus Crater is sitting in a region where a diverse lithology of a lunar surface is present. For example, where Copernicus Crater situates is suggested to be covered by a relative thin mare basalt lying on the top of a thick Imbrium Basin ejecta underlain by the pre-Imbrium megaregolith materials (Schmitt et al., 1967; McGetchin et al., 1973; Pike, 1974; De Hon, 1979; Haskin et al., 2000; Jolliff et al., 2000; Gaddis et al., 2006; Bugiolacchi et al., 2011). Extensive studies of spectral reflectance analysis for the range of geological features within the interior of Copernicus Crater (e.g., central peak, sinuous melt features, fresh craters) show a diversity of compositions of olivine-bearing materials, Mg-spinel, Mg-rich pyroxene and Fe/Ca-pyroxene (Pieters, 1982; Dhingra and Pieters, 2011; Dhingra et al., 2013; Bugiolacchi et al., 2011). However, it appears at odds with how melting of different lithological materials remains un-mixed with each individual lithology.

The other most likely mechanism is via the production of impact glass spherules by a Copernicus Crater sesquinary crater population. Secondary craters are excluded because they formed by a much lower impact velocity; below the escape velocity of the Moon results in a small peak pressure and a low melt production (Schaal and

Hörz, 1980; Hörz and Cintala, 1997; Kowitz et al., 2013). Sesquinary impact craters are formed via impact ejecta that escapes a satellite, going into the orbit around the primary, and later re-impact the same satellite (Zahnle et al., 2008). Such a large impact crater like Copernicus Crater may be capable of producing sesquinary impact craters (Kreslavsky, 2017). The impact velocity of possible lunar sesquinary craters, just above lunar escaped velocity, has been suggested to be enough to produce melts that were subsequently ejected and formed melt droplets that are precursor of glass spherules (Schaal and Hörz, 1980; Hörz and Cintala, 1997; Kowitz et al., 2013). If so, Copernicus Crater-forming sesquinary craters are likely to be the first choice for a global impact spike because it takes less than 10,000 years from geocentric orbit phase to re-impact the Moon (Kreslavsky, 2017). Once ejecta entered geocentric orbit, they lose their initial configurations and re-impact the Moon randomly (Gladman et al., 1995).

In order for hypothetical Copernicus sesquinary-forming spherules to be the source of the excess of “exotic” glass spherules seen in the regolith sample, the contribution of Copernicus sesquinary-forming spherules must be able to compete with the production of spherules by large craters under the nominal constant impact flux. The production of spherules by our hypothetical Copernicus Crater-forming sesquinary craters is highly dependent on at least three observational constraints: 1) the origin locations of Copernicus Crater sesquinary-forming spherules must match with observed “exotic” glass spherules, 2) sufficient debris must be generated by the Copernicus Crater-forming event to account for the excess of “exotic” glass spherules, and 3) sufficient melt (glass) is produced by moderately low velocity that formed sesquinary craters.

We have utilized a set of models including a fragmentation code, SALES_2, (Melosh et al., 1992; Head et al., 2002; Elliott and Melosh, 2018), an N-body orbit dynamics, REBOUND, (Rein and Liu, 2012), and abundance map data acquired by Lunar Prospector Gamma-Ray Spectrometer (Prettyman et al., 2006) to investigate whether or not our assumed glass spherules produced by Copernicus Crater-forming sesquinary

craters is sufficient to account for the excess of “exotic” glass spherules. Regarding the provenance of our “exotic” glass spherules, we used chemical oxide abundance maps acquired by Lunar Prospector Gamma-Ray Spectrometer with a linear least square method to provide a numerical quantification of provenance of “exotic glass spherules in Section 5.2. In Section 5.3, we have used a fragmentation code, SALES_2, combined with an orbit dynamic code, REBOUND, to obtain the final size frequency distribution of a possible Copernicus Crater-forming sesquinary craters that could have remained on the lunar surface. For the last constraint, we used planar impact approximation to estimate maximum shock pressures for a range of impact velocity that formed sesquinary craters (see Section 5.3). We presented an overall result in Section 5.4 and concluded our study in Section 5.5.

Our modeling result shows the Copernicus-forming sesquinary craters, if exists, are no larger than 500 m in diameter. Such a sub-kilometer sizes of craters appears to be inconsistent with the estimate provenances of our compiled “exotic” glass spherules that range from few hundred kilometers to up to 900 km away from collection sites. As all of our compiled “exotic” glass spherules have an origin location at least hundred kilometers away from the sites where regolith samples were collected, it is implausible to deliver glass spherules produced by Copernicus-forming sesquinary craters to a distance of hundred kilometers. Even though glass spherules experienced a considerable amount of impact transport on the Moon, the nature of low impact of lunar sesquinary crater yields a negligible amount of melt. Essentially, the melt, if ever produced by Copernicus Crater sesquinary-forming spherules, is too scarce to compete with the spherules delivered from large, distant cratering events. Our study presented one particular scenario and have attempted to clarify the relation between the formation age of Copernicus Crater and measured ages of ~ 700 -900 Ma from “exotic” glasses. It is possible that the current understanding to the target heterogeneity of Copernicus Crater region is sufficient to account for the compositional variation of those ~ 800 Ma-old exotic glass spherules. Alternatively, a better understanding of how impact glass spherules form, as well as a characterization on the provenance

of “exotic” glass spherules regarding their source crater may be helpful in addressing the question about those ~ 800 Ma-old “exotic” glasses.

5.2 Provenance Analysis of Observed “Exotic” Impact Glass Spherules

Our observed data set was compiled mainly from the $^{40}\text{Ar}/^{39}\text{Ar}$ -derived age measurements of lunar impact glass spherules of Zellner and Delano (2015), one age data point for the formation age of Copernicus Crater from the study of Bogard et al. (1994), and three new $^{40}\text{Ar}/^{39}\text{Ar}$ -derived age measurements for this study. Our compiled “exotic glass spherules, fifteen in total, were calculated from 42 glass spherules out of 103 impact glass spherules in Zellner and Delano. This yields forty-five glass spherules in total for further quantification of provenance of a glass spherule. Those 42 spherules are younger than 1 Ga (post-Copernican age) and have an impact origin, almost no inclusions and crusty/dusty outer rims, and non-crystalline textures (Zellner and Delano, 2015). Those dated ages are inferred from $>50\%$ of released $^{40}\text{Ar}/^{39}\text{Ar}$ in which “fair” and “good” are recommended for assessment of age (Zellner and Delano, 2015). We did not include one high silica glass spherule in the Apollo 14259 regolith sample because the formation mechanism of high silica sphere is less known and perhaps different from the formation of impact glass spherules. Table 5.1 summarized the geochemical data (TiO_2 , MgO , Al_2O_3 , and K_2O), $^{40}\text{Ar}/^{39}\text{Ar}$ -derived ages with analytical errors ($\pm 2\sigma$), our estimated provenance for fifteen “exotic” impact glass spherules and one data point of Apollo 12 ropy glasses that we used for our observed data set as shown in Figure 5.1.

The exotic origin of a glass spherule has been qualitative described (Delano, 1991; Zellner et al., 2003; Zellner et al., 2009), yet a quantitative analysis of origin location of a glass spherule has not been studied. To quantify the origin location of a glass spherule, we used the concept of the nearness of distance (NOD), in which the distance is defined from where the regolith sample containing a glass spherule was collected and the region where a chemical composition acquired by Lunar Prospector Gamma-Ray

Spectrometer matches (see Table 5.1). For a given composition of a glass spherule, a larger distance inferred from the chemical oxide abundance map gives us more confidence to the interpretation of the exotic origin of a glass spherule. We performed two sets of geochemical provenance analysis for our compiled forty-five glass spherules, ternary diagram and chemical oxide abundance maps. The use of ternary diagram is sufficient to filter out local glass spherules, leaving only “exotic” glass spherules for our study. In addition, one may be concerned with a higher abundance of local glass spherules as a consequence of this hypothetical Copernicus Crater sesquinary-forming event if exists. We believe it is difficult to be resolved those local hypothetical sesquinary-forming spherules from an impact record by local glass spherules because local spherules are subject to biases (Zellner and Delano, 2015; Huang et al., 2018), and their trace element measurements are not available (Norman, 2018). For the first order approximation, we focus on “exotic” glass spherule population.

The first set of geochemical provenance analysis is ternary diagram. We plot Titanium (Ti), Magnesium (Mg), and Aluminum (Al) in a triangle-shaped diagram, where Ti and Al are specific for characterizing a target surface crust, considering that Ti and Al are the most refractory lithophile elements (Lodders, 2003). The use of Magnesium in a ternary diagram characterizes mare basaltic surface. From the top corner of a triangle-shaped ternary diagram clock-wisely, it represents Ti, Al, and Mg. The specific multipliers of 25, 3, and 1 for Ti, Mg, and Al respectively are to enlarge the chemical difference among geological materials that are plotted in a ternary diagram (Delano et al., 2007). The sum of each point in a ternary diagram for these three elements is 100%. We used the Eq. 5.1 to calculate the quantities for Ti, Mg, and Al that considers the oxide weight, element weight, and multiplier,

$$Q_{Ti,Mg,Al} = \frac{W_{TiO_2,MgO,Al_2O_3} \times EW_{Ti,Mg,Al} \times M_{Ti,Mg,Al}}{TAW_{Ti,Mg,Al}} \quad (5.1)$$

where $Q_{Ti,Mg,Al}$ is quantity for an oxide as a function of weight percent of oxide ($W_{Ti,Mg,Al}$), element weight ($EW_{Ti,Mg,Al}$), multiplier ($M_{Ti,Mg,Al}$), and the percent of

total atomic weight ($TAW_{Ti,Mg,Al}$). The element weight is to convert from the molecular weight of the oxide to the weight of the element. For the oxides of Ti, Mg, and Al, their element weights are 0.5995, 0.60317, and 0.52913 respectively. The percent of total atomic weight is the ratio of the atomic weight of the element to the total atomic weight of all elements. For the Ti, Mg, and Al of the total atomic weight, these factors are 0.4827, 0.2452, and 0.2721 respectively. Each of these three quantities must be scaled by its total sum. Equation 5.2 calculate the relative position of Ti, Mg, and Al (expressed in 100%), $P_{Ti,Mg,Al}$,

$$P_{Ti,Mg,Al} = \frac{Q_{Ti,Mg,Al}}{Q_{Ti} + Q_{Mg} + Q_{Al}} \times 100\%. \quad (5.2)$$

Using equations 1 and 2, we plotted a ternary diagram of thirty-two impact glass spherules. These thirty-two impact glass spherules contain seventeen spherules with possible local origin and fifteen spherules with possible exotic origins. The relative positions of all those “exotic” fifteen impact glass spherules in Figure 5.1 are separate from the relative positions drawn for local regolith samples (see Figure 5.2). Not only these fifteen glass spherules carry a geochemically-distinct signature to their corresponding sampling site, but also their nearly non-overlapping $^{40}\text{Ar}/^{39}\text{Ar}$ ages indicate a unique impact event. As a result, it suggests that at least fifteen independent impact events occurred in the last 1 Ga. For ~ 800 Ma ages, they were present in all four landing sites; those specific ages are 783 Ma for Apollo 14 landing site, 820 Ma for Apollo 16 landing site, 800 Ma for Apollo 12 landing site (possibly Copernicus Crater), and 774 Ma for Apollo 17 landing site. There has four impact events occurring from 800 Ma to 1000 Ma. Two impact events occurred in the recent 1 million years (spherules 7 and 301 in Table 5.1). For the rest of “exotic” glass spherules, it appears an impact occurred every 100 Ma between 100 Ma and 700 Ma ago. The overall impact frequency ~ 800 Ma ago seems higher than other periods of time. Overall, 26 out of 45 spherules are exotic origin but 11 out of 26 exotic

spherules are found geochemically and temporally associated with our 15 identified cratering events (see the Dataset in supplementary materials).

The geochemical data of glass spherules with orbital data has demonstrated informative to provide geochemical constraints to lunar local and regional geology (Spudis et al., 2002; Zellner et al., 2002; Zellner et al., 2003). Prettyman determined the elemental abundance by using gamma ray spectral un-mixing method (Prettyman et al., 2006). Although the majority of mission phases acquired data from a high altitude (100 km), Prettyman derived a high resolution data set (2 degrees per pixel, <69 km) from comparing observation data acquired at low altitude phase (30 km) with Clementine reflectance data (Prettyman et al., 2006). Using the 2-degree abundance map by LP-GRS, we performed a linear least square regression for those fifteen “exotic” spherules by comparing them to a derived elemental abundance from each pixel of Lunar Prospector Gamma Ray and Neutron Spectrometer surface map (11306 pixels in total).

For each of fifteen impact glass spherules, we exhaustively compare the glass spherule chemical abundance with any pixel in the Lunar Prospector derived surface map starting from the center of a landing site outward to the whole lunar surface. We obtained the latitude and longitude of the landing site where the corresponding regolith sample was collected and treated it as the center site where we started to calculate a linear least squares. For any neighboring pixels, we summed a difference of abundances of four chemical oxides between the sampled glass spherule and a pixel in the LP-GRS map and recorded the distance between the center site and the calculated pixel. For any pixels being equal distance from the center site, we obtained the pixel that scores the minimum difference of four chemical oxide abundances. If the four oxide abundances of this pixel, plus <2 standard deviations, fall in the four oxide abundances of the sampled spherule, the distance between the location of this pixel and the center site is defined as “the nearest distance” (NOD). If not satisfying, we moved to the next pixel where it is further from the center site.

Table 5.1.: Summary of provenance analysis and $^{40}\text{Ar}/^{39}\text{Ar}$ ages of fifteen “exotic” lunar impact glass spherules.

Spherule	TiO ₂ (wt.%)	MgO (wt.%)	Al ₂ O ₃ (wt.%)	K ₂ O (wt.%)	$^{40}\text{Ar}/^{39}\text{Ar}$ Age (Ma)	$\pm 2\sigma$ (Ma)	Landing Site	NOD (km)	Ref.
7	1.43	14.15	13.76	0.16	45	12	14	626	(Zellner and Delano, 2015)
8	1.14	6.9	17.8	0.26	825	126	14	348	This study
14	0.3	7.93	27.4	0.05	983	216	14	904	(Zellner et al., 2009)
90	1.96	4.92	24.97	0.83	783	8	14	278	(Zellner et al., 2009)
165	1.42	4.92	17.21	2.18	345	10	14	208	(Zellner et al., 2009)
191	2.18	12	17.95	0.11	1000	230	16	417	This study
438	2.55	10.04	12.5	0.72	254	22	16	835	(Zellner and Delano, 2015)
455	2.47	6.54	15.76	0.36	988	44	16	556	(Zellner and Delano, 2015)
469	2.39	6.52	14.94	0.47	559	55	16	765	(Zellner and Delano, 2015)
484	2.26	6.95	15.62	0.44	707	16	16	695	(Zellner and Delano, 2015)
493	2.55	9.85	12.69	0.27	404	100	16	556	(Zellner and Delano, 2015)
505	2.37	6.42	15.7	0.39	820	64	16	695	(Zellner et al., 2009)
530	4.5	9.6	14.45	0.11	948	54	16	348	(Zellner and Delano, 2015)
301	0.82	9.83	23.39	0.1	102	20	17	278	(Zellner and Delano, 2015)
311	1.74	11.37	10.3	0.01	774	114	17	556	(Zellner et al., 2009)
Ropy	2.24	8.11	15.9	0.85	800	15	12	400	(Bogard et al., 1994; Wentworth et al., 1994)

In addition, if fitting with all major oxides and Phosphorus (P), Thorium (Th), and Uranium (U) for our 42 impact glass spherules, we found the estimated provenances of all glass spherules are far away from a landing site. It should not be the case for some local origin glass spherules because some glass spherules from the observed data set in this study are geochemically similar to a local regolith samples. Although this may be caused by a parameter over-fitting problem, it appears that using these four chemical oxides is sufficient to characterize the provenance of a glass spherule.

We noted that the provenance characterization of using only four chemical oxides may seem simple in comparison to the source crater identification of microtektites, a terrestrial analogue of lunar glass spherules. The source crater identification for microtektites uses a thorough analysis of major, trace elements and isotopes for target materials by which the source crater formed. However, the lunar surface composition is relatively straightforward. For example, the lunar nearside, where glass spherules used in our study collected, is dominated by KREEP signature while the lunar farside is essentially free of KREEP except for South Pole-Aitken (Jolliff et al., 2000). Although the measurements of Th and U for these fifteen lunar glass spherules are unavailable, the measurements of potassium oxide (K_2O) must be performed for $^{40}Ar/^{39}Ar$ -derived ages of glass spherules. Based on our provenance analysis, we suggest that the abundance of K_2O may be a potential candidate for distinguishing the origin of a glass spherule from a lunar surface.

One may also concern the chemical volatility of potassium element. Because potassium is considered moderately-volatile, its abundance would have been reduced by cratering-related process, such as bubble striping due to a high acceleration and diffusion from interacting with impact vapor (Folco et al., 2010b; Folco et al., 2010a; Melosh and Artemieva, 2004; Moynier et al., 2010). In fact, the abundance of K_2O for Australasian microtektites decreases with increasing distance from a proposed source crater (Folco et al., 2010b; Folco et al., 2010a). We neglected any reduction of potassium oxides by cratering process because the amount of impact vapor as well as acceleration rate on Moon are not as large as they are on Earth.

Our calculation result shows that seventeen out of our compiled 42 impact glass spherules including three new spherules can match the derived LP-GRS surface map within 2 pixels (<150 km), suggesting a local origin for those 17 spherules. On the other hand, twenty-five glass spherules are suggestive of exotic origin. Only fifteen impact glass spherules are possibly a representative of 15 independent impact events. For example, spherules 455 and 207 show a similarity in ages and geochemistry data (almost overlapped in ternary diagram). Table 5.1 shows the estimations of the nearest distance for the provenance of those fourteen spherules. The NODs of majority of exotic spherules (10 out of 15) are >500 km away from the landing site. Only two glass spherules are truly highland-derived (spherules 14 and 311), but many of them appear to originate in highland/mare boundaries (Zellner et al., 2003). It suggests the composition of glass spherules is nearside-origin that highland and mare basalt materials are well-mixed.

Regarding the specific provenance of our calculation result, several estimated provenances are associated with rayed craters. For example, spherules 505 and 438 are estimated to come from Mösting Crater (26 km in diameter); spherule 505 has an age around 820 Ma, and the age of spherule 438 is 254 Ma. Spherule 493 is close to Crater Triesnecker (26 km in diameter), appearing to be a rayed crater. The age of spherule 493 is 404 Ma. Mösting and Triesnecker Craters are about 60 radii from the Apollo 16 landing site. Spherule 165 collected from Apollo 14 landing site is close to a fresh, unnamed rayed crater. The diameter of this crater is ~12 km, and ~25 radii away from the Apollo 14 landing site. The age of spherule 165 is 345 Ma. Spherule 530 is close to Dionysius Crater, 17 km in diameter, that develops a dark ray pattern (Giguere et al., 2006). The age of spherule is 102 Ma. Dionysius Crater is 40 radii from Apollo 16 landing site. Spherule 7 from Apollo 14 landing site is close to Herigonius Crater (15 km in diameter), appearing to be a faint rayed crater. The age of spherule 7 is 45 Ma. It is unlikely since 45 Ma old crater would have prominent rays.

We considered how plausible all our compiled 800 Ma-old exotic glass spherules could have formed from melting subsurface materials of Copernicus Crater. To investigate this question, we compiled the samples that could best represent Copernicus Craters melts and its subsurface lithology. Apollo 12 mare basalts, soils, ropy glasses, KREEP melt breccias (KREEP glass fragments, Apollo 12 gray-mottled breccias and Imbrium-like melt breccias), and highland like materials serve as representatives of melts and subsurface lithology of Copernicus Crater (Figure 5.2). Those samples provide a constraint to the mixing ratio of subsurface materials upon melting during the formation of Copernicus Crater. First of all, the straightforward consideration is about whether any of our compiled 800 Ma-old exotic glass spherule could match the Apollo 12 ropy glasses that are thought to have originated from Copernicus Crater. The assignment of the origin location of Apollo 12 ropy glasses to the Copernicus Crater is reasonable because the composition of ropy glasses falls within one standard deviation of chemical oxide abundances for the center region of Copernicus Crater. The match between the composition of Apollo 12 ropy glasses and the spacecraft-derived compositions of center region of Copernicus Crater suggests a well calibration data of LP-GRS performed by Prettyman and supports the Copernicus Crater provenance for Apollo 12 ropy glasses. We found only spherule 505 shares a similar origin of Apollo 12 ropy glasses and is ~ 820 Ma-old. In addition, we noted that the prescribed provenance for Apollo 12 ropy glasses points out a limitation of Nearness of Distance method. The linear least squares method implemented with the concept of Nearness of Distance is programmed to score the nearest pixel of the abundance maps that satisfies the composition of a glass spherule, neglecting the regions farther away from the center site that may also match the composition of a glass spherule. For example, our estimate NOD for the origin location of Apollo 12 ropy glasses is 200 km, but the prescribed origin location of Copernicus Crater for the ropy glasses is 400 km from Apollo 12 site.

Like Apollo 12 ropy glasses, Copernicus Crater-forming spherules must have derived from the materials from its subsurface structure, in which the stratigraphy of

Copernicus Crater consists of local regolith, mare basalt, Imbrium Basin ejecta, and pre-Imbrium megaregolith materials (Schmitt et al., 1967; McGetchin et al., 1973; Pike, 1974; De Hon, 1979; Haskin et al., 2000; Jolliff et al., 2000; Gaddis et al., 2006). Figure 5.2 shows the ternary diagram with the relative positions of all our exotic glass spherules and representative samples for the stratigraphy of Copernicus Crater. Regarding the members of the stratigraphy of Copernicus Crater, its youngest member is local regolith and is represented by Apollo 12 regolith samples (Apollo 12 ropy glasses and Apollo 12 KREEP glass fragments are also included in this category for clarity) (Laul and Papike, 1980; Morris et al., 1983; Wentworth et al., 1994; Meyer et al., 1971). Underneath the local regolith is relatively thin mare basalts (De Hon, 1979), in which their thickness and iron content inferred from Clementine UV/VIS reflectance measurements on the crater walls of Copernicus Crater are suggested to decrease from the southern wall to the northern wall of the crater interior (Pieters et al., 1994). Four types of mare basalts collected from the Apollo 12 landing site include olivine, pigeonite, ilmenite, and feldspathic basalts (Papike et al., 1976; Rhodes et al., 1977; Neal et al., 1994), assuming as a possible mare basaltic layer in the region Copernicus Crater in this study. It is noteworthy that the low content of Ti in Apollo 12 mare basalts is consistent with the estimated abundance of Ti for Procellarum Oceanus Terrane from Clementine UV/VIS camera (Lucey et al., 2000).

Imbrium Basin ejecta likely covered the majority of the lunar nearside, including the region of Copernicus Crater (Haskin et al., 2000; Jolliff et al., 2000). Despite an active debate regarding the association of a KREEP melt breccia with a specific basin (e.g., Imbrium Basin) (James and Wright, 1972; Stöffler et al., 1985; Norman et al., 2010; Merle et al., 2014), we avoided KREEP impact melt breccias, in particular collected from Apollo 15 and 17 landing sites due to a uncertainty on their association with other basins (Deutsch and Stöffler, 1987; Stadermann et al., 1991; Dalrymple and Ryder, 1993). We focused on the data of Apollo 14 and 16 KREEP melt breccias that have been recommended in the literature for a possible candidate of Imbrium Basin ejecta as our representative of Imbrium Basin ejecta layer underneath

the region of Copernicus Crater (Tera et al., 1974; Norman et al., 2010). Apollo 14 KREEP samples numbers include 14063, 14078, 14276, and 14310. Most importantly, we specifically chose the data on the bulk composition of melt in a melt breccia. The reason for this selection is that if those 800 Ma-old exotic glass were formed from the substrate of Imbrium basin ejecta, the melting of Copernicus Crater forming event would have homogenized this compositionally-heterogeneous substrate. This is reasonable assumption for the case of impact-generated melt breccia because the matrix (melt) that binds fragments were formed from melting local substrate materials. For comparison, we also compiled the bulk chemical composition data of Apollo 16 low Fra-Mauro KREEP (LFMK) melt breccia samples that are thought to be brought from Imbrium Basin forming event (Korotev, 1994, sample No. are 60315, 62235, 65015, and 63355 in 1M and 1F types of Table 2). The $^{40}\text{Ar}/^{39}\text{Ar}$ -derived age measurements for the sample 60315, 62235, and 65015 are similar to the proposed age for Imbrium Basin, however, it is still challenging to tell whether or not those LFKM melt breccias were produced by Imbrium Basin (Norman et al., 2006).

For the lowest member of stratigraphy of Copernicus Crater, the data of ferroan anorthosites (FANs), feldspathic lunar meteorites, Mg-suite, and local Apollo 16 glass spherules are considered. In general, Figure 5.2 shows that the compositions of ~ 800 Ma-old exotic glass spherules lie in between Apollo 12 mare basalts and Apollo 16 local regolith. Despite the small number of our data, the composition of ~ 800 Ma-old exotic spherules uniformly spreads over a mare-like Apollo 12 site and a highland-like Apollo 16 site, suggesting a continuous mechanical mixing and material transport between the highland and mare over time (Huang et al., 2017). The provenance of spherules 505 and 455 collected from Apollo 16 site are closer to the provenance of Apollo 12 mare soils and ropy glasses. Specifically, spherules 505 and 455 including Apollo 12 soils and ropy glasses are of high KREEP Fra Mauro affinity (HKFM) (Naney et al., 1976; Ridley et al., 1973; Zeigler et al., 2004) that is thought to be exotic to Apollo 16 landing site (Zellner et al., 2003). The provenance of spherule 311 collected from Apollo 17 landing site lies in between the provenances of very low-Ti

(VLT) mare basaltic fragments found at Apollo 17 landing site and Apollo 12 mare basalts, suggesting a mare origin. The abundance of very low-Ti mare basalts in Apollo 17 landing site (present in lithic fragments instead of whole rocks) is scarce but not uncommon at the lunar surface (e.g., Mare Imbrium) (Vaniman and Papike, 1977; Giguere et al., 2000). Either Apollo 17 very low Ti basalt-origin or Apollo 12 mare basalt-origin suggest the exotic origin of spherule 311. The direct comparison of major element and trace elements (Na₂O and K₂O) between spherule 311 and Apollo 17 VLT mare basalt and Apollo 12 mare basalts shows that the contents of Na₂O and K₂O of spherule 311 are lower than Apollo 17 VLT and Apollo 12 mare basalts, but the content of TiO₂ in the spherule 311 is higher than the content of TiO₂ of Apollo 17 VLT basalts and lower than the content of TiO₂ of Apollo 12 mare basalts. The provenance of spherule 8 is near to the provenance of our compiled Imbrium-like KREEP melt breccia. However, the amount of FeO of spherule 8 (15 wt%) differs from the contents of average Apollo 14 KREEP melt breccias (5-9wt%). Spherule 14 is evidently highland-origin; its provenance is closer to the provenance of feldspathic lunar meteorites. Finally, the provenances of spherules 90 and 191 is challenging to be interpreted; the spherule 191 appears to closer to the mare and highland mixing boundary as show in Figure 5.2.

Lastly, we noted that a particular set of Apollo 12 samples, gray-mottled KREEP breccias (Anderson Jr et al., 1971) or light-colored particles (Meyer et al., 1971; Marvin et al., 1971), shows a wide range of variation in ternary compositions (Figure 5.2). Those gray-mottled KREEP breccias (Anderson Jr et al., 1971) also sometimes refer to orthopyroxene-plagioclase assemblage that are commonly attached to Apollo 12 ropy glasses (yellow-brown glasses) (Meyer et al., 1971) or Type A norite-anorthosite (Wood, 1972). The gray-mottled KREEP breccias must be brought from a cratering event because the anorthositic origin is evidently exotic to Apollo 12 site. Gray-mottled KREEP breccias attached to brown-yellow glasses are suggested to have not recrystallized and remained pristine mineral textures but assembled by a violent excavation of coarse-grained anorthositic bedrock, possibly Imbrium event (Marvin

et al., 1971). Because inclusions in Apollo 12 ropy glasses are noritic and basaltic in nature, Marvin suggested the mixture of both materials (gray-mottled materials and mare basalts) form ropy glasses from Copernicus Crater event. Figure 5.2 shows that Apollo 12 ropy glasses and Apollo 12 KREEP glass fragments have a narrow variation in ternary compositions than gray-mottled KREEP breccias. Although the composition of our compiled 800 Ma-old exotic spherules fall in between our prescribed stratigraphy of Copernicus Crater, it is challenging to reconcile with a seemingly small amount of mixing between our prescribed substrate materials for the region of Copernicus Crater. Overall, it appears that each of our compiled 800 Ma-old exotic spherules is better to be described by a specific substrate that is used to model the stratigraphy of Copernicus Crater without invoking a mixing process between different substrate materials.

5.3 Materials and Methods

One of our ultimate goals in this study is to see that under a constant impact rate how prominent an impact record that contains our hypothetical spherule population is compared to an impact record without this population. In the following Materials and Methods section, we investigated if Copernicus Crater-forming event and possible sesquinary craters could contribute to some portion of “exotic” glass spherules. The fraction of those sesquinary-forming glass spherules would determine if Copernicus Crater-forming sesquinary craters can make up the abundance of ~ 800 Ma-old “exotic” glass spherules seen in Apollo regolith samples. If too small, it suggests the excess of ages at ~ 700 - 900 Ma of “exotic” glass spherules may be predominantly produced by primary craters. If primary craters are responsible for the excess of ages of ~ 700 - 900 Ma-old exotic glass spherules, it may imply an increase in a lunar impact flux over the last 1 Ga. Furthermore, the coincidence of the formation age of Copernicus Crater and ~ 700 - 900 Ma-old ages from exotic glass spherules can be clarified.

In order to obtain a reasonable model for our hypothetical glass spherule population of Copernicus Crater sesquinarries, we generated the size frequency distribution (SFD) of a possible Copernicus Crater’s sesquinarries and then adopted some assumptions to estimate the production of melt and glass spherules. Using two independent sets of models, an impact fragmentation code, SALES_2, (Melosh et al., 1992; Head et al., 2002; Elliott and Melosh, 2018) and an N-body orbit dynamics, REBOUND, (Rein and Liu, 2012), allow us to obtain a plausible SFD of Copernicus Crater’s sesquinarries (see Section 5.3.1). Given that the size and ejection velocity of fragments are relatively known, we can approximate a glass spherule production of a sesquinary crater. Assume the sesquinary craters, on the order of hundreds of meters, are a low velocity impact formed in a porous target. Melt production in low velocity impact and porous target is still a work in progress, yet we applied knowledgeable constraints from the literature to the production of our hypothetical sesquinary-forming glass spherule (see Section 5.3.2). Indeed, our calculation shows a negligible fraction of Copernicus Crater-forming sesquinary craters are able to produce melt. Such a negligible amount of melt generated by Copernicus Crater-forming sesquinary craters suggests that the source of excess of “exotic” glass spherules must be more than Copernicus Crater-forming event, including its sesquinary craters if exists.

5.3.1 A possible size frequency distribution of Copernicus Crater-forming sesquinary craters

To compute Copernicus Crater-forming sesquinary crater distribution, we obtained the fraction of ejecta from Copernicus Crater that initially escapes the Moon and later re-impacts the Moon (see Table 5.2) and estimated the total mass and number of ejecta fragments that become Copernicus Crater-forming sesquinary craters. For the second estimation, we used a hybrid approach of the SALES_2 and iSALE codes to estimate the total amount of escaped ejecta in terms of size frequency distribution of fragments (Elliott and Melosh, 2018). For a given location of a cell in

Table 5.2.: Summary of REBOUND simulation result on the fraction of our 1000 test particles remaining in geocentric orbit system of Earth and Moon.

Launched velocity (km/s)	Moon (%)	Earth (%)	Escaped (%)
2.4	3.9	1.4	94.7
2.5	1.9	7.0	91.1
2.6	0.9	18.2	80.9
2.8	0.7	13.6	85.7
3.0	0.2	2.6	97.2
3.2	0.0	0.5	99.5

SALES_2, SALES_2 computed the damage accumulation of the cell and estimated the ejection velocity of a fragmented cell (Melosh et al., 1992). We were able to obtain a relation between ejection velocity and fragment size for Copernicus Crater. The impact conditions for Copernicus Crater simulation uses 7 km diameter basaltic impactor with the impact velocity of 10 km/s to vertically impact the basaltic target material. The largest fragment size is ~ 120 m in diameter, and the mean fragment size is 4–5 m in diameter. The total number of fragments larger than 5 cm in diameter is $\sim 10^{15}$ (see Figures 5.3 and 5.4).

Then, the orbital dynamic simulation using the Python and C++ based code, REBOUND (Rein and Liu, 2012), is to examine the fraction of escaped material at a given launch velocity that later comes back to the Moon. For each run with the same random seed and a given launch velocity (2.4 - 3.2 km/s), we distributed 1000 test particles uniformly 1 km above the lunar surface with velocity radiating from the Moon. The position and velocity of massive bodies (the Sun, Earth, and Moon) refer to the J2000 date from Jet Propulsion Laboratory HORIZON database. We found that for test particles launching at 2.4 km/s $\sim 4\%$ of them came back to the Moon, and 1-2% of them hit Earth within 160 years. Beyond 2.4 km/s, less than 2% hit the Moon, and the fraction of test particles hitting Earth increases until the launched

velocity reaches 2.6 km/s. Our calculations as shown in Table 5.2 are consistent with the previous estimates (Gladman et al., 1995; Kreslavsky, 2017). For ejecta launched at velocity larger than 3.2 km/s, the fraction of ejecta fell back to Moon is neglected. With the fractions of escaped ejecta that fall back to Moon, the impactor size frequency distribution for our model Copernicus Crater sesquinary craters can be determined. We applied the fractions of escaped ejecta with different velocities from REBOUND simulation to the size frequency distribution of fragments from SALES_2 simulation.

Figure 5.5 shows the sesquinary crater size frequency distribution for our model Copernicus Crater-forming debris population. We used π -group scaling laws to convert the mean fragment sizes that we combined REBOUND simulations with SALES_2 simulation result to the crater sizes. For any given cell in our SALES_2 simulation, we can obtain the number of fragments and mean ejection velocity in a cell. We counted the fragmented cells ejecting at above lunar escape velocity and obtained an impact velocity distribution. When converting to a crater size, we randomly drew from this impact velocity distribution. The range of the impact velocity distribution is the same as the range of launched velocities for REBOUND simulation (2.4 km/s - 3.2 km/s). It is reasonable to use the same launched velocity as the re-impacted velocity of a test particle because we found the re-impacted velocities are only few 10 m/s of difference of the initial launched velocity (we tested at least for the 100 test particles). An impact velocity is randomly drawn from the impact velocity distribution constructed from the fraction of our 1000 test particles that re-impacted the Moon. Our final size frequency distribution of Copernicus Crater's sesquinary craters is close to the total production of primary craters generated over 0.1 Ma using the Neukum Production Function, yet the SFD of craters >200 m in diameter decreases rapidly. The impact rate caused by a possible Copernicus Crater-forming debris is the number of ~ 4 for craters >10 m in diameter over the area of 1 km^{-2} during tens of thousand years.

5.3.2 A possible glass spherule production of Copernicus Crater's sesquinar- ies

Considering orbital dynamics of Copernicus Crater-forming ejecta that escaped the Moon, the remaining debris population that re-impacts the Moon appears equivalent to the production of primary craters over 0.1 Ma under a constant impact rate. Although the total number of sesquinary craters appears lesser than the total number of primary craters that have been generated over 800 Ma, it is still interesting to see how this impact record affects a bombardment record generated by primary crater-forming glass spherule populations. Regarding low impact velocity in the formation of lunar sesquinary craters, we noted that the production of glass spherules by sesquinary craters is highly variable.

Physical parameters of impact velocity and target properties are critical to determine if an incipient melting during cratering process can occur. In principle, as the impact velocity increases, the shock pressure intensifies. When a shock pressure reaches a certain threshold, a melting occurs. This critical shock pressure of incipient melting for a given material is of interest experimentally and theoretically. In experimental approach the measurement of critical shock pressure for incipient melting was performed using a single crystal. The experimental critical pressure for a single quartz crystal is 30 GPa. To our interest, the lunar surface and subsurface where tens of meter sized sesquinary craters form should be porous. Porous target can lead shock waves to decay faster, but as a result of collapse of pores within the material the shock pressure was observed to exceed the initial pressure. Therefore, it has been suggested that the critical pressure required for melting in a porous target is lower than the critical pressure melting non-porous materials (Wünnemann et al., 2008). Recently, the laboratory experiment and meso-scale numerical simulation in a low pressure range between 2.5 and 17.5 GPa in a dry, porous sandstone (20–30% of porosity) suggest a reduction in a critical pressure for incipient melting (kowitz2013diaplectic). They

found initial melting occurs as low as 5 GPa, and up to 80 vol.% of glass is produced when a shock pressure reaches 17.5 GPa.

We used planar impact approximation to estimate a peak pressure for impact velocities in a range of 2.4 km/s and 3.2 km/s. Planar impact approximation assumes an infinite slab with thickness equivalent to the diameter of a projectile impacts into a half space of a target surface. Applying a linear relation between shock wave velocity and particle velocity into Hugoniot's conservation equations, the simplest solution of a maximum shock pressure, assuming the same density of target and projectile, can be obtained (Melosh, 1989, Section 4.5), P_0 ,

$$P_0 = \rho u_{sh} u_p \quad (5.3)$$

where the particle velocity, $u_p = \frac{1}{2}v_{imp}$, is the half of an impact velocity of a projectile, the shock velocity, u_{sh} , is approximated by a linear relationship with the particle velocity, $u_{sh} = c + su_p$, in which the parameters of c and s are empirical-derived constants. The constant, c , is the intersection value at y-axis of the Hugoniot's curve in the particle velocity and shock wave velocity space (the unit is m/s), and the constant, s , is the slope of a roughly straight line between the particle velocity and shock wave velocity. If a target is porous, shock wave velocity is slower than the shock velocity in nonporous target for a given particle velocity. The constants of c and s for a porous target are needed to derive from shock experiments. GÜldemeister conducted a series of numerical experiments to study the porosity effect on a reduction of shock pressures. For their numerical samples with 20% of porosity and $\sim 1955\text{--}2297.0 \text{ kgm}^{-3}$ of density (GÜldemeister et al., 2013, Figure 12), the constant of c is estimated ~ 500 m/s, and the constant of s is roughly 3.17. Although applying these constants that were derived from shock experiments tested on terrestrial porous material to a lunar surface may seem arbitrary, it only serves the first order approximation for estimating melt and glass spherule production of our hypothetical sesquinary crater population.

Assuming a vertical impact, we obtained the maximum shock pressures of 11–20.4 GPa for the range of impact velocities between 2.4 and 3.2 km/s respectively.

If using the 30 GPa for criteria of incipient shock melting, none of our hypothetical sesquinary craters can produce melts, as well as glass spherules. Yet, Kowitz reported that up to 80% of melts was observed as the shock pressure applied to samples reaches 17.5 GPa (Kowitz et al., 2013). We feel reasonable to investigate the case where sesquinary craters were generated by the highest impact velocity, 3 km/s. For this impact velocity, there is still a very small fraction of escaped ejecta, 0.2%, that formed sesquinary craters. For impact velocity smaller than 3 km/s, a larger fraction of escaped material came back and hit the Moon but considering the inefficiency of melt production we neglected the escaped material ejected at <3 km/s. We calculated a conservative melt volume from a volume that is shocked from peak pressure (18.1 GPa) to the pressure of 17.5 GPa using a semi-analytical Gamma model for estimating the decay of shock pressure (decay exponent is -2.85),

$$17.5GPa = 18.1GPa \left(\frac{r}{r_{imp}} \right)^{-2.85} \quad (5.4)$$

where r_{imp} is the radius of a projectile, and r is the distance from the radius of a projectile to a point where the pressure of 17.5 GPa is reached. In fact, the thickness of shocked volume between 17.5 GPa and 18.1 GPa is $\sim 1\%$ of a projectile's radius. The exponent of -2.85 yields a faster decay of shock pressures, derived from fitting numerical shock pressure data in CTH and iSale simulations (Pierazzo et al., 1997; Monteux and Arkani-Hamed, 2016; Ruedas, 2017).

More importantly, the form of impact-generated melts produced by these low impact velocity sesquinary craters may not be melt droplets (glass spherules) even though the impact velocity of 3 km/s can produce melts. To investigate whether melts, forming in a porous surface, low impact velocity, is as the same as glass spherules produced by hypervelocity impact, we estimated the ejection velocity distribution of possible sesquinary-forming melts. Ejection velocity of impact-generated

melt products are critical; because melts behave like a liquid, for a high traveling speed the liquid breaks up to minimize its surface tension energy. In the field observation, it appears that the shapes and sizes of impact-generated melt products vary as a function of distance from where they were collected. For example, for a sufficiently large crater, the melt body partially filled up the cavity of a crater, and individual melt products with the range of sizes from centimeters to microns are common through ejecta deposits. An empirically-derived model primarily based on terrestrial melt products suggests a linear relationship between the sizes of melt products and the distances where melt products were collected from the center of a crater; the larger the melt products the nearer the distance to the center of a crater (Huang et al., 2018). They found lunar impact glass spherules are most efficiently to be produced at distances beyond 20 radii from a crater's center.

Assuming sesquinary craters formed in a porous surface, the porosity of a target surface can be a significant contributor to reduction in ejection velocity, therefore leading a slower ejecta upon a crater excavation. We adopted an equation derived empirically from π -group scaling laws and experiment work of Housen and Holsapple on weakly cemented basalts (porosity is 20%) (Housen and Holsapple, 2011, Table 3),

$$v_{ej} = C_1 v_{imp} \left[\frac{r}{r_{imp}} \left(\frac{\rho_t}{\rho_{imp}} \right)^\nu \right]^{-1/\mu} \quad (5.5)$$

where v_{ej} is the ejection velocity of ejecta generated by a sesquinary crater-forming event, C_1 , ν , and μ are constants determined from experiments for weakly cemented basalt, 0.18, 0.4, and 0.46 respectively. Assume the same density for a projectile and a lunar surface, impact velocity of 3 km/s, the maximum ejection velocity, 540 m/s ($C_1 v_{imp}$), occurs where ejecta is close to the edge of a projectile; this region is also where the most of melts is produced. Due to a low impact velocity, the generation of impact vapor appears implausible but the ejection velocity of melts within the distance of 1% of a projectile's radius from the impact center ranges in 526 and 540

m/s. This further suggests that those melts are likely in the form of melt droplets regardless of scarcity of possible glass spherules.

5.4 Results and Discussion

Ultimately, we are interested in how the total abundance of glass spherules for this hypothetical sesquinary crater population across the lunar surface is compared with the abundance of glass spherules generated by primary craters. Assuming the shocked zone between 17.5 GPa and 18 GPa is melted (see Eq. 5.4), the fraction of our defined melted zone should be ejected considering a residual particle velocity as a consequence of shock rarefaction (Melosh, 1985). Using Maxwell Z-model, the volume of ejected melts where a thin-shell shocked volume overlaps with an excavation flow can be analytically estimated. Previous empirical data on the spatial distribution of terrestrial microtektites suggests ejected melts at such distances (~ 150 km) for sub-km sized craters are likely to be in the form of glass spherules. We considered fragment larger than 5 cm that were ejected at the velocity ranging from 2950 to 3050 m/s and re-impacted to the Moon; we set 5 cm as the cutoff size of fragments to converse mass from our SALE_2 simulation result.

In addition, we took into account the impact angle on the fraction of sesquinary craters launched from 2950 to 3050 m/s in terms of melt production. We considered only sesquinary craters that produce peak pressure higher than a critical pressure for melting in the 20% porosity of target. The total volume of glass spherules according to our definition for this population is ~ 1200 m³. If we average this total glass spherule volume over the lunar surface, the number density of glass spherules with the prescribed size of 200 μ m in diameter per meter square is less than one spherule. Regarding the abundance of our defined glass spherule generated by primary craters under a constant impact rate, we used the root mean squared value of impact velocity for Moon, 18.3 km/s (Yue et al., 2013), and 45° of impact angle for all impactor larger than 5 cm in diameter (hard rock scaling law for transient crater size estimates: μ

$= 0.55$, $\rho=2500 \text{ kg/m}^3$). We found that the volume of our defined glass spherules is $\sim 134 \text{ m}^3$ for 3 years-long impact bombardment across the lunar surface. For 3 years under Neukum Production Function, the lunar surface received one largest crater with the size of $\sim 50 \text{ m}$ in diameter.

Regarding the relative contribution of sesquinary craters to “exotic” glass spherules, only a negligible fraction of 0.1 Ma-long bombardment of sesquinary craters produce melts. The total amount of sesquinary-forming glass spherules is approximately the total abundance of glass spherules produced by 3 year-long bombardment resulting from impactor population with diameter of $>5 \text{ cm}$. Based on this estimate, our sesquinary-forming glass hypothesis is considered unsatisfying because it conflicts with each of our three main observational constraints. For the first observational constraint, we demonstrated that the origin locations of our compiled fifteen “exotic” glass spherules are at least few hundred kilometers away from where regolith sample were collected. Take 200 km at face value, the largest diameter of sesquinary craters from the results of SALES_2 and REBOUND simulations, 500 m, is 800x crater radii away from a collection site. At this far distance, the ejecta thickness for $\sim 500 \text{ m}$ sized crater in diameter is estimated roughly $1 \mu\text{m}$ using an empirical power law relation between ejecta thickness and radial distance from a crater center (McGetchin et al., 1973). The distribution of glass spherules for the majority of sesquinary craters ($\sim 10 \text{ m} - 100 \text{ m}$) remains much more localized than sub-kilometer sized sesquinary craters. If exists, the origin of the majority of sesquinary-forming spherules is considered local. Thus, at the first glance, the Copernicus Crater-forming sesquinary craters cannot be responsible for the excess of ages of $\sim 700\text{-}900 \text{ Ma}$ measured from “exotic” glass spherules.

Even though our hypothetical Copernicus Crater sesquinary-forming spherules are expected to be not exotic initially, our second and third observational constraints raise a possibility that those sesquinary-forming spherules may become exotic during an 800 Ma-long post-Copernican bombardment. If sesquinary-forming spherules from Copernicus Crater event were sufficient, one cannot neglect the impact-driven transport

process of spherules during a post-Copernican bombardment. A complex exposure history of cratered materials is common at a lunar surface as revealed from returned lunar samples. For example, the Apollo 14 regolith breccia sample, 14315, contains multiple generations of microbreccia with varying abundance of KREEP material from highland basalt to high KREEPy (Wentworth and McKay, 1991). However, as the impact velocity that forms sesquinary craters is much lower than heliocentric velocity for primary crater population (almost one magnitude order larger from the lunar escape velocity), the primary crater-forming spherules outnumber sesquinary-forming spherules. If the simplifying assumptions for the estimate of melt production are correct, our sesquinary hypothesis also cannot satisfy the second and third observation constraints. As a consequence of unsatisfying explanations, the excess of ages of ~ 700 - 900 Ma for “exotic” glass spherules may remain puzzling. Under a particular scenario of Copernicus Crater-forming sesquinary craters we proposed in this study, we minimally clarified the concurrence of the formation age of Copernicus Crater and the excess of ~ 700 - 900 Ma ages of “exotic” glass spherules.

Our result does not support that Copernicus Crater-forming sesquinary crater contributes to the excess of 800 Ma-old “exotic” glass spherules. This finding may be reasonable because we did not see an excess of ages at ~ 100 Ma that coincides with the proposed formation age of Tycho Crater. A younger, similar sized Tycho Crater (85 km in diameter) would produce a sufficient amount of ejecta debris like Copernicus Crater. If Copernicus Crater-forming sesquinary craters are efficient at producing glass spherules that contribute to observed 800 Ma-old “exotic” glass spherules, Tycho Crater sesquinary craters should do the same. Because our compiled $^{40}\text{Ar}/^{39}\text{Ar}$ -derived age distributions of “exotic” glass spherule only spike at ~ 800 Ma, not 100 Ma, it suggests that either we have an insufficient number of samples to address this inconsistency or physical properties of target surfaces where Copernicus Crater and Tycho Crater formed are different, or sesquinary-forming glass spherules generated from craters as large as ~ 100 km in diameter are negligible. From our study, the abundance of sesquinary-forming glass spherules on Moon is suggested to

be negligible, at least for the size of Copernicus Crater, due to a low impact velocity of lunar escape velocity. However, for larger terrestrial planets such as Mars the martian escape velocity of 5 km/s is readily for incipient melting (Wünnemann et al., 2017). With more production of impact melts, the ejected volume of impact melts also increases. Thus, the abundance of post-cratering induced glass spherules on other celestial bodies, such as Mars, may not be neglected.

Possibly, Copernicus Crater-forming event alone may be sufficient to explain the excess of ~ 700 -900 Ma ages of “exotic” glass spherules. Considering a Copernicus Crater ray passing through the region of Apollo 12 landing site, it is expected that we have sampled Copernicus Crater-forming melt products (Apollo 12 ropy glasses). As slaggy, ropy glasses with mm-to-cm sizes predominate in the Apollo 12 landing site relative to other Apollo landing sites, the glass spherule population of Copernicus Crater-forming event may be also present at a lunar surface. The glass spherule population of Copernicus Crater-forming event have not been reported yet. Interestingly, our provenance analysis for the average composition of Apollo 12 ropy glasses (Wentworth et al., 1994, Table 4) match with the chemical oxide abundances within one standard deviation that are obtained from the center region of Copernicus Crater acquired from Lunar Prospector Gamma-Ray Spectrometer. We compared the composition of each of our compiled thirty-four glass spherules to the spacecraft-measured composition of center region of Copernicus Crater (within one standard deviation). Among ~ 700 -900 Ma-old exotic glass spherules, we found spherule 505 from Apollo 16 landing site is potentially a candidate for Copernicus Crater-forming glass spherules. If the glass spherule 505 were generated by Copernicus Crater-forming event, this reduces the magnitude of relative impact probability at ~ 700 -900 Ma from 6 impacts to 5 impacts. We also investigated how mixing prescribed substrate materials underneath the region of Copernicus Crater can account for the compositional diversity of ~ 800 Ma-old glass spherules. Unfortunately, we were unable to draw a conclusion due to the lack of understanding in the formation of impact glass spherules under the condition of a heterogeneous target surface (e.g., Copernicus Crater).

To conclude, we believed that our null result clarifies the coincidence of the formation age of Copernicus Crater and ~ 800 Ma-old “exotic” glass spherules. This coincidence may be correlated with a global increase in a lunar impact flux during post-Copernican period, but the production of ~ 800 Ma-old “exotic” glass spherules are less likely to be associated with the formation of Copernicus Crater or post-Copernicus Crater-forming event (sesquinary-forming glasses in this study). This further implies that each of ~ 800 Ma-old “exotic” glass spherules may represent a primary cratering event. In particular, spherule 14, 505, and 311 from Apollo 14, 16, and 17 landing sites respectively are estimated to have derived from a region that is greater than 500 km away. Spherule 14 and 311 are likely to be true highland basalt-origin (not derived from mare and highland boundaries), and spherule 505 are high KREEP origin. Based on our provenance analysis for exotic glass spherules, spherules 14 and 311 are found not associated with a rayed crater in highlands, while the provenance of spherule 505 at a lunar surface is estimated to be near to a 26 km sized Mösting Crater with faint rays. Besides of ages at ~ 800 Ma, other “exotic” glass spherules are in a wide range of $^{40}\text{Ar}/^{39}\text{Ar}$ -derived ages from 45 Ma to 988 Ma. This indicates that the mechanism of “exotic” material transport has at least continued for ~ 1 Ga. The exact transport history of each “exotic” glass spherule may remain unknown, yet it appears that this kind of “exotic” material transport occurs quite often as they are not uncommon in returned lunar samples. As primary craters, not sesquinary or secondary craters, are a main source of producing “exotic” glass spherules, their presences in a local regolith sample remain a useful medium to date large cratering events occurred in the past.

5.5 Conclusion

We have used a diverse set of models and simplifying assumptions to investigate the relationship between the formation of Copernicus Crater at ~ 800 Ma and the excess of $^{40}\text{Ar}/^{39}\text{Ar}$ -derived ages at ~ 700 -900 Ma of “exotic” glass spherules seen

in Apollo 14, 16, and 17 regolith samples. It appears that Copernicus Crater is often associated with the excess of ages at $\sim 700\text{-}900$ Ma without further clarification. This association emerges from coincidence of the formation age of Copernicus Crater and the clustered ages at ~ 800 Ma. We examined the most likely scenario that the sesquinary crater formation of Copernicus Crater possibly contributes to the excess of ages at $\sim 700\text{-}900$ Ma of “exotic” glass spherules from Apollo regolith samples. The numerical quantification of provenance of an “exotic” glass spherule gives a sense of size of a source crater that formed it, yet the exact size of a source crater is still unknown. Our defined Nearness of Distance (NOD) to quantify the provenance of an “exotic” glass spherule is first proposed in the field of lunar science. All our compiled fifteen “exotic” glass spherules appear to originate in more than hundreds of kilometers away from a landing site where astronauts collected regolith. The SALES_2 fragmentation simulation results for Copernicus Crater point to very few number of large fragments up to 100 m in diameter, yielding approximately the formation of sub-kilometer sized sesquinary crater. The estimated sizes of our Copernicus Craters sesquinary crater are consistent with the proposed sizes in other studies.

We then combined the size frequency distribution obtained from SALES_2 code with the N-body simulation, REBOUND, to estimate the size frequency distribution of sesquinary craters. The calculation of fraction of test particle launched at velocities in the range from 2.4 km/s to 3.2 km/s is consistent with at least two orbit dynamic studies in the literature. This gives us more confidence to proceed a further consideration. The most critical component in this study is the melt production in a low velocity impact of porous target. Because a negligible number of sesquinary craters impacts at a velocity high enough to produce melts, it only leads to the amount of glass spherules equivalent to ~ 3 year-long primary crater bombardment. Thus, it is likely that primary craters generate glass spherules way more than the sesquinary craters. As the formation of Copernicus Crater cannot be a primary contributor to the excess of ages at $\sim 700\text{-}900$ Ma, at least not through sesquinary-forming spherules, the spike seen in ~ 800 Ma may, therefore, imply a true increase in a lunar impact

flux in the last 800 Ma. Considering high uncertainties in our model, our conclusion may be elusive, but we hope to devote our understanding to the possibility of a global impact spike in the most recent lunar impact history.

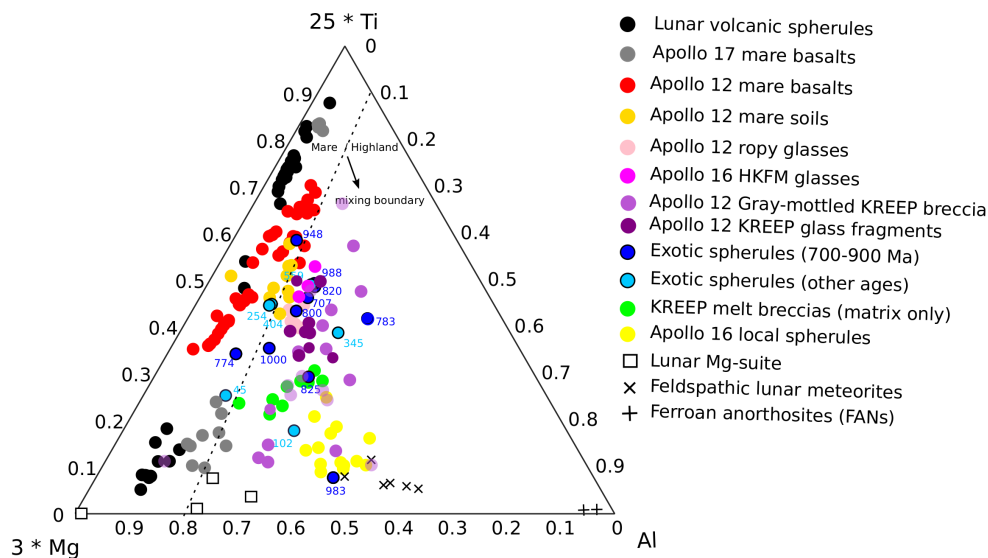


Figure 5.2.: Ternary diagram for our compiled exotic glass spherules and a diverse set of returned samples. The dashed line represents an approximate mixing boundary of lunar mare and highland (Delano et al., 2007). Black filled circles represent lunar volcanic glass spherules (Delano, 1986, Tables 3 and 5). Gray filled circles represent Apollo 17 high-Ti and very low-Ti mare basalts (Wentworth et al., 1979; Vaniman and Papike, 1977). Red filled circles represent Apollo 12 mare basalts (Neal et al., 1994; Rhodes et al., 1977; Papike et al., 1976). Orange filled circles represent Apollo 12 soils (Laul and Papike, 1980; Morris et al., 1983). Pink filled circles represent Apollo 12 ropy glasses (Wentworth et al., 1994). Magenta filled circles represent Apollo 16 HKFM glasses (Naney et al., 1976; Ridley et al., 1973; Kempa et al., 1980). Light and dark purple filled circles represent Apollo 12 gray-mottled KREEP breccias and KREEP glass fragments respectively (Meyer et al., 1971). Light and dark blue filled circles and yellow filled circles represent all glass spherules (Zellner and Delano, 2015, Appendix A). Green filled circles represent KREEP melt breccias (Sample No. 14063, 14078, 14276, 14310, 60315, 62235, 65015, and 63355) (Tera et al., 1974; Norman et al., 2010). Square symbols represent lunar Mg-suite (Sample No. 72415, 76535, 77075, and 78235). Cross symbols represent feldspathic lunar meteorites (Korotev et al., 2003). Plus symbols represent Ferroan anorthosites (Sample No. 60025 and 15415). The integers marked in dark blue color represent the $^{40}Ar/^{39}Ar$ -derived ages of exotic spherules. Opaque colors are for overlapped circles.

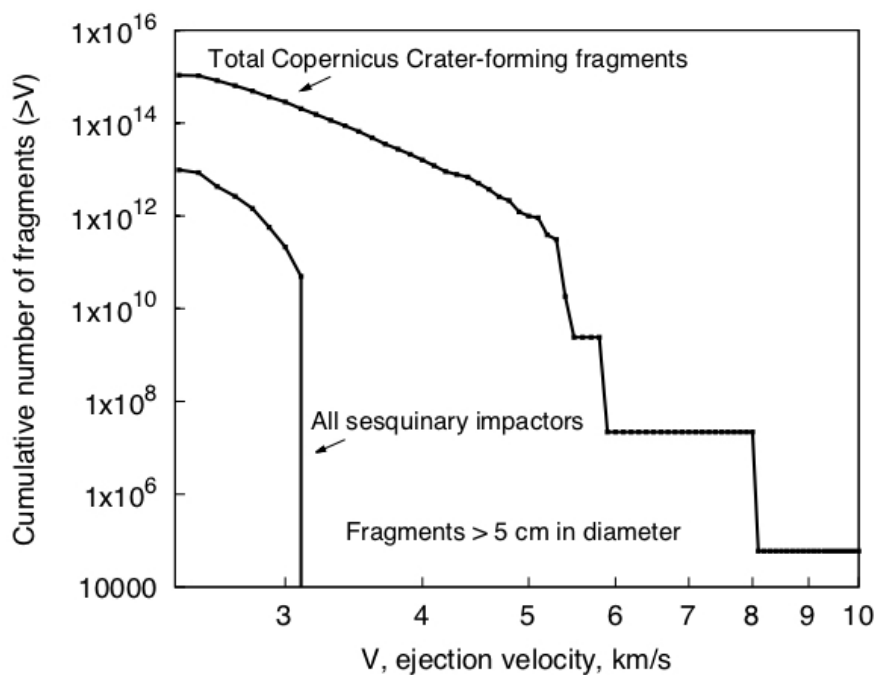


Figure 5.3.: Cumulative number of fragments higher than ejection velocity from the SALES_2 simulation result for Copernicus Crater. The line points in black color represent the cumulative number of fragments that escaped the lunar gravity. The line points labeled by “All sesquinary impactors” depict the cumulative number of fragments that initially escaped the lunar gravity but later hit the Moon. The x-axis is the ejection velocity of escaped fragments, and the y-axis is the cumulative number of escaped fragments higher than ejection velocity. The number of total fragments and the precursor of sesquinary impactors are $\sim 10^{15}$ and $\sim 10^{13}$ respectively (>5 cm).

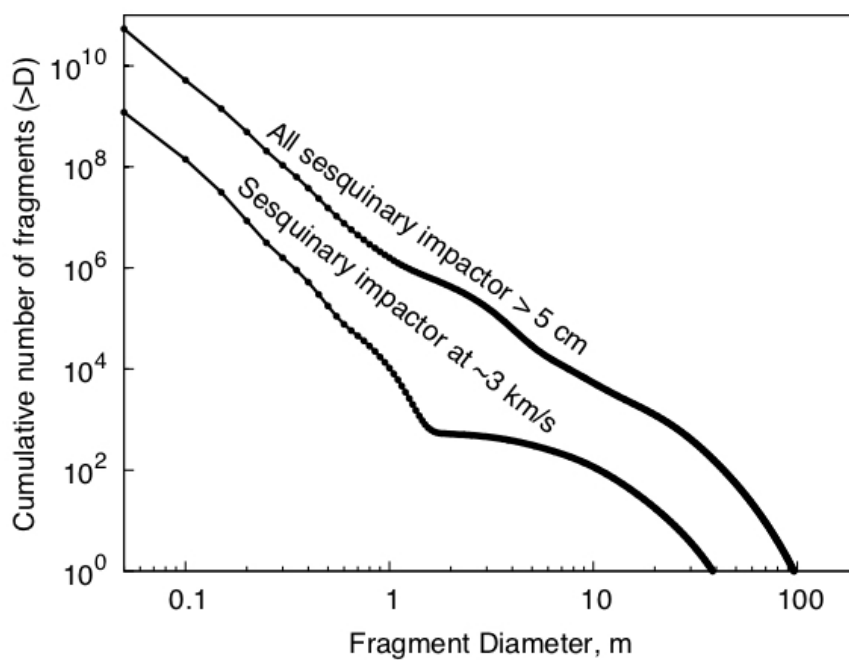


Figure 5.4.: Cumulative size frequency distributions (CSFD) of all Copernicus Crater-forming sesquinary impactor fragments and sesquinary impactors launched at ~ 3 km/s.

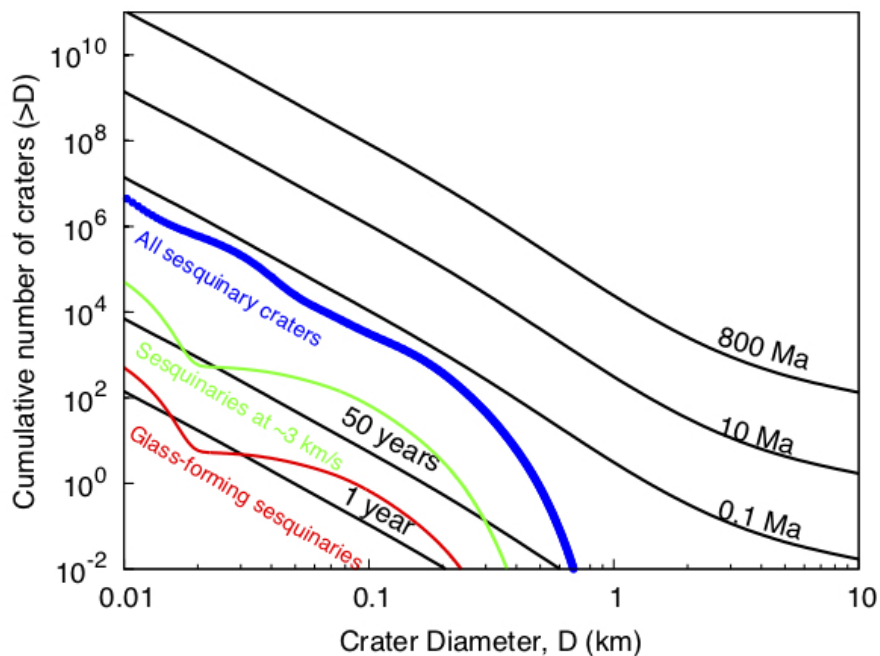


Figure 5.5.: Crater size frequency distributions (SFD) for Copernicus Crater-forming sesquinary craters. The solid black lines from the top to the bottom show total crater production of the lunar surface for 800 Ma, 10 Ma, 0.1 Ma, 50 years, and 1 year under the Neukum Production Function (NPF). The line marked in blue color represent the size frequency distribution of all sesquinary craters. The green line is sesquinary crater SFD for ejection velocity of ~ 3 km/s that we used the data of fragment sizes from SALES_2 code as impactor sizes and velocity distribution and converted them to crater sizes using π -group scaling laws. The red line is sesquinary crater population that may form melt.

6 SUMMARY

The lunar samples returned to Earth provide some of our best data for understanding Earth's moon. The first soil samples from the Moon that were returned from the Apollo 11 mission are fascinating because these samples reveal diverse mineralogy, hinting at a variety of processes that have operated at the surface over a long period. Impact cratering is one of the most important driving forces in the lunar surface evolution; it continually altered the lunar surface over all of lunar history. In particular, this persistent process allows us to investigate the changes in the impact flux in the Solar System over time, as well as to study the physics of impact cratering. The impact environment of the Moon can also hinder our understanding of the returned lunar samples. Because the impactors vary in a wide range of sizes from micrometeoroid impacts to basin formation, how to reliably address the makeup of a lunar surface can be a challenging process to model.

In fact, the makeup of a lunar surface is more or less regolith layers that were deposited by impact debris over the lunar impact bombardment history. For example, the texture of the Apollo 15 drilling core has been interpreted as composed of ~ 242 well-mixed layers with a thickness between a few millimeters to ~ 13 cm. Each ejecta layer depicts a unique history through its journey at the surface. Several models have been proposed to capture the stochastic nature of impact cratering process, including regolith accumulation, exposure history of regolith, and frequency of mixing process driven by impacts. Those quantitative models tell us that more than few kilometer-thick regoliths that have accumulated at a landing site, and the very topmost 1-millimeter layer of a lunar surface has been impact-gardened more than few times within one million years. Those models laid the groundwork for Monte Carlo typed cratering process and awaited further computational advancement. The improved

understanding of impact cratering allowed us to numerically simulate the evolution of the lunar landscape as it has been shaped by impact cratering process over time.

Cratered Terrain Evolution Model (CTEM), originally developed by Jim Richardson and modernized by David Minton, is a Monte Carlo code that can simulate the topography of heavily cratered surface and track the number of countable craters over time. The main effect of impact cratering that CTEM models is elevation changes of the landscape throughout the excavation process of craters, the deposition of ejecta, and the degradation by topographic diffusion and distal ejecta. However, the bulk of Moon underneath the topography contains a stack of impact-generated ejecta layers that carry a rich abundance of information, including composition and datable impact products, such as impact glasses. Therefore, understanding how an individual impact-generated ejecta sourced from varying depths of the subsurface is essential. The end result needs to be calibrated with analysis of lunar samples, as well as remote sensing data. In order to model the distribution of material with varying types in a sample, I developed extensions to the CTEM code that can track all ejecta generated during a simulation. The ultimate goal of this dynamic ejecta tracking system was to mimic the complex history of the lunar regolith, and better understand what the lunar sample collection tells us about the impact history of the Moon.

I tested the foundation of this dynamic ejecta tracking system using two different aspects of material transport on the Moon, 1) binary composition (mare basalt and highland anorthosite) and 2) impact glasses. First of all, the calibration data that I used for this binary composition on the Moon is to constrain the bulk of impact-generated ejecta over the most recent 3 billion years of impacts (more certain as compared to early lunar impact bombardment). We looked into material transport across mare and highland contacts; both remote sensing data and surface samples provide a simple and well-calibrated data set. Correlations between abundances of two end members (basalt and anorthosite) and distance from the contact shows a non-linear mixing profile within the distance of 4-5 km from the contact. The non-linear behavior across the contact is accounted for by the source of non-mare components.

For example, the excess of non-mare materials in mare soil samples that were collected over 100 km from the contact is significant (up to 70%).

Examining an effect of impact-generated ejecta (distal ejecta versus proximal ejecta) in a sample was limited until we had a better understanding of impact cratering and available computation simulation. I set up a numerical experiment that examined four related factors: 1) distal ejecta, 2) proximal ejecta, 3) cm-to-mm scaled cratering, and 4) the spatial heterogeneity of distal ejecta. I demonstrated that distal ejecta is critical to both the width of 4-5 km of non-linear mixing zones and the excess of non-mare materials in observed soil samples. While a large portion of distal ejecta with a high concentration of exotic materials is delivered to a local site, it is further buried with pre-existing materials by cm-to-mm scale impact gardening.

Distal ejecta is spatially heterogeneous, due to being confined into ray structures. My work showed that the spatial heterogeneity of distal ejecta may be the primary reason for some soil samples that contain an anomalously high concentration of non-mare materials even though they were collected far from mare/highlands contacts. Impact-generated ejecta is concentrated into those relative narrow ray structures, so an in-situ sample that is collected within a rayed region can contain materials with a distinct composition than other local soil samples. The excess of exotic materials seen in mare soils collected in over 100 km away from a mare/highlands contact may be due to the samples being taken within the ray of a distant, large crater. The Apollo 12 landing site, where one of the discrepant soil samples was taken, is crossed by a ray from Copernicus Crater.

As the binary component tracking system (mare and highland materials) driven by impacts in CTEM produces a consistent result with remote sensed data and returned lunar samples, we are more comfortable extend the work of the binary material tracking system to multiple component. Among impact-generated ejecta on the Moon, a melt (glass) component inside the ejecta has been a fascinating subject for the age-dating purposes. In particular, an impact glass spherule is considered as a direct product of an impact event. As impact glass spherules are quite common in a lunar

soil, the data set from $^{40}\text{Ar}/^{39}\text{Ar}$ derived age measurements of impact glass spherules is beneficial to understanding an abundance of a different type of lunar materials, more importantly to the impact history of the Moon. In Chapter 4, we studied an intriguing, common observation that were reported from at least four different research groups (Culler, Levine, Hui, and Zellner). Several research groups found that an excess of $^{40}\text{Ar}/^{39}\text{Ar}$ -derived ages of impact glass spherules have been generated within the last 500 Ma. One interpretation suggests that more impacts occurred in the last 500 Ma, producing relatively more young spherules than prior to 500 Ma. Quantitative relative probability from age distributions of impact glass spherules implies that the impact flux has increased by a factor of 2-3 during post-Copernican period. Though this young spike seen in <500 Ma is no longer present after argon diffusion correction for glass spherules has been made. This has been brought to our attention that a sampling bias needs to be evaluated to the age distribution of impact glass spherules. And the scenario that an impact flux has remained constant over the last 3 Gy may still hold.

We cautioned that processes related to impact spherules can potentially induce a bias. Those relevant processes we modeled are 1) their formation upon impact-induced melting, 2) distribution during excavation stage, 3) transport and destruction subject to subsequent impacts, and finally 4) sampling process by lunar astronauts. It appears that each of those four process has some degree of uncertainty, as well as observational constraints. The glassy nature of impact glass spherules indicates that they originated in a region where intense heating and vaporizing occur and were rapidly quenched in the space. As being quenched rapidly in the space it is suggestive of a high initial ejection speed upon the creation of an impact glass spherule. In fact, this information is consistent with observations on the distribution of microtektite strewn fields, terrestrial analogue of lunar impact glass spherules, which were found hundred-to-thousand kilometers away from a source crater. Another major uncertainty is related to a sampling process performed by Apollo astronauts. We noted that lunar soil samples were collected from a limited depth, on the order of a few

centimeters by the Apollo astronauts. The shallow depth together with the distribution and production of impact glass spherules determines how much it makes those impact glass spherules available to the very topmost surface. I found that even if the impact rate has remained constant over the last 3 Ga, I could reproduce the observed age distribution of glass spherules using a simulated 10 cm sampling depth.

Following the glass spherule work, the final chapter of this dissertation continued to work on another interesting observation: an excess of ~ 700 - 900 Ma ages of “exotic” impact glass spherules. A similar age of 800 Ma on a lunar chronology commonly refers to the formation of Copernicus Crater. However, the concurrence of excess of ~ 700 - 900 Ma ages and the formation age of Copernicus Crater has not been clarified. We created a most likely scenario to understand how possible the Copernicus Crater-forming event contributes to the excess of ~ 700 - 900 Ma ages of “exotic” glass spherules. The main scenario in this study is that Copernicus Crater forming event generates sufficient amount of glass spherules. We first investigated the compositional provenance of those ~ 800 Ma-old exotic spherules by comparing with an extensive data set of lunar returned samples that could potentially represent the stratigraphy of Copernicus Crater region. Also, we have employed a fragmentation code (SALES_2), orbit dynamic code (REBOUND), and planar impact approximation technique to obtain the total abundance of sesquinary-forming spherules. We found this scenario unlikely because of that 1) the ternary compositions of exotic spherules is contradictory with mixing substrate materials assumed for Copernicus Crater region, and 2) lunar sesquinary craters produce a scarce amount of glass spherules due to its moderately low impact velocity.

We noted that the origin of impact glass spherules is critical for future investigation. Assume that the composition of a glass spherule is representative of a fraction of a lunar surface. We applied a linear least squares method to the chemical oxide abundance maps acquired by Lunar Prospector Gamma-Ray Spectrometer for a given composition of an impact glass spherule. This quantitative method returns the value of a distance measured from the collection site to the estimate origin location that

matches the composition of an impact glass spherule within <2 standard deviations. It appears that more than half of geochemically-distinct glass spherules are estimated to have an origin location at least 500 km away from collection sites (treated as a local origin if falling into one pixel). In addition, we also applied this method to our compiled glass spherules for a potential candidate of Copernicus glass spherules. We found only one spherule matching with the composition of center region of Copernicus Crater interpreted from Lunar Prospector Gamma-Ray Spectrometer. For the rest of ~ 800 Ma-old exotic spherules, their compositional diversity appears to not reconcile with mixing of assumed lunar samples that are prescribed to be the stratigraphy of Copernicus Crater region.

Returned lunar samples have demonstrated a hard evidence of intense material transport driven by impacts on the Moon. In this dissertation, I focused on impact-driven material transport over the last three billion years. Controversy may remain in the assumption of a constant impact rate over the last three billion years, yet I found the assumption of a constant impact rate particularly useful in modeling returned lunar samples. In order to simulate returned samples, our three-dimensional regolith transport model based on Cratered Terrain Evolution Model (CTEM) was calibrated with theoretical and empirical cratering laws. Our dynamic data structure implemented with the concept of Maxwell Z-model was applied to study the diffusion problem across mare and highland contacts. With the assumption of the constant impact rate, the result of material transport across mare and highland contacts matches with the observational diffusion profile across the contacts. In hindsight over ~ 3 Ga may smash out the stochastic nature of impact cratering or the change in a lunar impact flux. In the chapters 4 and 5 our numerical framework demonstrated a novel approach for modeling returned lunar samples. We have found some interesting facts; examples include how sampling depth affects an interpretation of impact age record and how “exotic” versus local origins of impact glass spherules tell a different story about a lunar impact flux. It is fascinating and rewarding when I applied this new approach to study old problems that some of them lasts for several decades. In the end,

I strongly encourage everyone to look at some pre-existing and excellent problems and go for science.

REFERENCES

REFERENCES

- Abramov, O., Wong, S. M., and Kring, D. A. (2012). Differential melt scaling for oblique impacts on terrestrial planets. *Icarus*, 218(2):906–916.
- Alibert, C., Norman, M. D., and McCulloch, M. T. (1994). An ancient sm-nd age for a ferroan noritic anorthosite clast from lunar breccia 67016. *Geochimica et Cosmochimica Acta*, 58(13):2921–2926.
- Alvarez, L. W., Alvarez, W., Asaro, F., and Michel, H. V. (1980). Extraterrestrial cause for the Cretaceous-Tertiary extinction. *Science*, 208(4448):1095–1108.
- Anderson Jr, A., Newton, R., and Smith, J. (1971). Apollo 12 mineralogy and petrology: Light-colored fragments, minor-element concentrations, and petrologic development of moon. In *Second Lunar Science Conference (unpublished proceedings)*.
- Artemieva, N., Karp, T., and Milkereit, B. (2004). Investigating the Lake Bosumtwi impact structure: Insight from numerical modeling. *Geochemistry, Geophysics, Geosystems*, 5(11).
- Artemieva, N., Wünnemann, K., Krien, F., Reimold, W., and Stöffler, D. (2013). Ries crater and suevite revisited—Observations and modeling Part II: Modeling. *Meteoritics & Planetary Science*, 48(4):590–627.
- Arvidson, R., Drozd, R. J., Hohenberg, C. M., Morgan, C. J., and Poupeau, G. (1975). Horizontal transport of the regolith, modification of features, and erosion rates on the lunar surface. *The Moon*, 13(1-3):67–79.
- Austin, M., Thomsen, J., Ruhl, S., Orphal, D., Borden, W., Larson, S., and Schultz, P. (1981). Z-model analysis of impact cratering—an overview. In *Multi-ring basins: Formation and Evolution*, pages 197–205.
- Baldwin, R. (1949). *The Face of the Moon*. University of Chicago Committee on Publications in the Physical Sciences. University of Chicago Press.
- Baldwin, R. B. (1963). *The Measure of the Moon*. University of Chicago, Chicago, 1st edition.
- Barnouin-Jha, O. S., Yamamoto, S., Toriumi, T., Sugita, S., and Matsui, T. (2007). Non-intrusive measurements of crater growth. *Icarus*, 188(2):506–521.

- Barra, F., Swindle, T. D., Korotev, R. L., Jolliff, B. L., Zeigler, R. a., and Olson, E. (2006). $^{40}\text{Ar}/^{39}\text{Ar}$ dating of Apollo 12 regolith: Implications for the age of Copernicus and the source of nonmare materials. *Geochimica et Cosmochimica Acta*, 70(24):6016–6031.
- Bart, G. D., Nickerson, R. D., Lawder, M. T., and Melosh, H. J. (2011). Global survey of lunar regolith depths from LROC images. *Icarus*, 215(2):485–490.
- Berg, O., Richardson, F., and Burton, H. (1973). Apollo 17 preliminary science report. *NASA SP-330*, 16.
- Bjork, R., Kreyenhagen, K., and Wagner, M. (1967). *Analytical study of impact effects as applied to the meteoroid hazard*. Number 757. National Aeronautics and Space Administration.
- Bjorkman, M. D. and Holsapple, K. A. (1987). Velocity scaling impact melt volume. *International Journal of Impact Engineering*, 5(1-4):155–163.
- Boehnke, P. and Harrison, T. M. (2016). Illusory late heavy bombardments. *Proceedings of the National Academy of Sciences*, 113(39):10802–10806.
- Bogard, D. D., Garrison, D. H., Shih, C. Y., and Nyquist, L. E. (1994). ^{39}Ar - ^{40}Ar dating of two lunar granites: The age of Copernicus. *Geochimica et Cosmochimica Acta*, 58(14):3093–3100.
- Bohor, B. F., Foord, E. E., Modreski, P. J., and Triplehorn, D. M. (1984). Mineralogic evidence for an impact event at the Cretaceous-Tertiary boundary. *Science*, 224:867–870.
- Bohor, B. F. and Glass, B. P. (1995). Origin and diagenesis of K/T impact spherules—From Haiti to Wyoming and beyond. *Meteoritics & Planetary Science*, 30(2):182–198.
- Borchardt, R., Stöffler, D., Spettel, B., Palme, H., Wänke, H., Wacker, K., and Jessberger, E. (1986). Composition, structure, and age of the apollo 16 subregolith basement as deduced from the chemistry of post-imbrium melt bombs. *Journal of Geophysical Research: Solid Earth*, 91(B13):E43–E54.
- Borg, J., Comstock, G. M., Langevin, Y., and Maurette, M. (1976). A Monte Carlo model for the exposure history of lunar dust grains in the ancient solar wind. *Earth and Planetary Science Letters*, 29(1):161–174.
- Borg, L., Norman, M., Nyquist, L., Bogard, D., Snyder, G., Taylor, L., and Lindstrom, M. (1999). Isotopic studies of ferroan anorthosite 62236: a young lunar crustal rock from a light rare-earth-element-depleted source. *Geochimica et Cosmochimica Acta*, 63(17):2679–2691.
- Bottke, W. F. and Norman, M. D. (2017). The late heavy bombardment. *Annual Review of Earth and Planetary Sciences*, 45.
- Bottke, W. F., Vokrouhlicky, D., and Nesvorny, D. (2018). Forming the flora family: Implications for the near-earth asteroid population and large terrestrial planet impactors. In *AAS/Division for Planetary Sciences Meeting Abstracts*, volume 50.

Budney, C. J. and Lucey, P. G. (1998). Basalt thickness in Mare Humorum: The crater excavation method. *Journal of Geophysical Research*, 103(E7):16855–16870.

Bugiolacchi, R., Mall, U., Bhatt, M., McKenna-Lawlor, S., Banaszekiewicz, M., Brønstad, K., Nathues, A., Søråas, F., Ullaland, K., and Pedersen, R. B. (2011). An in-depth look at the lunar crater copernicus: Exposed mineralogy by high-resolution near-infrared spectroscopy. *Icarus*, 213(1):43–63.

BVSP (1981). Basaltic volcanism on the terrestrial planets.

Cannon, K. M. and Mustard, J. F. (2015). Preserved glass-rich impactites on Mars. *Geology*, 43(7):635–638.

Carr, M. H., Howard, K. A., and El-Baz, F. (1971). Geologic maps of the Apennine-Hadley region of the moon, map 1-72. *U.S. Geological Survey, Washington, D.C.*

Chapman, C. R. and McKinnon, W. B. (1986). Cratering of planetary satellites. In *IAU Colloq. 77: Some Background about Satellites*, pages 492–580.

Cintala, M. J. and Grieve, R. A. (1998). Scaling impact melting and crater dimensions: Implications for the lunar cratering record. *Meteoritics & Planetary Science*, 33(4):889–912.

Collins, G. S. (2014). Numerical simulations of impact crater formation with dilatancy. *Journal of Geophysical Research E: Planets*, 119(12):2600–2619.

Collins, G. S., Morgan, J., Barton, P., Christeson, G. L., Gulick, S., Urrutia, J., Warner, M., and Wünnemann, K. (2008). Dynamic modeling suggests terrace zone asymmetry in the Chicxulub crater is caused by target heterogeneity. *Earth and Planetary Science Letters*, 270(3):221–230.

Collins, G. S. and Wünnemann, K. (2005). How big was the Chesapeake Bay impact? Insight from numerical modeling. *Geology*, 33(12):925–928.

Coney, L., Reimold, W. U., Gibson, R. L., Koeberl, C., and Ogilvie, P. (2010). Melt particle characteristics of the within-and out-of-crater suevites from the Bosumtwi impact structure, Ghana: Implications for crater formation. *Geological Society of America Special Papers*, 465:411–442.

Costello, E. S., Ghent, R. R., and Lucey, P. G. (2018). The mixing of lunar regolith: Vital updates to a canonical model. *Icarus*, 314:327–344.

Croft, S. K. (1980). Cratering flow fields-implications for the excavation and transient expansion stages of crater formation. In *Lunar and Planetary Science Conference Proceedings*, volume 11, pages 2347–2378.

Croft, S. K. (1982). A first-order estimate of shock heating and vaporization in oceanic impacts. *Geological Society of America Special Papers*, 190:143–152.

Cross, C. and Fisher, D. (1968). The computer simulation of lunar craters. *Monthly Notices of the Royal Astronomical Society*, 139(2):261–272.

Culler, T. S., Becker, T. A., Muller, R. A., and Renne, P. R. (2000). Lunar impact history from $^{40}\text{Ar}/^{39}\text{Ar}$ dating of glass spherules. *Science*, 287(5459):1785–1788.

Dalrymple, G. B. and Ryder, G. (1993). $^{40}\text{Ar}/^{39}\text{Ar}$ age spectra of apollo 15 impact melt rocks by laser step-heating and their bearing on the history of lunar basin formation. *Journal of Geophysical Research: Planets*, 98(E7):13085–13095.

Dalrymple, G. B. and Ryder, G. (1996). Argon-40/argon-39 age spectra of apollo 17 highlands breccia samples by laser step heating and the age of the serenitatis basin. *Journal of Geophysical Research: Planets*, 101(E11):26069–26084.

De Hon, R. (1979). Thickness of the western mare basalt. In *Lunar and Planetary Science Conference*, volume 10, pages 274–276.

De Hon, R. A. (1974). Thickness of mare material in the Tranquillitatis and Nectaris basins. *Proceedings of the Fifth Lunar Conference*, 1:53–59.

Delano, J., Lindsley, D., and Rudowski, R. (1982). Glasses of impact origin from Apollo 11, 12, 15, and 16 - Evidence for fractional vaporization and mare/highland mixing. In *Lunar and Planetary Science Conference Proceedings*, volume 12, pages 339–370.

Delano, J., Zellner, N., Barra, F., Olson, E., Swindle, T., Tibbetts, N., and Whittet, D. (2007). An integrated approach to understanding Apollo 16 impact glasses: Chemistry, isotopes, and shape. *Meteoritics & Planetary Science*, 42(6):993–1004.

Delano, J. W. (1986). Pristine lunar glasses: Criteria, data, and implications. *Journal of Geophysical Research: Solid Earth*, 91(B4):201–213.

Delano, J. W. (1991). Geochemical comparison of impact glasses from lunar meteorites alha81005 and mac88105 and apollo 16 regolith 64001. *Geochimica et Cosmochimica Acta*, 55(11):3019–3029.

Dence, M. R. (1965). The extraterrestrial origin of canadian craters. *Annals of the New York Academy of Sciences*, 123(2):941–969.

Dence, M. R. (1971). Impact melts. *Journal of Geophysical Research*, 76(23):5552–5565.

Deutsch, A. and Stöffler, D. (1987). Rb-sr-analyses of apollo 16 melt rocks and a new age estimate for the imbrium basin: Lunar basin chronology and the early heavy bombardment of the moon. *Geochimica et Cosmochimica Acta*, 51(7):1951–1964.

Dhingra, D. and Pieters, C. (2011). Mg-spinel rich lithology at crater copernicus. In *Annual Meeting of the Lunar Exploration Analysis Group*, volume 1646, page 9.

Dhingra, D., Pieters, C. M., Head, J. W., and Isaacson, P. J. (2013). Large mineralogically distinct impact melt feature at copernicus crater—evidence for retention of compositional heterogeneity. *Geophysical Research Letters*, 40(6):1043–1048.

Dienes, J. and Walsh, J. (1970). Theory of impact: Some general principles and the method of eulerian codes. *High-velocity impact phenomena*, 45.

Donnelly, T. and Chao, E. (1973). Microtektites of late eo-cene age from the eastern caribbean sea: in edgar, nt, saunders, jb, et al. *Initial Reports of the Deep Sea Drilling Project, Washington, DC: US Government Printing Office*, 7:607–672.

Drake, E. T. and Komar, P. D. (1984). Origin of impact craters: Ideas and experiments of hooke, gilbert, and wegener. *Geology*, 12(7):408–411.

- Duncan, A. R., Sher, M. K., Abraham, Y. C., Erlank, A. J., Willis, J. P., and Ahrens, L. H. (1975). Compositional variability of the Apollo 15 regolith. *6th Lunar Science Conference*, 6:220–222.
- El-Baz, F. (1980). Gilbert and the moon. *The scientific ideas of GK Gilbert*, pages 69–80.
- Elliott, J. and Melosh, H. (2018). The effects of target heterogeneities on impact spallation and fragmentation. In *Lunar and Planetary Science Conference*, volume 49.
- Elliott, J. R., Huang, Y. H., Minton, D. A., and Freed, A. M. (2018). The length of lunar crater rays explained using secondary crater scaling. *Icarus*, 312:231–246.
- Engelhardt, W., Arndt, J., Fecker, B., and Pankau, H. (1995). Suevite breccia from the Ries crater, Germany: Origin, cooling history and devitrification of impact glasses. *Meteoritics & Planetary Science*, 30(3):279–293.
- Evans, A. J., Soderblom, J. M., Andrew-Hanna, J. C., Solomon, S. C., and Zuber, M. T. (2016). Identification of buried lunar impact craters from GRAIL data and implications for the nearside maria. *Geophysical Research Letters*, 43(6):2445–2455.
- Farrand, W. H. (1988). Highland Contamination and Minimum Basalt Thickness in Northern Mare Fecunditatis. *Proc. Lunar Planet. Sci. Conf. 18th*, pages 319–329.
- Fassett, C. I. and Thomson, B. J. (2014). Crater degradation on the lunar maria: Topographic diffusion and the rate of erosion on the Moon. *Journal of Geophysical Research: Planets*, 119(10):2255–2271.
- Fazio, A., Folco, L., D’Orazio, M., Frezzotti, M. L., and Cordier, C. (2014). Shock metamorphism and impact melting in small impact craters on Earth: Evidence from Kamil crater, Egypt. *Meteoritics & Planetary Science*, 49(12):2175–2200.
- Fischer, E. M. and Pieters, C. M. (1995). Lunar surface aluminum and iron concentration from Galileo solid state imaging data, and the mixing of mare and highland materials. *Journal of Geophysical Research*, 100(E11):23279.
- Fitzgerald, A. (1953). A new feature: Plates illustrating celestial objects. *Irish Astronomical Journal*, 2:159.
- Folco, L., Glass, B., D’Orazio, M., and Rochette, P. (2010a). A common volatilization trend in transantarctic mountain and australasian microtektites: Implications for their formation model and parent crater location. *Earth and Planetary Science Letters*, 293(1-2):135–139.
- Folco, L., Perchiazzi, N., D’Orazio, M., Frezzotti, M., Glass, B., and Rochette, P. (2010b). Shocked quartz and other mineral inclusions in australasian microtektites. *Geology*, 38(3):211–214.
- Gaddis, L., Skinner Jr, J., Hare, T., Tanaka, K., Hawke, B., Spudis, P., Bussey, B., Pieters, C., and Lawrence, D. (2006). The lunar geologic mapping program and status of copernicus quadrangle mapping. In *37th Annual Lunar and Planetary Science Conference*, volume 37.
- Galilei, G., Kepler, J., and Carlos, E. (1880). *The Sidereal Messenger of Galileo Galilei: And a Part of the Preface to Kepler’s Dioptrics Containing the Original Account of Galileo’s Astronomical Discoveries*. Rivingtons.

- Gault, D. E. (1970). Saturation and equilibrium conditions for impact cratering on the lunar surface: Criteria and implications. *Radio Science*, 5(2):273–291.
- Gault, D. E. and Wedekind, J. A. (1978). Experimental studies of oblique impact. *Proc. Lunar Sci. Conf. 9th*, 9:3843–3875.
- Gault, E. D., Hörz, F., Brownlee, E., and Hartung, B. J. (1974). Mixing of the lunar regolith. *Proceedings of the Fifth Lunar Conference*, 3:2365–2386.
- Gielis, J. (2003). A generic geometric transformation that unifies a wide range of natural and abstract shapes. *American journal of botany*, 90(3):333–338.
- Giguere, T., Hawke, B., Gaddis, L., Blewett, D., Gillis-Davis, J., Lucey, P., Smith, G., Spudis, P., and Taylor, G. (2006). Remote sensing studies of the dionysius region of the moon. *Journal of Geophysical Research: Planets*, 111(E6).
- Giguere, T. A., Taylor, G. J., HAWKE, B. R., and Lucey, P. G. (2000). The titanium contents of lunar mare basalts. *Meteoritics & Planetary Science*, 35(1):193–200.
- Gilbert, G. K. (1893). *The Moon's face: A study of the origin of its features*. Philosophical Society of Washington.
- Gladman, B. J., Burns, J. A., Duncan, M. J., and Levison, H. F. (1995). The dynamical evolution of lunar impact ejecta. *Icarus*, 118(2):302–321.
- Glass, B., Muenow, D., Bohor, B., and Meeker, G. (1997). Fragmentation and hydration of tektites and microtektites. *Meteoritics & Planetary Science*, 32(3):333–341.
- Glass, B. P. (1968). Glassy objects (microtektites?) from deep-sea sediments near the Ivory Coast. *Science*, 161(3844):891–893.
- Glass, B. P., Baker, R. N., Storzer, D., and Wagner, G. A. (1973). North American microtektites from the Caribbean sea and their fission track age. *Earth and Planetary Science Letters*, 19(2):184–192.
- Glass, B. P. and Simonson, B. M. (2012). *Distal impact ejecta layers: A record of large impacts in sedimentary deposits*. Springer-Verlag Berlin Heidelberg.
- Goles, G. G., Duncan, A. R., Lindstrom, D. J., Martin, M. R., Beyer, R. L., Osawa, M., Randle, K., Meek, L. T., Steinborn, T. L., and McKay, S. M. (1971). Analyses of Apollo 12 specimens: Compositional variations, differentiation processes, and lunar soil mixing models. *Proc. 2nd Lunar Sci. Conf.*, 2:1063–1081.
- Gomes, R., Levison, H. F., Tsiganis, K., and Morbidelli, A. (2005). Origin of the cataclysmic late heavy bombardment period of the terrestrial planets. *Nature*, 435(7041):466.
- Grange, M., Nemchin, A., Pidgeon, R., Timms, N., Muhling, J., and Kennedy, A. (2009). Thermal history recorded by the apollo 17 impact melt breccia 73217. *Geochimica et Cosmochimica Acta*, 73(10):3093–3107.

Greeley, R., Kadel, S. D., Williams, D. A., Gaddis, L. R., Head, J. W., McEwen, A. S., Murchie, S. L., Nagel, E., Neukum, G., Pieters, C. M., Sunshine, J. M., Wagner, R., and Belton, M. J. S. (1993). Galileo Imaging Observations of Lunar Maria and Related Deposits. *Journal of Geophysical Research-Planets*, 98(E9):17183–17205.

Grieve, R. A. F. (1984). The impact cratering rate in recent time. *Journal of Geophysical Research*, 89:B403–B408.

GÜLDemeister, N., WÜNNemann, K., Durr, N., and Hiermaier, S. (2013). Propagation of impact-induced shock waves in porous sandstone using mesoscale modeling. *Meteoritics & Planetary Science*, 48(1):115–133.

Hartmann, W. (1988). Crater saturation equilibrium in the solar system: New evidence. In *Lunar and Planetary Science Conference*, volume 19.

Hartmann, W. and Kuiper, G. P. (1962). Concentric structures surrounding lunar basins. *Communications of the Lunar and Planetary Laboratory*, 1:51–66.

Hartmann, W. K. (1965). Terrestrial and lunar flux of large meteorites in the last two billion years. *Icarus*, 4(2):157–165.

Hartmann, W. K. (1975). Lunar cataclysm: A misconception? *Icarus*, 24(2):181–187.

Hartmann, W. K. (1984). Does crater saturation equilibrium occur in the solar system? *Icarus*, 60(1):56–74.

Hartmann, W. K. (1995). Planetary cratering 1. the question of multiple impactor populations: Lunar evidence. *Meteoritics*, 30(4):451–467.

Hartmann, W. K. and Gaskell, R. W. (1997). Planetary cratering 2: Studies of saturation equilibrium. *Meteoritics & Planetary Science*, 32(1):109–121.

Hartmann, W. K., Quantin, C., and Mangold, N. (2007). Possible long-term decline in impact rates: 2. Lunar impact-melt data regarding impact history. *Icarus*, 186(1):11–23.

Haskin, L. A., Gillis, J. J., Korotev, R. L., and Jolliff, B. L. (2000). The materials of the lunar procellarum creep terrane: A synthesis of data from geomorphological mapping, remote sensing, and sample analyses. *Journal of Geophysical Research: Planets*, 105(E8):20403–20415.

Haskin, L. A., Korotev, R. L., Rockow, K. M., and Jolliff, B. L. (1998). The case for an imbrium origin of the apollo thorium-rich impact-melt breccias. *Meteoritics & Planetary Science*, 33(5):959–975.

Hawke, B. R., Blewett, D. T., Lucey, P. G., Peterson, C. A., Campbell, B. A., and Robinson, M. S. (1999). The compositional and origin of selected lunar crater rays. *Workshop on New Views of the Moon II*, page 22.

Hawke, B. R., Peterson, C. A., Lucey, P. G., and Coombs, C. R. (1995). Remote sensing studies of the Grimaldi region of the Moon. *Lunar and Planetary Science XXVI*, 26:561–562.

- Head, J. N., Melosh, H. J., and Ivanov, B. A. (2002). Martian meteorite launch: High-speed ejecta from small craters. *Science*, 298(5599):1752–1756.
- Head, J. W. (1974). Orientale multi-ringed basin interior and implications for the petrogenesis of lunar highland samples. *The Moon*, 11(3-4):327–356.
- Head, J. W. (1982). Lava flooding of ancient planetary crusts - Geometry, thickness, and volumes of flooded lunar impact basins. *The Moon and the Planets*, 26:61–88.
- Head, J. W., Fassett, C. I., Kadish, S. J., Smith, D. E., Zuber, M. T., Neumann, G. A., and Mazarico, E. (2010). Global distribution of large lunar craters: Implications for resurfacing and impactor populations. *science*, 329(5998):1504–1507.
- Head, J. W. and Wilson, L. (1992). Lunar mare volcanism: Stratigraphy, eruption conditions, and the evolution of secondary crusts. *Geochimica et Cosmochimica Acta*, 56(6):2155–2175.
- Hertz, H. (1896). *Miscellaneous papers*. Macmillan.
- Hiesinger, H., Bogert, C. H. V. D., Pasckert, J. H., Funcke, L., Giacomini, L., Ostrach, L. R., and Robinson, M. S. (2012). How old are young lunar craters? *Journal of Geophysical Research*, 117(E12):E00H10.
- Hirabayashi, M., Howl, B., Fassett, C., Soderblom, J., Minton, D., and Melosh, H. (2018). The role of breccia lenses in regolith generation from the formation of small, simple craters: Application to the apollo 15 landing site. *Journal of Geophysical Research: Planets*, 123(2):527–543.
- Hirabayashi, M., Minton, D. A., and Fassett, C. I. (2017). An analytical model of crater count equilibrium. *Icarus*, 289:134–143.
- Hirayama, K. (1918). Groups of asteroids probably of common origin. *Proceedings of the Tokyo Mathematio-Physical Society. 2nd Series*, 9(17):354–361.
- Holsapple, K. and Schmidt, R. (1987). Point source solutions and coupling parameters in cratering mechanics. *Journal of Geophysical Research: Solid Earth*, 92(B7):6350–6376.
- Holsapple, K. A. (1993). The scaling of impact processes in planetary sciences. *Annual Review of Earth and Planetary Sciences*, 21:333–73.
- Hopkins, M. and Mojzsis, S. (2015). A protracted timeline for lunar bombardment from mineral chemistry, ti thermometry and u–pb geochronology of apollo 14 melt breccia zircons. *Contributions to Mineralogy and Petrology*, 169(3):30.
- Horton, J. W., Gohn, G. S., Powars, D. S., and Edwards, L. E. (2007). Origin and emplacement of impactites in the Chesapeake Bay impact structure, Virginia, USA. *Geological Society of America Special Papers*, 437:73–97.
- Hörz, F. (1978). How thick are lunar mare basalts? *Proc. Lunar Sci. Conf. 9th*, pages 3311–3331.
- Hörz, F. (2000). Time-variable cratering rates? *Science*, 288(5474):2095–2095.

- Hörz, F. and Cintala, M. (1997). The barringer award address presented 1996 July 25, Berlin, Germany: Impact experiments related to the evolution of planetary regoliths. *Meteoritics & Planetary Science*, 32(2):179–209.
- Housen, K. R. and Holsapple, K. A. (2011). Ejecta from impact craters. *Icarus*, 211(1):856–875.
- Housen, K. R., Schmidt, R. M., and Holsapple, K. A. (1983). Crater Ejecta Scaling Laws: Fundamental Forms Based on Dimensional Analysis. *Journal of Geophysical Research*, 88(B3):2485–2499.
- Howard, K. and Wilshire, H. (1973). Flows of Impact Melt at Lunar Craters. *Abstracts of the Lunar and Planetary Science Conference*, 4:389.
- Howard, K. A. (1974). Fresh Lunar Impact Craters: Review of Variations with Size. *Proceedings of Fifth Lunar Conference*, 1(5):61–69.
- Huang, Y.-H., Minton, D. A., Hirabayashi, M., Elliott, J. R., Richardson, J. E., Fassett, C. I., and Zellner, N. E. B. (2017). Heterogeneous impact transport on the moon. *Journal of Geophysical Research: Planets*, 122(6):1158–1180.
- Huang, Y.-H., Minton, D. A., Zellner, N. E., Hirabayashi, M., Richardson, J. E., and Fassett, C. I. (2018). No change in the recent lunar impact flux required based on modeling of impact glass spherule age distributions. *Geophysical Research Letters*, 45(14):6805–6813.
- Hubbard, N. J., Meyer, C., Gast, P. W., and Wiesmann, H. (1971). The composition and derivation of Apollo 12 soils. *Earth and Planetary Science Letters*, 10(3):341–350.
- Hui, M. S., Norman, M., and Jourdan, F. (2009). Tracking formation and transport of Apollo 16 lunar impact glasses through chemistry and dating. In *Proc. 9th Australian Space Sci. Conf.* (eds. Wayne Short and Ivo Cairns). National Space Society of Australia Ltd., Sydney, pages 43–54.
- Ivanov, B. (1983). The model of cratering in ideal-plastic media. In *Lunar and Planetary Science Conference*, volume 14, pages 343–344.
- James, O. B. and Wright, T. L. (1972). Apollo 11 and 12 mare basalts and gabbros: Classification, compositional variations, and possible petrogenetic relations. *Geological Society of America Bulletin*, 83(8):2357–2382.
- Jéhanno, C., Boclet, D., Froget, L., Lambert, B., Robin, E., Rocchia, R., and Turpin, L. (1992). The Cretaceous-Tertiary boundary at Beloc, Haiti: No evidence for an impact in the Caribbean area. *Earth and Planetary Science Letters*, 109(1-2):229–241.
- Johnson, B. and Melosh, H. (2014). Formation of melt droplets, melt fragments, and accretionary impact lapilli during a hypervelocity impact. *Icarus*, 228:347–363.
- Johnson, B. C., Blair, D. M., Collins, G. S., Melosh, H. J., Freed, A. M., Taylor, G. J., Head, J. W., Wieczorek, M. A., Andrews-Hanna, J. C., Nimmo, F., et al. (2016). Formation of the orientale lunar multiring basin. *Science*, 354(6311):441–444.

- Jolliff, B. L., Gillis, J. J., Haskin, L. A., Korotev, R. L., and Wieczorek, M. A. (2000). Major lunar crustal terranes: Surface expressions and crust-mantle origins. *Journal of Geophysical Research: Planets*, 105(E2):4197–4216.
- Kempa, M. J., Papike, J., and White, C. (1980). The apollo 16 regolith—a petrographically-constrained chemical mixing model. In *Lunar and Planetary Science Conference Proceedings*, volume 11, pages 1341–1355.
- Knight, C., Swain, M. V., and Chaudhri, M. (1977). Impact of small steel spheres on glass surfaces. *Journal of Materials Science*, 12(8):1573–1586.
- Korotev, R. L. (1994). Compositional variation in apollo 16 impact-melt breccias and inferences for the geology and bombardment history of the central highlands of the moon. *Geochimica et Cosmochimica Acta*, 58(18):3931–3969.
- Korotev, R. L., Jolliff, B. L., Zeigler, R. A., Gillis, J. J., and Haskin, L. A. (2003). Feldspathic lunar meteorites and their implications for compositional remote sensing of the lunar surface and the composition of the lunar crust. *Geochimica et Cosmochimica Acta*, 67(24):4895–4923.
- Korotev, R. L., Zeigler, R. A., and Floss, C. (2010). On the origin of impact glass in the apollo 16 regolith. *Geochimica et Cosmochimica Acta*, 74(24):7362–7388.
- Kovach, R., Watkins, J., and Landers, T. (1971). Active seismic experiment. *Apollo 14 Preliminary Science Report NASA Spec Paper SP-272*, 163.
- Kowitz, A., Güldemeister, N., Reimold, W., Schmitt, R., and Wünnemann, K. (2013). Diaplectic quartz glass and sio₂ melt experimentally generated at only 5 gpa shock pressure in porous sandstone: Laboratory observations and meso-scale numerical modeling. *Earth and Planetary Science Letters*, 384:17–26.
- Kreiter, T. (1960). Dating lunar surface features by using crater frequencies. *Publications of the Astronomical Society of the Pacific*, 72(428):393–398.
- Kreslavsky, M. (2017). Sesquinary craters on the moon can form clusters. In *Lunar and Planetary Science Conference*, volume 48.
- Kring, D. A., Swindle, T. D., Britt, D. T., and Grier, J. A. (1996). Cat mountain: A meteoritic sample of an impact-melted asteroid regolith. *Journal of Geophysical Research: Planets*, 101(E12):29353–29371.
- Kuiper, G. P. (1960). *Photographic Lunar Atlas: Based on Photographs Taken at the Mount Wilson, Lick, Pic Du Midi, McDonald, and Yerkes Observatories. With the Collaboration of DWG Arthur [and Others]*. University of Chicago Press.
- Kuiper, G. P., Fujita, Y., Gehrels, T., Groeneveld, I., Kent, J., Van Biesbroeck, G., and Van Houten, C. (1958). Survey of asteroids. *The Astrophysical Journal Supplement Series*, 3:289.
- Kurosawa, K. (2015). Impact-driven planetary desiccation: The origin of the dry venus. *Earth and Planetary Science Letters*, 429:181–190.
- Kurosawa, K. and Takada, S. (2019). Impact cratering mechanics: A forward approach to predicting ejecta velocity distribution and transient crater radii. *Icarus*, 317:135–147.

- Kyte, F. T., Bostwick, J. A., and Zhou, L. (1996). The Cretaceous-Tertiary boundary on the Pacific plate: Composition and distribution of impact debris. In Ryder, G., Fastovsky, D., and Gartner, S., eds., *The Cretaceous-Tertiary event and other catastrophes in Earth history: Geological Society of America Special Paper*, volume 307, pages 389–401.
- Labotka, T. C., Kempa, M. J., White, C., Papike, J. J., and Laul, J. C. (1980). The lunar regolith: Comparative petrology of the Apollo sites. *Proc. Lunar Planet. Sci. Conf. 11th*, pages 1285–1305.
- Lampson, C. (1950). Effects of atomic weapons.
- Laul, J. C. and Papike, J. J. (1980). The lunar regolith: Comparative chemistry of the Apollo sites. *Proc. Lunar Planet. Sci. Conf. 11th*, pages 1307–1340.
- Levine, J., Becker, T. A., Muller, R. A., and Renne, P. R. (2005). $^{40}\text{Ar}/^{39}\text{Ar}$ dating of Apollo 12 impact spherules. *Geophysical Research Letters*, 32:L15201.
- Li, L. and Mustard, J. F. (2000). Compositional gradients across mare-highland contacts: Importance and geological implication of lateral transport. *Journal of Geophysical Research*, 105(E8):20431.
- Li, L. and Mustard, J. F. (2005). On lateral mixing efficiency of lunar regolith. *Journal of Geophysical Research E: Planets*, 110(11):1–16.
- Li, L., Mustard, J. M., and He, G. (1997). Compositional Gradients across mare-highland contacts: The importance of lateral mixing. *Lunar and Planetary Science XXVIII*.
- Lindsay, F. N., Delaney, J. S., Herzog, G. F., Turrin, B. D., Park, J., and Swisher, C. C. (2015). Rheasilvia provenance of the kapoeta howardite inferred from 1 ga $^{40}\text{Ar}/^{39}\text{Ar}$ feldspar ages. *Earth and Planetary Science Letters*, 413:208–213.
- Lodders, K. (2003). Solar system abundances and condensation temperatures of the elements. *The Astrophysical Journal*, 591(2):1220.
- LSPET (1970). Preliminary Examination of Lunar Samples from Apollo 12. *Science*, 167(3923):1325–1339.
- LSPET (1971). Preliminary examination of lunar samples from apollo 14. *Science*, 173(3998):681–693.
- LSPET (1972). The Apollo 15 Lunar Samples : A Preliminary Description. *Science*, 175(4020):363–375.
- Lucey, P. G., Blewett, D. T., and Jolliff, B. L. (2000). Lunar iron and titanium abundance algorithms based on final processing of clementine ultraviolet-visible images. *Journal of Geophysical Research: Planets*, 105(E8):20297–20305.
- Marcus, A. H. (1970). Comparison of equilibrium size distributions for lunar craters. *Journal of Geophysical Research*, 75(26):4977–4984.
- Mark, K. (1987). Meteorite craters.

- Marvin, U. B. (1978). *Apollo 12 Course Fines (2-10): Sample Locations, Description and Inventory*. National Aeronautics and Space Administration, Lyndon B. Johnson Space Center.
- Marvin, U. B., Wood, J., Taylor, G., Reid Jr, J., Powell, B., Dickey Jr, J., and Bower, J. (1971). Relative proportions and probable sources of rock fragments in the apollo 12 soil samples. In *Lunar and Planetary Science Conference Proceedings*, volume 2, page 679.
- Maurer, P., Eberhardt, P., Geiss, J., Grögler, N., Stettler, A., Brown, G., Peckett, A., and Krähenbühl, U. (1978). Pre-imbrian craters and basins: ages, compositions and excavation depths of apollo 16 breccias. *Geochimica et Cosmochimica Acta*, 42(11):1687–1720.
- Maxwell, D. and Seifert, K. (1974). Modeling of cratering, close-in displacements, and ejecta. *Tech. rep., Defense Nuclear Agency, Washington, DC*.
- Maxwell, D. E. (1977). Simple Z model for cratering, ejection, and the overturned flap. *Impact and Explosion Cratering: Planetary and Terrestrial Implications*, 1:1003–1008.
- Mazrouei, S., Ghent, R., and Bottke, W. (2015). Has the lunar impact flux rate changed in the past billion years? In *Lunar and Planetary Science Conference*, volume 46, page 2331.
- McEwen, A. S., Moore, J. M., and Shoemaker, E. M. (1997). The phanerozoic impact cratering rate: Evidence from the farside of the moon. *Journal of Geophysical Research: Planets*, 102(E4):9231–9242.
- McGetchin, T. R., Settle, M., and Head, J. (1973). Radial thickness variation in impact crater ejecta: Implications for lunar basin deposits. *Earth and Planetary Science Letters*, 20(2):226–236.
- McHugh, C. M., Snyder, S. W., and Miller, K. G. (1998). Upper Eocene ejecta of the New Jersey continental margin reveal dynamics of Chesapeake Bay impact. *Earth and Planetary Science Letters*, 160(3):353–367.
- McKay, D., Heiken, G., Basu, A., Blanford, G., Simon, S., Reedy, R., French, B. M., and Papike, J. (1991). The lunar regolith. *Lunar sourcebook*, pages 285–356.
- McKay, D. S., Heiken, G. H., and Waits, G. (1978). Core 74001/2 Grain size and petrology as a key to the rate of in-situ reworking. *Proc. Lunar Sci. Conf. 9th*, pages 1913–1932.
- Melosh, H. (1982). A simple mechanical model of valhalla basin, callisto. *Journal of Geophysical Research: Solid Earth*, 87(B3):1880–1890.
- Melosh, H. (1984). Impact ejection, spallation, and the origin of meteorites. *Icarus*, 59(2):234–260.
- Melosh, H. (1985). Impact cratering mechanics: Relationship between the shock wave and excavation flow. *Icarus*, 62(2):339–343.
- Melosh, H. and Artemieva, N. (2004). How does tektite glass lose its water? In *Lunar and Planetary Science Conference*, volume 35.

- Melosh, H. and McKinnon, W. B. (1978). The mechanics of ringed basin formation. *Geophysical Research Letters*, 5(11):985–988.
- Melosh, H., Ryan, E., and Asphaug, E. (1992). Dynamic fragmentation in impacts: Hydrocode simulation of laboratory impacts. *Journal of Geophysical Research: Planets*, 97(E9):14735–14759.
- Melosh, H. and Vickery, A. (1991). Melt droplet formation in energetic impact events. *Nature*, 350(6318):494.
- Melosh, H. J. (1979). Acoustic fluidization: A new geologic process? *Journal of Geophysical Research: Solid Earth*, 84(B13):7513–7520.
- Melosh, H. J. (1989). *Impact Cratering: A Geologic Process*. Oxford Univ. Press, New York.
- Melosh, H. J. (2011). *Planetary surface processes*, volume 13. Cambridge University Press.
- Merle, R., Nemchin, A., Grange, M., Whitehouse, M., and Pidgeon, R. (2014). High resolution u-pb ages of ca-phosphates in apollo 14 breccias: Implications for the age of the imbrium impact. *Meteoritics & Planetary Science*, 49(12):2241–2251.
- Metzger, A., Haines, E., Parker, R., and Radocinski, R. (1977). Thorium concentrations in the lunar surface. i-regional values and crustal content. In *Lunar and Planetary Science Conference Proceedings*, volume 8, pages 949–999.
- Metzger, A., Trombka, J., Peterson, L., Reedy, R., and Arnold, J. (1973). Lunar surface radioactivity: Preliminary results of the apollo 15 and apollo 16 gamma-ray spectrometer experiments. *Science*, 179(4075):800–803.
- Meyer, C. J., Brett, R. J., Hubbard, N. J., Morrison, D. A., McKay, D. S., Aitken, F. K., Takeda, H., and Schonfeld, E. (1971). Mineralogy, chemistry, and origin of the KREEP component in soil samples from the Ocean of Storms. *Proc. 2nd Lunar Sci. Conf.*, 1:393–411.
- Meyer, C. J. and Hubbard, N. J. (1970). High potassium, high phosphorous glass as important rock type in the Apollo 12 soil samples. *Meteoritics*, 5(9):210–211.
- Michael, G., Basilevsky, A., and Neukum, G. (2018). On the history of the early meteoritic bombardment of the moon: Was there a terminal lunar cataclysm? *Icarus*, 302:80–103.
- Minton, D., Fassett, C., Hirabayashi, M., Howl, B., and Richardson, J. (2018). Topographic degradation by impact cratering on airless bodies is dominated by diffusive erosion from distal ejecta. In *Lunar and Planetary Science Conference*, volume 49.
- Minton, D. A., Richardson, J. E., and Fassett, C. I. (2015). Re-examining the main asteroid belt as the primary source of ancient lunar craters. *Icarus*, 247:172–190.
- Mitchell, J. K., Bromwell, L. G., Carrier, W. D., Costes, N. C., and Scott, R. F. (1972). Soil mechanical properties at the Apollo 14 site. *Journal of Geophysical Research*, 77(29):5641–5664.

- Monteux, J. and Arkani-Hamed, J. (2016). Scaling laws of impact induced shock pressure and particle velocity in planetary mantle. *Icarus*, 264:246–256.
- Moore, H., Hodges, C., and Scott, D. (1974). Multiringed basins-illustrated by orientale and associated features. In *Lunar and Planetary Science Conference Proceedings*, volume 5, pages 71–100.
- Moore, H. J. and Baldwin, R. B. (1968). Ranger VIII and Gravity Scaling of Lunar Craters. *Science*, 159:333–4.
- Morgan, J. V., Gulick, S. P., Bralower, T., Chenot, E., Christeson, G., Claeys, P., Cockell, C., Collins, G. S., Coolen, M. J., Ferrière, L., et al. (2016). The formation of peak rings in large impact craters. *Science*, 354(6314):878–882.
- Morris, R. (1978). In situ reworking (gardening) of the lunar surface: Evidence from the Apollo cores. *Proc. Lunar Planet. Sci. Conf. 9th*, pages 1801–1811.
- Morris, R., Score, R., Dardano, C., and Heiken, G. (1983). Handbook of lunar soils, planetary materials branch pub. 67.
- Morris, R. V., See, T. H., and Hörz, F. (1986). Composition of the Cayley Formation at Apollo 16 as inferred from impact melt splashes. *Journal of Geophysical Research: Solid Earth*, 91(B13).
- Moynier, F., Koeberl, C., Beck, P., Jourdan, F., and Telouk, P. (2010). Isotopic fractionation of cu in tektites. *Geochimica et Cosmochimica Acta*, 74(2):799–807.
- Muller, P. M. and Sjogren, W. L. (1968). Mascons: Lunar mass concentrations. *Science*, 161(3842):680–684.
- Murray, J. (1980). Oscillating peak model of basin and crater formation. *The moon and the planets*, 22(3):269–291.
- Nahm, A. L., Öhman, T., and Kring, D. A. (2013). Normal faulting origin for the cordillera and outer rook rings of orientale basin, the moon. *Journal of Geophysical Research: Planets*, 118(2):190–205.
- Naney, M., Crawl, D., and Papike, J. (1976). The apollo 16 drill core-statistical analysis of glass chemistry and the characterization of a high alumina-silica poor/hasp/glass. In *Lunar and Planetary Science Conference Proceedings*, volume 7, pages 155–184.
- NASA Technical Report Server (1972). Apollo 15 Preliminary Science Report. Technical report.
- NASA Technical Report Server (1973). Apollo 17 Preliminary Science Report. Technical report.
- Neal, C. R., Hacker, M. D., Snyder, G. A., Taylor, L. A., Liu, Y.-G., and Schmitt, R. A. (1994). Basalt generation at the apollo 12 site, part 1: New data, classification, and re-evaluation. *Meteoritics*, 29(3):334–348.
- Nemchin, A., Pidgeon, R., Healy, D., Grange, M., Whitehouse, M., and Vaughan, J. (2009). The comparative behavior of apatite-zircon u-pb systems in apollo 14 breccias: Implications for the thermal history of the fra mauro formation. *Meteoritics & Planetary Science*, 44(11):1717–1734.

Nemchin, A., Pidgeon, R., Whitehouse, M., Vaughan, J. P., and Meyer, C. (2008). Sims u–pb study of zircon from apollo 14 and 17 breccias: implications for the evolution of lunar krep. *Geochimica et Cosmochimica Acta*, 72(2):668–689.

Nesvorný, D., Morbidelli, A., Vokrouhlický, D., Bottke, W., and Brož, M. (2002). The flora family: A case of the dynamically dispersed collisional swarm? *Icarus*, 157(1):155–172.

Neukum, G. (1983). Meteorite bombardment and dating of planetary surfaces. dissertation on attaining *venia legendi* (tenure) in the geophysics department in the faculty of geological sciences of the ludwig-maximilians university, munich, west germany. 186 pp. (translated from german).

Neukum, G. and Ivanov, B. (1994). Crater size distributions and impact probabilities on earth from lunar, terrestrial-planet, and asteroid cratering data. *Hazards due to Comets and Asteroids*, 359.

Neukum, G., Ivanov, B. A., and Hartmann, W. K. (2001). Cratering records in the inner solar system in relation to the lunar reference system. In *Chronology and evolution of Mars*, pages 55–86. Springer.

Norman, M., Adena, K., and Christy, A. (2012). Provenance and pb isotopic ages of lunar volcanic and impact glasses from the apollo 17 landing site. *Australian Journal of Earth Sciences*, 59(2):291–306.

Norman, M., Duncan, R. A., and Huard, J. J. (2010). Imbrium provenance for the apollo 16 descartes terrain: Argon ages and geochemistry of lunar breccias 67016 and 67455. *Geochimica et Cosmochimica Acta*, 74(2):763–783.

Norman, M. D. (2018). Impact ages, compositions, and bio-tectonic implications of lunar regolith glasses. In *The Geological Society America Annual Meeting*.

Norman, M. D., Duncan, R. A., and Huard, J. J. (2006). Identifying impact events within the lunar cataclysm from 40ar–39ar ages and compositions of apollo 16 impact melt rocks. *Geochimica et Cosmochimica Acta*, 70(24):6032–6049.

Norman, M. D. and Nemchin, A. A. (2014). A 4.2 billion year old impact basin on the moon: U–pb dating of zirconolite and apatite in lunar melt rock 67955. *Earth and Planetary Science Letters*, 388:387–398.

Nozette, S., Rustan, P., Pleasance, L. P., Kordas, J. F., Lewis, I. T., Park, H. S., Priest, R. E., Horan, D. M., Regeon, P., Lichtenberg, C. L., Shoemaker, E. M., Eliason, E. M., McEwen, a. S., Robinson, M. S., Spudis, P. D., Acton, C. H., Buratti, B. J., Duxbury, T. C., Baker, D. N., Jakosky, B. M., Blamont, J. E., Corson, M. P., Resnick, J. H., Rollins, C. J., Davies, M. E., Lucey, P. G., Malaret, E., Massie, M. a., Pieters, C. M., Reisse, R. a., Simpson, R. a., Smith, D. E., Sorenson, T. C., Breugge, R. W., and Zuber, M. T. (1994). The Clementine mission to the Moon: scientific overview. *Science*, 266(5192):1835–1839.

Oberbeck, V., Quaide, W., Mahan, M., and Paulson, J. (1973). Monte Carlo calculations of lunar Regolith thickness distributions. *Icarus*, 19(1):87–107.

Oberbeck, V. R. (1975). The Role of Ballistic Erosion and Sedimentation in Lunar Stratigraphy. *Reviews of Geophysics*, 13(2):337–362.

- Oberbeck, V. R. and Quaide, W. L. (1967). Estimated Thickness of a Fragmental Surface Layer of Oceanus Procellarum. *Journal of Geophysical Research*, 72(18):4697–4704.
- Oberbeck, V. R. and Quaide, W. L. (1968). Genetic Implications of Lunar Regolith Thickness Variations. *Icarus*, 9(1-3):446–465.
- O’Keefe, J. D. and Ahrens, T. J. (1977). Impact-induced energy partitioning, melting, and vaporization on terrestrial planets. In *Lunar and Planetary Science Conference Proceedings*, volume 8, pages 3357–3374.
- O’Keefe, J. D. and Ahrens, T. J. (1981). Impact cratering: The effect of crustal strength and planetary gravity. *Reviews of Geophysics*, 19(1):1–12.
- Öpik, E. (1958). Meteor impact on solid surface. *Irish Astronomical Journal*, 5:14.
- Öpik, E. (1960). The lunar surface as an impact counter. *Monthly Notices of the Royal Astronomical Society*, 120(5):404–411.
- Öpik, E. J. (1916). A note on the meteoric theory of lunar craters. *Mirovedenie*, 5:125–34. In Russian. [Reprinted in unpublished posthumous collection of early papers of Öpik from 1912–1921, compiled by J. McFarland in the Armagh Observatory in 1985, pp. 93–102].
- Öpik, E. (1958). On the catastrophic effect of collisions with celestial bodies. *Irish Astronomical Journal*, 5:34.
- Osae, S., Misra, S., Koeberl, C., Sengupta, D., and Ghosh, S. (2005). Target rocks, impact glasses, and melt rocks from the Lonar impact crater, India: Petrography and geochemistry. *Meteoritics & Planetary Science*, 40(9-10):1473–1492.
- Papike, J., Hodges, F., Bence, A., Cameron, M., and Rhodes, J. (1976). Mare basalts: crystal chemistry, mineralogy, and petrology. *Reviews of Geophysics*, 14(4):475–540.
- Park, J., Turrin, B. D., Herzog, G. F., Lindsay, F. N., Delaney, J. S., Swisher III, C. C., Uesugi, M., Karouji, Y., Yada, T., Abe, M., et al. (2015). 40Ar/39Ar age of material returned from asteroid 25143 itokawa. *Meteoritics & Planetary Science*, 50(12):2087–2098.
- Pierazzo, E., Vickery, A., and Melosh, H. (1997). A reevaluation of impact melt production. *Icarus*, 127(2):408–423.
- Pieters, C. M. (1982). Copernicus crater central peak: Lunar mountain of unique composition. *Science*, 215(4528):59–61.
- Pieters, C. M., Adams, J. B., Smith, M. O., Mouginiis-Mark, P. J., and Zisk, S. H. (1985). The nature of crater rays: The Copernicus example. *Journal of Geophysical Research*, 90(B14):12393–12413.
- Pieters, C. M., Staid, M. I., Fischer, E., Tompkins, S., and He, G. (1994). A sharper view of impact craters from clementine data. *Science*, 266(5192):1844–1848.

- Pike, R. (1977). Apparent depth/apparent diameter relation for lunar craters. In *Lunar and planetary science conference proceedings*, volume 8, pages 3427–3436.
- Pike, R. J. (1974). Depth/diameter relations of fresh lunar craters: Revision from spacecraft data. *Geophysical Research Letters*, 1(7):291–294.
- Pilkington, M. and Grieve, R. (1992). The geophysical signature of terrestrial impact craters. *Reviews of Geophysics*, 30(2):161–181.
- Pollastro, R. M. (1993). Origin and clay-mineral genesis of the Cretaceous/Tertiary boundary unit, western interior of North America. *Clays and Clay Minerals*, 41:7–25.
- Pope, K. O., Ocampo, A. C., Fischer, A. G., Alvarez, W., Fouke, B. W., Webster, C. L., Vega, F. J., Smit, J., Fritsche, A. E., and Claeys, P. (1999). Chicxulub impact ejecta from Albion island, Belize. *Earth and Planetary Science Letters*, 170(4):351–364.
- Potter, R. W. (2015). Investigating the onset of multi-ring impact basin formation. *Icarus*, 261:91–99.
- Potter, R. W., Kring, D. A., and Collins, G. S. (2013). Quantifying the attenuation of structural uplift beneath large lunar craters. *Geophysical Research Letters*, 40(21):5615–5620.
- Press, W. H., Teukolsky, S. A., Vetterling, W. T., and Flannery, B. P. (1992). Numerical recipes in fortran 77, vol. 1. *New York, NY: Press Syndicate of the University of Cambridge*.
- Prettyman, T., Hagerty, J., Elphic, R., Feldman, W., Lawrence, D., McKinney, G., and Vaniman, D. (2006). Elemental composition of the lunar surface: Analysis of gamma ray spectroscopy data from lunar prospector. *Journal of Geophysical Research: Planets*, 111(E12).
- Pyne, S. J. (1980). a great engine of researchg. us geological survey. *The Scientific Ideas of GK Gilbert: An Assessment on the Occasion of the Centennial of the United States Geological Survey (1879-1979)*, 183:1.
- Quaide, W. and Oberbeck, V. (1975). Development of the mare regolith: Some model considerations.
- Quaide, W. L. and Oberbeck, V. R. (1968). Thickness determinations of the lunar surface layer from lunar impact craters. *Journal of Geophysical Research*, 73(16):5247–5270.
- Quantin, C., Mangold, N., Hartmann, W. K., and Allemand, P. (2007). Possible long-term decline in impact rates: 1. Martian geological data. *Icarus*, 186(1):1–10.
- Racki, G., Koeberl, C., Viik, T., Jagt-Yazykova, E. A., and Jagt, J. W. (2014). Ernst julius öpik’s (1916) note on the theory of explosion cratering on the moon’s surfacethe complex case of a long-overlooked benchmark paper. *Meteoritics & Planetary Science*, 49(10):1851–1874.
- Rasorenov, S., Kanel, G., Fortov, V., and Abasehov, M. (1991). The fracture of glass under high-pressure impulsive loading. *International Journal of High Pressure Research*, 6(4):225–232.

- Reid, A. M., Duncan, A. R., and Richardson, S. H. (1977). In search of LKFM. In *Lunar and Planetary Science Conference Proceedings*, volume 8, pages 2321–2338.
- Rein, H. and Liu, S.-F. (2012). Rebound: an open-source multi-purpose n-body code for collisional dynamics. *Astronomy & Astrophysics*, 537:A128.
- Rhodes, J., Blanchard, D., Dungan, M., Brannon, J., and Rodgers, K. (1977). Chemistry of apollo 12 mare basalts-magma types and fractionation processes. In *Lunar and Planetary Science Conference Proceedings*, volume 8, pages 1305–1338.
- Rhodes, J. M. (1977). Some Compositional Aspects of Lunar Regolith Evolution. *Philosophical Transactions of the Royal Society A: Mathematical, Physical and Engineering Sciences*, 285(1327):293–301.
- Rhodes, J. M., Rodgers, K. V., Shih, C., Bansal, B. M., and Nyquist (1974). The relationships between geology and soil chemistry at the Apollo 17 landing site. *Proc. 5th Lunar Sci. Conf., Geochim. cosmochim. Acta Suppl.*, 5(2):1097–1117.
- Richardson, J. E. (2009). Cratering saturation and equilibrium : A new model looks at an old problem. 204:697–715.
- Richardson, J. E. (2011). Modeling impact ejecta plume evolution: A comparison to laboratory studies. *Journal of Geophysical Research: Planets*, 116(E12).
- Richardson, J. E., Melosh, H. J., Lisse, C. M., and Carcich, B. (2007). A ballistics analysis of the Deep Impact ejecta plume: Determining Comet Tempel 1’s gravity, mass, and density. *Icarus*, 191(2 SUPPL.):176–209.
- Ridley, W., Reid, A., Warner, J., Brown, R., Gooley, R., and Donaldson, C. (1973). Glass compositions in apollo 16 soils 60501 and 61221. In *Lunar and Planetary Science Conference Proceedings*, volume 4, page 309.
- Righter, K., Abell, P., Agresti, D., Berger, E. L., Burton, A. S., Delaney, J. S., Fries, M., Gibson, E., Haba, M. K., Harrington, R., et al. (2015). Mineralogy, petrology, chronology, and exposure history of the chelyabinsk meteorite and parent body. *Meteoritics & Planetary Science*, 50(10):1790–1819.
- Robbins, S. J. (2014). New crater calibrations for the lunar crater-age chronology. *Earth and Planetary Science Letters*, 403:188–198.
- Robinson, M. S., Brylow, S. M., Tschimmel, M., Humm, D., Lawrence, S. J., Thomas, P. C., Denevi, B. W., Bowman-Cisneros, E., Zerr, J., Ravine, M. a., Caplinger, M. a., Ghaemi, F. T., Schaffner, J. a., Malin, M. C., Mahanti, P., Bartels, a., Anderson, J., Tran, T. N., Eliason, E. M., McEwen, a. S., Turtle, E., Jolliff, B. L., and Hiesinger, H. (2010). Lunar Reconnaissance Orbiter Camera (LROC) Instrument Overview. *Space Science Reviews*, 150(1-4):81–124.
- Ross, H. P. (1968). A simplified mathematical model for lunar crater erosion. *Journal of Geophysical Research*, 73(4):1343–1354.
- Ruedas, T. (2017). Globally smooth approximations for shock pressure decay in impacts. *Icarus*, 289:22–33.
- Russ, P. G., Burnett, D. S., and Wasserburg, G. J. (1972). Lunar neutron stratigraphy. *Earth and Planetary Science Letters*, 15(2):172–186.

- Ryder, G. (1990). Lunar samples, lunar accretion and the early bombardment of the moon. *Eos, Transactions American Geophysical Union*, 71(10):313–323.
- Schaal, R. and Hörz, F. (1980). Experimental shock metamorphism of lunar soil. In *Lunar and Planetary Science Conference Proceedings*, volume 11, pages 1679–1695.
- Schmitt, H. H., Trask, N. J., and Shoemaker, E. M. (1967). *Geologic map of the Copernicus quadrangle of the Moon*. US Geological Survey.
- Schmitz, B., Häggström, T., and Tassinari, M. (2003). Sediment-dispersed extraterrestrial chromite traces a major asteroid disruption event. *Science*, 300(5621):961–964.
- Schnetzler, C. C. and Philpotts, J. A. (1971). Alkali, alkaline earth, and rare-earth element concentrations in some Apollo 12 soils, rocks, and separated phases. *Proc. 2nd Lunar Sci. Conf.*, 2:1101–1122.
- Schonfeld, E. and Meyer, C. J. (1972). The abundances of components of the lunar soils by a least-squares mixing model and the formation age of KREEP. *Proc. 3rd Lunar Sci. Conf. (Suppl. 3, Geochemica et Cosmochimica Acta)*, 2:1397–1420.
- Schulte, P., Stinnesbeck, W., Stüben, D., Kramar, U., Berner, Z., Keller, G., and Adatte, T. (2003). Fe-rich and K-rich mafic spherules from slumped and channelized Chicxulub ejecta deposits in the northern La Sierrita area, NE Mexico. *International Journal of Earth Sciences*, 92(1):114–142.
- Schultz, P. H. and Mustard, J. F. (2004). Impact melts and glasses on Mars. *Journal of Geophysical Research: Planets*, 109:E01001.
- Sheehan, W. and Baum, R. (1995). Observations and inference: Johann Hieronymus Schroeter, 1745-1816. *Journal of the British Astronomical Association*, 105:171–175.
- Shoemaker, E., Batson, R., Bean, A., Conrad Jr, C., Dahlem, D., Goddard, E., Hait, M., Larson, K., Schaber, G., Schleicher, D., et al. (1970). Preliminary geologic investigation of the Apollo 12 landing site: Part A: Geology of the Apollo 12 landing site. *NASA SP-235*, pages 113–156.
- Shoemaker, E. M. (1959). Impact mechanics at meteor crater, arizona. Technical report, US Geological Survey],.
- Shoemaker, E. M. (1965). Preliminary Analysis of the Fine Structure of the Lunar Surface in Mare Cognitum.
- Shoemaker, E. M. (1970). Origin of fragmental debris on the lunar surface and the history of bombardment of the Moon.
- Shoemaker, E. M., Wolfe, R. F., and Shoemaker, C. S. (1990). Asteroid and comet flux in the neighborhood of Earth. *Geological Society of America Special Papers*, 247:155–170.
- Simon, S. B., Papike, J. J., Gosselin, D. C., Laul, J. C., Hughes, S. S., and Schmitt, R. A. (1990). Petrology and Chemistry of Apollo 17 Regolith Breccias: A History of Mixing of Highland and Mare Basalt. *Proceeding of 20th Lunar and Planetary Science Conference*, pages 219–230.

Simon, S. B., Papike, J. J., and Laul, J. C. (1981). The lunar regolith: Comparative studies of the Apollo and Luna sites. Petrology of soils from Apollo 17, Luna 16, 20, and 24. *Proc. Lunar Planet. Sci. Conf. 12B*, pages 371–388.

Smit, J. and Hertogen, J. (1980). An extraterrestrial event at the Cretaceous-Tertiary boundary. *Nature*, 285(5762):198–200.

Soderblom, L. A. (1970). A model for small-impact erosion applied to the lunar surface. *Journal of Geophysical Research*, 75(14):2655–2661.

Solomon, S. C. and Head, J. W. (1980). Lunar Mascon Basins ' Lava Filling , Tectonics , and Evolution of the Lithosphere. *Reviews of Geophysics and Space Physics*, 18:107–141.

Speyerer, E. J., Povilaitis, R. Z., Robinson, M. S., Thomas, P. C., and Wagner, R. V. (2016). Quantifying crater production and regolith overturn on the moon with temporal imaging. *Nature*, 538(7624):215.

Spudis, P., Zellner, N., Delano, J., Whittet, D., and Fessler, B. (2002). Petrologic mapping of the moon: a new approach. In *Lunar and Planetary Science Conference*, volume 33.

Spudis, P. D. and Ryder, G. (1985). Geology and petrology of the Apollo 15 landing site: Past, present, and future understanding. *Eos. Trans. AGU*, 66(43):721–726.

Stadermann, F. J., Heusser, E., Jessberger, E. K., Lingner, S., and Stöffler, D. (1991). The case for a younger imbrium basin: New 40Ar-39Ar ages of apollo 14 rocks. *Geochimica et Cosmochimica Acta*, 55(8):2339–2349.

Stewart, S. T. and Valiant, G. J. (2006). Martian subsurface properties and crater formation processes inferred from fresh impact crater geometries. *Meteoritics & Planetary Science*, 41(10):1509–1537.

Stöffler, D., Bischoff, A., Borchardt, R., Burghelle, A., Deutsch, A., Jessberger, E., Ostertag, R., Palme, H., Spettel, B., Reimold, W., et al. (1985). Composition and evolution of the lunar crust in the descartes highlands, apollo 16. *Journal of Geophysical Research: Solid Earth*, 90(S02):C449–C506.

Stöffler, D., Ryder, G., Ivanov, B. A., Artemieva, N. A., Cintala, M. J., and Grieve, R. A. F. (2006). Cratering History and Lunar Chronology. *Reviews in Mineralogy & Geochemistry*, 60(4):519–596.

Strom, R. G., Malhotra, R., Ito, T., Yoshida, F., and Kring, D. A. (2005). The origin of planetary impactors in the inner solar system. *Science*, 309(5742):1847–1850.

Swain, M. and Hagan, J. (1976). Indentation plasticity and the ensuing fracture of glass. *Journal of Physics D: Applied Physics*, 9(15):2201.

Swann, G. A., Bailey, N. C., Batson, R. M., Freeman, V. L., Hait, M. H., Head, J. W., Holt, H. E., Howard, K. A., Irwin, J. B., Larson, K. B., Muehlberger, W. R., Reed, V. S., Rennilson, J. J., Schaber, G. G., Scott, D. R., Silver, L. T., Sutton, R. L., Ulrich, G. E., Wilshire, H. G., and Wolfe, E. W. (1972). Preliminary geologic investigation of the Apollo 15 landing site. *Apollo 15 Preliminary Science Report, NASA SP-289*.

Swann, G. A., Bailey, N. G., Batson, R. M., Eggleton, R. E., Hait, M. H., Holt, H. E., Larson, K. B., Reed, V. S., Schaber, G. G., Sutton, R. L., Trask, N., Ulrich, G. E., and Wilshire, H. G. (1977). Geology of the Apollo 14 landing site in the Fra Mauro highlands. *Geological Survey Professional Paper 880*.

Swindle, T. and Kring, D. (2008). Chronological evidence for the late heavy bombardment in ordinary chondrite meteorites. In *Workshop on the Early Solar System Impact Bombardment*, volume 1439, pages 59–60.

Swindle, T. D., Isachsen, C. E., Weirich, J. R., and Kring, D. A. (2009). 40Ar-39Ar ages of h-chondrite impact melt breccias. *Meteoritics & Planetary Science*, 44(5):747–762.

Symes, S. J., Sears, D. W., Akridge, D., Huang, S., and BENOIT, P. H. (1998). The crystalline lunar spherules: Their formation and implications for the origin of meteoritic chondrules. *Meteoritics & Planetary Science*, 33(1):13–29.

Taylor, S. R. (1982). *Planetary Science: A Lunar Perspective*. Lunar and Planetary Institute.

Tera, F., Papanastassiou, D., and Wasserburg, G. (1973). A lunar cataclysm at ~ 3.95 ae and the structure of the lunar crust. In *Lunar and Planetary Science Conference*, volume 4.

Tera, F., Papanastassiou, D., and Wasserburg, G. (1974). Isotopic evidence for a terminal lunar cataclysm. *Earth and Planetary Science Letters*, 22(1):1–21.

Thein, J. (1987). A tektite layer in Upper Eocene sediments of the New-Jersey continental-slope (site-612, leg-95). *Initial reports of the deep sea drilling project*, 95:565–579.

Timoshenko, S. and Goodier, J. (1982). *Theory of Elasticity*. Engineering societies monographs. McGraw-Hill.

Tompkins, S. and Pieters, C. M. (2010). Spectral characteristics of lunar impact melts and inferred mineralogy. *Meteoritics & Planetary Science*, 45(7):1152–1169.

Trombka, J. I., Arnold, J. R., Adler, I., Metzger, A. E., and Reedy, R. C. (1974). Lunar elements analysis obtained from the Apollo Gamma-Ray and X-ray remote sensing experiment. *THE PROCEEDINGS OF THE SOVIET-AMERICAN CONFERENCE ON THE COSMOCHEMISTRY OF THE MOON AND PLANETS*.

Turner, G. and Cadogan, P. H. (1975). The history of lunar bombardment inferred from Ar-40-Ar-39 dating of highland rocks. In *Lunar and Planetary Science Conference Proceedings*, volume 6 of *Lunar and Planetary Science Conference Proceedings*, pages 1509–1538.

Vaniman, D. and Papike, J. (1977). Very low ti/vlt/basalts-a new mare rock type from the apollo 17 drill core. In *Lunar and Planetary Science Conference Proceedings*, volume 8, pages 1443–1471.

Vokrouhlický, D., Bottke, W. F., and Nesvorný, D. (2017). Forming the Flora family: Implications for the Near-Earth asteroid population and large terrestrial planet impactors. *The Astronomical Journal*, 153(4):172.

- Wanke, H., Baddenhausen, H., Balacesu, A., Teschke, F., Spettel, B., Dreibus, G., Palme, H., Quijano-Rico, M., Kruse, H., Wlotzka, F., and Begemann, F. (1972). Multielement analyses of lunar samples and some implications of the results. *Proc. 3rd Lunar Sci. Conf.*, Supplement:1251–1268.
- Wasson, J. T. and Baedeker, P. A. (1972). Provenance of Apollo 12 KREEP. *Proc. 3rd Lunar Sci. Conf.*, 2:1315–1326.
- Wegener, A. L. (1920a). Die aufsturzhypothese der mondkrater. *Sirius*, 53:189–194.
- Wegener, A. L. (1920b). Versuche zur aufsturztheorie der mondkrater: Nova acta abhandlungen der leopoldina-carolinae deutschen akademie der naturforscher 106, 111 p.
- Wegener, A. L. (1921). Die entstehung der mondkrater: Braunschweig, druck und verlag von friedrich vieweg und sohn, 48 p. (translated by a. m. clal sengr, 1975, in the origin of lunar craters: The moon, v. 14, p. 211-236.).
- Weirich, J., Swindle, T., and Isachsen, C. (2012). 40ar-39ar age of northwest africa 091: More evidence for a link between l chondrites and fossil meteorites. *Meteoritics & Planetary Science*, 47(8):1324–1335.
- Wentworth, S. and McKay, D. (1991). Apollo 14 glasses and the origin of lunar soils. In *Lunar and Planetary Science Conference Proceedings*, volume 21, pages 185–192.
- Wentworth, S., McKay, D., Lindstrom, D., Basu, A., Martinez, R., Bogard, D., and Garrison, D. (1994). Apollo 12 ropy glasses revisited. *Meteoritics & Planetary Science*, 29(3):323–333.
- Wentworth, S., Taylor, G., Warner, R., Keil, K., Ma, M.-S., and Schmitt, R. (1979). The unique nature of apollo 17 vlt mare basalts. In *Lunar and Planetary Science Conference Proceedings*, volume 10, pages 207–223.
- Wilhelms, D. E. (1987). The geologic history of the Moon. *U.S. Geological Survey Professional Paper 1348*, pages 283–292.
- Wood, C. and Head, J. (1976). Comparison of impact basins on mercury, mars and the moon. In *Lunar and Planetary Science Conference Proceedings*, volume 7, pages 3629–3651.
- Wood, J. A. (1970). Petrology of the Lunar Soil and Geophysical Implications. *Journal of Geophysical Research*, 75(32):6497–6513.
- Wood, J. A. (1972). Fragments of terra rock in the apollo 12 soil samples and a structural model of the moon. *Icarus*, 16(3):462–501.
- Wood, J. A., Dickey, J. S., J., Marvin, U. B., and Powell, B. N. (1970a). Lunar anorthosites and a geophysical model of the moon. *Proceeding of the Apollo 11 Lunar Science Conference*, 1:965–988.
- Wood, J. A., Dickey Jr, J., Marvin, U. B., and Powell, B. (1970b). Lunar anorthosites and a geophysical model of the moon. *Geochimica et Cosmochimica Acta Supplement*, 1:965.

- Wood, J. A., Marvin, U. B., Powell, B. N., and Dickey, J. S., J. (1970c). Mineralogy and petrology of the Apollo 11 lunar samples. *Smithsonian Astrophys. Observ. Spec. Rep.*, 307.
- Woronow, A. (1978). A general cratering-history model and its implications for the lunar highlands. *Icarus*, 34(1):76–88.
- Wünnemann, K., Collins, G., and Osinski, G. (2008). Numerical modelling of impact melt production in porous rocks. *Earth and Planetary Science Letters*, 269(3-4):530–539.
- Wünnemann, K., Engelmann, J., Luther, R., and Hamann, C. (2017). Impact-induced shock melting and ejection of material in an asteroidal environment-implications for the deficit in melt agglutinates in itokawa samples. In *Lunar and Planetary Science Conference*, volume 48.
- Xiao, Z. and Werner, S. C. (2015). Size-frequency distribution of crater populations in equilibrium on the moon. *Journal of Geophysical Research: Planets*, 120(12):2277–2292.
- Yamamoto, S., Barnouin-Jha, O. S., Toriumi, T., Sugita, S., and Matsui, T. (2009). An empirical model for transient crater growth in granular targets based on direct observations. *Icarus*, 203(1):310–319.
- Yamamoto, S., Hasegawa, S., Suzuki, A., and Matsunaga, T. (2017). Impact velocity dependence of transient cratering growth. *Journal of Geophysical Research: Planets*, 122(5):1077–1089.
- Yamamoto, S., Wada, K., Okabe, N., and Matsui, T. (2006). Transient crater growth in granular targets: An experimental study of low velocity impacts into glass sphere targets. *Icarus*, 183(1):215–224.
- Young, R. A. (1976). The morphological evolution of mare-highland contacts: A potential measure of relative mare surface age. *Proc. Lunar Sci. Conf. 7th*, pages 2801–2816.
- Yue, Z., Johnson, B., Minton, D., Melosh, H., Di, K., Hu, W., and Liu, Y. (2013). Projectile remnants in central peaks of lunar impact craters. *Nature Geoscience*, 6(6):435.
- Zahnle, K., Alvarellós, J. L., Dobrovolskis, A., and Hamill, P. (2008). Secondary and sesquinary craters on europa. *Icarus*, 194(2):660–674.
- Zeigler, R., Korotev, R., Jolliff, B., Haskin, L., and Floss, C. (2004). Apollo 16 mafic glass: Geochemistry, provenance, and implications. In *Lunar and Planetary Science Conference*, volume 35.
- Zeigler, R. A., Korotev, R. L., Jolliff, B. L., Haskin, L. A., and Floss, C. (2006). The geochemistry and provenance of apollo 16 mafic glasses. *Geochimica et Cosmochimica Acta*, 70(24):6050–6067.
- Zellner, N. (2018). The first billion years: Impacts and life on earth (and mars?). *LPI Contributions*, 2107.

Zellner, N. and Delano, J. (2015). $^{40}\text{Ar}/^{39}\text{Ar}$ ages of lunar impact glasses: Relationships among ar diffusivity, chemical composition, shape, and size. *Geochimica et Cosmochimica Acta*, 161:203–218.

Zellner, N., Delano, J., Swindle, T., Barra, F., Olsen, E., and Whittet, D. (2006). Did a transient increase in the impact flux occur 800 ma ago? In *37th Annual Lunar and Planetary Science Conference*, volume 37.

Zellner, N., Delano, J., Swindle, T., Barra, F., Olsen, E., and Whittet, D. (2009). Evidence from $^{40}\text{Ar}/^{39}\text{Ar}$ ages of lunar impact glasses for an increase in the impact rate 800 ma ago. *Geochimica et Cosmochimica Acta*, 73(15):4590–4597.

Zellner, N., Spudis, P., Delano, J., Whittet, D., and Swindle, T. (2003). Geochemistry and impact history at the apollo 16 landing site. In *Lunar and Planetary Science Conference*, volume 34.

Zellner, N., Swindle, T., Barra, F., Delano, J., Tibbetts, N., Whittet, D., and Spudis, P. (2005). Chemical and isotopic analyses of apollo 16 glasses: an integrated approach. In *36th Annual Lunar and Planetary Science Conference*, volume 36.

Zellner, N. E. (2017). Cataclysm no more: new views on the timing and delivery of lunar impactors. *Origins of Life and Evolution of Biospheres*, 47(3):261–280.

Zellner, N. E. B., Spudis, P. D., Delano, J. W., and Whittet, D. C. B. (2002). Impact glasses from the Apollo 14 landing site and implications for regional geology. *Journal of Geophysical Research*, 107:1–13.

Zuber, M. T., Smith, D. E., Neumann, G. A., Goossens, S., Andrews-Hanna, J. C., Head, J. W., Kiefer, W. S., Asmar, S. W., Konopliv, A. S., Lemoine, F. G., et al. (2016). Gravity field of the orientale basin from the gravity recovery and interior laboratory mission. *Science*, 354(6311):438–441.

VITA

YA-HUEI HUANG 黃雅惠

EDUCATION

Ph.D. in Earth, Atmospheric, and Planetary Sciences, Purdue University, USA 2012-2018 (defended, November 2 2018)

M. Sc. in Physics, National Tsing Hua University, Taiwan 2008-2010

B. Sc. in Physics, National Chung Cheng University, Taiwan, 2003-2008

EMPLOYMENT

Graduate Research Assistant, Purdue University, 2014-present (Advisor: Dr. David Minton)

Graduate Teaching Assistant, Purdue University, 2012-2014

Research Assistant, National Taiwan Normal University, 2010-2012 (Employer: Dr. Chi-Ming Chen)

Graduate Research Assistant, National Tsing Hua University 2008-2010 (Advisor: Dr. Ing-Guey Jiang)

Undergraduate Research Assistant, National Chung Cheng University, 2007 (Advisor: Dr. Chih-Yung Chien, Johns Hopkins University)

RESEARCH PUBLICATIONS

Y.-H. Huang, D.A. Minton, N.E.B. Zellner, M. Hirabayashi, J.E. Richardson, C.I. Fassett (2018). "No Change in Recent Lunar Impact Flux Required Based on Modeling of Impact Glass Spherule Age Distributions." *Geophysical Research Letters*, 45, 6805-6813.

J. R. Elliott, **Y.-H. Huang**, D.A. Minton, A.M. Freed (2018). "The Length of Lunar Crater Rays Explained Using Secondary Crater Scaling." *Icarus*, 312, 231-246.

Y.-H. Huang, D.A. Minton, M. Hirabayashi, J.R. Elliott, C.I. Fassett, N.E.B. Zellner (2017), "Heterogeneous Impact Transport on the Moon." *Journal of Geophysical Research: Planets*, 122, 1158-1180.

Y.-H. Huang, and C.-M. Chen (2012), "Statistical Analysis and Computational Prediction of Helical Kinks in Membrane Proteins." *Journal of Computer-Aided Molecular Design*, 10, 1171-1185.

Y.-H. Huang, and I.-G. Jiang (2010), "The Velocity-Size Relation for Members of Asteroid Families." (Master thesis)

AWARDS

NASA Earth and Space Science Fellowship 2015-2018

"No Change in Recent Lunar Impact Flux Required Based on Modeling of Impact Glass Spherule Age Distributions" on Daily News in *NewScientist* "Why a rake on the moon messed up our theories of life on Earth", September, 14 2018.

"No Change in Recent Lunar Impact Flux Required Based on Modeling of Impact Glass Spherule Age Distributions" on News in *Phys.org* "Age bias exists even in outer spacein samples collected by Apollo astronauts", September 11, 2018.

"Heterogeneous Impact Transport on the Moon" on Research Spotlight in *Eos*, June 7 2017

Purdue Research Foundation Research Assistantship 2014-2015

Taiwan Fund for Children and Families Scholarship 2003-2010

Private Ming-Da High School Scholarship 2000-2003

TEACHING AND OUTREACH

ScienceScape Camp held by Purdue's The Science Diversity Office, June 2018
 Second Annual Earth Science Passport Day held in Imagination Station 2017
 Imagination Station Outreach Event 2016
 Certification for Classroom Communication in ESL for TAs (Purdue University) 2014
 Spring Fest Event (Department of Earth, Atmospheric, and Planetary Sciences Purdue University) 2013
 International Global Fest (International Center, Purdue University) 2012
 General Physics I and II Teaching Assistant (National Tsing Hua University) 2010

CONFERENCE ABSTRACTS

- Y.-H. Huang, D.A. Minton, N.E.B. Zellner, M. Hirabayashi, J.R. Elliott, C.I. Fassett (2018) "WHAT DO APOLLO IMPACT GLASSES TELL US ABOUT POST-COPERNICAN IMPACT FLUX?" Geological Society of America Annual Meeting held in Indianapolis, U.S. A. (Invited talk).
- Y.-H. Huang, D.A. Minton, J.R. Elliott, N.E.B. Zellner. (2018) "WHAT HAPPENED 800 MILLION YEARS AGO ON THE MOON?" *Bombardment: Shaping Planetary Surfaces and Their Environments workshop* (Talk).
- Y.-H. Huang, D.A. Minton, N.E.B. Zellner, M. Hirabayashi, J.E. Richardson, C.I. Fassett. (2018) "No Change in the Lunar Impact Flux Through the Copernican Period from Modeling Impact Glass Spherule Age Distribution in Lunar Regolith." 49th Lunar Planetary Science Conference (Talk).
- Y.-H. Huang, D.A. Minton, N.E.B. Zellner, M. Hirabayashi, J.E. Richardson, C.I. Fassett. (2017) "No Change in the Lunar Impact Flux Through the Copernican Period from Modeling Impact Glass Spherule Age Distribution in Lunar Regolith." Geological Society of America Annual Meeting held in Seattle, U.S.A. (Talk).
- Y.-H. Huang, D.A. Minton, M. Hirabayashi, J.R. Elliott, C.I. Fassett, N.E.B. Zellner. (2017) "Heterogeneous Impact Transport on the Moon." New View of the Moon 2 Conference (Talk).
- Y.-H. Huang, T. Hirabayashi, D.A. Minton, J.R. Elliott, A. Freed, C.I. Fassett, J.E. Richardson. (2016) "The Role of Vertical Mixing Process Across Mare and Highland Contacts." 47th Lunar and Planetary Science Conference. (Poster)
- T. Hirabayashi, D.A. Minton, H.J. Melosh, C. Milbury, Y.-H. Huang, J.M. Soderblom. (2016) "Equilibrium State in Impact-Generated Porosity on a Lunar Surface." 47th Lunar and Planetary Science Conference. (Poster)
- J. R. Elliott, Y.-H. Huang, D.A. Minton, A.M. Freed. (2016) "The Length of Lunar Crater Rays Explained Using Secondary Crater Scaling." 47th Lunar and Planetary Science Conference. (Poster)
- Y.-H. Huang, D.A. Minton, J. Richardson, B. Cohen, C. Fassett, and N. Zeller. (2015) "Simulating Three-Dimensional Regolith Transport with the Cratered Terrain Evolution Model." Workshop on Issues in Crater Studies and the Dating of Planetary Surfaces. (Talk)
- Y.-H. Huang and D.A. Minton (2014). "Modeling the Provenance of Crater Ejecta." Division for Planetary Sciences Meeting. (Poster)
- S. Saikia, A. Das, F. Laipert, C. Dapkus, J. Kendall, T. Bowling, J. Steckloff, S. Holbert, K. Graves, T. Antony, R. Bobick, Y.-H. Huang, J. Stuart, D. A. Minton, J. M. Longuski. (2014) "Marching Towards Troy: Exploration of Jupiter Trojan Asteroids." 11th International Planetary Probe Workshop (First Prize Outstanding Student Poster).
- S. Saikia, A. Das, F. Laipert, C. Dapkus, J. Kendall, T. Bowling, J. Steckloff, S. Holbert, K. Graves, T. Antony, R. Bobick, Y.-H. Huang, J. Stuart, D. A. Minton, J. M. Longuski. (2014) "Voyage to Troy: A

Mission Concept for the Exploration of the Trojan Asteroids.” Asteroids, Comets, and Meteors (ACM).

- Y.-H. Huang, D.A. Minton, J.E. Richardson (2014). “Modeling Topographic Change by the Ballistic Sedimentation from Orientale Ejecta.” 45th Lunar and Planetary Science Conference.
- Y.-H. Huang, and I.-G. Jiang (2010). “The Velocity-Size Relation for Members of Asteroid Families.” The Royal Physical Society of Republic of China. (Poster)